Advanced Optical Microscopy Toolkits for Non-Invasive Imaging in Oncology

by

Sam Osseiran

B.Eng., Polytechnique Montréal (2013)

Submitted to the Harvard-MIT Program in Health Sciences and Technology
in partial fulfillment of the requirements for the degree of

Doctor of Philosophy in Medical Engineering and Medical Physics

at the

MASSACHUSETTS INSTITUTE OF TECHNOLOGY

September 2018

Signature redacted

Author .....
Harvard-MIT Program in Health Sciences and Technology
August 24, 2018

Signature redacted

Certified by .....
Conor L. Evans, PhD
Assistant Professor of Dermatology, Harvard Medical School,
Wellman Center for Photomedicine, Massachusetts General Hospital
Thesis Supervisor

Signature redacted

Accepted by .....
Emery N. Brown, MD, PhD
Director, Harvard-MIT Program in Health Sciences and Technology
Professor of Computational Neuroscience and Health Sciences and Technology

Advanced Optical Microscopy Toolkits for Non-Invasive Imaging in Oncology

by

Sam Osseiran

Submitted to the Harvard-MIT Program in Health Sciences and Technology
on August 24, 2018, in partial fulfillment of the
requirements for the degree of
Doctor of Philosophy in Medical Engineering and Medical Physics

Abstract

Despite significant advances in the fields of biophotonics and oncology alike, several challenges persist in the study, assessment, and treatment of cancer, ranging from the accurate identification and examination of potential risk factors, early diagnosis of dysplastic lesions, and monitoring of the complex heterogeneity of cellular populations within tumors. To study such dynamics at the microscale, non-invasive optical toolkits offer the potential to identify, characterize, and visualize key molecules and their interactions in their native biological context, ranging from *in vitro* cell cultures to *in vivo* studies in both animal models and humans. In the present thesis, examples of such applications of optical tools will be presented, including: (1) the assessment of cellular oxidative stress in *ex vivo* human skin cultures by imaging endogenous and exogenous fluorescent compounds using two-photon excitation fluorescence (TPEF) and fluorescence lifetime imaging microscopy (FLIM); (2) visualizing water and lipid distribution as well as cellular morphology using coherent Raman scattering (CRS) imaging techniques in the stratum corneum, the most superficial layer of the epidermis; (3) using photoconvertible labels to optically tag cell subpopulations of interest *in situ* for long-term monitoring of heterogeneous cell cultures from *in vitro* monolayers to *in vivo* xenograft models; (4) visualizing melanin species in the context of melanoma with coherent anti-Stokes Raman scattering (CARS) and sum-frequency absorption (SFA) microscopies. Altogether, development of such advanced microscopy toolkits will serve to improve both understanding of cancer pathology, as well as to validate clinical diagnostic and therapeutic strategies.

Thesis Supervisor: Conor L. Evans, PhD
Title: Assistant Professor of Dermatology, Harvard Medical School, Wellman Center for Photomedicine, Massachusetts General Hospital

Acknowledgments

None of the work presented in this thesis would have been possible without all the wonderful people that I have had the pleasure of calling my friends and colleagues throughout the past 5 years. First and foremost, an enormous thank you to all the members — past and present — of the Evans team. I have had the incredible privilege of working closely with a number of talented graduate students (Alex Nichols and Joachim "Api" Pruessner), postdoctoral fellows (Tracy Wang, Lauren Austin, Zongxi Li, Manolis Rousakis, Gayatri Joshi, Sinyoung Jeong, Haley Marks, Alex Fast, Amin Feizpour, John Nguyen, Juanpe Cascales-Sandoval, and others), lab technicians (Nick Nowell, Jawad Hoballah, Fatima Mubarak, Raymond Lopez, and Michael Murphy), as well as our quintessential lab admin (Alice Chao). Of course, this fantastic team was led by Conor Evans, who has taught me virtually all I know about the implementation and use and optical imaging. From the informal white board chalk talks in his office to his coaching sessions at my very first international conference (SPIE Photonics West back in January 2015), Conor has mentored me throughout all critical stages of graduate school. It is thanks to him — and, of course, the various iterations of the lab team — that I have become the well-rounded scientist I am today. Of all the learning and life experiences I will have gained throughout the 5 years spent within the Evans group however, the daily banter, general camaraderie, and truly awesome work atmosphere within the team is certainly what I will remember and cherish most of all.

On the topic of mentorship, I would also like to extend my thanks to Dr. Jagesh Shah, who has served as my thesis committee chair, as well as Dr. Gabriela Schlau-Cohen, who agreed to take the role of thesis reader. Their considerable advice and guidance have helped navigate my scientific curiosity throughout the final years of graduate school, in addition to helping shape this thesis into the complete body of work that it is.

Next, I owe many thanks to my roommates over the past few years: Chris Lee, Benny Maimon, Fernando Martinez, and Gio Sturla. Each one of you have con-

tributed in your own ways to making life on Saint Paul Street the adventure that it was. Additional thanks go out to Taylor Gill and Colin Buss, without whom Thursday nights would not have been the same. Another particular round of thanks go out to my dearest friends Emily Lindemer and Liam Loscalzo, who have been my family away from home for my entire time in Boston. From the evenings spent hanging at the apartment with Zoom to the many trivia nights at Charlie's we've so joyously lost, my life in Boston would not at all have been the same without you.

I would also like to thank all my friends from back home in Montreal who have taken the time to come down to visit me in Boston throughout the years. I warmly extend acknowledgements to Max Lefèvre, Phil Cazelais, Marc-Antoine Dumoulin, and Francis Hamel (RIP); Andréanne Goyette, Steph Andrieux, Ariane Couture, and Amélie Duval Courchesne; Max Milanovic, Laura Glenn, Simran Dewan, Evan Weber, and Max Bellefeuille; Vincent Boulé and Charlotte Girod; Stéphanie Bernard and Sarah Power; and all others who have kindly stopped by to send their regards while in town. It certainly would have been a long 5 years without the continuous visits from my dearest friends from my hometown.

Additionally, I would like to express a warm thanks to all the members of my family who have supported me throughout my graduate school path. Foremost, I thank my parents Bita Danechi and Amir Osseiran for their unwavering support every step of the way; my sister Lina Osseiran, as well as my brother-in-law Quentin Dutilleul and my nephew Félix Dutilleul; my aunt Hana Osseiran; and all other family members who have been so warm and welcoming during each and every single one of my return trips home.

Finally, I would like to express my greatest thanks to my fiancée Alexandra Peebles. We had initially met when I was less than halfway through graduate school, back in December 2015, and endured the vast majority of our relationship apart. Nevertheless, she has been my source of comfort and peace since the day we started dating, supporting me through the most stressful aspects of graduate life. Whether it was anxiety related to meeting deadlines or rehearsing for upcoming presentations, she would offer rational advice and guidance to help me navigate through my most

difficult moments. Alexandra, thank you for your unfaltering love and support, and simply for making my life what it now is — I cannot wait to see what our future has in store for us.

Contents

List of Figures

List of Tables

Chapter 1

Theory and Principles of Nonlinear Optics for Biomedical Imaging

1.1 Introduction

Prior to understanding the fundamentals of nonlinear optics, it is a useful exercise to consider what is meant by *linear* optics. When a material is exposed to an electric field $\vec{E}$ (such as light, for example), the material exhibits a polarization $\vec{P}$ that is linearly proportional to the field $\vec{E}$ as shown in Equation 1.1.

$$\vec{P} \approx \epsilon_0 \chi \vec{E} \tag{1.1}$$

The proportionality is defined by ϵ_0, a universal constant known as the permittivity of free space, and χ, the material's electric susceptibility. This linear relationship implies superposition; that is, the polarization response of a material exposed to a sum of fields simply corresponds to the sum of the polarization responses to each field considered individually. In addition, this also implies that the incident fields cannot interact with one another to generate new frequencies at the system's output. This is a relation commonly introduced in most introductory optics and/or electromagnetic fields classes in undergraduate science and engineering programs; however, this equation is but a simple and convenient approximation. In reality, nonlinear polarization

responses do exist – they simply require an enormous amount of incident power in order to generate a detectable signal as a result of the vanishingly small nonlinear electric susceptibility coefficients. In fact, this is because the susceptibility χ of a given material can be represented by a Taylor series expansion, where nonlinear material properties emerge with incident fields that are sufficiently strong. This relation is shown more clearly in Equation 1.2. Considering the large amount of input energy that is required to elicit this nonlinear optical polarization responses however, an ensuing question naturally arises: if extremely high irradiation powers are required to induce nonlinear optical polarizations, how are nonlinear optical signals generated in biological samples in a non-destructive manner? The answer lies in the use of ultrafast laser sources.

$$\vec{P} = \epsilon_0 \left(\chi^{(1)} \vec{E} + \chi^{(2)} \vec{E}^2 + \chi^{(3)} \vec{E}^3 + ... \right) \tag{1.2}$$

These are laser systems that, instead of emitting a constant beam of coherent light (unlike continuous wave, or CW, laser sources), emit extremely short – but extremely powerful – pulses of light. These short pulse durations can range from a few nanoseconds all the way down to the femtosecond regime. In the case of the various studies documented in the context of the present thesis, the Spectra-Physics InSight DeepSee — a commercial femtosecond laser source — is the laser source of choice. One output can be selectively tuned from 680 up to 1300 nm in single-nanometer increments, while the other is fixed at 1040 nm. The concurrent use of two laser beams will become clear in the context of particular nonlinear optical imaging applications that will be presented in depth in Sections 1.4.2 and 1.6. The pulse durations are about 120 fs in duration, and the laser has a repetition rate of 80 MHz. This also implies an interpulse period of 12.5 ns, which implies that when the laser is in operation, no light is being emitted 99.999% of the time. However, for the brief 0.001% of the time where a pulse is emitted, it propagates with a peak power exceeding 100 kW. The time-averaged power for the laser source nevertheless remains in the milliwatt range, thereby minimizing photodamage. It is also worth specifying

that for nonlinear optical imaging, the photon density is crucial factor to consider from an imaging standpoint. That is, not only does one require kilowatt-range peak powers, but this energy must also be focused into a small focal volume in order to generate any appreciable signal. This is conveniently advantageous, because it is this property that ensures the "intrinsic optical sectioning" that is a hallmark of nonlinear optical microscopy.

These intrinsic properties of nonlinear optical microscopy eliminate the need for a confocal pinhole as in the case of single-photon confocal fluorescence microscopy, for example, used to suppress the out-of-focus light. Given that the signal is strictly generated at the focus of the microscope objective, full 3D volumetric reconstructions of biological samples can be achieved by simply scanning the objective focus across the X, Y, and Z dimensions.

With this introductory framework for nonlinear optics in mind, the following sections will build on these foundations, ranging from two-photon excitation fluorescence (TPEF) to coherent Raman scattering (CRS) to sum-frequency and transient absorption (SFA and TA) imaging techniques.

1.2 Two-Photon Excitation Fluorescence (TPEF)

Two-photon excitation fluorescence (TPEF) is a nonlinear optical interaction whereby two photons are simultaneously absorbed by a molecule in order to generate a single output photon. This nonlinear optical phenomenon was first implemented as a microscopy technique back in 1990 by Denk and colleagues [9]. It is worth noting, however, that because TPEF requires the simultaneous absorption of two incident photons, this nonlinear optical effect is symmetry-forbidden in non-centrosymmetric molecules. This is because materials and molecules that exhibit inversion symmetry (i.e. compounds that are centrosymmetric) have even-ordered nonlinear electric susceptibilities equal to zero. Nevertheless, even-ordered nonlinear optical effects may still be generated in such media by breaking its symmetry. This can be done by coupling with the molecule's vibrational and/or rotational modes with odd symmetry in

order to enable excitation.

It is also worth noting that TPEF is not a lossless process. Upon the simultaneous absorption of two incident photons by a molecule, there is some non-radiative decay, followed by a transient residency in an excited electronic state for a given period of time τ called the fluorescence lifetime, finally resulting in the emission of a fluorescent photon as the molecule returns to its ground state. In addition, two-photon excitation spectra are more complex than simply doubling the wavelength of the single-photon excitation spectrum. This discrepancy is due to differences in Frank-Condon factors, which can be better appreciated by taking a look at the 1- and 2-photon spectra of common fluorophores. Moreover, because TPEF is a $\chi^{(2)}$ process, the signal intensity is proportional to the square of the incident power, i.e. $I^2(t)$.

1.3 Fluorescence Lifetime Imaging Microscopy (FLIM)

Fluorescence lifetime imaging microscopy (FLIM) can be viewed as an extension TPEF when implemented in a two-photon setting, whereby the fluorescence lifetime τ of a given fluorophore can be probed in addition to its intensity [10]. In addition to probing the optical properties of fluorophores (i.e. excitation and emission parameters), FLIM is a tool also capable of probing their temporal dynamics. To this aim, this imaging technique requires specific hardware (i.e. time-correlated single photon counting, or TCSPC), and the resulting data can be processed either in the time domain or in the frequency domain, the latter of which is typically performed using phasor analysis. FLIM is therefore an extremely useful modality in the context of molecular imaging, as it provides researchers with an additional dimension of imaging contrast [11].

1.3.1 Time-Correlated Single Photon Counting (TCSPC)

The implementation of FLIM relies on the operating principles of time-correlated single photon counting (TCSPC) [12]. In such a case, the detector (i.e. photomultiplier tube, or PMT) is connected to pre-amplifier, which is in turn connected to the TC-

SPC module. For multiple detectors, the each PMT pre-amplifier is first connected to a routing block before the TCSPC module, whereby the PMTs independently emit an electronic impulse signal at each photon detection event for multiplexed detection. In parallel, a synchronization module registers the timing of the laser excitation pulse. In turn, the time-to-amplitude converter (TAC) measures the time difference between the arrival of the detected photon and the emission of the following excitation laser pulse. The difference between this measured time interval and the laser repetition period (given by the inverse of the pulse repetition frequency, an intrinsic property of the laser source) corresponds to the fluorescence emission delay for that particular photon. The hardware network has an overall dead time on the order of 100 ns or so [12]; for this reason, each incident laser pulse must result in the detection of at most 1 fluorescence photon per detector in order to limit lifetime biasing towards shorter values. In other words, this implementation of TCSPC for FLIM does not allow for over-counting of photons, which would otherwise result in inaccurate lifetime measurements.

Once the FLIM data is acquired using the TCSPC techniques described above, each pixel of the acquired XYT dataset can be analyzed using either time-domain or frequency-domain analysis — the latter of which is most commonly referred to as "phasor analysis".

1.3.2 Time-Domain Analysis

Time-domain analysis of FLIM data typically involves curve fitting of fluorescent decay traces on a pixel-by-pixel basis using a sum of exponential decays. In such a context, each fluorophore of a given decay trace is characterized by its respective time constant τ_i and relative weight α_i, defining its contribution to the overall fluorescence signal in the pixel in question. The relation between a pixel's temporal decay trace $I_{(t)}$ and the fluorophores therein is summarized in Equation 1.3.

$$I(t) = \sum_{i=1}^{N} \alpha_i e^{-\frac{t}{\tau_i}} \tag{1.3}$$

As will be discussed in further detail in Chapter 4, time-domain analysis requires a fair bit of familiarity with the sample at hand. This encompasses not only the number of compounds to distinguish, but also an *a priori* idea of their respective fluorescent lifetimes [13]. To complicate matters further, there is an added dimension of complexity when imaging cellular and tissue autofluorescence, including flavin and nicotinamide adenine dinucleotides (FAD and NADH, respectively). Such compounds naturally exhibit multiple lifetimes, which in turn vary based on their molecular conformation and binding states [14, 15, 16]. Bearing in mind that time-domain analysis is based on iterative curve fitting, the task of resolving multiple sources of fluorescence that themselves have multiple lifetimes rapidly becomes computationally demanding. To add to the present challenge, accurate time-domain analysis of fluorescence lifetimes often requires a prohibitively large number of photon counts per pixel (typically exceeding 5000 photons), particularly when the fluorescence from one compound dwarfs the other [13]. This requirement is due to shot noise (also known as Poisson noise), which is related to the particle nature of light. Considering that photon emission can be described as a Poisson process, the signal-to-noise ratio (SNR) is given by $SNR = N/\sqrt{N} = \sqrt{N}$, where N is the number of detected photons. Such elevated photon counts inherently demand longer acquisition times and/or higher laser excitation power. However, due to the fragile nature of typical biological samples, these imaging parameters may be incompatible with specimens of interest — particularly living samples.

1.3.3 Phasor Analysis

As an alternative to time-domain analysis, frequency-domain analysis — more commonly referred to as phasor analysis — is much less demanding in terms of prior sample knowledge [17]. Moreover, this approach yields an intuitive and convenient visual interpretation of the sample data. Instead of performing curve fitting on a pixel-by-pixel basis, phasor analysis involves a simple mathematical transform of each pixel's temporal decay trace. This transformation, related to the Fourier transform, yields a pair of coordinates (G, S) that describe a so-called phasor, which is characterized

by its modulus $M = \sqrt{G^2 + S^2}$ and phase angle $\phi = \arctan(S/G)$. Specifically, the phasor coordinates (G, S) are obtained by computing the real and imaginary components of the Fourier transform of the temporal decay trace evaluated at the angular laser repetition frequency ω, normalized by its area under the curve. These relations are summarized in Equations 1.4 and 1.5.

$$G = \frac{\int_0^\infty I(t)\cos(\omega t)\mathrm{d}t}{\int_0^\infty I(t)\,\mathrm{d}t} \tag{1.4}$$

$$S = \frac{\int_0^\infty I(t)\sin(\omega t)\mathrm{d}t}{\int_0^\infty I(t)\,\mathrm{d}t} \tag{1.5}$$

The angular frequency is defined by $\omega = 2\pi f$, where f corresponds to the laser repetition frequency in the case of pulsed sources (typically on the order of 80 MHz). On the other hand, single-photon FLIM systems require intensity modulation of a continuous wave (CW) laser, where f then corresponds to the modulation frequency.

In the special case of a fluorophore characterized by a single well-defined lifetime, the phasor transform results in a set of phasor coordinates that obey the relation shown in Equation 1.6, which describes a semicircle with radius 0.5 centered at $(0.5, 0)$ [17].

$$(G - 0.5)^2 + S^2 = 0.25 \tag{1.6}$$

In the FLIM community, this is referred to as the universal semicircle. In the case of a decay trace characterized by two fluorescence lifetimes, the transformed phasor coordinates lie along a line connecting the two individual lifetimes on the universal semicircle. The specific phasor coordinates along that line in turn depend on the relative contributions of either fluorescent compound [17, 18]. Given a mixture of fluorescent compounds, FLIM data analysis in the phasor domain therefore conveniently offers the ability to estimate the relative fluorescence contribution of each compound at every pixel in the image based on the relative distances between each pixel's corresponding phasor location and the respective reference phasor clusters of the fluorophores at hand.

1.4 Raman Scattering

There are a wide variety of coherent Raman scattering (CRS) techniques, but for the purposes of the present discussion, the fundamentals of spontaneous Raman scattering will first be discussed, follow by an overview of two of the most commonly used implementations of CRS, namely coherent anti-Stokes Raman scattering (CARS) and stimulated Raman scattering (SRS).

1.4.1 Spontaneous Raman Scattering

Raman scattering is a non-parametric process related to the interaction of light with a molecule and its associated vibrational states. This process was discovered by Sir Chandrasekhara Venkata Raman in 1928, when he observed the scattering of an entire spectrum of light upon illumination of a sample with monochromatic light of frequency ω_P. As he expected, the most prominent feature of the spectrum occurred at the incident light frequency ω_P, which is attributed to an elastic interaction known as Rayleigh scattering. However, weak spectral lines were also observed, which were later understood to occur as a result of inelastic interactions between incident photons and the molecular vibrations present in a sample. As energy is transferred during this process, the spectral lines had shifted frequencies $\omega_P \pm \omega_R$, corresponding to what are now known as Stokes $(\omega_P - \omega_R)$ and anti-Stokes shifts $(\omega_P + \omega_R)$. Raman observed that these shifts and their resulting spectra were highly material specific — a discovery that was awarded the 1930 Nobel Prize in physics. It is worth noting that in most use cases, the incident field at ω_P is within the visible or infrared range of the electromagnetic spectrum, while the molecular vibrations themselves can be directly probed at ω_R that lie in the mid- or long-wavelength infrared ranges.

Fundamentally, Raman scattering is derived from interactions with the time-varying electromagnetic field of light and the time-varying electric polarizability caused by molecular vibrations. When a molecule interacts with a photon, it can experience an instantaneous coupling with the photon's electric field, leading to a polarization of the molecule. This coupling can result in the creation of a scattered

photon at frequency $\omega_P - \omega_R$ if some of the energy from the incident light is converted to drive the molecular vibration; it is scattered at $\omega_P + \omega_R$ if the molecule is already in an excited vibrational state, whereupon the scattered photon exits with energy equal to the sum of those of the incident photon and the molecular vibration. These interactions at $\omega_P - \omega_R$ and $\omega_P + \omega_R$ correspond to Stokes and anti-Stokes shifts, respectively. However, this process is far from efficient, as the creation of a frequency-shifted photon hinges on an infrequent interaction with the vacuum field. Given that a spontaneous emission process is defined by the creation of a photon in a previously unoccupied mode, this Raman process is deemed *spontaneous* [19].

It should be noted that Raman transitions depend on the rate of change of polarizability with respect to the molecule's geometry. This implies that Raman scattering is only possible for certain symmetries of molecular vibrations, which forms the basis for the so-called selection rules for Raman scattering. While the formalism here predicts the existence of Stokes and anti-Stokes frequency components, it fails to consider the strength of individual Raman transitions, which would otherwise require a more elaborate quantum mechanical formalism that is beyond the scope of the present discussion. The reader is encouraged to refer to the textbook by Long for a more rigorous quantum mechanical approach to the principles of Raman scattering [20].

It is also worth noting that there exists a mechanism whereby the Raman scattering response of a molecule can be increased by several order of magnitude, known as surface-enhanced Raman scattering (SERS), which involved adsorption of the molecule onto a roughened or nano-sized metallic substrate. Metallic or plasmonic nanoparticles are known for their unique interaction with light that results in the excitation of their localized surface plasmon resonance (LSPR). LSPR excitation results in not only enhanced light absorption and scattering from the nanoparticle, but also produces an enhanced electromagnetic field around the surface of the nanoparticle that can be readily exploited for Raman enhancement [21, 22, 23, 24]. When a molecule is adsorbed onto or is within close proximity of the nanoparticle surface, the EM field felt by the molecule is that of the incident field and the enhanced EM field at the nanoparticle surface. While the in-depth discussion of SERS is beyond

the scope of the present thesis work, a more detailed mathematical description of plasmonic nanoparticle Raman signal enhancement can be found in several excellent texts by Van Duyne and colleagues [21, 23].

1.4.2 Coherent Raman Scattering (CRS)

Coherent Raman scattering is a term that refers to a class of stimulated interactions where Raman processes are driven coherently, leading to the generation of strong scattering signals. This differs from traditional Raman scattering, which is dependent on spontaneous interactions. As was previously mentioned, spontaneous Raman scattering depends on an infrequent interaction with the vacuum field. In coherent Raman scattering, two light fields are introduced into a sample that have an energy difference equal to a molecular vibration of interest. These two fields act to stimulate, or drive, the Raman process, increasing its efficiency by several orders of magnitude [19].

Though many types of coherent Raman scattering processes have been discovered and developed [25, 26], two types of coherent Raman scattering have been specifically developed towards biomedical applications: stimulated Raman scattering (SRS) and coherent anti-Stokes Raman scattering (CARS). Both mechanisms of signal generation are so-called "four-wave mixing" processes, which implies that incident photons interact with the material's vibrational properties to produce scattering contrast that can be used for imaging. Important distinctions exist between CARS and SRS however, resulting in differences in detection schemes and image contrast. Schematically, the energy diagrams for spontaneous Raman scattering, SRS, and CARS are presented in Figure 1-1.

Conceptually, SRS and CARS both involve the use of two incident fields at frequencies ω_P and ω_S, respectively referred to as the pump and Stokes beams, where the difference between these two frequencies is tuned to match a molecular vibration of interest. In the case of SRS, the introduction of electric fields at both frequencies allows for a transfer of photons at the pump frequency to photons at the Stokes frequency due to coupling with the sample's endogenous molecular vibrations. This

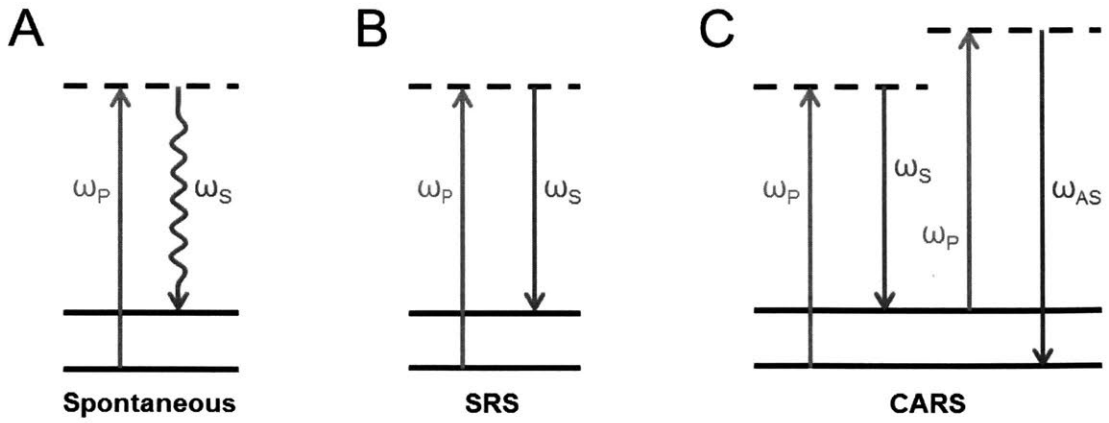

Figure 1-1: Schematic representation of the fields involved in Raman scattering processes. (A) Spontaneous Raman scattering, (B) stimulated Raman scattering (SRS), and (C) coherent anti-Stokes Raman scattering (CARS). The pump, Stokes, and anti-Stokes frequencies are respectively designated by ω_P, ω_S, and ω_{AS}, while the dashed and solid lines respectively refer to virtual and real molecular states. In spontaneous Raman scattering, a pump photon scatters inelastically, thus generating a Stokes photon. In SRS, both pump and Stokes fields are incident on the sample simultaneously; if there is a vibrational band gap that corresponds to the energy difference between the two beams, the pump field decreases (stimulated Raman loss, SRL), while the Stokes field is amplified (stimulated Raman gain, SRG). Finally, in CARS, a new field is created at the anti-Stokes frequency and can be readily detected *via* optical filters, as it is blue-shifted relative to the incident pump and Stokes fields.

implies that the pump beam intensity decreases in the presence of a Raman-active molecule, while that of the Stokes beam increases. In order to pick up this small energy transfer, SRS microscopy is achieved either by detecting the decrease in pump intensity (stimulated Raman loss, SRL) or the increase in Stokes intensity (stimulated Raman gain, SRG).

SRL is achieved through high-frequency modulation (typically on the order of several MHz to circumvent laser noise and improve both imaging speed and detection sensitivity [27]) of the Stokes beam *via* an acousto-optic or electro-optic modulator (AOM and EOM, respectively). This implies that the SRS signal will manifest itself as a high-frequency modulation superimposed onto the intensity of the pump beam (Figure 1-2). Detection thus requires the use of a lock-in amplifier (LIA) or demodulation to isolate the high-frequency component of the pump intensity. Conversely,

SRG is performed by modulating the pump beam and detecting the high-frequency fluctuations of the Stokes intensity. Additional information on SRS microscopy is provided in section 1.7.

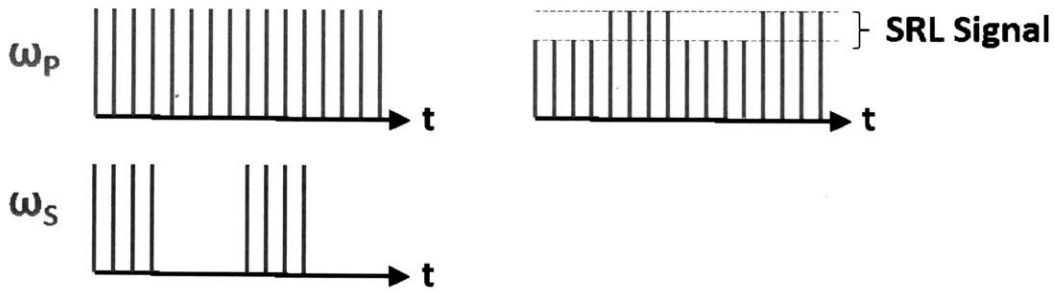

Figure 1-2: Detection scheme for stimulated Raman loss (SRL). Conversely, stimulated Raman gain (SRG) is detected by modulating the pump beam and detecting the fluctuations of the Stokes beam.

The CARS process, on the other hand, can be conceptually perceived as an initial induction of a coherent vibrational oscillation of the material, achieved by tuning the difference ("beat") frequency between the pump and Stokes beams to a given vibrational transition. This results in the creation of a macroscopic, coherently driven polarization change in the sample at the excited vibrational state of interest. An interaction of pump photons with this macroscopic polarizability then results in the strong scattering of photons at the anti-Stokes frequency. In terms of implementation for microscopy, CARS is simpler than SRS in that it does not require signal modulation nor lock-in amplification for detection, since a new wavelength is generated altogether. As such, detection of the anti-Stokes signal simply requires the use of proper short-pass and/or band-pass filters that can adequately block out any residual pump or Stokes light. Additional details on CARS microscopy are described in section 1.7. For further reading, various reviews on the topic are also available [28, 29].

One major difference between CARS and SRS is the existence of the so-called "non-resonant" background in the CARS signal. This background contribution arises due to the fact that CARS is a parametric process — that is, the energy state of the molecule is unchanged after CARS. This differs from SRS and spontaneous Raman, where molecules gain or lose a quantum of vibrational energy. The parametric nature

of CARS enables a second, non-resonant, set of interactions that are derived from purely electronic processes. The end result is that the CARS signal contains both resonant and non-resonant contributions. This set of additional coherent interactions has the practical effects of adding a nonspecific, background contribution to CARS that can also result in shifted and complex vibrational spectra [26].

1.5 Fluorescence Photoconversion

The previous sections of the present chapter focused on microscopy techniques well-suited for probing the intrinsic properties of endogenous molecular species in a label-free manner (although they may certainly be used to probe exogenous compounds as well). In contrast, fluorescent labeling comprises a widely used technique in microscopy applications in order to allow for the specific visualization of biological features of interest [11, 30, 31]. These techniques are highly diverse in their implementation: standard immunofluorescence (IF) can be used to visualize specific proteins [32]; genetic engineering allows for the genomic insertion of fluorescent reporter proteins that in turn allow for the monitoring of genetic expression [33, 34, 35, 36, 37]; organelle-specific fluorescent dyes allow for various cytological measurements, both quantitative and qualitative in their nature [38, 39, 40].

Despite their widespread adoption however, traditional fluorescence-based labeling techniques are static. That is, they cannot serve to monitor specific cell populations of interest over time. In fact, there exists a wide variety of applications where the ability to monitor specific cell subpopulations over time would be of great interest. As an example, genetic reporters such as green fluorescent protein (GFP) can be useful in determining whether cells in a cultured population express a particular gene [35, 36]. On the other hand, tracking the fate or lineage of specific cells that express (or do not express) the gene of interest within the same culture over prolonged periods would pose a significant challenge [41]. This difficulty is of particular relevance in the study of treatment resistance in the context of cancer, where resistant subpopulations in heterogeneous cultures are of particular interest.

In order to fill this technological niche, so-called "photoconvertible" fluorescent labels have been developed [41, 42, 43, 44]. Much like conventional fluorescent reporters, these molecules exhibit characteristic excitation and emission profiles. However, they differ from conventional fluorophores in that their optical properties can be converted to a new set of excitation and emission spectra. The specific set of optical signatures pre- and post-conversion, as well as the reversibility of the process, are intrinsic properties of each photoconvertible molecule.

While the excitation and emission properties of biologically relevant fluorescent reporters can span the entire visible spectrum — ranging from the UV all the way to the NIR [30] — the red end of the spectrum is typically of greatest value for intravital imaging. Longer wavelengths such as those in the NIR range have a considerably lower tendency to be absorbed and scattered by tissues compared to their bluer counterparts, allowing for increased signal generation and collection, in turn maximizing penetration depth [11, 30, 45]. One such commercially available NIR fluorescent label is DiR (1,1'-dioctadecyltetramethyl indotricarbocyanine iodide), a cell membrane dye with excitation and emission peaks at 748 nm and 780 nm, respectively [41]. This particular reporter has been shown to exhibit irreversible photoconversion following irradiation with 750 nm femtosecond pulses [41], and is thus particularly well-suited for the longitudinal monitoring of heterogeneous cancer cell populations (see Chapter 6).

1.6 Sum-Frequency and Transient Absorption (SFA and TA)

Finally, the same modulation transfer scheme used for acquiring SRS images can more generally be used to detect any signal where the presence of one beam affects the intensity of the other beam following an optical interaction with the sample. In the case of sum-frequency and transient absorption (SFA and TA, respectively), a signal is generated typically in the case of a strong absorber that can absorb one

photon from each beam. In the case of SFA, this absorption process is simultaneous; in the context of TA, the process is step-wise, implying the absorption of one photon to promote the molecule to a real excited state, followed by a second absorption event promoting it to an even higher (i.e. more energetic) state. These modalities are thus ideal for visualizing pigments and chromophores such as hemoglobin and melanin, for example [46, 47, 48, 49, 50, 51, 52].

1.7 Instrumentation and Microscopy Setup

Nonlinear optical imaging technologies have begun to see a strong push in research and development that is gaining momentum particularly in the field of cancer research over the last couple of decades. In the case of coherent Raman scattering for example, it was not until 1999 that CARS microscopy was developed by Zumbusch *et al.*, where three-dimensional vibrational imaging of chemical and biological samples was reported for the first time [53]. Since then, significant strides have been made into applying these imaging technologies to answer questions in oncology using tools that simply were not previously available [54].

In order to build a nonlinear optical imaging system, one or more pulsed laser sources are first required, depending on the imaging modality. The high peak powers of such pulsed sources are necessary to probe the higher-order optical properties of samples, while their low average powers avoid damaging the cells and/or tissues at hand. Early nonlinear optical microscope designs used Ti:sapphire lasers and optical parametric oscillators (OPO) or amplifiers (OPA) that were tuned to emit near-infrared (NIR) wavelengths. More recently, commercial laser manufacturers such as APE, Spectra-Physics, and Coherent have designed automated dual output laser sources (including an integrated OPO system to allow for wavelength tunability), which are most useful in the case of imaging techniques requiring more than one beam (e.g. CARS, SRS, SFA, TA, etc.). For such applications, these sources provide a fixed NIR output, typically used as the Stokes beam, and another that can be selectively tuned over a very wide range (generally 680 nm to 1300 nm). The tunable output can

be readily used for TPEF and FLIM imaging, for example, as they only require one excitation source. The tunable nature offers the ability to selectively probe a wide range of fluorophores either sequentially or simultaneously by judiciously selecting the proper excitation wavelength. The advent of such technology greatly reduces the complexity of the imaging system, as different molecules can be selectively imaged by changing the tunable output *via* the provided laser software in a matter of seconds, rather than painstakingly adjusting crystal temperatures and cavity length.

In addition to laser wavelength, pulse duration must also be considered when designing a nonlinear optical platform. In the case of multiphoton processes such as TPEF, shorter pulses simply imply a greater temporal flux of photons, implying greater signal generation. In the case of coherent Raman scattering, additional factors must be considered. Namely, the shorter a pulse is in the temporal domain, the wider its profile becomes in the spectral domain. Thus, the spectral pulse width of picosecond laser sources is orders of magnitude narrower than that of femtosecond pulses. The dependence of pulse duration on spectral resolution thus influences the performance of a coherent Raman imaging system, which is optimized when the spectral pulse widths of the laser sources overlap with that of the Raman peak of interest.

Regarding microscope design, the two external beams are combined using a dichroic mirror (or, in the case of TPEF and FLIM, the excitation source is simply routed towards the input port of the microscope). The beams are then raster-scanned across the sample through a high numerical aperture (NA) objective. Such objectives are preferred for nonlinear optical imaging — particularly in the case of CRS imaging — in order to tightly focus the incident light into a small focal volume for optimal signal generation. Moreover, in the case of CARS, these objectives ensure that the so-called "phase-matching condition" is met such that anti-Stokes radiation is constructively generated [53]. Finally, as with all nonlinear optical techniques, the signal strictly originates from the focal point of the objective. Therefore, the distribution of the compound of interest can be mapped in three dimensions by raster scanning the focus across the sample, and detecting the fluorescence or anti-Stokes light using

a photomultiplier tube (PMT) downstream of appropriate optical filters.

A branching point in coherent Raman imaging was met in 2008 with the advent of SRS microscopy [55], following the success of CARS as a label-free microscopy platform. To this end, Freudiger *et al.* used essentially the same configuration as a CARS microscope, but modulated the Stokes beam via an electro-optic modulator (EOM) in order to detect a minuscule variation in the pump beam intensity using a high-end lock-in amplifier. Such a tool is essential in the context of SRS microscopy, since the signal originates from small fluctuations of the pump intensity at the modulation frequency over a significantly larger input power level. As was mentioned earlier, this configuration is referred to as stimulated Raman loss (SRL), while modulation of the pump beam and subsequent detection of modulation amplitude in the Stokes beam is known as stimulated Raman gain (SRG). This same setup is used in SFA and TA imaging, where the modulation transfer of energy (and therefore, signal amplitude) is used to detect the presence of strongly absorbing molecules such as hemoglobin or melanin.

Translation of coherent Raman microscopes from the laboratory to the clinic has recently begun as well. JenLab now offers the MPTflex CARS, a standalone portable system with a pivoting handheld scan head capable of both multiphoton fluorescence and CARS imaging [56]. For a more directed use in intra-operative settings, Invenio Imaging offers a state of the art portable SRS/CARS imaging system based on fiber lasers in the form of a compact microscope [57]. The advent of such novel technologies is promising for the medical community, in that rapid label-free assessments can be made directly on patients or biopsies in order to improve cancer diagnostic speed and quality, leading to improved patient well-being.

Chapter 2

Raman Scattering Technologies for Cancer Research and Oncology

2.1 *In Vitro/Ex Vivo* Detection and Diagnostics

2.1.1 Biofluids

The ideal biological specimens for diagnostic tests are biofluids (i.e. blood, urine, or saliva) as their collection — also known as a "fluid biopsy" — is non-invasive and they can be repeatedly collected without harm to the patient. Additionally, biofluids contain a vast amount of important and clinically relevant chemical components, including DNA, hormones, proteins, and metabolites. Thus, a considerable amount of research has been focused on assessing the utility of Raman technologies to analyze biofluids in cancerous and non-cancerous patients [58, 59, 60]. The following discussion involves prostate, oral and breast cancers; however, a list of additional cancers diagnosed using biofluid samples and Raman techniques can be found in Table 2.1. Table 2.2 also provides a compilation of common Raman bands identified in these studies.

Table 2.1: Summary of cancers diagnosed using various Raman techniques and selected representative associated references. Please note that this list is not meant to be absolute or all encompassing.

Type of cancer	Biofluid	*Ex vivo* tissue	*In vivo* model
Prostate	Blood, urine	Human	—
Oral	Blood, urine, saliva	Human	Human
Breast	Blood, urine, saliva	Human	Mouse
Skin	—	Human	Human, mouse
Brain	—	Human, pig, mouse	Human, mouse
Lung	—	Human	Human
Gastrointestinal	Blood	Human	Human, pig, rat
Leukemia	Blood	—	—
Head and neck	Blood	Human	—
Cervical	Blood	Human	Human
Liver	Blood	Human	—
Ovarian	—	Human	Mouse
Circulating tumor cells	Blood	—	—

Prostate Cancer

In 2003, Porter and co-workers reported one of the first immunoassays that utilized SERS for the detection of prostate specific antigen (PSA) in human serum [61]. For specificity to PSA and signal enhancement, Raman probes were prepared by functionalizing 30 nm gold nanoparticles (AuNPs) with an anti-human PSA antibody and the Raman reporter 5,5'-dithiobix(succinimidyl-2-nitrobenzoate) (DSNB). Based upon their previous studies, the authors found that covalently linking the PSA antibodies to the Raman reporter and in turn the gold nanoparticles increased performance over physisorption techniques. Solutions of anti-human PSA-gold nanoparticles and human serum samples containing free PSA were allowed to react, dry onto anti-free PSA antibody treated gold slides, and interrogated by a fiber-optic Raman system equipped with a 632 nm HeNe laser. Using the symmetric nitro stretch of DSNB at 1338 cm^{-1}, PSA levels were detected down to 1 pg/mL and were comparable to commercially available assays. Raman spectroscopy was also coupled with support vector machine (SVM) analysis to evaluate blood serum from prostate cancer

Table 2.2: Common Raman band assignments used in cancer diagnostic studies [1, 2, 3, 4, 5, 6, 7, 8]. Please note that Raman vibrations may shift in wavenumber depending on the sample and that these values should not be regarded as absolute.

Raman shift (cm^{-1})	Vibrational mode	Assignment
481		Glycogen
558	ν(C-C)	Uric acid
600	ν(N-CH_3), δ(C=O), ring vibrations	Creatinine
621	t(C-C)	Phenylalanine
650	t(C-C)	Tryptophan, uric acid
678	ν(N-CH_2), ν(C=O), ring vibrations	Creatinine
685	t(C-S)	Proteins
692	δ(O-C=O)	Creatinine
798	ν(N-H)	Uric acid
825	as(O-P-O)	DNA backbone
840	δ(N-CH_2), ring vibrations	Creatinine
903	ν(C-C-N)	Creatinine
912	ν(C-C)	Calcium oxalate dihydrate
960	$\nu(PO_4^{-3})$	Calcium hydroxyapatite
1004	ν(C-C), ring breathing	Phenylalanine
1049	ν(C-O), ν(C-N)	Proteins
1155		β-carotene
1176	ν(C-H)	Tyrosine
1217	ν(C-C_6H_5)	Tyrosine, phenylalanine
1265	ν(C-N), δ(N-H), amide III	Proteins, α-helix, collagen
1310	t(C-H)	Lipids
1340	w(CH_3-CH_2)	Collagen, lipids
1445	δ(CH_2)	Collagen, lipids
1477	ν(C-O)	Calcium oxalate dihydrate
1523		β-carotene
1586	δ(C=C)	Phenylalanine
1654	ν(C=C)	Fatty acids
1655	ν(C=O), amide I	Proteins, α-helix, collagen
1739	ν(C=O)	Cholesterol esters
2081		Pheomelanin
2845	ν(CH_2)	Lipids
2940	ν(CH_3)	Proteins, lipids

patients and healthy volunteers [1]. While the collected serum samples were investigated using both conventional Raman spectroscopy and SERS, SERS with bare silver

nanoparticles showed the greatest diagnostic capabilities. The acquired SERS spectra from cancerous and normal patients revealed biochemical changes that correlated to a malignant state. In prostate cancer serum samples, Raman bands at 481 cm^{-1} (glycogen), 1217 cm^{-1} (C-C_6H_5 — phenylalanine, tryptophan) and 1445 cm^{-1} (CH_2 bending — collagen/lipids) were seen to decrease, while increases were seen at 650 cm^{-1} (C-C twist, tryptophan), 685 cm^{-1} (C-S twist) and 1586 cm^{-1} (C=C bending — phenylalanine). Spectra classified using the Gaussian radial basis function kernel SVM model resulted in diagnostic metrics of 100% specificity, 96% sensitivity, and 98% accuracy.

Diagnosis of prostate cancer using SERS has also been extended to urine analysis [62]. In this study, filtered urine samples were mixed with gold nanoparticles and then spotted onto a CaF_2 microscope slide for measurement. Examination of the difference spectra revealed an increase in Raman bands associated with the metabolite hypoxanthine in prostate cancer samples. Using PCA-LDA for classification, a sensitivity of 100%, a specificity of 89%, and an accuracy of 95% were achieved. While the sample size for this study was limited, this work demonstrates the potential feasibility of urinalysis *via* SERS and multivariate spectral analysis for cancer diagnoses.

Oral Cancers

Blood sample analysis via Raman spectroscopy has also been carried out for oral cancers [63, 64, 65]. In 2013, Sahu *et al.* demonstrated that conventional Raman spectroscopy could be used to delineate between serum samples from patients that had been diagnosed with buccal mucosa and tongue cancer, and those from healthy volunteers [63]. An efficacy of 85% was found when all spectra were independently analyzed, while 78% efficacy was reported when replicate measurements for independent patients were averaged prior to analysis. PCA-LDA was used as the data analysis model for classification generation. Similar to that seen in prostate cancer analysis, changes in Raman bands associated with amino acids and lipids were most significant. This same group demonstrated that Raman spectroscopy on serum samples could potentially predict reoccurrence of oral cancer [65].

Additionally, urine has been investigated for the detection of oral cancer using Raman spectroscopy [2]. In this study, voided raw urine was collected from 167 patients (73 healthy and 93 cancerous) and evaluated for its chemical components between 500–1800 cm^{-1} using 785 nm excitation. Molecular vibrations associated with uric acid, specifically C-C stretching at 558 and 649 cm^{-1} and N-H stretching at 798 cm^{-1}, showed elevated intensities in cancer patients compared to those that were healthy. Four Raman bands related to creatinine also showed increases, while the band at 692 cm^{-1} (O-C=O deformation) was only present in cancer patients. Other urinary metabolites — urea, DNA, indoxyl sulfate, pteridine, flavin, tryptophan, and phenylalanine — showed differences between cancer and healthy patients. PCA-LDA spectral analysis resulted in a diagnostic sensitivity, specificity, and accuracy of 98.6%, 87.1%, and 93.7%, respectively. Oral cancer detection has been extended to saliva analysis through coupling Raman spectroscopy and PCA [66].

Breast Cancer

Diagnostic evaluations using blood, urine and saliva for breast cancer have also been performed. Blood serum analysis using conventional Raman spectroscopy coupled with PCA-LDA was able to distinguish between normal and cancerous patient samples with 97% sensitivity and 78% specificity [67]. In order to acquire ample signal, samples were frozen and solid residues were removed for spectral analysis. Multivariate analysis revealed seven Raman band ratios that led to the discrimination between cancerous and non-cancerous samples; these discriminatory band ratios involved the amino acids phenylalanine, tryptophan and tyrosine as well as polysaccharides and β-carotene. Bhattacharjee *et al.* demonstrated the feasibility of using urine as a sample platform for breast cancer diagnosis [68]. Urine was collected from control and breast tumor bearing rats, and was then evaluated with Raman spectroscopy in either an unprocessed or concentrated form. The acquired Raman spectra from unprocessed urine revealed bands associated with urea (1006 cm^{-1} and 1161 cm^{-1}) and creatinine (680 cm^{-1} and 850 cm^{-1}). The use of urine concentration led to additional spectral features being revealed. Still, even with additional features present, the Raman bands

at 680 cm^{-1} and 1006 cm^{-1} showed the greatest change between control and tumor bearing rats. Spectral analysis using PCA-LDA resulted in classification efficiencies of 72% and 91% when using unprocessed and concentrated urine samples, respectively.

Saliva has also been recently evaluated as a biological matrix to diagnosis breast cancer using SERS [3]. Saliva was collected from 33 healthy patients and 31 cancerous patients, and then mixed with silver nanoparticles immediately before acquiring the Raman measurement. Difference spectra revealed saliva acquired from cancerous patients had protein band decreases at 621 cm^{-1} (C-C twist phenylalanine), 1049 cm^{-1} (C-O, C-N proteins) and 1176 cm^{-1} (C-H tyrosine) and protein band increases at 1004 cm^{-1} (C-C phenylalanine), 1208 cm^{-1} (C-C_6H_5 phenylalanine) and 1340 cm^{-1} (CH_3CH_2 wagging collagen). A partial least square (PLS)-DA algorithm was used to categorize the data and resulted in diagnostic sensitivities above 72%, specificities above 81%, and accuracies above 78%.

2.1.2 Tissue

Ex vivo tissue examination through histopathological techniques is regarded as the gold standard for cancer diagnosis. Histopathology, while reliable, does not allow for *in vivo* evaluation, which would be extremely beneficial during surgery; the complete removal of tumor margins is heavily correlated to increased survival [69, 70, 71]. Thus, the use of Raman technologies to delineate between cancerous and non-cancerous tissues *ex vivo* has been readily explored as first step toward the potential intraoperative, real-time evaluation of tissue during surgery [72, 58, 59]. Although the below discussion focuses on breast, lung, skin and brain cancers, a list of other cancers diagnosed using *ex vivo* tissue samples and Raman techniques can be found in Table 2.1. Common Raman bands identified in these works can be found in Table 2.2.

Breast Cancer

With over 260,000 total cases of breast cancer reported each year [73], it is not surprising that breast tissue has been heavily interrogated using Raman techniques. One

of the first reports of breast tissue evaluation using Raman spectroscopy was published more than 20 years ago [74]. This work focused on the characterization of molecular components in normal breast tissue as well as the optimization of spectroscopic experimental parameters, such as the excitation wavelength, laser power, and the use of a fiber optic probe for spectral acquisition. A year later, the same group used these results to assess the potential spectral differences between normal and cancerous (invasive ductal carcinoma, IDC) breast tissues [75]. Using a NIR excitation source with relatively low power (100–200 mW), the authors reported cancerous tissue having significant differences, especially in bands correlated to lipid content. For statistical analysis, the band area ratios of 1654 cm^{-1} (C=C stretching in fatty acids) and 1439 cm^{-1} (CH_2 scissoring) were chosen due to their sensitivity towards histopathological variations. Discrimination between normal and diseased tissue was also possible using a fiber optic probe placed 1 mm into the tumor. It should be noted that both conventional and fiber optic based Raman systems used in this study were unable to distinguish between benign (fibrocystic change) and cancerous samples. Feld and co-workers later published a series of works that reported the discrimination and molecular characterization of breast tissue from normal, fibrocystic change, fibroadenoma and infiltrating carcinoma pathologies through the combination of a Raman microspectroscopic setup and linear combination models [76, 77, 78]. Their analysis model revealed that bands associated with fat and collagen were important algorithmic parameters and led to a diagnostic classification sensitivity of 94% and a specificity of 96%. Much work since these foundational studies has been focused on investigating the utility of different combinations of Raman spectral features and multivariate analysis techniques to discriminate between normal, benign and diseased breast tissue [79, 80, 81, 82, 83].

Raman spectroscopy of calcified species has also been reported as a plausible method to differentiate between normal and cancerous breast tissue. While calcifications are regarded as harmless when found in bones, their presence in soft tissue, especially breast tissue, is often associated with disease. Calcifications are generally composed of either calcium oxalate dihydrate (COD) or calcium hydroxyapatite

(HAP), and are extremely difficult to distinguish using traditional pathology techniques [84]. Haka *et al.* reported that bands located at 912 cm^{-1} (C-C stretching) and 1477 cm^{-1} (C-O stretching) were indicative of COD calcifications while HAP had a prominent spectral signature at 960 cm^{-1} that corresponded to phosphate stretching [85]. While benign tissues could be distinguished using the COD calcification Raman bands alone, differentiation between benign and diseased tissues using HAP band measurements required the use of PCA. PCA resulted in a diagnostic sensitivity of 88% and specificity of 93% when monitoring the increase in bands associated with calcium carbonate and the decrease in protein bands. Stone and Matousek also explored the use of transmission Raman spectroscopy for distinguishing between HAP and COD in breast phantoms at depths translatable to *in vivo* detection [86]. In a push towards rapid clinical translation, Barman *et al.* demonstrated the feasibility of simultaneously identifying between HAP and COD calcifications and diagnosing breast cancer lesions in real-time during a stereotactic core needle biopsy [87]. A combination of Raman spectroscopy and SVM analysis resulted in a 100% positive predicative value, a 95.6% negative predictive value, a 62.5% sensitivity, and a 100% specificity for diagnosing breast cancer tissues with or without calcifications. An 82% overall accuracy for calcification status and breast cancer diagnosis was also reported. However, the most impressive result from this study was the ability of their SVM algorithm to diagnose ductal carcinoma *in situ* (DCIS), which was not possible with their previously developed algorithms for biopsy Raman analysis.

While many studies have focused on utilizing conventional Raman spectroscopy, Wong and co-workers employed CARS imaging and quantitative data analysis to distinguish between normal, benign and cancerous breast tissue [88]. In addition, the team demonstrated the ability of CARS to classify cancer subtypes (DCIS, high grade and low grade invasive ductal carcinoma (IDC), and lobular carcinoma). CARS imaging using the CH_2 vibration located at 2845 cm^{-1} revealed normal breast tissue was dominated by adipose and fibrous structures, while malignant tissues showed morphological alterations especially within tumor cells that were confined to the basement membrane and duct space. Diagnostic features from the acquired images were

selected according to pathological standards. Using their developed methodology, 80% of intermediate-grade IDC and 85% high-grade IDC samples were accurately distinguished.

Lung Cancer

Ex vivo tissue analysis using Raman spectroscopy has also been performed on lung cancer samples. In 2001, Hamaguchi and co-workers demonstrated the possibility of distinguishing between normal and malignant lung tissues by using NIR Raman spectroscopy [89]. By using 1064 nm laser excitation, resolvable biological spectra could be acquired with only minimal tissue autofluorescence. Cancerous tissues were found to have strong bands located at 1448 cm^{-1} and 1666 cm^{-1}, which corresponded to collagen. Huang *et al.* also utilized NIR Raman spectroscopy, probing between 700–1800 cm^{-1} with a 785 nm diode laser, to distinguish between normal and diseased bronchial tissues from 10 patients [4]. Their measurements revealed significant spectral differences of bands associated with amino acids, collagen, nucleic acids and phospholipids, with the ratio of Raman band intensities at 1445 cm^{-1} and 1655 cm^{-1} serving as a metric of differentiation. The Wong group used CARS microscopy to discriminate between normal, benign, and malignant lung tissues [90, 91]. Malignancies were categorized using CARS imaging into different subtypes. Distinguishing between normal and cancerous tissues required 11 features and resulted in classification accuracies of 91% and 92%, respectively. In order to separate adenocarcinoma from squamous cell carcinoma samples, 25 features were required and led to 76% and 72% classification accuracies. Shifted subtracted Raman spectroscopy has also been explored as a diagnostic technique for the evaluation of lung tissue samples [92].

Skin Cancer

Skin cancer can be divided into three major subtypes: melanoma, basal cell carcinoma (BCC) and squamous cell carcinoma (SCC), with melanoma accounting for less than 2% of all skin cancer cases, but responsible for 75% of skin cancer deaths [73]. BCC and SCC are often referred to as nonmelanoma skin cancers (NMSCs) and

their detection has been heavily investigated in the Raman community. One of the first reported studies to investigate the utility of Raman spectroscopy to identify NMSCs was conducted by Gniadecka *et al.* and compared the spectral features of BCC to those of normal skin biopsies [93]. Using a NIR Fourier transform (FT) Raman spectrometer with a 1064 nm Nd:YAG excitation laser, this work revealed alterations in protein, lipid and polysaccharide bands. BCC spectra showed a decrease at 1270 cm^{-1} (amide III — protein) and 1650 cm^{-1} (amide I — protein) and were correlated to disturbances in the α-helix secondary structure of the skin. Additional spectral alterations were seen at 850, 870, 950, 1420 and 1450 cm^{-1} and were associated with changes in protein and lipid structures. The authors employed an artificial neural network analysis technique to achieve complete separation between BCC and normal tissues using spectral changes in the regions of 830–900 cm^{-1}, 900–990 cm^{-1} and 1220–1360 cm^{-1}. Building upon this work, Puppels and co-workers used a logistic regression model to differentiate BCC from the surrounding normal, healthy epidermis. Their analytical approach resulted in 100% sensitivity and 93% specificity for BCC diagnosis [94]. This same group later reported the ability to distinguish between BCC and surrounding healthy tissue using high wavenumber (2800–3125 cm^{-1}) Raman spectroscopy [95]. They achieved 100% and 99% prediction accuracies for BCC and healthy tissue, respectively. As high wavenumber analysis eliminates background signals in the fingerprint region that arise from the use of fused-silica-based optical fibers, this work demonstrated the potential feasibility of using a fiber optic probe to diagnose tumor borders in BCC.

Multimodal imaging consisting of CARS, second harmonic generation (SHG), and two-photon excitation fluorescence (TPEF) has also been explored as a potential technique to discriminate between BCC and normal tissues. Multimodal imaging allows for not only structural information (SHG — collagen) but also spatial (TPEF — endogenous fluorophores) and chemical (CARS — lipids) information to be resolved. Vogler *et al.* used this multimodal imaging strategy in 2010 and revealed that BCC tumor cells could be distinguished due to their undetectable collagen structures and large patches of fat reservoirs [96]. Three years later, this group used the same ap-

proach to distinguish between BCC and SCC as well as normal tissues [97]. BCC and SCC both showed a lack of collagen structure, but BCC also demonstrated a weaker CARS (lipid) signal than that of SCC. Additional morphological features that are traditionally seen in H&E stains could also be visualized using this strategy and added to the strength of diagnosis.

Melanoma and NMSCs have also been able to be distinguished from one another. Wulf and co-workers utilized NIR FT-Raman spectroscopy to delineate melanoma from pigmented nevi, BCC, seborrheic keratoses and normal tissue [5]. Visual differentiation was based upon band intensity decreases at 1660 cm^{-1} (amide I — protein) as well as increases at 1310 and 1330 cm^{-1} (CH twisting and wagging — lipids) for BCC and SCC, respectively. As proposed in other studies, the decrease in in the amide I band was attributed to conformational changes in proteins of diseased tissue. When neural network analysis was employed for tissue discrimination, a melanoma diagnostic sensitivity of 85% and specificity of 99% was achieved while a sensitivity of 97% and a specificity of 98% were attained for BCC. These metrics are comparable to those achieved with trained pathologists, demonstrating the potential utility and translation of this methodology for melanoma and BCC diagnosis. BCC and melanoma discrimination has also been achieved using PCA for spectral analysis [98, 99].

Brain Cancer

Brain cancer accounts for over 250,000 diagnosed cancer cases and 189,000 deaths annually worldwide [100]. Of these reported cases, approximately 50% are identified as gliomas, which are known for their highly aggressive nature. That said, it is not surprising that the majority of work in the Raman community has been geared toward the identification of gliomas. In one of the first reported investigations, Koljenović *et al.* evaluated 20 unfixed cryosections of glioblastoma by Raman spectroscopy and LDA for separating vital and necrotic tissues [6]. The dominating spectral signatures from difference spectra (necrotic minus glioblastoma) resembled that of cholesterol and cholesterol esters, indicating necrotic tissues possess higher concentrations of

cholesterol. Subtle band changes, corresponding to carotenoids and calcifications, were also observed. Cluster analysis resulted in 100% diagnostic accuracy when run on 9 independent tissue samples. This group further explored the utility of Raman spectroscopy for brain cancer diagnosis using high wavenumber (2400–3800 cm^{-1}) Raman spectroscopy [101] and a single-fiber optical probe Raman system [102].

Raman spectroscopy was also compared with IR spectroscopy for the delineation of glioma, meningioma and schwannoma from normal tissues in a study conducted by Krafft *et al.* [103]. In this work, both Raman and IR spectroscopic analysis resulted in significant differences between diseased and normal tissue samples; however, Raman spectroscopy was determined to be the better technique due its lack of "contamination" from water and its ability to spatially resolve a greater number of chemical components. For meningioma, Raman spectral decreases were seen at 857, 939, 1246 and 1684 cm^{-1} when compared to normal tissue. As these bands correspond to collagen, their observed decreases agree well with the notion that tumors have irregular collagen structures. Glioma tissues were evaluated against tissue that had been subjected to a hemorrhage, and spectral analysis showed that hemorrhage tissues had increased band intensities at 661, 751, 1003, 1124, 1258, 1346, 1454 and 1603 cm^{-1}. These bands were correlated to the presence of hemoglobin. When compared to meningioma, close analysis revealed that glioma tissues had greater band intensities at 719 cm^{-1} indicating differentiations could be based on phosphatidylcholine levels. Schwannomas also showed distinct spectral features at 426 cm^{-1} and 508 cm^{-1} when compared to glioma and meningioma tissues. These bands were attributed to the presence of tricalciumphosphate within the lesions. Krafft and colleagues later used Raman microscopic imaging and a spectral unmixing algorithm to investigate histopathological features such as cell density and nuclei [104]. Raman signatures in combination with the unmixing algorithm revealed high-grade glioblastomas had increased nucleic acid levels (782, 1099 and 1576 cm^{-1}) over low-grade tissues. Furthermore, this group utilized hyperspectral unmixing of Raman images to correlate morphological (i.e. number and diameter of cell nuclei) and biochemical (i.e. proteins, lipids and nucleic acids) components with the degree of malignancy in brain

tissues [105].

Coherent Raman imaging has found applications in the identification and microscale mapping of gliomas. In 2009, Evans et al. demonstrated the ability of CARS to delineate fresh astrocytoma samples, a type of glioma, from normal brain tissue in mouse models of human brain cancer [106]. Images were constructed by using the lipid CH_2 stretching mode located at 2845 cm^{-1} and revealed accurate tumor margins when compared to traditional H&E stains. Kirsch and co-workers have recently used CARS to evaluate primary and secondary brain tumors against normal tissue [107]. Primary glioblastoma tumors and brain metastases of breast and melanoma where shown to exhibit decreased CARS signals and were thus distinguishable from normal surrounding tissues. Tumor infiltrates were also identified by the gradual disappearance of the 2845 cm^{-1} CARS signal into the tumorous region. Additionally, the use of CARS in a multimodal imaging format similar to that described for skin cancer (BCC) has also been used to analyze brain tumors [108].

Gliomas have also been identified *via* another coherent Raman technique, namely SRS. Building upon their work in 2008 that demonstrated the ability of two-color SRS imaging to produce high quality brain tissue images [55], Xie and colleagues evaluated the use of this Raman imaging modality to delineate between diseased and normal brain tissues as well as differentiate between primary and secondary tumors [7]. Multicolored SRS images were created using two Raman vibrational modes: 2845 cm^{-1} (CH_2 stretching — lipids) and 2940 cm^{-1} (CH_3 stretching — lipids and proteins). While the CH_2 stretching vibration was used alone to produce images of cytoplasm and myelin sheaths, images of nuclear morphology resulted from the difference image of CH_2 stretching (2845 cm^{-1}) subtracted from CH_3 stretching (2940 cm^{-1}). Using this type of image acquisition, brain tumor tissues showed increased cellularity compared to normal brain tissue and exhibited similar diagnostic features as conventional H&E tissue analysis. Primary glioma tumors were further distinguishable from brain metastases from the breast by monitoring the tumor margin. Primary glioma tissue samples displayed infiltrating glial cells along the white matter tracts of the *corpus callosum*, while a defined tumor margin could be seen with tissue samples of brain

metastases. This group was later able to quantify and correlate acquired SRS signals at 2845 cm^{-1} and 2930 cm^{-1} for the differentiation of cellular regions — solid tumor, cortex and white matter — in human glioblastoma xenografts [109]. The ratio of Raman signals (2930 cm^{-1}/2845 cm^{-1}) revealed solid tumor regions had high levels of protein compared to both cortex and white matter regions. By monitoring this Raman signal ratio across the gray matter-tumor interface, tumor infiltration was detectable. Fresh human tumor samples were also analyzed using this multicolor SRS imaging approach. SRS analysis not only revealed hypercellularity (i.e. increased protein content), but also cellular and nuclear pleomorphism, pseudopalisading necrosis and microvascular proliferation. The identified features matched those seen with traditional H&E analysis further. These impressive studies demonstrate the potential clinical utility of SRS for intraoperative use in brain tumor cytoreduction surgery cases as SRS provides ample information to aid in tumor margin identification.

2.2 *In Vivo* Detection and Diagnostics

2.2.1 Animal Models

Animal models are one of the most invaluable components in translating a diagnostic or treatment strategy to the clinic. While they do not fully recapitulate the genetic and epigenetic heterogeneity found in human cancers, animal models allow researchers to investigate harmful and fatal diseases without risking human lives [110]. Preclinical studies investigating the utility of Raman spectroscopy for the identification of cancerous lesions have heavily relied on animal models, namely murine models. While several cancer models have been explored (Table 2.1), the following discussion will focus on brain and breast cancer detection, as these are the most heavily investigated. A list of common Raman bands used for *in vivo* detection and diagnostics can be found in Table 2.2.

Brain Cancer

The gold standard for brain tumor detection is histological analysis on biopsied tissues; however this method does not allow surgeons to differentiate infiltrating lesions from normal tissue in real-time in the operating room. While several groups have focused on characterizing spectral differences of these tissue populations in *ex vivo* tissues, the use of *in vivo* Raman detection strategies is still in its early stages, with the majority of work being conducted on experimental animal models. In 2010, Beljebbar *et al.* demonstrated the potential for *in vivo* glioblastoma detection using a microprobe coupled to a portable Raman spectrometer [111]. In this study, rat C6 glioma cells were injected into neonatal Wistar rats and intracerebral tumor development was monitored up to 20 days using the Raman microprobe. The microprobe utilized an 830 nm laser excitation source, a fiber optic probe to deliver incident laser light and collect the Raman scattered light, and a spectrograph to record Raman spectra. Alterations in bands associated with proteins, lipids and DNA were observed, and hierarchical cluster analysis of these spectral features showed strong separation between brain tissue pre-injection (i.e. normal) and tissue from the developed tumor. That same year, Krafft and co-workers reported the *in vivo* detection of brain metastases using a Raman spectroscopic imaging system with a 785 nm laser source [112]. Metastatic brain tumors were induced using murine melanoma cells injected into the carotid artery of nude mice. Due to the presence of melanin and its associated Raman signatures (i.e. 587, 976, 1404, and 1595 cm^{-1}), the location of melanoma cells and their developed metastases could be visualized in cortical and subcortical regions. While the Raman images had lateral resolutions of 250 μm and required several minutes to acquire, this work demonstrated the intraoperative potential of Raman spectroscopic imaging for brain tumor resection.

Recently, SERS has also been recently employed for the *in vivo* identification of brain lesions, specifically for fine margin resection. Kircher *et al.* described the use of a triple-modality nanoparticle that allowed the combination of MRI, photoacoustic imaging, and Raman imaging for the intraoperative identification of brain tumor mar-

gins in live mice [113]. This imaging combination resulted in the location of the whole brain tumor to be identified (MRI) as well as the tumor's three-dimensional structure at a high spatial resolution to be visualized (photoacoustic imaging). Raman imaging further allowed for brain tumor margins to be delineated as confirmed by histological analysis. To enable the triple imaging strategy, 60 nm spherical gold nanoparticles were functionalized with Raman reporter and MRI contrasting molecules. Under this design the nanoparticles served as a photoacoustic contrasting agent, provided signal enhancement of the Raman tag, and carried contrasting molecules for MRI. The nanoparticles were injected into the tail vein of orthotopic glioblastoma bearing mice, and were able to cross the blood-brain barrier and accumulate in tumor cells *via* the enhanced permeability and retention (EPR) effect. Tumor site localization allowed for high signal to noise ratios in all imaging modalities and significantly aided in the complete resection of glioblastomas. The use of a handheld Raman scanner in combination with silica coated gold nanoparticles has also been reported [114]. The handheld scanner allowed for real-time Raman scans of the tumor region and revealed additional cancer laden regions that were otherwise undetectable by conventional Raman and SERS imaging systems.

The Xie group has demonstrated the use of SRS for rapid and label-free visualization of glioblastoma multiforme (GBM) brain tumors [109]. Accurate resections are of particular importance in the context of brain cancer, given that 85% of recurrent GBM tumors arise at the resection margin where cancer cells were left behind [115]. Ji *et al.* used an infiltrative human GBM xenograft mouse model fitted with a cranial window in order to image the brain tissue non-invasively. Two Raman spectral peaks: 2845 cm^{-1} and 2930 cm^{-1}, which correspond to lipids and proteins, respectively, were chosen to contrast healthy tissue from the brain tumor. These bands were selected given the marked decrease in lipid content in cancerous tissue, thus offering a source of endogenous contrast. They showed that while the bright-field image of the tumor border appears grossly normal, it is readily distinguishable in SRS. While the authors caution that SRS microscopy still requires rigorous evaluation and validation prior to clinical translation, their work is among the first to introduce *in vivo* coherent Raman

microscopy to the field of cancer research.

Breast Cancer

In an effort to better reconcile rodent models of breast cancer with its human counterpart, Bhattacharjee *et al.* evaluated the Raman spectra from C57, Swiss albino, Swiss bare, and agouti mice, as well as Sprague-Dawley rats [116]. They first found that white-haired rodents provided better signal-to-noise ratio and less background relative to their colored kin in terms of their Raman spectra. A further investigation of white-haired and hairless mice across various anatomical sites was then carried out in order to evaluate the contributions from skin *versus* those of the mammary tissue. It was found that the highest quality spectra were obtained from Swiss bare mice, suggesting they are best suited for future transcutaneous spectroscopic investigations of breast cancer in animal models.

As for the application of SERS in the context of breast cancer, Qian *et al.* explored the applicability of using gold nanorod probes to optically detect breast cancer tumors *in vivo via* tagging with polyethylene glycol (PEG) and 3,3-diethylthiatricarbocyanine iodide (DTTC), a NIR fluorophore and Raman probe [117]. Male nude mice were first xenografted with human breast cancer cells and maintained until the tumors reached an approximate size of 5 mm in diameter. The mice were then injected with the functionalized nanoprobes and imaged at several time points post-injection. Their work showcased the potential for using SERS and fluorescence simultaneously on a single platform to map tumors and sentinel lymph nodes in the context of breast cancer.

A later study by Dinish *et al.* made use of gold nanoparticles tagged with three Raman reporters bound to three antibodies for intrinsic breast cancer biomarkers: Cy5 to TGFβRII, MGITC to CD44, and Rh6G to EGFR [118]. Nude female mice were inoculated with a human metastatic breast cancer cell line, and nanoprobes were injected at the center of the tumor once it reached a palpable size. By targeting a single spectral peak from each Raman reporter, the authors observed the multiplex SERS spectra in the tumor region up to 48 hours post-administration, followed by

their clearance after 72 hours. This research suggests the possibility of selectively targeting and imaging subtypes of breast cancer *in vivo* for improved diagnosis and treatment monitoring.

Finally, Jeong *et al.* recently developed a fluorescence-Raman endomicroscopic system (FRES) using nanoprobes for simultaneously acquiring fluorescence and SERS measurements [119]. The nanoprobes consisted of a large silica nanoparticle (200 nm diameter) covered in smaller Raman-labeled silver nanoparticles (10 nm diameter), all coated in a silica shell that was conjugated to AF610, a fluorescent dye (10 nm thickness). To evaluate system performance on a murine breast cancer model, four mice were xenografted with a human breast cancer cell line expressing high levels of HER2 and EGFR, both common biomarkers of breast cancer. The authors report successful molecular detection of the xenografted tumors endoscopically with high sensitivity *via* multiplexed active targeting. This technology could thus be translated to routine endoscopic procedures where diagnosis of particular cancer subtypes in their early stages is most critical.

2.2.2 Human Studies

Due to the ethical standards surrounding human research, the exploration of Raman spectroscopy techniques for cancer diagnostics has so far been somewhat limited. However, the works presented here have been conducted on easily accessible regions that do not require invasive procedures or anatomical regions that can be accessed through endoscopic probes. Thus the following discussion focuses on skin, gastrointestinal, cervical and brain cancer detection. Other cancers that have been investigated using *in vivo* Raman technologies can be found in Table 2.1. Raman bands associated with these studies can be found in Table 2.2.

Skin Cancer

Skin cancer is arguably one of the most studied forms of neoplasia *in vivo via* Raman spectroscopy, primarily due to the ease of access of suspicious lesions. This avoids

the need for endoscopy and favors the use of handheld fiber-based Raman probes for rapid, accurate, and point-of-care diagnosis and classification of suspect skin lesions.

The current clinical standard for skin cancer diagnosis relies on visual inspection of suspect lesions, often assisted by dermoscopy. This diagnostic methodology leaves a fair degree of variability in the accuracy of skin cancer diagnosis based on the experience and training of the dermatologist. This subjectivity thus warrants the development of tools that are non-invasive, rapid, and portable for a more objective and rigid framework for evaluating suspicious skin lesions.

To this aim, the Zeng group has been investigating the applicability of Raman spectroscopy for skin cancer diagnostics. In 2012, the group conducted a clinical study investigating various types of skin cancer as well as a variety of benign skin diseases, where the integration time for their studies was set at 1 second or less. They confirmed the ability to distinguish malignant and pre-malignant lesions from benign ones, melanomas from nevi (benign pigmented lesions, commonly referred to as moles), and melanomas from seborrheic keratoses. For highly sensitive detection (ranging from 95% to 99% sensitivity), a specificity ranging from 15% to 54% was reported, suggesting the applicability of Raman spectroscopy as a tool for screening suspicious lesions non-invasively [120]. In a related report, it was also shown that intentional photobleaching of skin can be a useful technique to reduce the autofluorescence of the sample, effectively increasing the overall signal-to-noise ratio of the spectroscopic measurements [121]. More recently, the group conducted an independent validation of their automatic skin cancer detection methodology, where they used 518 cases from a prior study as a training set and 127 new cases for testing. This study validated prior work, yielding diagnostic accuracy matching previous findings [122].

In parallel, the Meinke group conducted an *in vivo* clinical study using Raman spectroscopy to discriminate skin cancer from normal tissue *via* a fiber-coupled probe. In measuring spectra from 104 cases of various skin cancers, accuracies of 73%, 85%, and 91% in distinguishing basal cell carcinoma, squamous cell carcinoma, and malignant melanoma from normal skin, respectively, were found [123].

Related work conducted by the Wulf group further revealed that Raman spectroscopy could be used in the context of skin cancer diagnostics in a manner that is independent of skin pigmentation. Specifically, it was reported that while the degree of pigmentation does influence the Raman spectra, proper background correction can negate the contributions from pigments and thus allow for spectral bands of interest to be interpreted unambiguously [124].

Recent efforts have been made in combining imaging and spectroscopic modalities to further improve the accuracy of skin cancer diagnostics. One such effort led by the Tunnell group found that Raman spectroscopy alone was sufficient to distinguish malignant melanoma from benign pigmented lesions with a diagnostic accuracy of 100%. However, in the case of nonmelanoma skin cancers, the diagnostic accuracy was improved when reflectance and fluorescence measurements were combined with the Raman data. In this case, they were able to distinguish actinic keratoses as well as squamous and basal cell carcinomas from normal skin with a sensitivity and specificity of 90% and 85%, respectively [125]. Another study conducted by Moryatov and co-workers found that combining measurements from optical coherence tomography (OCT), backscattering, and Raman spectroscopy into a multimodal platform for diagnosing skin cancer increased sensitivity and specificity by 9% and 8%, respectively, when compared to Raman spectroscopy alone. In particular, they were able to distinguish melanoma from nonmelanoma tumors with 89% sensitivity and 93% specificity, and basal cell carcinoma (BCC) from non-BCC tumors with 100% sensitivity and 96% specificity [126]. These two promising trials illustrate that the advent of multimodal imaging and spectroscopic platforms can be used to improve skin cancer diagnostics over the use of Raman spectroscopy alone.

Gastrointestinal Cancers

Cancers of the gastrointestinal tract can occur anywhere between the oral cavity and the anus, and represent a particularly difficult diagnostic challenge. Raman spectroscopy has been used in several studies investigating mouth or oral cancer, properly known as oral squamous cell carcinoma (OSCC). Considerable progress in this field

has been made by the Krishna group, where a study in 2012 on 10 normal and 10 cancerous *ex vivo* tissues, as well as 10 *in vivo* measurements, revealed differences in the spectra of normal *versus* cancerous samples. Moreover, they showed that the spectra from the normal *in vivo* and *ex vivo* tissues were similar enough to warrant further *in vivo* study in the use of Raman spectroscopy as a diagnostic tool for OSCC [127]. Indeed, the group later published an investigation of premalignant lesions of the mouth *in vivo*, finding that premalignant lesions can effectively be distinguished from normal and cancerous sites in patients with and without smoking habits [128]. The group further studied the applicability of Raman spectroscopy for OSCC diagnostics by investigating whether early changes associated with cancer — including malignancy-associated changes (MAC) and cancer field effects (CFE) — can be identified spectroscopically. In acquiring 722 spectra from a total of 84 subjects, it was found that early neoplastic transformation can indeed be detected *via* Raman spectroscopy [129].

Esophageal and gastric cancers have been another focus of diagnostic research in the field of Raman spectroscopy, with particular emphasis on the precancerous cellular transformation from squamous to gastric cells in the lower esophagus — a condition known as Barrett's esophagus (BE). To this aim, the Huang and Yeoh groups have put forth a number of reports investigating the applicability of Raman spectroscopy for esophageal and stomach cancer diagnoses, beginning with an *in vivo* assessment of gastric dysplasia. Using narrow-band image-guided Raman spectroscopy, 30 patients were included in a study where 54 spectra were acquired from normal tissues and 18 from dysplastic gastric tissues, yielding 94.4% sensitivity and 96.3% specificity [130]. In a related study, the same team examined 67 gastric patients and identified gastric cancer with a diagnostic accuracy of 93.7% (94.0% sensitivity and 93.4% specificity) [131]. The ability of Raman spectroscopy to distinguish between benign and malignant stomach ulcers was then tested, and sensitivities of 90.8%, 84.7%, and 82.1% as well as specificities of 93.8%, 94.5%, and 95.3% for classification of normal tissue, benign ulcers, and malignant ulcers, respectively, were found [132]. Using more elaborate data processing algorithms to improve overall accuracy, an *in vivo* gastric

cancer diagnostic accuracy of 94.6% was subsequently achieved [133].

The Stone group has also significantly contributed to the translation of Raman technologies from the laboratory to the clinic. In 2011, Kendall *et al.* evaluated a custom Raman probe designed for esophageal diagnostics on excised biopsy samples. They studied normal, low risk (Barrett's esophagus), and high risk (dysplasia and cancer) samples, where 1304 Raman spectra were acquired from a total of 123 samples. In classifying test spectra against a training set, their methodology resulted in sensitivity and specificity of 66–84% and 81–96%, respectively [134]. Subsequent work by Almond *et al.* in 2014 reported the development of a novel custom Raman probe, where a confocal design was implemented to specifically interrogate superficial tissues (150 μm) in an attempt to better detect surface lesions that may be cured *via* endoscopic therapy. While their study was limited to validation on *ex vivo* resected samples, their endoscopic Raman spectroscopy setup detected Barrett's esophagus-associated high-grade dysplasia (HGD) and esophageal adenocarcinoma with 86% sensitivity and 88% specificity [135]. While this technology has yet to be fully tested *in vivo*, this group is currently focusing on building various probes and adjusting tolerances to maximize performance in a clinical trial evaluating their implementation of endoscopic Raman spectroscopy in patients with Barrett's esophagus.

Extending the use of Raman spectroscopy further into the gastrointestinal tract, Bergholt *et al.* investigated Raman spectra from tissues of the esophagus and stomach, both *ex vivo* and *in vivo*. This study found that there is significant variability between the spectra from the esophagus as compared to those of the stomach, but the spectra from different anatomical sites within a given tissue were fairly similar. Moreover, cancerous tissues from the esophagus and stomach were found to be distinguishable with accuracies of 94.7% and 89.3%, respectively [136]. A subsequent study showcased the relevance of combining Raman spectroscopy with autofluorescence measurements *in vivo*, yielding a diagnostic accuracy for gastric cancer of 92.2%, greater than either of the two approaches evaluated independently (89.7% for Raman spectroscopy alone, and 86.3% for autofluorescence alone) [137]. A later study by Bergholt *et al.* showed that esophageal cancer could be diagnosed with an accuracy

of 96.0% when the Raman spectroscopic assessment is guided by a wide-field imaging modality such as white light reflectance, narrow-band imaging, or autofluorescence imaging in the context of a clinical endoscopic examination [138]. A fully automated online Raman spectroscopy platform with multimodal image-guided sampling for gastric cancer diagnosis was then developed, where 305 patients were examined yielding a diagnostic accuracy of 85.6% [139]. Later work demonstrated that the technology can be further exploited to target biopsy sites more specifically, as well as providing a platform for distinguishing between dysplastic and neoplastic lesions more consistently [140].

Subsequently, using a fiber optic confocal Raman endoscope, Bergholt *et al.* evaluated the potential for *in vivo* detection of high-grade dysplasia in Barrett's esophagus and identified diagnostic sensitivity and specificity of 87.0% and 84.7%, respectively [141]. Different endoscope configurations have also been investigated, where it was found that a beveled probe tip coupled to a ball lens outperformed the standard volume Raman probe via selective interrogation of the superficial tissue and suppression of autofluorescence contributions [142]. Even more recently, Wang *et al.* investigated spectral bands in the fingerprint and high-wavenumber regions of Raman spectra from the esophagus, and distinguished esophageal squamous cell carcinoma (ESCC) from normal tissue with a diagnostic accuracy of 97.3% [143].

Finally, Raman spectroscopy has also been investigated for the diagnosis colorectal tissue for cancer by the Huang group. They developed a novel fiber optic probe capable of acquiring fingerprint and high-wavenumber bands simultaneously from the subsurface of the colorectal tissue and identified a diagnostic accuracy of 88.8% in detecting colorectal cancer, with 93.3% sensitivity and 88.3% specificity [144].

Cervical Cancer

The diagnostic potential of Raman spectroscopy has also been studied in the context of cervical cancer, where it was found that spectral variations within normal tissue were an obstacle in properly identifying cervical cancer lesions. To this aim, the Mahadevan-Jansen group identified various classes of cervical tissue that can be

considered normal: truly normal, previously diseased normal, and adjacent-to-disease normal. The inclusion of these subcategories increased classification accuracy to 97% [145].

In parallel, the Huang group studied 105 spectra from 29 patients (65 normal and 40 precancerous spectra) using genetic algorithm-partial least squares-discriminant analysis (GA-PLS-DA), yielding 82.9% diagnostic accuracy (72.5% sensitivity and 89.2% specificity) [146]. As was done in the context of esophageal and gastric cancer described above, they furthered their research by examining the fingerprint and high-wavenumber spectral bands of the cervical Raman spectra. Combining the data from both spectral domains into their analysis, a diagnostic accuracy of 82.6% was identified for the 476 spectra (356 normal and 120 precancerous) collected from 44 patients [147]. Duraipandian *et al.* then evaluated the use of confocal Raman spectroscopy against near-infrared autofluorescence (NIR AF) spectroscopy alone as well as composite NIR AF/Raman spectroscopy. They found confocal Raman spectroscopy to have a diagnostic accuracy of 84.1%, an increase over the composite approach (82.3%), as well as NIR AF spectroscopy alone (59.6%) [148].

Finally, the Krishna group identified a particular challenge in the diagnosis of cervical cancer in the Indian subcontinent: most cervical cancers in such parts of the world are already advanced upon detection, leaving few intact cervical regions for assessment of normal tissue. In order to find normal baseline tissue, they explored the possibility of using vaginal tissue as an internal control for spectroscopic assessment of the cervical tissue. Indeed, the spectral features of normal vaginal and cervical tissues were found to be closely similar, such that cervical cancer diagnoses based on Raman spectroscopy could be facilitated in conditions where normal cervical tissue is otherwise unavailable [149].

Brain Cancer

In the context of brain cancer, proper surgical resection of the tumorous mass is critical to minimize the odds of recurrence. To address this need, the Leblond group developed a handheld Raman spectroscopy probe for the classification of brain tissue

intraoperatively [150]. They conducted a study on 17 patients with gliomas ranging from grade 2 to 4, where a total of 161 spectral measurements were collected. Their study revealed a diagnostic accuracy of 92%, with 93% sensitivity and 91% specificity [69]. These results were contrasted with the surgeon's visual inspection of the affected brain tissue using bright-field microscopy and magnetic resonance (MR) guidance, which yielded an accuracy of 73%, a sensitivity of 67%, and a specificity of 86%. This study thus illustrates the utility of Raman spectroscopy in detecting brain tumors intraoperatively, and sets a robust foundation for pursuing clinical trials to further contrast the effectiveness of Raman spectroscopy against the current standard of care for guiding brain cancer resections.

Chapter 3

Quantification of Oxidative Stress in *Ex Vivo* Human Skin Exposed to Chemical Sun Filters Using TPEF and FLIM

3.1 Introduction

Despite the growing use of sunscreen products, skin cancer incidence steadily remains on the rise, with one in five Americans expected to develop some form of skin cancer throughout their life [151, 152]. Furthermore, while some evidence of sunscreen protection against melanoma has been obtained [153], this was rather modest and challenging to demonstrate, in comparison to other cutaneous tumors [154]. One potential explanation for this discrepancy involves the chemical sun filters in sunscreens, which are responsible for absorbing ultraviolet radiation to minimize DNA damage to underlying skin cells. Prior studies have shown that some commercial chemical sun filters are capable of generating reactive oxygen species (ROS) when exposed to ultraviolet (UV) radiation under *in vitro* experimental conditions [155]. Consequently, it has been proposed that these compounds may generate ROS *in vivo* at the site of

application, thereby inducing oxidative stress in skin [155, 156]. Over a prolonged period of time, chronic oxidative stress may in turn contribute to skin aging, actinic keratosis, DNA damage, as well as the onset and pathogenesis of squamous and basal cell carcinomas [157, 158, 159, 160].

The study of oxidative stress in biological samples can be carried out using a wide variety of techniques. Traditional tissue processing methods can be used to extract, isolate, and quantify the amount of flavin and nicotinamide adenine dinucleotides (FAD and NADH, respectively), two key coenzymes in redox metabolism, using western blotting, quantitative polymerase chain reaction (qPCR), immunohistochemistry (IHC), or liquid chromatography/tandem mass spectrometry (LC/MS-MS) [161, 162]. However, the processing necessary for these techniques is either inherently destructive or does not provide spatial information, and as such, bars the ability to assess heterogeneous cellular-level responses within the tissue. On the other hand, exogenous labels such as fluorogenic probes can be used to preserve spatial integrity, and have had great success mapping spatial patterns of ROS generation *in vitro* [155]. These dyes, however, can be challenging when used in skin, whether *ex vivo* or *in vivo*, as many probes experience uneven uptake within skin [163]. This irregular diffusion leads to regional differences in probe signal intensity that may arise primarily due to uneven distribution rather than true contrast in oxidative stress.

Given these challenges, label-free optical imaging techniques have been found to be well suited for probing oxidative stress within tissues [164]. These tools capture fluorescence signals that arise from metabolic coenzymes of interest, enabling the mapping of oxidative stress on the sub-cellular level with submicron spatial resolution throughout intact tissue. Label-free imaging also removes any artifacts that can result from processing and permeabilizing tissue, as the imaging contrast arises from endogenous fluorescence rather than exogenous reporters of ROS.

To study oxidative stress within skin without such exogenous labels, one advantageous approach is two-photon excitation fluorescence (TPEF) microscopy, which directly assesses the fluorescence intensities of FAD and NADH [162, 165, 166, 167]. The intrinsic fluorescence of these metabolic coenzymes is advantageous for study-

ing cellular metabolic perturbations, as FAD only fluoresces in its oxidized form, while NADH is strictly fluorescent in its reduced form; their counterparts, $FADH_2$ and NAD^+, are not fluorescent. Together, these coenzymes act as electron carriers during the catabolic processes that result in ATP production, and the relative oxidized-to-reduced coenzyme ratio, commonly referred to as the redox ratio, can be used to make inferences about a cell's metabolic state. By imaging these intrinsic fluorophores within a given biological sample, one can then compare the signals obtained from both molecules in order to quantitatively assess oxidative stress using the ratio of FAD fluorescence intensity to that of NADH, i.e. FAD/NADH [164]. The normalized optical redox ratio (NORR), defined as FAD/(NADH+FAD), is also a commonly used imaging metric of oxidative stress, as it is strictly bound between 0 and 1 and more closely follows a normal distribution [162, 168].

This study sought to devise a method to non-invasively and non-destructively examine the impact of chemical sun filter exposure on the redox metabolism of epidermal skin cells, and determine whether these compounds can cause an oxidative shift in skin tissue. Viable, cultured *ex vivo* models of human skin were imaged using TPEF microscopy to quantify the change in optical redox ratio on a cell-to-cell level throughout the epidermis of skin based on the endogenous fluorescence of FAD and NADH [164]. A minimalist model formulation of sunscreen was designed for the present study containing five commonly used chemical sun filters in proportions that emulate a sun protection factor (SPF) of roughly 45. This minimalist approach was preferred in order to avoid any potential interference from inactive sunscreen ingredients, while adhering to FDA guidelines on maximum concentrations for each individual sun filter [169].

Due to the competing fluorescence contribution of sun filter compounds, however, a new analysis method based on FLIM and phasor analysis had to be developed to extract the optical redox ratio and map oxidative stress changes within skin. Indeed, the fluorescence from sunscreen formulations is not only fairly weak, but also varies depending on the combination and relative concentrations of chemical sun filters therein [170]. In turn, this variability limits the use of hyperspectral fluorescence

imaging to provide accurate and reliable contrast between endogenous and exogenous sources of fluorescence. In contrast, the photophysical dynamics of these sun filters are consistently short-lived [160, 171], warranting a highly sensitive time-correlated approach such as FLIM to accurately decouple the endogenous tissue fluorescence from that of the exogenous compounds based on differences in fluorescence lifetime. This method successfully enabled the quantification of oxidative stress caused by both ultraviolet light exposure and sun filters, and additionally allowed for the direct imaging of sun filters as they diffused through skin tissue.

It is worth noting that TPEF imaging is not exclusive to NADH and FAD, as some other endogenous compounds in skin exhibit fluorescent properties as well, including melanin, elastin, collagen, and keratin. Conveniently, the optimal excitation and emission parameters for probing melanin autofluorescence are distinct from those of NADH and FAD; moreover, the signal from these coenzymes dominates the autofluorescence from the stratum spinosum layer of the epidermis [172]. As for fluorescent extracellular proteins, elastin and collagen are primarily found within the dermis, while keratin forms within the more superficial layers of the epidermis. As such, the imaging parameters described in the present study are based on commonly used methods to maximize signals from NADH and FAD within the stratum spinosum roughly 50 μm below the skin surface [161, 162, 168, 173].

3.2 Materials and Methods

3.2.1 Sun Filter Formulation

The minimalist model formulation of sunscreen was composed of five commonly used chemical sun filters (avobenzone, octocrylene, homosalate, octisalate, and oxybenzone) dissolved in a lipophilic solvent typically included in sunscreen formulations (C12-15 alkyl benzoate, also known as Finsolv TN) in proportions that emulate a SPF of roughly 45 (see Table 3.1). The fluorescence of the formulation is primarily attributed to the presence of avobenzone, one of the most commonly used chemical

sun filters in sunscreens [160, 174].

Table 3.1: Composition of sun filter formulation

Compound	Concentration (% m/m)
Avobenzone	3
Octocrylene	4
Homosalate	8
Octisalate	5
Oxybenzone	4
Finsolv TN	76

3.2.2 Tissue Culture and Processing

In order to study oxidative stress in human skin in response to chemical sun filters, discarded skin tissues were obtained from elective patient surgeries in compliance with the institutional review board of Massachusetts General Hospital (MGH IRB protocol #2014P00135). The skin was then processed on arrival, where it was cut into square pieces roughly 1–2 cm^2 in size, placed on an RPMI-agarose nutritive gel bed, and maintained in an incubator at 37°C with 5% atmospheric CO_2. *Ex vivo* human skin explants were imaged using FLIM under 4 different experimental conditions: treatment with a 30 μL topical dose of either the sun filter formulation described in Table 3.1 or Finsolv TN alone as a vehicle-only control, and subsequently immediately exposed to either 0 or 20 J/cm^2 of UVA irradiation. This corresponds to 1 minimal erythemal dose (MED) for a fair-skinned individual of Fitzpatrick skin type I, i.e. the minimum amount of UVA irradiation necessary to elicit a reddening response in skin [175, 176]. Three distinct areas were then imaged for each skin sample, where each field of view consisted of a representative slice of the stratum spinosum within the viable epidermis, roughly 50 μm below the skin surface.

3.2.3 TPEF and FLIM Imaging

In using a fluorescence-based approach to study the effects of exogenous compounds like chemical sun filters, a common challenge often arises: many of these compounds are natively fluorescent [170], and may therefore interfere with the fluorescent signals from NADH and/or FAD. In the case of this study, it was found that the mixture of chemical sun filters was itself fluorescent, with excitation and emission properties similar to those of NADH. The formulation was not found to be emissive in the FAD spectral range. Because of this fluorescence, optical redox ratio measurements cannot be obtained on tissue exposed to the formulation, since there is no way to distinguish the fluorescence signal of the sun filters from that of NADH using TPEF microscopy alone. To circumvent this obstacle, the sun filter formulation was imaged using two-photon FLIM to determine if its fluorescence can be distinguished from that of NADH based on lifetime.

The laser source used to perform TPEF imaging is a dual-output femtosecond pulsed laser system (Spectra-Physics Insight DeepSee), where one output can be tuned to any integer wavelength ranging from 680 to 1300 nm. The beam was directed into the input port of a commercial inverted microscope (Olympus FV1000) for imaging with a 60× water immersion objective (Olympus UPLSAPO 60XW, 1.20 NA), and the total laser power at the output of the objective was below 35 mW for all imaging experiments. The fluorescence signals were detected using two distinct photomultiplier tubes (Hamamatsu H7422P-40 for NADH and H7422P-50 for FAD). The FLIM data was collected using time-correlated single photon counting (TCSPC) hardware (Becker & Hickl SPC-150), with each image containing 256 × 256 pixels in area and 256 time bins for each pixel's associated fluorescence decay trace. The imaging acquisition parameters resulted in photon count rates ranging from 2×10^4 to 2×10^5 photons per second, with a total acquisition period of 90 seconds. Calibration of the FLIM system was ensured using a solution of fluorescein (pH 9.0) with a known lifetime of 4.05 ns. Each area was first imaged with 755 nm laser light for multiphoton excitation of NADH with detection of fluorescence from 445 to 480 nm,

followed by 860 nm excitation for FAD with emission detection from 500 to 550 nm.

3.2.4 CARS Imaging

The Finsolv TN molecule can be readily visualized using coherent anti-Stokes Raman scattering (CARS) microscopy by probing the symmetric CH_2 stretching vibration at 2845 cm^{-1} of its long C12-15 hydrocarbon tail. As such, the tunable output of the laser source was set to 803 nm as the pump beam and the fixed 1040 nm output was used as the Stokes beam to generate a strong anti-Stokes signal at 654 nm, allowing for the monitoring of solvent penetration dynamics in skin. To this aim, an *ex vivo* skin sample was given a single topical treatment of Finsolv TN, and subsequently monitored at 15-minute intervals over the course of 2 hours, examining depths 0, 40, and 80 μm below the skin surface.

3.2.5 Non-Euclidean Phasor Analysis

The separation of fluorescent species based on their lifetime is best achieved using the phasor approach [168, 17, 177, 18]. This method is derived from Fourier analysis, where rather than fitting a linear combination of decaying exponentials onto a decay trace $I_{ij}(t)$ in the temporal domain, the data is transformed into a phasor with coordinates (G_{ij}, S_{ij}) defined as

$$G_{ij} = \frac{\int_0^\infty I_{ij}(t)\cos(\omega t)\mathrm{d}t}{\int_0^\infty I_{ij}(t)\,\mathrm{d}t} \tag{3.1}$$

and

$$S_{ij} = \frac{\int_0^\infty I_{ij}(t)\sin(\omega t)\mathrm{d}t}{\int_0^\infty I_{ij}(t)\,\mathrm{d}t}, \tag{3.2}$$

where the subscripts ij denote the coordinates of a given pixel, ω is the angular frequency related to the laser pulse repetition rate defined as $\omega = 2\pi f$, and f here corresponds to 80 MHz. For a pixel characterized by a single exponential decay, the phasor transform results in a set of coordinates that lies on the so-called universal

semicircle described as

$$(G - 0.5)^2 + S^2 = 0.25\,. \tag{3.3}$$

For a fluorescence decay trace that contains two lifetimes, the phasor transform results in a coordinate pair that lies within the semicircle rather than on its boundary. The phasor coordinates here are determined by a linear combination of the two phasors corresponding to the two fluorescent species contributing to the signal. In order to compute the fluorescent lifetimes of a two-compound mixture, the eigenvector associated with the largest eigenvalue of the phasor cluster covariance matrix is commonly used to determine the orientation of the cluster's major axis. By extending this axis across the phasor plot, the short and long fluorescent lifetimes can be determined by the two intersections of the major axis with the universal semicircle [17, 178].

When there are three lifetimes, as expected in samples exposed to the sun filter formulation (sun filters: 120 ps; free NADH: 300–800 ps; bound NADH: 1.0–6.5 ns), the phasor coordinates are enclosed within a triangle whose vertices are located on the universal semicircle and correspond to the individual lifetimes of the three components [17]. In the context of this study, the goal is to use phasor analysis to distinguish the NADH fluorescence (a compound with two lifetimes) from that of the chemical sun filters (a mixture with a third, distinct lifetime). To this aim, one method would be to compare the phasor coordinates of a given pixel to that of phasor clusters generated from (1) NADH alone and (2) sun filter formulation alone. This comparison could be quantified by computing the Euclidean distance between said pixel's phasor coordinates and those of the NADH and sun filter phasor cluster means. However, by strictly and only considering the mean coordinates of the NADH and sun filter phasors, all information relating to their distributions is essentially discarded.

Classically, NADH fluorescence lifetimes are typically thought of as either short or long, depending on whether the coenzyme is free or protein-bound, respectively. However, recent work suggests that these protein-bound complexes can result in an

entire subset of long lifetimes that are dependent on the nature of the protein to which NADH is bound [179, 180]. As a result, the phasor cluster corresponding to NADH fluorescence is fairly broad due to its multi-lifetime nature, warranting a separation technique that considers the statistical distributions of reference clusters for improved separation accuracy.

To this aim, the use of the Mahalanobis distance is proposed, where this metric describes the distance between a given observation and an entire distribution, rather than simply the distribution's mean [181]. Mathematically, given an observation $\overrightarrow{x_{ij}} = [G_{ij}\,, S_{ij}]^{\mathrm{T}}$ from a pixel with spatial coordinates ij, and a reference set with mean $\overrightarrow{\mu_{\mathrm{ref}}} = [G_{\mu}\,, S_{\mu}]^{\mathrm{T}}$ and covariance matrix $\mathbf{C}_{\mathrm{ref}}$, the Mahalanobis distance is defined as

$$D_{ij,\mathrm{ref}} = \sqrt{(\overrightarrow{x_{ij}} - \overrightarrow{\mu_{\mathrm{ref}}})^{\mathrm{T}}\, \mathbf{C}_{\mathrm{ref}}^{-1}\, (\overrightarrow{x_{ij}} - \overrightarrow{\mu_{\mathrm{ref}}})}\,. \tag{3.4}$$

For a given pixel with spatial coordinates ij, the proportion k_{ij} of photons that strictly arose from NADH as opposed to chemical sun filters is given by the ratio of its Mahalanobis distance to the sun filter mixture, $D_{ij,\mathrm{SF}}$, divided by the Mahalanobis distance from the NADH reference sample mean to the sun filter mixture, $D_{\mathrm{NADH,SF}}$. If k_{ij} is computed to be < 0.5 (i.e. if more than half of the pixel's fluorescence can be attributed to the exogenous compound), then the perspective is flipped: the Mahalanobis distance from the phasor to the NADH reference cluster, $D_{ij,\mathrm{NADH}}$, is now divided by the Mahalanobis distance from the sun filter reference sample mean to the NADH reference cluster, $D_{\mathrm{SF,NADH}}$. This ratio is then subtracted from 1 in order to provide the fraction of signal that arose from NADH as opposed to the sun filters. Mathematically, these relations can be expressed as

$$k_{ij} = \frac{D_{ij,\mathrm{SF}}}{D_{\mathrm{NADH,SF}}};$$

if

$$k_{ij} < \frac{1}{2}, \tag{3.5}$$

then

$$k_{ij} = 1 - \frac{D_{ij,\mathrm{NADH}}}{D_{\mathrm{SF,NADH}}}.$$

By inspection, it is readily apparent that if a given phasor is very far from the sun filter phasor cluster, the computed proportion of photons generated from NADH approaches 1; conversely, as said phasor approaches the sun filter phasor cluster, the value of k_{ij} approaches 0. With this in mind, FLIM images containing fluorescence signals from both NADH and sun filters can be processed on a pixel-by-pixel basis to produce entire k-arrays whose elements are bound between 0 and 1. The element-wise product of these arrays with the original TPEF intensity images can then be computed in order to isolate the fluorescence signal arising strictly from NADH. In turn, these processed images can be used in conjunction with FAD intensity images to compute optical redox ratios on a pixel-by-pixel basis to allow for quantification of oxidative stress in skin cells.

3.2.6 Simulation and Validation

In order to validate the improved accuracy of the proposed non-Euclidean approach over traditional Euclidean-based separation, simulated image data was generated and processed in MATLAB. First, endogenous and exogenous compounds were simulated to generate multivariate normally-distributed random phasors with mean $\overrightarrow{\mu_{\mathrm{endo}}} = [0.42\,, 0.35]^{\mathrm{T}}$ and covariance matrix $\mathbf{C}_{\mathrm{endo}} = 10^{-4} \times [9\,, -2\,; -2\,, 2.25]$ for the endogenous compound, and mean $\overrightarrow{\mu_{\mathrm{exo}}} = [0.96\,, 0.05]^{\mathrm{T}}$ and covariance matrix $\mathbf{C}_{\mathrm{exo}} = 10^{-5} \times [6.4\,, -1\,; -1\,, 1.6]$ for the exogenous compound. The simulation then generates a set of three synthetic images 256 $\times$ 256 pixels in size: an endogenous reference

image, an exogenous reference image, and a simulated test image.

For the test image, the concentration of endogenous compound is set to 1 on the far left pixel column and 0 on the far right, with a sigmoidal decay horizontally across the image. Conversely, the concentration of exogenous compound is 0 on the far left and 1 on the far right, with the sigmoidal decay in the opposite direction, such that the total compound content at any given pixel is 1. The sigmoid describing the middle 254 columns is described by Equation 3.6, where the column subscripts j strictly range from 2 to 255, inclusively.

$$k(j) = \frac{1}{1 + \exp\left(\frac{j-128.5}{20}\right)} \tag{3.6}$$

The test image is then processed by the algorithm described in Section 3.2.5 using the simulated endogenous and exogenous images as NADH and chemical sun filter references, respectively. In addition, the test image is also processed using the classical Euclidean approach, where the endogenous fluorescence contribution is computed by dividing the Euclidean distance between the phasor and the exogenous reference by the sum of the Euclidean distances between the phasor and each reference image phasor cluster [18]. The two analysis approaches are then compared by taking column-wise means in order to generate line plots, which intuitively illustrate the differences between the two methods from the expected simulated results.

3.2.7 Quantification of Oxidative Stress

In order to accurately calculate the fraction of fluorescence contributed by NADH as opposed to the chemical sun filters, the NADH images were first spatially binned using a mask 5×5 pixels in size. Only pixels with a minimum photon count of 1000 were considered for subsequent processing, where a custom script written in MATLAB served to transform the data using the phasor approach and separate out the NADH fluorescence signal versus that of the chemical sun filters based on the non-Euclidean distance metric described in Section 3.2.5. Using the isolated fluorescence signal from NADH, NORR values for each field of view were then generated by com-

puting FAD/(NADH+FAD) on a pixel-by-pixel basis. Given that both NADH and FAD are predominantly found within the cytoplasm and mitochondria with weaker fluorescence signals coming from nuclear regions, this correlated spatial distribution results in fairly consistent pixel-wise NORR values across the cell. As such, these pixel values can be averaged to obtain a single NORR value for each cell within a field of view [161, 162, 168]. Individual cells were manually segmented from each resulting image using FIJI image analysis software. From there, mean NORR values were computed for each individual cell, from which an average NORR value could be computed for each individual field of view, representative of the cells present therein. The triplicate NORR values from all three imaged fields of view for each experimental condition were then used to compute a mean and a standard deviation. These triplicate measurements were then used for statistical comparison using the R software package for all statistical calculations. A one-way ANOVA was first calculated between all conditions, with the null hypothesis rejected. Pairwise Student's t-test corrected using Holm's method were then carried out between groups to test for significance using R defaults. Results were considered statistically significant if $p < 0.01$.

3.3 Results and Discussion

Beginning with the sun filter formulation alone, it is found to be transparent with no visible aggregates under trans-illumination at 755 nm, as can be seen in Figure 3-1(a); in Figure 3-1(b), however, the formulation's fluorescence intensity in the NADH channel is readily notable. The corresponding phasor plot (Figure 3-1(c)) shows the vast majority of the pixels forming a tightly bound cluster near the bottom right of the plot, highlighting its short lifetime. The formulation's fluorescence lifetime is on the order of 120 ps, as computed by fitting an exponential decay to the fluorescence decay trace of the sun filter mixture using SPCImage software (Figure 3-1(d)).

An *ex vivo* examination of NADH fluorescence in the stratum spinosum of human epidermis at a depth of 50 μm below the skin surface revealed bright signals from the

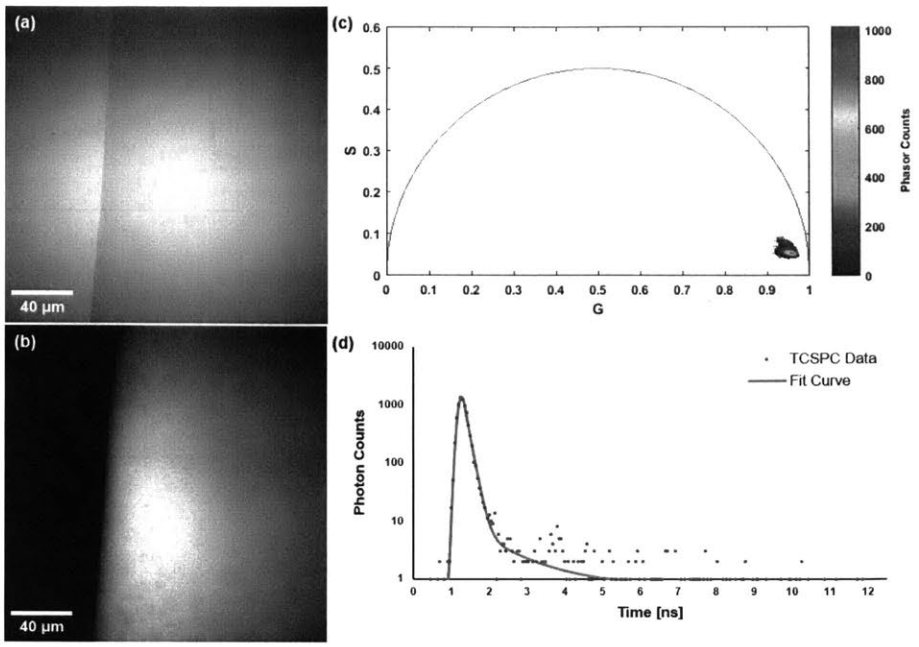

Figure 3-1: Fluorescent properties of the sun filter formulation. (a) Trans-illumination image of the edge of a droplet of sun filter formulation, acquired with 755 nm light. (b) TPEF image of the sun filter formulation acquired with 755 nm excitation light and fluorescence detection from 445 to 480 nm. (c) Phasor plot of the FLIM data associated with (b), highlighting the short fluorescence lifetime of the sun filter formulation. (d) Temporal decay trace of a typical pixel from (b), illustrating the rapid decay of the sun filter fluorescence.

cytoplasm, as NADH is located primarily in the mitochondria and cytosol (Figure 3-2(a)). The corresponding phasor plot is shown in Figure 3-2(b), where the NADH phasors cluster around the central upper region within the universal semicircle; the associated fluorescence decay of NADH is shown in Figure 3-2(c). In the case of skin topically treated with the sun filter formulation, a coalesced pool of sun filter formulation can be appreciated in the bottom right portion of Figure 3-2(d). In this scenario, the associated phasors are distributed between the original NADH cluster and the pure sun filter formulation cluster, as is made apparent by the elongated tail of the phasor plot in Figure 3-2(e). Finally, Figure 3-2(f) illustrates the decay trace of a pixel with a strong fluorescence contribution from the chemical sun filters.

The use of FLIM throughout the course of this study thus adds a temporal dimension over TPEF imaging alone, enabling the distinction of photons emitted by sun filters from those emitted by NADH using the algorithm described in Section

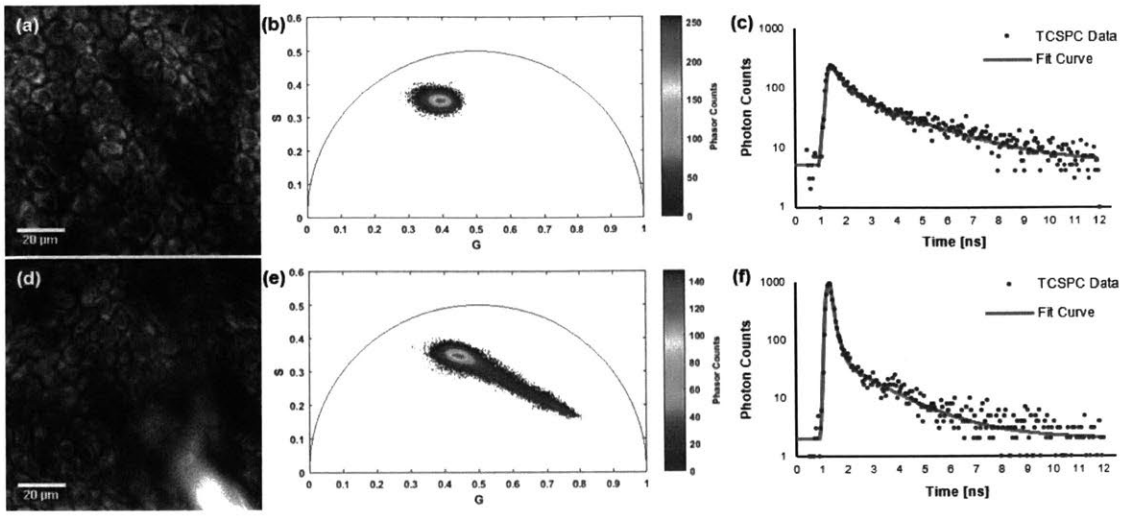

Figure 3-2: Fluorescence detected from the stratum spinosum layer of the viable epidermis, acquired at a depth of 50 μm below the skin surface. (a) TPEF image of human skin treated with vehicle only, showing endogenous NADH fluorescence. (b) Phasor plot of the FLIM data associated with (a). (c) Temporal decay trace of a pixel from (a), showing the progressive decay of NADH fluorescence. (d) TPEF image of human skin treated with sun filter formulation, showing both endogenous NADH fluorescence across the field of view, as well as exogenous fluorescence from the sun filters seen in the lower right region of the image. (e) Phasor plot of the FLIM data associated with (d). (f) Temporal decay trace of a pixel from (d) with a strong fluorescence contribution from chemical sun filters.

3.2.5 based on the Mahalanobis distance. In order to validate the accuracy of the developed method, simulated images of endogenous and exogenous references (i.e. NADH and chemical sun filters, respectively) as well as a test image were generated as described in Section 3.2.6. The phasor plots generated for the simulated endogenous reference, exogenous reference, and test sample are shown in Figure 3-3(a–c). The actual fluorescence contribution of the endogenous sample in the test image is shown in Figure 3-3(d). Next, the traditional Euclidean method (Figure 3-3(e)) and the proposed non-Euclidean approach based on the Mahalanobis distance (Figure 3-3(f)) are both used to estimate the endogenous fluorescence contribution. Finally, Figure 3-3(g) shows the column-wise means of the endogenous fluorescence contribution images from Figure 3-3(d–f). While both methods accurately distinguish the two simulated fluorophores when their relative contributions are comparable, the traditional Euclidean method fails particularly in scenarios where one fluorophore with

a broad phasor distribution dominates over another. This can be appreciated in the leftmost region of the curve in Figure 3-3(g), where the Euclidean estimates plateau around 0.95 as the endogenous fluorescence begins to dominate, while the proposed Mahalanobis-based approach consistently follows the simulated data curve.

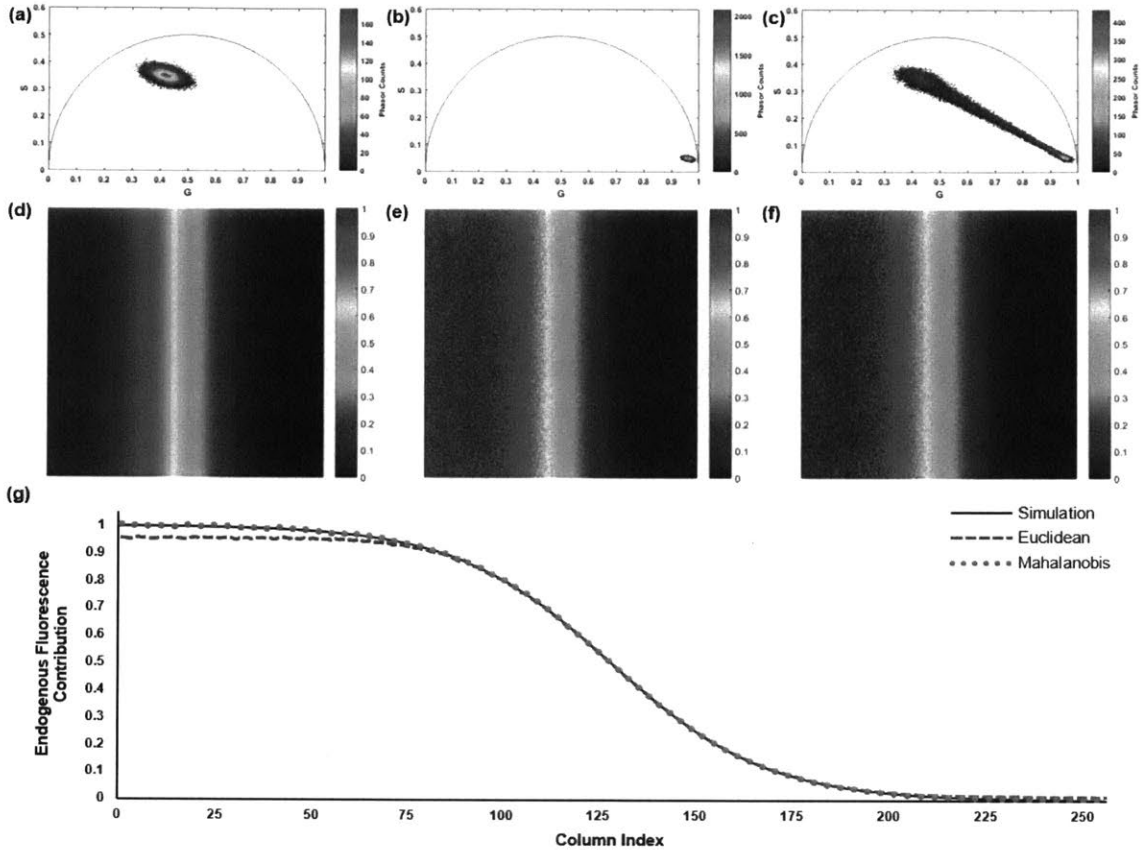

Figure 3-3: Simulation to validate the proposed non-Euclidean separation algorithm. (a) Phasor plot of simulated endogenous fluorescence reference sample. (b) Phasor plot of simulated exogenous fluorescence reference sample. (c) Phasor plot of simulated test image, consisting of both fluorophores with concentrations varying in opposite sigmoidal fashion. (d) Simulated endogenous fluorescence contribution to the test image. (e) Estimation of endogenous fluorescence contribution computed using the traditional Euclidean method. (f) Estimation of endogenous fluorescence contribution using the proposed non-Euclidean method based on the Mahalanobis distance. (g) Column-wise means of the images in (d–f), illustrating the superior accuracy of the proposed method over the classical Euclidean approach.

Having validated the proposed approach on simulated data, the algorithm was applied to all NADH image sets in order to decouple the endogenous fluorescence from

that of the chemical sun filters. The performance of the algorithm is demonstrated in Figure 3-4, showing the TPEF intensity image (Figure 3-4(a)), the Euclidean estimate of the endogenous fluorescence contribution (Figure 3-4(b)), and the same estimate computed using the proposed non-Euclidean method (Figure 3-4(c)). Taken together, the results shown in Figures 3-3 and 3-4 support the applicability of the described non-Euclidean separation algorithm for distinguishing endogenous NADH fluorescence from topically applied exogenous compounds with a similar fluorescence signature but a distinct lifetime.

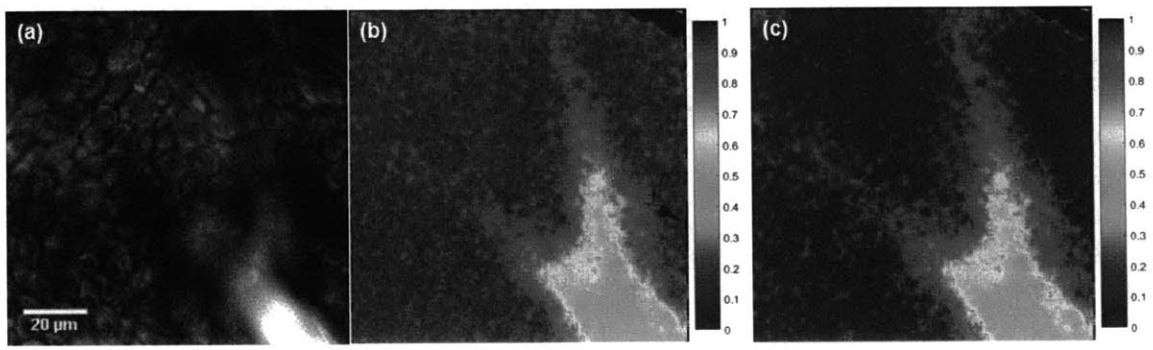

Figure 3-4: Comparison of processing methods to optimally determine endogenous fluorescence contribution. (a) TPEF intensity image of human skin treated with chemical sun filters, showing a diffusing pool of formulation in the bottom right portion of the image. (b) Estimate of the endogenous fluorescence contribution computed using the traditional Euclidean method. (c) Estimate of the endogenous fluorescence contribution as determined by the proposed non-Euclidean approach based on the Mahalanobis distance metric.

While commercial sunscreens are typically formulated to remain in the uppermost layers of skin with minimal transdermal penetration, the FLIM data counterintuitively suggested that the chemical sun filters in the model formulation diffused throughout the viable epidermis. This diffusion into the skin is important to understand, as the pharmacokinetics of the sun filters will influence its oxidative effects.

The optimal design of topical formulations is challenging, as solvents/carriers and solutes may propagate throughout the tissue at different rates based on their charge, polarity, and structure [163]. While the imaging approach based on FLIM and phasor analysis developed here indeed demonstrates the ability to distinguish endogenous from exogenous fluorescence, coherent Raman imaging is a label-free modality that

can be used to longitudinally visualize the diffusion of a solvent throughout the tissue by directly probing its molecular vibrational properties [55].

Sunscreen formulations tend to be complex mixtures of diverse ingredients, while the model formulation studied here simply consisted of five chemical sun filters dissolved in Finsolv TN, a lipophilic solvent commonly used in sunscreen. Considering its molecular properties and the lipophilic nature of the sun filters, it was hypothesized that the solvent was acting as a carrier, thereby dragging the formulation contents into the deeper layers of the epidermis. To verify whether this was indeed the case, a 5 μL droplet of Finsolv TN was topically applied to *ex vivo* human skin and visualized using CARS microscopy. CARS is a parametric four-wave mixing process where a known molecular vibrational resonance can be probed by interacting with two incident pulsed laser beams, known as the pump and Stokes beams, in order to generate a unique and spectrally distinct anti-Stokes signal that can be readily detected using an appropriate set of optical filters [28]. In the case of Finsolv TN, the molecule has an alkyl tail 12 to 15 carbons in length; by probing the symmetric CH_2 stretching vibrational mode at 2845 cm^{-1}, the solvent can be readily visualized as it diffuses throughout the tissue.

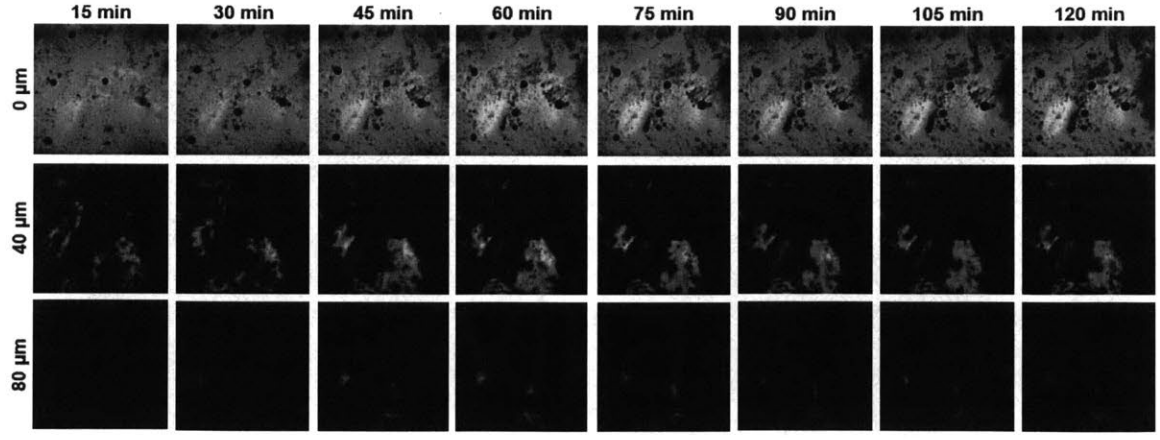

Figure 3-5: Diffusion of the lipophilic solvent throughout various layers of human epidermis (0, 40, and 80 μm below the skin surface), as visualized using CARS microscopy to probe the CH_2 vibrational mode of Finsolv TN at 2845 cm^{-1} at 15-minute intervals over the course of 2 hours. All images are 318 μm $\times$ 318 μm in size.

As can be seen in Figure 3-5, the solvent droplet shows bright CARS signals at

the topmost layer of skin that progressively fades over time as the solvent diffuses and penetrates into the underlying strata. At 40 and 80 μm below the surface, the intensity is seen to progressively rise, peak around 60 minutes following application, and fall thereafter as the Finsolv TN continues to diffuse radially throughout the epidermis. The use of CARS microscopy thereby confirmed the penetration of the formulation solvent into the deeper layers of the epidermis, consistent with the prior observation of sun filter fluorescence in the stratum spinosum using FLIM. More generally, this application of CARS imaging showcases the use of a distinct nonlinear optical modality for visualizing the formulation's solvent itself, which can prove useful in the optimization and validation of topical formulations, among other applications.

Having validated the penetration of and diffusion of both the sun filters and their solvent, we next studied whether these agents induce oxidative stress onto the cells of the viable epidermis. To this aim, NADH and FAD fluorescence intensities are used to compute NORR values, defined as FAD/(NADH+FAD), with a representative image set shown in Figure 3-6.

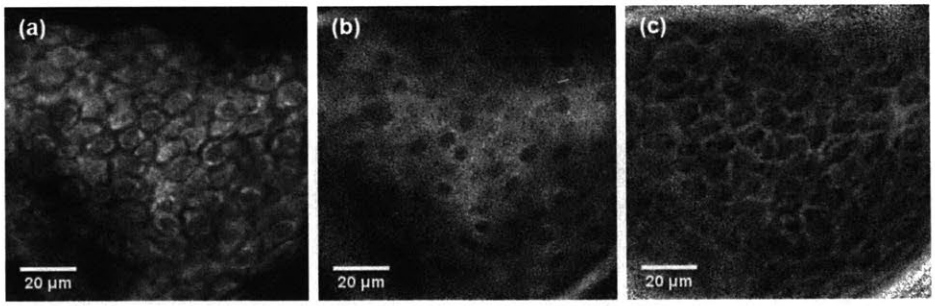

Figure 3-6: Fluorescence intensity and computed NORR images of a typical skin sample. (a) NADH fluorescence intensity. (b) FAD fluorescence intensity. (c) NORR image, obtained by computing FAD/(NADH+FAD) on a pixel-by-pixel basis.

This study's key finding is shown in Figure 3-7, which shows the magnitude of redox perturbations in skin caused by both UVA and sun filter exposure. The greatest redox perturbation is a large oxidative shift triggered by exposure to UVA irradiation. This transition to an oxidative stress state is known to arise from the generation of ROS via UVA photochemistry and matches well what has been observed previously [158, 159, 167, 182, 183, 184]. Interestingly, we do indeed observe a small shift in

redox state towards oxidative stress in skin tissues exposed only to the minimalist sun filter formulation ($p = 0.08971$), which would warrant further investigation with larger sample sizes. It is also worth noting that had the vehicle- and formulation-treated samples been solely considered, the calculated p-value would have been below the 0.05 threshold for statistical significance. However, in order to account for the family-wise error rate stemming from multiple pair-wise comparisons when considering all treatment conditions, the Holm-Bonferroni correction was used and resulted in a corrected p-value exceeding 0.05. Nevertheless, the observed oxidative shift is likely caused by the ROS generation mechanism previously described in *in vitro* studies, where the long triplet state lifetime of the chemical sun filters enables them to react with ground state triplet molecular oxygen, thereby promoting it to an excited singlet state [155, 171, 185, 186, 187]. Importantly, however, when sun filter-treated skin was exposed to UVA irradiation, there is a clear benefit, with the chemical sun filters limiting the oxidative stress induced by UV light exposure. This protection was observed even though a substantial concentration of the study's sun filter formulation was found to penetrate into the viable epidermis, indicating that these chemical absorbers still serve an important function even if they are not confined to the epidermal surface.

3.4 Conclusions

These results have important implications in the context of commercial sunscreen formulations, and motivate the need for future studies investigating these effects. First, commercial sunscreens are purposely designed to limit the majority of skin penetration to the topmost layers of the epidermis; given that the formulation studied here primarily consisted of Finsolv TN, it is expected that the penetration of chemical sun filters observed in this context is not entirely representative of commercial sunscreen behavior [163]. Second, sunscreens contain a wide variety of additional ingredients ranging from moisturizers to antioxidants, which could limit redox state perturbations, though the exact effects of these additives are not well characterized *in vivo*

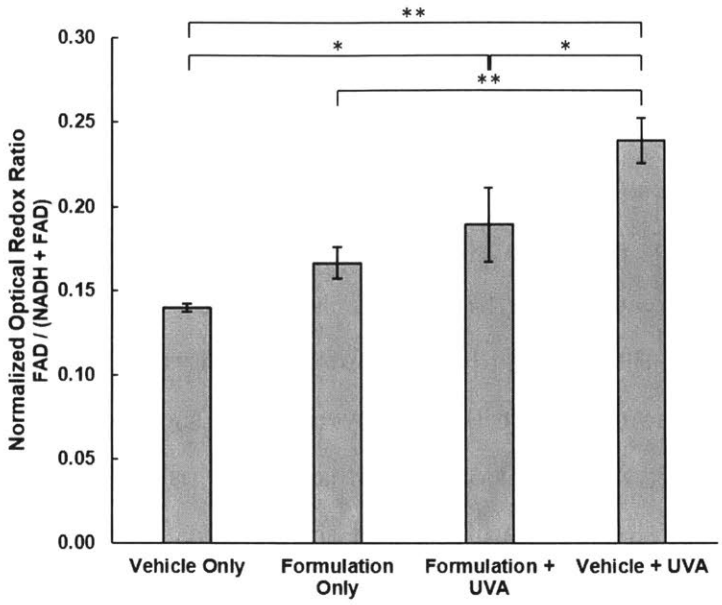

Figure 3-7: Normalized optical redox ratio (NORR) of cells in the stratum spinosum layer of the viable epidermis treated with either vehicle only or sun filter formulation, and exposed to either 0 or 20 J/cm^2 (1 MED) of UVA irradiation. Bars correspond to mean NORR measurement of cells from N = 3 fields of view, and error bars represent ± 1 standard deviation. Statistical significance determined by pair-wise Student's t-test corrected using Holm's method, annotated with * if $p < 0.01$ and ** if $p < 0.005$.

[155, 158, 184]. Still, the small redox changes observed due to the sun filter formulation begs the question as to what occurs following exposure to commercial products, and could be helpful in understanding how to best design topical sunscreens and sunscreen-containing cosmetics in the future.

It should be noted that while small oxidative shifts caused by the sun filters in this study were observed, the patient sample sizes in this preliminary work are small, and are therefore not intended to support general claims regarding oxidative stress *in vivo*. Instead, this study describes a methodology that can now be expanded to investigate the effects of topical agents applied to skin in a non-invasive manner, in spite of the intrinsic fluorescence of the applied compounds. Specifically, it was found that the fluorescent nature of the studied chemical sun filters and, perhaps more importantly, their intrinsically short fluorescent lifetime, allow for spatiotemporal mapping of these compounds within skin. By exploiting the brevity of their fluorescence lifetime, the treated skin samples' time-correlated fluorescent emission from 445 to 480 nm can be

transformed using the phasor approach to distinguish photons emitted from NADH versus chemical sun filters. This separation allows for analysis of redox state perturbations by processing the isolated NADH signals together with those of FAD to characterize the response of viable epidermal cells to chemical sun filter and/or UVA exposure. In addition, this method enables the tracking of exogenous fluorescent compounds as they penetrate and permeate throughout the epidermis, as was shown in the present study with chemical sun filters, and further validated using CARS microscopy to monitor the solvent itself. As such, the proposed methodology can be applied to study a wide range of topical agents, provided the fluorescence lifetimes of the exogenous compounds are distinct from those of endogenous fluorophores.

This method is now ready for translation to clinical settings, where large-scale investigations into the kinetics and physiological dynamics of sun filters can be studied on human patients. Mobile two-photon FLIM systems are already commercially available, and would be suitable for capturing the sun filters' diffusion and redox perturbations in skin [172, 188]. Importantly, future studies can focus on the use of more realistic commercial sun filter formulations to better inform the dermatology community, commercial sunscreen manufacturers, and consumers alike.

Chapter 4

FLIM Data Analysis in Phasor Space: A Simulated Comparison of Euclidean and Non-Euclidean Distance Metrics to Distinguish Fluorescent Species

4.1 Introduction

Fluorescence lifetime imaging microscopy (FLIM) is an extremely useful tool in the context of molecular imaging, as it provides microscopists with an additional dimension of imaging contrast [10]. In addition to probing the excitation and emission properties of fluorophores, FLIM is a tool also capable of probing the temporal dynamics of these molecules. When a fluorophore absorbs electromagnetic energy — whether in the form of a single photon or multiple photons simultaneously — it is promoted to an excited state. Following some degree of rapid non-radiative decay, the molecule then relaxes back down to its ground state, thereby emitting a photon in the process. This decay back to the ground state is a stochastic process that follows

a Poisson distribution, characterized by a time constant known as the fluorescence lifetime, denoted by τ [11].

The fluorescence lifetime of a molecule is a characteristic property, much like its optical excitation and emission properties. However, this does not imply that the lifetime is invariant; to the contrary, it can be influenced by the molecule's local environment. For example, naturally fluorescent coenzymes such as flavin and nicotinamide adenine dinucleotides (FAD and NADH, respectively) can exhibit a strong shift in fluorescence lifetime depending on whether they are free in solution or protein-bound [165, 164, 14, 15]. Other microenvironmental factors such as temperature, pH, viscosity, solvent polarity, molecular conformation, and metal ion chelation among others can also have an impact on fluorescence lifetime [16]. In a typical biological context however, the factors most likely to have an observable and measurable effect within a given field of view are enzymatic binding, ion chelation, or molecular quenching, as in the case of Förster resonance energy transfer (FRET) [189, 190, 17, 191]. With this in mind, the fluorescence lifetime of each fluorophore within an imaging field can therefore be viewed as an intrinsic characteristic property; FLIM can thus readily serve to distinguish a mixture of multiple fluorescent species at hand.

This complementary source of imaging contrast in the specific context of NADH and FAD imaging has already yielded considerable insight into the metabolic states of cells and tissues [165, 192, 191, 193, 164, 162, 167, 177, 180, 15]. These far-reaching applications in cancer research range from validation of therapeutics in the laboratory space to characterization of dysplastic and cancerous lesions *in situ* in the context of clinical research. Other applications include the ability to discern cellular and tissue autofluorescence from exogenous compounds in order to study the pharmacokinetics and pharmacodynamics of exogenous compounds as they are administered to a given biological system [14, 16].

Despite its noteworthy benefits, one persistent challenge that often arises in the interpretation of FLIM data lies in the accurate distinction of fluorophores within a mixture, particularly in the case of a large discrepancy in their respective concentrations [14, 16]. FLIM data analysis can broadly be categorized into two major approaches:

time-domain and frequency-domain (more commonly referred to as phasor analysis) [17, 18]. Traditional time-domain analysis of FLIM data entails multi-exponential curve fitting of the fluorescent decay traces on a pixel-by-pixel basis, where each of the N fluorophores within a given pixel's decay trace are distinguished based on their time constants τ_i and relative weights α_i, as in Equation 4.1.

$$I(t) = \sum_{i=1}^{N} \alpha_i e^{-\frac{t}{\tau_i}} \tag{4.1}$$

This approach requires considerable *a priori* knowledge of the sample at hand, both in terms of the number of compounds N to distinguish, as well as a general idea of their respective fluorescent lifetimes [13]. An additional layer of complexity arises in distinguishing exogenous compounds from cellular and tissue autofluorescence, which may arise from compounds such as NADH and FAD — compounds that naturally have multiple lifetimes already, based on their molecular conformation and binding state [14, 15, 16]. Given that time-domain analysis is fundamentally based on iterative curve fitting, the distinction of exogenous sources of fluorescence from endogenous sources that themselves have multiple lifetimes quickly becomes computationally demanding. Moreover, this approach often requires a prohibitively large number of photon counts per pixel (typically in excess of 5000 photons) in order to ensure accurate lifetime estimates, particularly when the concentration of one fluorophore is significantly larger than the other [13]. Such photon counts require longer sample exposure times and/or higher excitation power, which may be incompatible with the biological sample at hand. It is worth noting that known fluorescent lifetimes may be specifically defined as part of the model function used to fit the experimental data to save on computation time and to favor convergence around biologically representative values. The trade-off, however, is that fitting such a model would assume that there is no variance in lifetime-discrete states — an assumption that is not always valid in biology, particularly in the context of endogenous coenzymes such as FAD and NADH.

For the purposes of limiting sample photodamage as well as facilitating data anal-

ysis and interpretation, phasor analysis is quickly becoming the preferred approach for processing FLIM data. This alternative methodology requires substantially less prior knowledge about the sample and conveniently offers an intuitive visual representation of the data at hand. Rather than curve fitting, phasor analysis involves a transformation of each pixel's temporal decay trace into a pair of coordinates (G, S) that describe a phasor, characterized by its coordinates in two-dimensional space [17]. The transformations correspond to the real and imaginary components of the Fourier transform of the temporal decay trace normalized by its area under the curve, evaluated at the angular laser repetition frequency ω, as shown in Equations 4.2 and 4.3.

$$G = \frac{\int_0^\infty I(t)\cos(\omega t)\mathrm{d}t}{\int_0^\infty I\,(t)\,\mathrm{d}t} \tag{4.2}$$

$$S = \frac{\int_0^\infty I(t)\sin(\omega t)\mathrm{d}t}{\int_0^\infty I\,(t)\,\mathrm{d}t} \tag{4.3}$$

Note that the angular frequency ω is related to the laser pulse repetition rate f by $\omega = 2\pi f$. In the case of pulsed laser sources, f is typically on the order of 80 MHz; with single-photon FLIM systems, a continuous wave (CW) laser is intensity-modulated, where f then corresponds to the modulation frequency. In the case of a single fluorophore characterized by a unique lifetime, the phasor transform results in a set of phasor coordinates that obey the relation shown in Equation 4.4, describing a semicircle with radius 0.5 centered at $(0.5, 0)$ [17].

$$(G - 0.5)^2 + S^2 = 0.5^2 \tag{4.4}$$

In the context of phasor analysis of FLIM data, this is referred to as the universal semicircle. For a decay trace characterized by two fluorescence lifetimes, its transformed phasor coordinates would lie along a line connecting the two individual lifetimes on the universal semicircle. The exact phasor coordinates along that line would naturally depend on the relative concentrations of the two fluorescent species [17, 18]. It follows that for a heterogeneous binary mixture of fluorescent species,

the transformed FLIM image would result in an elongated cluster stretching one set of reference phasor coordinates to the other. Given such a mixture, FLIM data analysis offers the ability to estimate the relative fluorescence contribution of each compound at every pixel in the image based on the relative distances between each pixel's corresponding phasor location and the respective reference phasor clusters of the fluorophores at hand.

A challenge arises however in discerning the two fluorescent species when the reference phasor clusters are inherently broad. This can result from a number of contributing factors, including low photon counts and intrinsic variability of the fluorescence lifetime of one or both compounds, as is typically the case with endogenous fluorophores such as NADH. In such cases, estimating the contribution of either compound using traditional Euclidean distances in phasor space becomes problematic, resulting in decreased accuracy when pixels from the binary mixture image are dominated by one compound over the other. This is because the pixel's corresponding phasor falls within the variance of the reference phasor cluster, thereby complicating accurate distinction. To reduce this inaccuracy, we have previously proposed the use of the Mahalanobis distance, a non-Euclidean metric, for phasor analysis in the context of signal separation and compound distinction in a binary mixture [14]. Instead of simply considering the mean phasor cluster coordinates of the reference sample, this distance metric additionally considers the cluster's covariance, thereby taking into account the spread of the cluster for separation purposes. The Mahalanobis distance is given by Equation 4.5 [181].

$$D^{(M)}_{ij,\mathrm{ref}} = \sqrt{\left(\overrightarrow{x_{ij}} - \overrightarrow{\mu_{\mathrm{ref}}}\right)^{\mathrm{T}} \mathbf{C}^{-1}_{\mathrm{ref}} \left(\overrightarrow{x_{ij}} - \overrightarrow{\mu_{\mathrm{ref}}}\right)} \tag{4.5}$$

In this context, $D_{ij,\mathrm{ref}}$ is the Mahalanobis distance between the phasor of a given pixel ij and a reference cluster; $\overrightarrow{x_{ij}}$ is a vector composed of the (G, S) phasor coordinates of the pixel ij; $\overrightarrow{\mu_{\mathrm{ref}}}$ is a vector composed of the mean (G, S) phasor coordinates of the reference phasor cluster; and $\mathbf{C}^{-1}_{\mathrm{ref}}$ is the 2×2 covariance matrix of the reference phasor cluster. Note that the Euclidean distance can be obtained by replacing the

covariance matrix in Equation 4.5 with the identity matrix, yielding Equation 4.6.

$$D^{(E)}_{ij,\text{ref}} = \sqrt{\left(\overrightarrow{x_{ij}} - \overrightarrow{\mu_{\text{ref}}}\right)^{\text{T}} \left(\overrightarrow{x_{ij}} - \overrightarrow{\mu_{\text{ref}}}\right)} \tag{4.6}$$

In the present analysis, the Euclidean and Mahalanobis (i.e. non-Euclidean) distance metrics are compared and contrasted in terms of their ability to estimate the relative contributions of each fluorescent compound in a heterogeneous mixture. Three particular contexts are considered here: a binary mixture of compounds with well-defined single fluorescence lifetimes; a binary mixture of fluorophores with multiple lifetimes; and a ternary mixture of single-lifetime fluorescent species.

4.2 Materials and Methods

All simulations presented herein were performed in the MATLAB R2017b environment (MathWorks, Natick, MA). The various functions and scripts are provided in Appendix A.

4.2.1 Simulation of a Binary Mixture

The main script for simulating a binary mixture of fluorescent compounds and estimating their respective concentrations is provided in `simulationMain_Binary.m`. Throughout the first few lines of code, the user must specify the dimensions of the imaging field of view in terms of the numbers of pixels along the Y and X dimensions (`numPixelsY` and `numPixelsX`, respectively). Next, the lifetimes of the two compounds (`tauTheoretical_A` and `tauTheoretical_B`) must be specified, as well as the relative uncertainty on these values (`tau_error`). In the case of a compound with multiple lifetimes, the relative weights of each lifetime (`alpha1_B`, `alpha2_B`, and so forth) as well as the uncertainty of these weighting coefficients (`alpha_error`) must also be specified. Finally, the number of photons per pixel must also be defined (`totalNumPhotonsSignal`), in addition to the number of spurious noise photons for each set of images (`totalnumPhotonsNoise_A`, `totalnumPhotonsNoise_B`,

and `totalnumPhotonsNoise_Mix`).

Next, a row vector is defined such that the squared sine and cosine functions describing the concentration of either compound in the mixture image are evaluated over the course of one full amplitude cycle. Stated mathematically, x is a row vector with `numPixelsX` elements spanning 0 to π, and the concentration of compound A (`conc_A`) is defined as $\sin^2 x$ while that of compound B (`conc_B`) is given by $\cos^2 x$. These row vectors are then replicated vertically `numPixelsY` times in order to generate the mixture image.

The phasor transform and plotting parameters are then specified by the user. These include: the harmonic number used for the phasor transform itself (`harnomicNumer`, default: 1); the 2D histogram step size in phasor space (`steps`, default: 0.0025); the laser repetition frequency in Hz (`freq0`, default: 80×10^6); the minimum threshold in order to display a histogram bin count value in the phasor plot relative to the largest bin value (`histogramThreshold`, default: 0.001, i.e. bins with at least 0.1% of the counts in the largest bin will be displayed in the phasor plot); the preferred colormap for the phasor plot (`cmap`, default: `'jet'`); flags determining whether or not the 95% confidence ellipse is to be drawn around each generated phasor plot (`drawEllipse_A`, `drawEllipse_B`, and `drawEllipse_Mix`; defaults: all 0); flags determining whether or not the intercepts between the major axis of the 95% confidence ellipse and the universal semicircle are to be indicated on the phasor plot (`drawIntercepts_A`, `drawIntercepts_B`, and `drawIntercepts_Mix`; defaults: all 0); and finally, the number of fluorescent compounds present in each reference image (`numSpecies_A` and `numSpecies_B`; defaults: all 1) and the mixture image (`numSpecies_Mix`, default: 2).

Additional imaging parameters are then set by default, although they can readily be changed by the user to evaluate different simulation conditions. These include: the number of time bins for the histogram decay traces (`numTimeBins`, default: 256) as well as a pre-defined instrument response function (`IRF`) used to compute the phasor transform.

Using all the above input parameters, the simulated images are finally generated, where each image pixel has its associated fluorescence decay trace defined in terms of

photon counts in the temporal domain over `numTimeBins` bins. For each decay trace, a time constant τ is defined by the theoretical lifetime `tauTheoretical` provided by the user adjusted by some random variable normally distributed around 0 with a standard deviation of `tauSigma` given by `tau_error` $\times$ `tauTheoretical`. The resulting time constant is then used to generate an exponential probability density function. This function is convolved with the instrument response function (IRF), yielding Equation 4.7.

$$f(t) = \frac{1}{\tau} e^{-\frac{t}{\tau}} * \mathrm{IRF}(t) \tag{4.7}$$

This is the probability density function from which photon arrival times are drawn using the MATLAB function `datasample`. If spurious noise photons are also included in the simulated decay trace, they are simply drawn from a uniform temporal distribution across the laser pulse period. It is worth noting that the photon arrival times are drawn from a continuous basis; in order to simulate a decay trace, they are binned into `numTimeBins` bins in order to generate the decay trace histogram.

Next in the simulation comes the phasor transform of each individual decay trace in order to generate all (G, S) coordinates as well as the phasor plots. The phasor transform function computes the results of Equations 4.2 and 4.3 by trapezoidal numerical integration. The phasor plots are then generated by binning the (G, S) coordinates in a 2D histogram and displaying the resulting cluster in a plot along with the universal semicircle.

In the case of the traditional Euclidean approach for estimating the contribution of a pair of fluorophores in a binary mixture, the contribution $k_A^{(E)}$ of compound A for a given phasor can be estimated by computing the ratio of the Euclidean distance between the phasor and the mean coordinates of cluster B, to the sum of the Euclidean distances between the phasor and the mean coordinates of clusters A and B together. This relation is best summarized by Equation 4.8, where the values $D_{ij,A}^{(E)}$ and $D_{ij,B}^{(E)}$ can be computed using Equation 4.6 [18, 177].

$$k_A^{(E)} = \frac{D_{ij,B}^{(E)}}{D_{ij,A}^{(E)} + D_{ij,B}^{(E)}} \tag{4.8}$$

It is readily apparent that a phasor located at the mean coordinates of cluster A will result in a $k_A^{(E)}$ value of 1, signifying a pixel whose fluorescence is completely dominated by compound A. Conversely, a phasor at the center of cluster B will yield a value of 0, implying the absence of compound A.

In using the Mahalanobis distance however, the mathematics are somewhat more nuanced. Given that the computed distances are non-Euclidean, they operate in a space governed by the covariance of each respective reference phasor cluster. For this reason, Mahalanobis distances calculated using different references cannot be summed together as is the case of the denominator in Equation 4.8. Instead, the contribution $k_A^{(M)}$ of compound A for a given phasor estimated using the Mahalanobis distance is given Equation 4.9.

$$k_A^{(M)} = \frac{\frac{D_{ij,B}^{(M)}}{D_{A,B}^{(M)}} + \left(1 - \frac{D_{ij,A}^{(M)}}{D_{B,A}^{(M)}}\right)}{2} \tag{4.9}$$

In this context, $D_{ij,B}^{(M)}$ corresponds to the Mahalanobis distance between the phasor of pixel ij and the mean coordinates of reference phasor cluster B; $D_{A,B}^{(M)}$ is the Mahalanobis distance between the mean coordinates of phasor cluster A from reference cluster B. The converse relations are true for $D_{ij,A}^{(M)}$ and $D_{B,A}^{(M)}$. In this case, it can still be observed that a phasor located at the center of cluster A would yield $k_A^{(M)} = 1$, since this would imply $D_{ij,B}^{(M)} = D_{A,B}^{(M)}$ and $D_{ij,A}^{(M)} = D_{A,A}^{(M)} = 0$. Consistently, a phasor located at the mean coordinates of cluster B would result in $k_A^{(M)} = 0$, considering $D_{ij,A}^{(M)} = D_{B,A}^{(M)}$ and $D_{ij,B}^{(M)} = D_{B,B}^{(M)} = 0$.

4.2.2 Simulation of a Ternary Mixture

The simulation of a ternary mixture is essentially similar in implementation to that of the binary mixture, but with a few key differences. The resulting script is available in `simulationMain_Ternary.m`.

In this case, there are three compounds to be simulated, where all parameters related to the third fluorophore are denoted `tauTheoretical_C`, `totalNumPhotonsNoise_C`, and so forth. In order to generate a ternary mixture with uniform pixel intensity, the adopted approach is to simulate three distinct sinusoidal concentration patterns, each phase-shifted relative to one another by $2\pi/3$ radians. Mathematically, this implies defining a row vector x spanning 0 to 2π, where the concentrations of compounds A, B, and C are defined by $(1+\cos(x))/2$; $(1+\cos(x+2\pi/3))/2$; and $(1+\cos(x-2\pi/3))/2$. The functions used to simulate the decay traces and associated images are otherwise the same as those used in Section 4.2.1.

It is worth recalling that a fluorescence decay trace characterized by three distinct lifetimes results in a set of phasor coordinates located somewhere within a triangle whose vertices are located along the circumference of the universal semicircle. The vertex coordinates in turn are determined by the individual lifetimes of the three compounds at hand. The exact position of the decay trace's corresponding phasor depends on the relative weights of each fluorescent compound: if one compound dominates strongly over the other two, the phasor will be located nearest to that corresponding triangle vertex.

With this foundation in mind, one may consider a triplet of fluorescent compounds A, B, and C, each resulting in phasor clusters A, B, and C, corresponding to the vertices of the triangle containing all phasors of the ternary mixture. In order to estimate the contribution of compound A to a pixel from the mixture image corresponding to a phasor denoted X, the Euclidean approach now involves calculating the areas of two triangles in phasor space: triangles ABC and XBC [194]. The sides of these triangles are computed using the Euclidean distances between triangle vertices. This relation can be expressed by Equation 4.10.

$$k_A^{(E_3)} = \frac{A_{\triangle XBC}}{A_{\triangle ABC}} \tag{4.10}$$

By inspection, it is clear that if phasor X is located at the mean coordinates of phasor cluster A, then $A_{\triangle XBC} = A_{\triangle ABC}$ and therefore $k_A^{(E_3)} = 1$, implying that the

decay trace is strictly the result of compound A fluorescence. If phasor X is located anywhere along the line connecting vertices B and C, then $A_{\triangle XBC} = 0$, resulting in a null value of $k_A^{(E_3)}$. In such a case, the areas of triangles XAC and XAB can be computed in order to estimate the relative contributions of compounds B and C, respectively, by dividing them by the area of triangle ABC as per Equation 4.10.

In the case of ternary separation using the Mahalanobis distance, triangular areas in phasor space cannot be computed in a straightforward manner. This is because the Mahalanobis distance is a normalized distance metric that considers the covariance of a reference distribution. Therefore, computing arithmetic operations such as the area of a triangle using Mahalanobis distances obtained from different reference samples is analogous to calculating the area of a geometric shape whose sides are each expressed in different spatial units. This approach is mathematically incorrect, and results in wildly inaccurate concentration estimates.

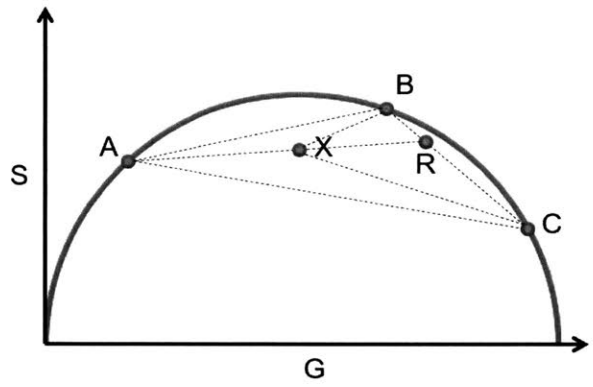

Figure 4-1: Phasor plot showing the mean coordinates of phasor clusters A, B, and C, as well as the phasor of a given pixel X. A line is drawn between phasor X and the mean coordinates of reference cluster A, where its intersection with the line connecting clusters B and C yields the coordinates of R.

To overcome this challenge, an alternative approach can be implemented. Rather than computing the ratio between the areas of a pair of triangles, one may first compute the Mahalanobis distance between the coordinates of a given phasor X and a reference sample A. Next, a line can be drawn between the mean coordinates of phasor cluster A and phasor X, where the intersection of this line with the line connecting phasor clusters B and C is denoted R (Figure 4-1). The Mahalanobis

distance between coordinates R and phasor cluster A is then computed, whereby the Mahalanobis contribution of compound A to the total fluorescence signal of the decay trace associated with phasor X is obtained via Equation 4.11.

$$k_A^{(M_3)} = 1 - \frac{D_{X,A}^{(M)}}{D_{R,A}^{(M)}} \tag{4.11}$$

If phasor X is located along the line connecting phasors clusters B and C, then $k_A^{(M_3)} = 0$. On the other hand, if it is located at the center of phasor cluster A, then $k_A^{(M_3)} = 1$. These mathematical relationships are consistent with those described in the binary separation case.

4.3 Results and Discussion

4.3.1 Binary Mixture with Single Lifetimes

The first accuracy comparison is that of a mixture of two fluorescent compounds A and B, heterogeneously distributed across a simulated field of view 512 × 512 pixels in size. In order to ensure a uniform fluorescence intensity across the field of view, the concentration of compound A is distributed horizontally following a squared sine function over one full cycle; that of compound B is similarly distributed, but following a squared cosine function over one cycle. Their fluorescence lifetimes are set to 4.100 ± 0.205 ns for compound A and 0.200 ± 0.010 ns for compound B, where the uncertainties correspond to $\pm 5\%$ of the corresponding lifetime value. In order to test the limits of performance of the separation algorithms, the photon count per pixel is set to 100 for all simulated FLIM images here. The resulting phasor plots are shown in Figure 4-2.

With larger and larger photon counts, both methods eventually converge to the correct solution. However, in the present context, low photon counts are simulated in order to evaluate the separation accuracy of the two methods under strenuous imaging conditions. As a result, the generated phasor clusters are abnormally broad, posing a challenge in accurately estimating the contributions of either fluorophore. In applying

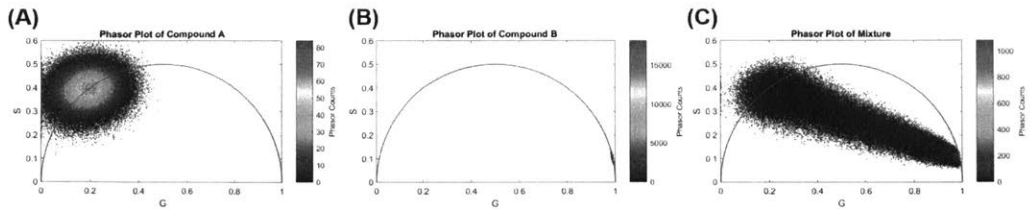

Figure 4-2: Phasor plots of the simulated data used to test the accuracy of the separation algorithms in the context of a binary mixture of single-lifetime fluorophores. (A) Phasor plot of compound A with a lifetime of 4.100 ± 0.205 ns. (B) Phasor plot of compound B with a lifetime of 0.200 ± 0.010 ns. (C) Phasor plot of the binary mixture of compounds A and B.

Equations 4.8 and 4.9 to the heterogeneous mixture image simulated using squared sine and cosine distributions of compounds A and B, Euclidean and Mahalanobis concentration maps of each compound can be generated as seen in Figure 4-3.

In the case of a pair of fluorescent compounds with well-defined single lifetimes that are on opposite sides of the universal semicircle in phasor space, both the Euclidean and Mahalanobis approaches for estimating fluorescence contributions perform similarly overall. However, it is worth noting the increased accuracy in the case of the Mahalanobis method, specifically when one compound with a broad phasor cluster dominates the other in terms of concentration. This observation is particularly evident in Figure 4-3(G,H), where the Mahalanobis-based approach more accurately identifies the dominant contribution of compound A and the corresponding absence of compound B. While both estimates still deviate slightly from the simulated values in the case of pixels dominated by compound A fluorescence due to the low SNR, the Mahalanobis algorithm is found to be of equal or superior accuracy relative to the Euclidean approach in all cases.

4.3.2 Binary Mixture with Multiple Lifetimes

In the second set of simulations, a fluorophore with a single lifetime of 2.500 ± 0.125 ns is compared to another with 4 distinct lifetimes, intended to represent the various possible lifetimes of the endogenous fluorophore NADH [15]. The lifetimes are set to $\tau_1 = 0.770 \pm 0.0385$ ns, $\tau_2 = 1.210 \pm 0.0605$ ns, $\tau_3 = 3.710 \pm 0.1855$ ns, and $\tau_4 =$

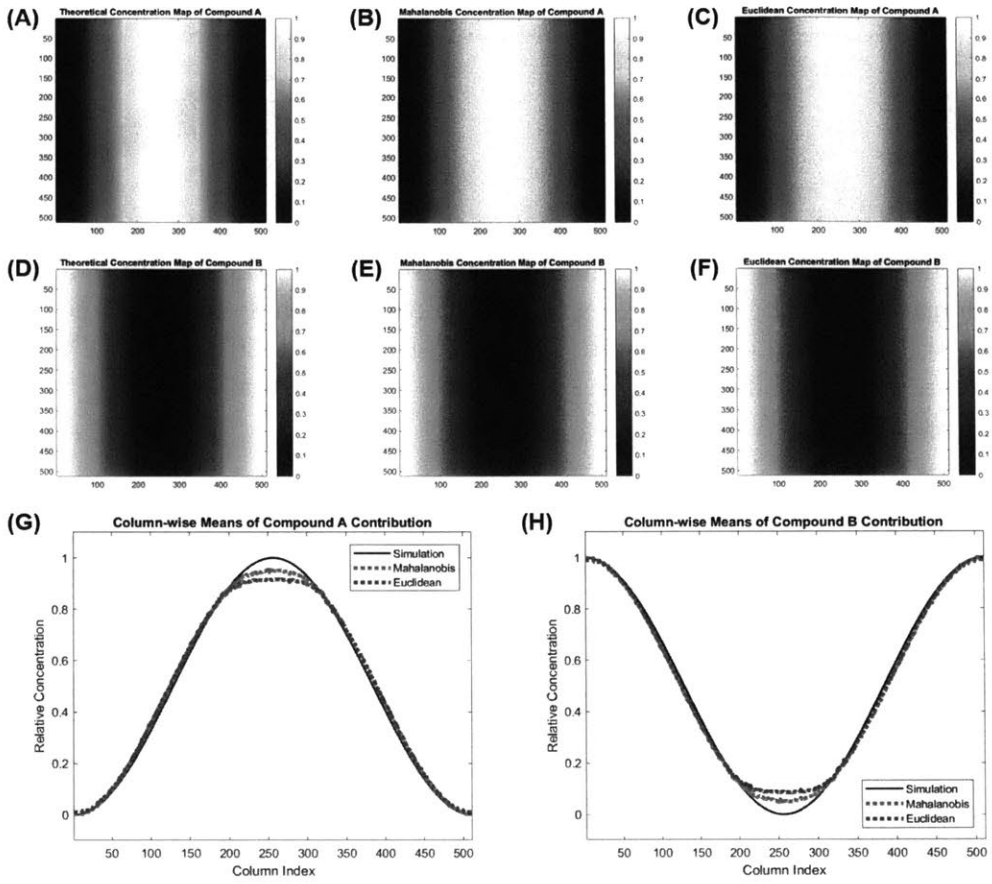

Figure 4-3: Estimated concentration maps of either compound in a binary mixture of single-lifetime fluorophores. (A,D) Theoretical concentration maps of compounds A and B, spatially distributed following squared sine and cosine functions, respectively. (B,E) Concentration maps of compounds A and B, respectively, estimated using the Mahalanobis distance metric. (C,F) Concentration maps of compounds A and B, respectively, estimated using the Euclidean distance metric. (G) Column-wise means of panels A–C. (H) Column-wise means of panels D–F.

0.770 ± 0.239 ns. The weights of each respective lifetime are set to $\alpha_1 = 15 \pm 2.25\%$, $\alpha_2 = 25 \pm 3.75\%$, $\alpha_3 = 35 \pm 5.25\%$, and $\alpha_4 = 25 \pm 3.75\%$. These weighted lifetimes are consistent with what is experimentally observed of NADH fluorescence in cells and tissues in terms of its phasor cluster size, position, and orientation [15].

In running the same set of simulations as in Section 4.3.1 for this second pair of fluorophores, the phasor plots shown in Figure 4-4 are generated. It is worth noting that in this case, a higher number of photons are required to properly resolve the two clusters given their close proximity in phasor space. The photon count per pixel is

therefore set to $N = 1000$. As expected, the phasor cluster of compound A is located along the universal semicircle since it is defined by a single lifetime (Figure 4-4(A)). On the other hand, that of compound B (i.e. a simulated rendition of NADH) is located within the semicircle, roughly at the center of a quadrilateral whose vertices lie on the semicircle coordinates given by each of its four defining lifetimes (Figure 4-4(B)) [15]. The phasor plot of the mixture image, composed of compounds A and B distributed horizontally across the simulated field of view following squared sine and cosine distributions, shows a bimodal phasor cluster as expected (Figure 4-4(C)).

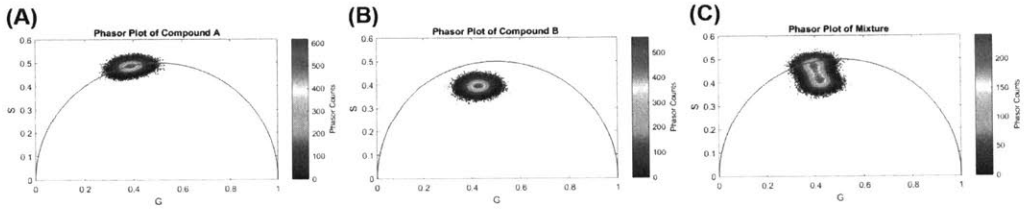

Figure 4-4: Phasor plots of the simulated data used to test the accuracy of the separation algorithms in the context of a binary mixture of fluorophores with multiple lifetimes. (A) Phasor plot of compound A with a lifetime of 4.100 ± 0.205 ns. (B) Phasor plot of compound B, characterized by a combination of 4 distinct lifetimes. (C) Phasor plot of the binary mixture of compounds A and B.

In examining these phasor plots, one can reasonably expect the traditional Euclidean approach to result in a fairly inaccurate estimate of each compound's respective contribution to the fluorescence signals simulated in the binary mixture image. As was discussed prior, this is because the Euclidean approach strictly considers the mean coordinates of the reference phasor clusters. Given their overlapping distributions, a methodology using a metric that factors in their relative spreads in phasor space — such as the Mahalanobis distance — would be expected to outperform the Euclidean method.

To test this hypothesis, the Euclidean and Mahalanobis algorithms are both evaluated in terms of their ability to estimate the relative concentrations of either compound in the binary mixture image, similarly to the procedure in Section 4.3.1. The resulting estimated concentration maps are shown in Figure 4-5.

In the case of two fluorophores whose phasor clusters significantly overlap in pha-

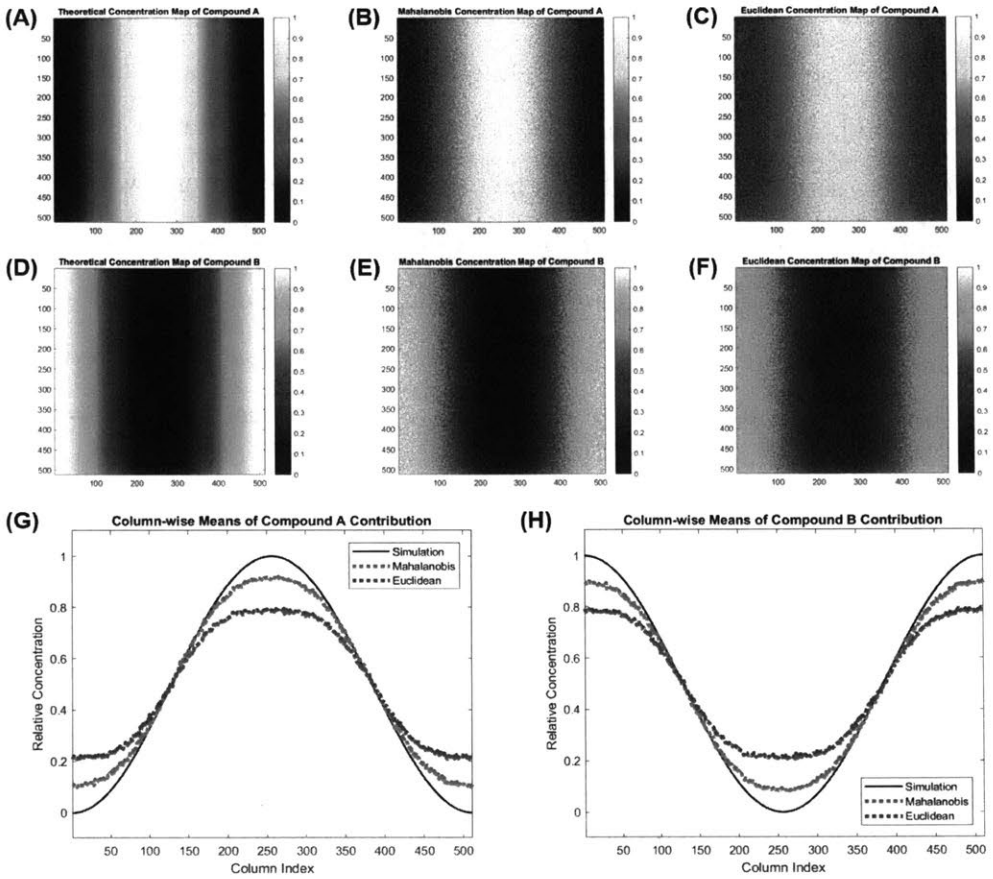

Figure 4-5: Estimated concentration maps of either compound in a binary mixture of fluorophores with multiple lifetimes. (A,D) Theoretical concentration maps of compounds A and B, spatially distributed following squared sine and cosine functions, respectively. (B,E) Concentration maps of compounds A and B, respectively, estimated using the Mahalanobis distance metric. (C,F) Concentration maps of compounds A and B, respectively, estimated using the Euclidean distance metric. (G) Column-wise means of panels A–C. (H) Column-wise means of panels D–F.

sor space, the algorithmic approach based on the Mahalanobis distance indeed vastly outperforms the traditional Euclidean method, as made evident by the column-wise means of the estimated concentration maps (Figure 4-5(G,H)). In this particular scenario, the Euclidean approach results in concentration estimates that plateau around 80% and 20% when they should be 100% and 0%, respectively; the Mahalanobis methodology, on the other hand, results in more accurate estimates around 90% and 10%, respectively. As in the previous simulation, these deviations from simulated values (particularly in the context of one fluorophore dominating over the other) are

partially related to low SNR. The accuracies of both algorithms increase with larger photon counts and decreased uncertainty of fluorescence lifetime values, with the Mahalanobis approach converging at a significantly faster rate.

The simulated performances of both algorithmic approaches assessed in Section 4.3.1 showed generally comparable separation accuracies. This is because the two compounds at hand were on opposite sides of the universal semicircle, and thus naturally offered a high degree of contrast. In such a scenario, opting for one method over the other is unlikely to result in any significant discrepancy in data interpretation. In the present set of simulations however, the differences are indeed significant, where the Mahalanobis approach is seen to roughly halve the overall separation error. Given a binary mixture of one compound with a lifetime of 2.5 ns (such as Coumarin 6, for example) and another that is representative of NADH autofluorescence, this set of simulations shows the great value in using the proposed non-Euclidean approach for distinguishing exogenous from endogenous fluorescence.

4.3.3 Ternary Mixture with Single Lifetimes

These separation techniques can also be generalized from a binary mixture to a ternary mixture and beyond. For the purposes of the present work, the simulations are limited to a three-compound mixture, where the performances of both the Euclidean and Mahalanobis techniques are contrasted.

In order to simulate a ternary mixture with constant fluorescence intensity across the field of view, the concentrations of each respective compound are spread horizontally according to cosine functions, each phase-shifted with respect to one another by $2\pi/3$ radians. The reference phasor clusters of compounds A, B, and C, each defined by fluorescence lifetimes of 4.100 ± 0.205 ns, 1.600 ± 0.080 ns, and 0.600 ± 0.030 ns, as well as the phasor plot of the ternary mixture are all shown in Figure 4-6.

The three-phase cosine distributions of compounds A, B, and C result in an elliptical phasor pattern as seen in Figure 4-6(D). It is worth noting that this ellipse is contained within the triangle whose vertices lie at the centers of phasor clusters A, B, and C. The application of the Euclidean and Mahalanobis separation algo-

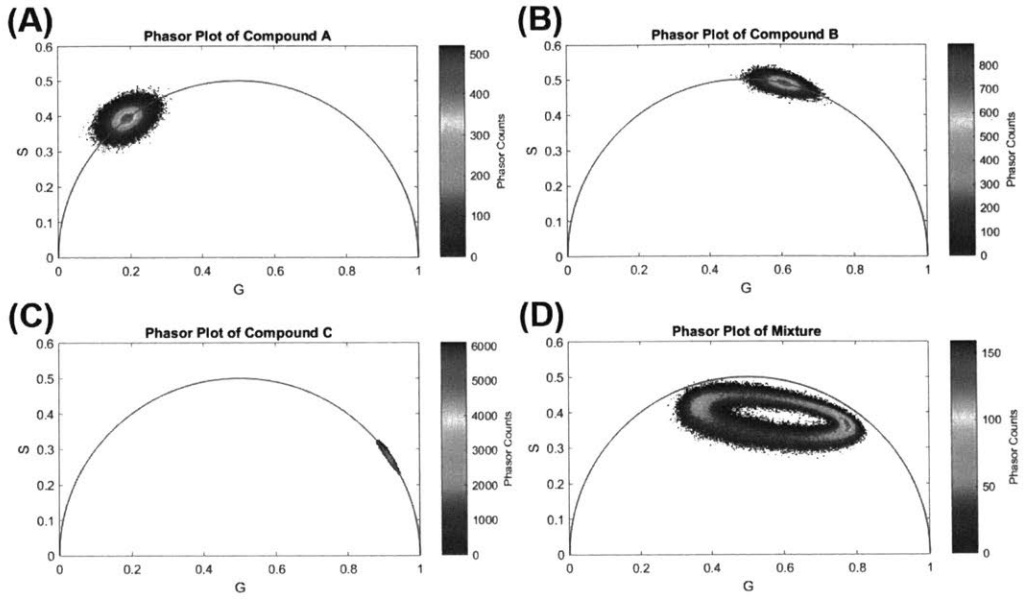

Figure 4-6: Phasor plots of the simulated data used to test the accuracy of the separation algorithms in the context of a ternary mixture of single-lifetime fluorophores. (A) Phasor plot of compound A with a lifetime of 4.100 ± 0.205 ns. (B) Phasor plot of compound B with a lifetime of 1.600 ± 0.080 ns. (C) Phasor plot of compound C with a lifetime of 0.600 ± 0.030 ns. (D) Phasor plot of the ternary mixture of compounds A, B, and C.

rithms for ternary mixtures as previously described in Equations 4.8 and 4.9 yield the concentration estimates shown in Figure 4-7.

In the case of the Euclidean separation method based on computed areas of triangles, it is clear that this standard approach is extremely accurate, failing only in the absence of a compound it is tasked to detect. Even in such circumstances however, the Euclidean algorithm yields an estimated concentration of the absent compound below 5%.

In contrast, the Mahalanobis distance is not found to be as effective in the context of a ternary mixture as it was in the previous simulations of binary mixtures. Here, the reference phasor clusters tend to be elongated, with orientations more or less parallel to the line connecting the opposite two phasor clusters. With a smaller covariance along the axis connecting the phasors of the mixture image to the reference phasor cluster, small spatial deviations along said axis result in large differences in concentration estimates. Moreover, because the covariance of the reference cluster is

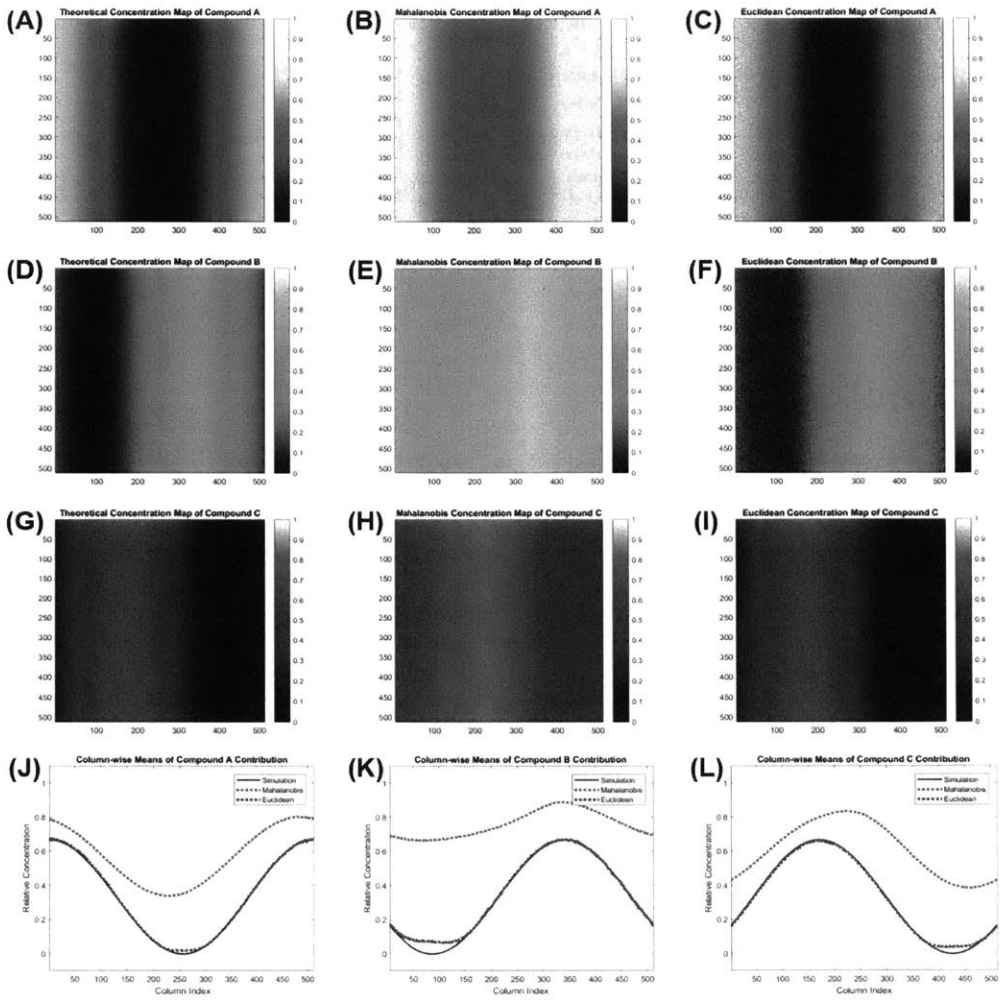

Figure 4-7: Estimated concentration maps of each compound in a ternary mixture of single-lifetime fluorophores. (A,D,G) Theoretical concentration maps of compounds A, B, and C, respectively, spatially distributed following cosine functions phase-shifted with respect to one another by $2\pi/3$ radians (B,E,H) Concentration maps of compounds A, B, and C, respectively, estimated using the Mahalanobis distance metric. (C,F,I) Concentration maps of compounds A, B, and C, respectively, estimated using the Euclidean distance metric. (J,K,L) Column-wise means of panels A–C, D–F, and G–I, respectively.

considered in computing the Mahalanobis distance, the angular differences between phasors in the mixture image and a particular reference cluster result in asymmetrical concentration estimates. This observation is most apparent in the Mahalanobis estimates of compound C, where the peak of the red dashed curve in Figure 4-7(L) is both spatially offset and slanted relative to the simulated theoretical data.

Given a ternary mixture, the Euclidean approach involving the computation of

ratios of triangle areas is therefore objectively superior to the Mahalanobis method in terms of estimation accuracy. This is also true of mixtures involving $N > 3$ compounds, where areas of N-sided polygons can be computed using Euclidean distances to estimate the contributions of each respective fluorescent compound in the sample mixture.

4.4 Conclusion

In the present work, two separation algorithms were compared and contrasted in the context of distinguishing mixtures of fluorescent compounds using simulated fluorescence lifetime imaging data. Specifically, these approaches were based on Euclidean and Mahalanobis distance metrics, where it was found that the Mahalanobis approach outperformed the Euclidean method in a binary mixture in all tested conditions. This superior accuracy is the result of additional considerations that are taken into account in computing the relative concentration of the simulated fluorescence compounds. Namely, the Mahalanobis distance considers the covariance matrix of the reference phasor clusters at hand, dramatically improving the estimation accuracy — particularly in the case of spatially broad phasor clusters.

Interestingly, it was found that this conclusion only held true in the case of binary mixtures of fluorescent species. In ternary mixtures, the Euclidean approach involving the calculation of triangle areas in phasor space resulted in a vastly superior separation accuracy, while the Mahalanobis approach resulted in consistently faulty concentration estimates. In the case of a ternary mixture, the shape and relative orientation of reference phasor clusters worked against the separation algorithm, resulting in displaced and asymmetric concentration peaks.

Of course, it is impossible to simulate each and every conceivable mixture of fluorescent compounds, each with their own respective lifetimes. It is for this reason that the various scripts and functions are provided to the reader in Appendix A. Using the attached software tools, it is possible to simulate any fluorescent compound by adjusting parameters such as the fluorescence lifetime (and its associated uncertainty),

the number of photons per pixel, the number of temporal bins in the decay trace histogram, the image size, the fluorescence intensity pattern, and so on. In providing these tools to the FLIM community, it is hoped that researchers will be empowered to bridge the gap between theory and application by validating their experimental observations with simulations in order to ultimately strengthen the foundations of their imaging experiments.

Chapter 5

Characterization of Human Stratum Corneum Structure, Barrier Function, and Chemical Composition Using CRS

5.1 Introduction

The particular functions of skin beyond its role as an interface are diverse and include thermal insulation and regulation [195], defense against foreign pathogens [196], touch-based sensation [197], vitamin D production [198], and prevention of water loss [199, 200]. These roles are dependent on the skin's unique structure and composition, of which the epidermis serves as the outermost selectively permeable barrier that interfaces with the environment.

The epidermis is itself a multilayered structure. The deepest cell layer consists of the stratum basale which underlies the stratum spinosum, followed by the stratum granulosum, and finally followed by the stratum corneum at the skin's surface. Depending on anatomical site, the stratum corneum typically ranges in thickness from 10 to 30 layers of enucleated cells known as corneocytes and is the primary source

of the skin's barrier function [201]. This is accomplished through the structural organization of these cells, which are stacked like protein-rich bricks glued together by a lipid-rich ceramide mortar [202]. The biochemical compositions of both the intracellular and extracellular spaces of the stratum corneum thus play important roles in the skin's barrier function and maintaining hydration.

The stratum corneum can be compromised by a wide variety of factors, both internal and external. Internal perturbations include abnormal enzyme activity, a decrease in natural moisturizing factors, and reductions in stratum corneum water content. These chemical changes can all contribute to a decrease in corneodesmolysis, where the rivet-like proteinaceous complexes that bind neighboring corneocytes together ultimately remain intact rather than undergoing enzyme-driven breakdown, resulting in the formation of powdery flakes at the skin surface. In contrast, external factors such as a dry environment can lead to the gradual dehydration of epidermal layers starting with the stratum corneum. As the deeper layers of the epidermis dehydrate, various inflammatory mediators are progressively released which induce keratinocyte proliferation and disruption of epidermal differentiation. This cascade can ultimately lead to a haphazard synthesis of inadequately structured extracellular matrix elements and hampers the natural barrier function of healthy stratum corneum [203, 200, 204].

The management of dry skin is most commonly achieved using topical agents such as cosmetic moisturizers due to their humectant properties [205, 206]. These compounds, including glycerin and hyaluronic acid, tend to draw and retain water due to their abundant hydroxyl groups and can also influence the phase of the extracellular lipid matrix under dry environmental conditions [207]. Glycerin, for example, favors an appropriately fluid lamellar arrangement of extracellular lipids rather than the solid crystalline phase that tends to form under dry conditions [208, 204].

In order to quantitatively monitor skin hydration, conventional methods based on the measurement of skin electrical properties have been developed and validated. One such industry standard involves the use of a corneometer, a device equipped with a pen-sized handheld probe that is gently pressed onto the skin surface to measure

hydration based on the capacitance of the skin itself [209]. Given the high dielectric constant of water under standard ambient conditions, its capacitive properties can be probed for non-invasive inferences of skin hydration. Despite its status as a commercial standard, recent studies have identified sources of small but significant experimental variation in corneometry measurements. One study in particular reported a measurement dependence on the contact pressure applied between the probe and the skin, with increasing pressure resulting in overestimated hydration values [210]. The same group later found intra-sample variability in cases where hydration levels approached saturation, suggesting a decrease in probe sensitivity at the upper limits of hydration [211]. Despite these rather modest sources of variability, corneometry has been widely used in the validation and efficacy testing of cosmetic products and topical drug formulations as well as in occupational health studies [212, 213, 209, 214, 215, 216].

While corneometry is a simple, rapid, and effective method for the indirect assessment of skin hydration via capacitance measurements, it is inherently limited to point-based acquisitions over a bulk surface area of approximately 1 cm^2. Because of this, corneometry lacks the sub-cellular spatial resolution needed to identify differences between intracellular versus extracellular hydration and it cannot be used to distinguish the hydration of the various layers and sublayers that constitute human skin [211]. Such information would be useful in assessing and validating treatment strategies by offering spatial information at the cellular scale in a depth-resolved manner. With such specificity, it would be possible to identify the problematic anatomical component requiring treatment (e.g. decreased water retention within corneocyte cell bodies, altered lipid composition of the extracellular matrix), in addition to monitoring the effects of the treatment strategy over time. Dermatological investigations that would otherwise require such levels of contextual detail are technologically limited to destructive sampling techniques such as histology or cryo-scanning electron microscopy [217].

As of now, a critical niche remains unaddressed for assessing skin hydration, structure, and composition in a non-invasive and non-destructive manner with subcellular

3D resolution on living tissues. A potential solution to this problem lies within the non-linear optical imaging modalities that have seen increasing use over the past few decades along with the significant advances in endogenous molecular imaging [218, 28, 164, 158, 172, 219, 220]. In particular, coherent Raman scattering (CRS) imaging techniques have become a valuable tool in biomedical research by enabling the visualization of specific chemical groups via contrast based on molecular vibrational signatures [54, 29, 27]. Of these techniques, coherent anti-Stokes Raman scattering (CARS) and stimulated Raman scattering (SRS) are two complementary CRS techniques that can be readily used to visualize and quantify both the structure and the chemical composition of skin. Moreover, these optical processes occur simultaneously; it follows that an appropriate microscopy setup allows for simultaneous CARS and SRS imaging.

In this chapter, the parallel use of both CRS microscopy and corneometry are reported to characterize the structure, barrier function, and chemical content of human *ex vivo* skin samples undergoing dehydration and humectant-induced rehydration. In addition to the bulk hydration assessment offered by corneometry, CRS image stacks of the stratum corneum in *ex vivo* skin explants were acquired to examine the distribution of lipid, protein, and water content by probing their molecular vibrational signatures in two separate experimental contexts designed to determine the morphological and chemical imaging metrics that best explain skin hydration.

5.2 Results and Discussion

5.2.1 CRS Imaging Metrics

The focus of this study was to build an imaging and analysis method for the chemical and morphological characterization of the stratum corneum under changing hydration conditions. An *ex vivo* skin model was imaged with CRS microscopy techniques without *a priori* biases such that the data could be assessed post-acquisition using mathematical and statistical methods. As an exploratory characterization study, the

number of subjects was initially set at $N = 3$ per experiment, noting that hundreds of individual cells and their associated parameters were measured to characterize changes in skin.

For non-invasive investigations of human skin in a laboratory setting, *ex vivo* human skin samples acquired from discarded tissues as a result of elective patient surgeries are typically used as a model to recapitulate the active physiology of a living individual's skin [221, 14]. In the context of this study, such human skin explants were imaged via CRS microscopy to visualize the architecture and biochemical content of the stratum corneum. Hydration-relevant parameters such as lipid content can be measured by probing the symmetric CH_2 stretching vibrational mode at 2845 cm^{-1} [28] while the CH_3 molecular vibration at 2950 cm^{-1} can be used to detect proteins by their hydrophobic amino acids with methyl groups [222]. Water molecules themselves can be readily detected by probing the strong OH stretching vibrational mode at 3220 cm^{-1} [223].

Representative CARS and SRS images of the stratum corneum acquired simultaneously by probing each of the three vibrational bands of interest are shown in Figure 5-1, illustrating the particularly strong contrast observed between the intracellular and extracellular spaces. Corneocytes appear as polygonal cells surrounded by a bright extracellular matrix rich in lipids (Figure 5-1(a,d)) and proteins (Figure 5-1(b,e)). Water content (Figure 5-1(c,f)), on the other hand, is mostly confined within the corneocyte cell bodies, with a much lower abundance in the extracellular space.

While both imaging modalities generate similar contrast, CARS images uniquely contain an inherent background anti-Stokes signal that is generated independently of Raman-active molecules, known as the non-resonant background (NRB). While the anatomical features in CARS images of the stratum corneum can be readily appreciated, the interpretation of individual pixel values becomes challenging due to the unspecific contribution from the NRB, which manifests as a broad and homogenous distribution of background signal centered within the field of view. Importantly, the generation of NRB is exclusive to CARS; the SRS signals in Figure 5-1(df) strictly

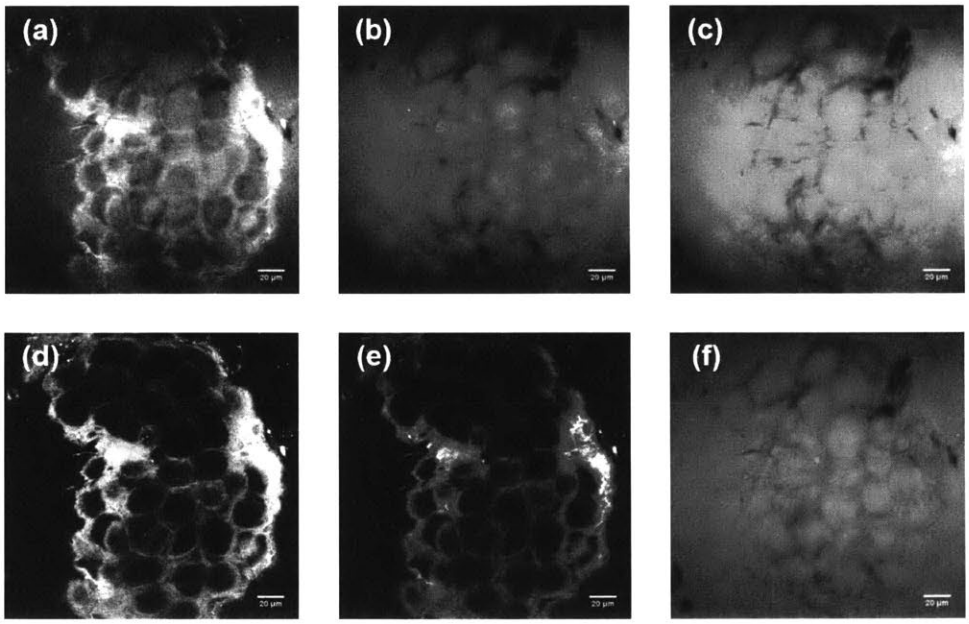

Figure 5-1: CRS images of human stratum corneum acquired from *ex vivo* skin explants. (a–c) CARS and (d–f) SRS images of stratum corneum showing (a,d) lipid-weighted content; (b,e) protein-weighted content; and (c,f) water-weighted content. The NRB in the CARS data manifests itself as a homogeneous and unspecific haze distributed across the field of view.

arise from the targeted Raman-active molecules. Conveniently, since these processes occur simultaneously, the acquisition of CARS data in addition to SRS comes at no additional cost.

The CRS microscopy platform used to image human stratum corneum in the context of this study was capable of generated a total of 35 imaging metrics, although not all metrics were found to be of value, as will be discussed later. First, the system is equipped with two simultaneous imaging modalities (i.e. CARS and SRS) to probe the distribution of three chemical species of interest, namely lipids, proteins, and water, thereby generating 6 metrics. The relative ratios between these chemical species (i.e. lipid-to-protein, lipid-to-water, and protein-to-water) can also be assessed by computing image intensity ratios on a pixel-by-pixel basis, thus bringing the metric count to 12. With manual segmentation of corneocytes and generation of regions of interest (ROIs) as shown in Figure 5-2, each of the 12 previously defined metrics can be redefined with respect to anatomical component (i.e. intracellular vs. extracellular).

This then doubles the metric count once more for a total of 24 metrics regarding skin hydration. By further considering intracellular-to-extracellular ratios of chemical content for both modalities, 6 more metrics are added to the count. Finally, using the manually generated ROIs for each corneocyte, 5 morphological parameters can be defined based on cellular geometry: cell diameter, perimeter, and circularity, as well as the nearest neighbor distances (NND) between adjacent corneocyte cell centers ($NND_{Centers}$) and cell walls (NND_{Walls}). Together with corneometer measurements acquired in parallel with CRS imaging, this investigative toolkit is therefore capable of characterizing 36 observable morphological and chemical metrics for each skin sample at a given timepoint under a particular set of experimental conditions. However, imaging metrics generated using CARS microscopy were ultimately discarded due to the generation of strong NRB resulting in poorly interpretable longitudinal data.

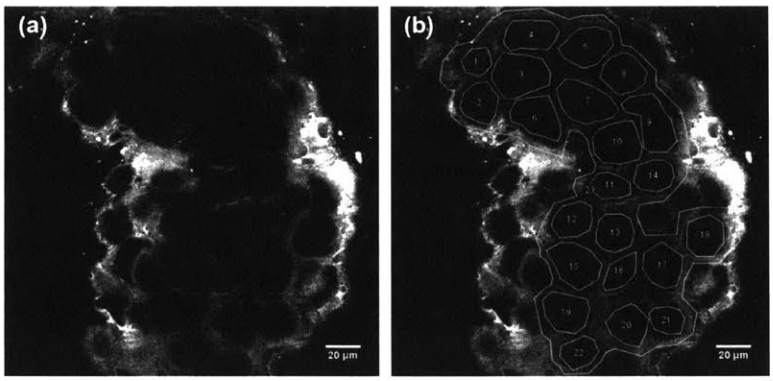

Figure 5-2: Manual segmentation of SRS lipid content image to distinguish intracellular and extracellular spaces for subsequent analysis. (a) Unlabeled image. (b) Manually segmented image, showing corneocytes identified by indices 1 through 22, and extracellular space corresponding to the surrounding region identified by index number 23.

Initial assessment of the acquired CRS imaging data found a strikingly similar contrast in the protein and lipid channels across all experimental conditions (Figure 5-1(d,e), for example). This is not surprising, as femtosecond laser sources such as the one used in this study have an inherently broad frequency spectrum. As such, such laser sources can generate strong CRS signals at the cost of decreased spectral specificity [28]. Following acquisition of the imaging data, it was unclear whether the observed similarities truly illustrated correlations in the distribution of lipids and

proteins, or whether the femtosecond laser sources used were too spectrally broad to resolve the two vibrational peaks of interest (2845 and 2950 cm^{-1} for lipids and proteins, respectively). To verify whether this was indeed the case, the SRS lipid and protein chemical content image sets were statistically analyzed to determine whether the observed SRS lipid intensity in each cell could be explained by its corresponding SRS protein intensity. As seen in Figure 5-3, a strong correlation was indeed observed between the SRS lipid and protein signals (Pearson's $R = 0.921$). This lipid-protein correlation was less strong in the case of CARS, but nevertheless significant (Pearson's $R = 0.812$). Therefore, protein-associated imaging metrics were not considered for the statistical analysis of the dehydration and rehydration results that follow. It is worth noting, however, that methods to increase the spectral specificity in femtosecond CRS microscopy – collectively referred to as "spectral focusing" – have been previously reported [222, 224, 225], and can be implemented to include the ability to reliably probe protein content within cells and tissues.

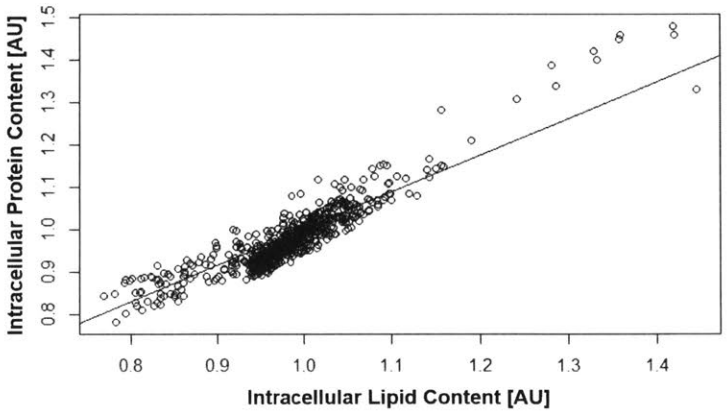

Figure 5-3: Scatter plot of all intracellular lipid and protein data collected via SRS, showing a strong correlation (Pearson's $R = 0.921$) between the observed metrics and therefore indicative of spectral overlap.

5.2.2 Stratum Corneum Dehydration

For the dehydration investigation, *ex vivo* skin explants were first imaged with CRS microscopy and probed with the corneometer immediately upon retrieval from the

incubator. Following the first set of data acquisition, one set of skin samples was allowed to dry on a plastic substrate while the other was maintained in parallel on its nutritive gel under ambient conditions bed to limit dehydration. Imaging was then performed at two additional timepoints alongside corneometer measurements performed in triplicates for each experimental timepoint and each treatment condition. The corneometer data is shown over time for both the dehydrated and moist conditions in Figure 5-4, and illustrates a net overall decrease in skin hydration as the skin samples are left to dry. As expected, the skin samples that were maintained on the moist gel bed retained their hydration more efficiently.

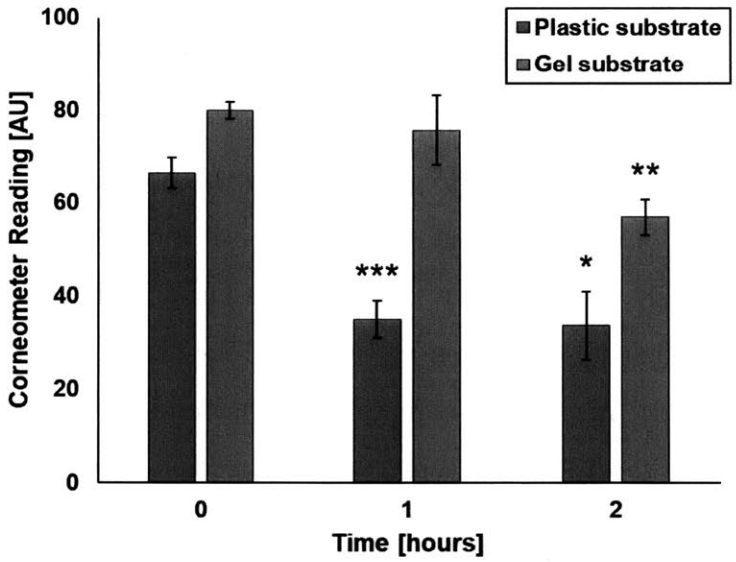

Figure 5-4: Corneometer measurements obtained from *ex vivo* human skin throughout the dehydration time course on a plastic substrate (i.e. rapid dehydration) and a gel substrate (i.e. slow dehydration). Data points correspond to the mean of the triplicate corneometer measurements with error bars indicating the standard error of the mean. Statistically significant deviations from the corresponding initial timepoint are denoted by asterisks and determined via Student's t-test (*: $p < 0.05/N$; **: $p < 0.01/N$; ***: $p < 0.001/N$, adjusted using Bonferroni correction with $N = 4$ pairwise comparisons).

Linear regression analysis was performed for each CRS imaging metric and corneometer measurement in order to find statistically significant trends over time and to investigate the environmental influence on these dynamics. A linear mixed effect model for each metric was designed to explore the possibility of modeling each ob-

served metric as a linear function of time (a fixed factor). Each patient was considered as a random factor and each field of view per patient as a nested random factor within each patient, given that each skin sample for each patient was imaged at 3 different areas per treatment condition. Note that the given area imaged at each timepoint was different. As opposed to a marginal model which would indiscriminately consider the means from all subjects together, this conditional model approach allows for subject-specific statistical analysis. Given that patient number and patient sample area were exchangeable (since all samples were completely anonymized), they could readily be assigned as random factors. The linear mixed model was adopted while holding the treatment condition constant by first modeling the data collected under the rapid drying condition before modeling the kinetics of slowed dehydration over a moist nutritive gel substrate.

CARS imaging data was closely explored during this step of the analysis. As mentioned above, CARS microscopy images contain both a chemically specific response as well as a nonspecific response (i.e. NRB). This latter nonspecific response arises as a function of the density of a given material and its electronic polarizability; these two factors mix to give rise to a coherent signal that adds to the chemically specific signal. In analyzing the CARS imaging data, it became clear that the CARS data contained at least two responses to dehydration: not only were there changes in the chemical content of the skin, but there were changes in cellular morphology as well. These morphological changes, which included changes in tissue thickness, cell size, and intercellular distance, could lead to variations in the proportion of the CARS signal that arises from non-resonant contributions. As this nonspecific factor leads to chemically independent changes in the total CARS signal intensity [28], chemically-weighted CARS imaging data was not included in the statistical analysis. CARS imaging is therefore used to inform manual image segmentation and morphological assessment, i.e. metrics independent of chemical signatures.

The hourly rates of change for each metric under both dehydration conditions are listed in Table 5.1 along with the 95% confidence intervals and p-values. The most significant changes observed under both conditions were primarily morphological,

with parameters such as cell diameter and perimeter seen to decrease, while the NND between cell walls was observed to increase. These observations suggest that corneocytes undergo a generalized decrease in size as they dehydrate in addition to progressively retracting away from one another, consistent with previous findings using cryo-scanning electron microscopy [217].

As seen in Table 5.1, relative water content as determined by SRS water intensity was found to decrease at an average rate of approximately 7% per hour for both intracellular and extracellular spaces under the dry environmental condition. This rapid dehydration rate was diminished by the wet gel substrate where the time-dependent variation of tissue water content was no longer significant. Interestingly, these changes are also reflected in the corneometry measurements where a dramatic dehydration rate of -15.3 units per hour was recorded on the plastic substrate while the corresponding rate on the gel substrate was found to be roughly 35% slower (i.e. -9.92 units per hour). The lipid-to-water ratio in both intracellular and extracellular spaces was consistently seen to increase only under the dry condition and more so in the case of the extracellular space. While the intracellular lipid content also decreased slightly over time under both conditions, this decrease was more rapid over the plastic substrate which further contributed to the contrast in lipid-to-water ratios between the two experimental conditions.

Despite the small number of patient samples, this imaging based approach was able to measure and visualize a large number of cells needed to generate a significant body of data. Overall, marked differences in hydration dynamics were observed between *ex vivo* patient samples depending on the type of substrate, most strikingly in the case of intracellular water content assessed via SRS microscopy. Given these newfound nuances, the proposed methodology supports the applicability of using CRS imaging to complement corneometry in order to non-invasively and non-destructively measure cellular morphology and probe hydration-relevant metrics with subcellular resolution. Whereas corneometry relies on making bulk 1 cm^2 point measurements that extends down to the dermal layer, CRS imaging in the context of this study was able to detect subtle chemical changes in a micron-thin slice of the stratum corneum on a pixel-by-

Table 5.1: Stratum corneum metric dynamics measured over the time course of *ex vivo* human skin dehydration on two different substrates. For the plastic substrate, asterisks denote rates of change significantly different from zero; for the gel substrate, they denote rates of change that are significantly different from the plastic substrate (*: $p < 0.05$; **: $p < 0.01$; ***: $p < 0.001$, where p-values are adjusted using Holm-Bonferroni correction with $N = 36$ metrics. IER: intracellular-to-extracellular ratio; NND: nearest neighbor distance; CI: confidence interval.)

METRIC	PLASTIC SUBSTRATE			GEL SUBSTRATE		
	Hourly rate of change	95% CI	p-value	Hourly rate of change	95% CI	p-value
Corneometry						
Corneometer	-15.3 **	[-22.1, -8.57]	3.13×10^{-3}	-9.92	[-21.6, 1.79]	1.00
Water content						
Intracellular	-6.66 % ***	[-8.35, -4.97] %	1.38×10^{-5}	-2.46 % ***	[-4.33, -0.60] %	2.90×10^{-22}
Extracellular	-6.95 % ***	[-9.08, -4.82] %	1.26×10^{-5}	-1.98 %	[-5.67, 1.71] %	6.84×10^{-2}
IER	0.17 %	[-0.18, 0.53] %	1.00	-0.42 %	[-1.03, 0.19] %	0.543
Lipid content						
Intracellular	-4.42 %	[-6.62, -2.21] %	7.55×10^{-2}	-2.56 % ***	[-4.86, -0.27] %	1.43×10^{-6}
Extracellular	-3.20 %	[-5.96, -0.44] %	1.00	-2.74 %	[-6.41, 0.92] %	1.00
IER	-1.23 %	[-2.57, 0.11] %	0.821	0.14 %	[-2.02, 2.29] %	1.00
Lipid-to-water ratio						
Intracellular	2.26 %	[0.61, 3.91] %	0.256	-0.02 % ***	[-1.85, 1.81] %	5.74×10^{-7}
Extracellular	3.73 % *	[1.88, 5.57] %	1.48×10^{-2}	-0.49 % *	[-3.14, 2.17] %	1.44×10^{-2}
Morphology						
Cell diameter	-7.06 μm *	[-14.6, 0.51] μm	4.94×10^{-2}	-3.97 μm	[-13.0, 5.09] μm	0.545
Cell perimeter	-4.92 μm	[-8.70, -1.13] μm	0.756	-3.61 μm	[-9.58, 2.36] μm	1.00
$NND_{Centers}$	-0.28 μm	[-0.96, 0.41] μm	1.00	0.45 μm	[-0.54, 1.45] μm	0.912
NND_{Walls}	2.01 μm	[0.79, 3.23] μm	0.0265	1.11 μm	[-0.75, 2.97] μm	1.00

pixel basis. With a field of view of 212×212 μm^2, objects such as single corneocytes and entire extracellular spaces surrounding collections of corneocytes can be analyzed at high resolution with chemical specificity. Thus, while total probed volume for CRS measurements is several orders of magnitude smaller than that of the corneometer, it can still serve as a useful complementary tool between in hydration studies.

5.2.3 Stratum Corneum Rehydration

The second portion of this study was focused on the rehydration dynamics of skin following topical application of two humectant agents: glycerin and hyaluronic acid. To simulate dehydrated skin tissue, *ex vivo* skin explants were removed from the incubator and allowed to dry under ambient conditions prior to humectant treatment. As confirmed by a plateau in the corneometer hydration measurements, samples in this model approach were considered dehydrated at the initial timepoint of the CRS rehydration study. Experiments were carried out in subject batches, where each batch

encompassed a single day of experiments of all conditions on all tissue samples from a single subject.

Linear mixed effect model regression analysis was performed for each CRS imaging metric along for each corneometer measurements in order to find statistically significant trends in treatment response over time and to investigate the environmental influence on these dynamics.

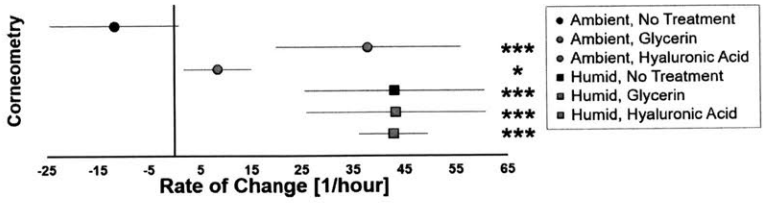

Figure 5-5: Corneometry-based assessment of *ex vivo* human skin hydration dynamics during rehydration under various environmental and treatment conditions. Data points correspond to the rate of change of corneometer measurements per hour, with error bars showing the 95% confidence interval. For the ambient condition without treatment (control), asterisks denote rates of change significantly different from zero; for all other conditions, they denote rates of change that are significantly different from the control (*: $p < 0.05$; **: $p < 0.01$; ***: $p < 0.001$, where p-values are adjusted using Holm-Bonferroni correction with $N = 36$ metrics).

Corneometer measurements performed throughout the various rehydration condition time courses are shown in Figure 5-5. From the results, it can be seen that the sample left under ambient conditions without topical treatment continued to dehydrate slightly, albeit without statistical significance. Interestingly, all treatment conditions significantly improved the rehydration rate and successfully restored skin hydration as verified by corneometry.

Interestingly, the most significant metric impacted by both time course and topical treatment was the intracellular water and lipid contents of corneocytes as measured by SRS microscopy (Figure 5-6(a,b)). Under both dry and hydrated conditions, the intracellular water and lipid contents were found to decrease over time, except in the event of glycerin application under ambient conditions — the only condition where intracellular chemical content increased at a positive rate. This was also the condition under which the intracellular lipid-to-water ratio decreased most significantly

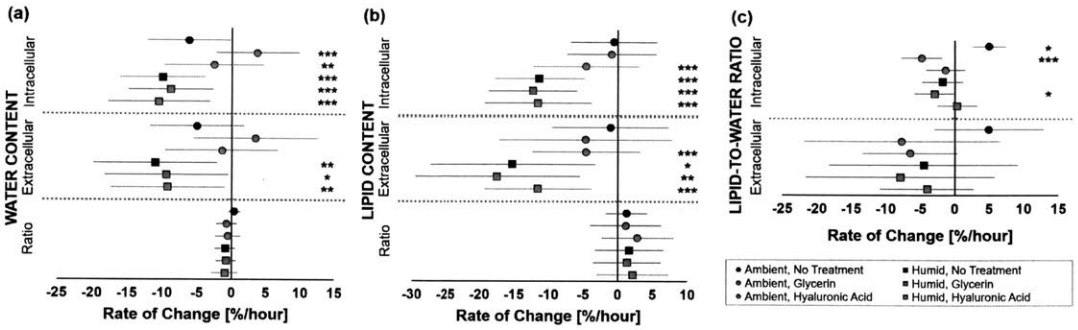

Figure 5-6: Chemical content dynamics of *ex vivo* human skin during rehydration under various environmental and treatment conditions. Data points correspond to the rate of change of CRS imaging metrics per hour, with error bars showing the 95% confidence interval. For the ambient condition without treatment (control), asterisks denote rates of change significantly different from zero; for all other conditions, they denote rates of change that are significantly different from the control (*: $p < 0.05$; **: $p < 0.01$; ***: $p < 0.001$, where p-values are adjusted using Holm-Bonferroni correction with $N = 36$ metrics).

throughout the rehydration process (Figure 5-6(c)). In contrast to these CRS results, corneometry indicated an increase in skin hydration following both glycerin and hyaluronic acid treatment, although the hydration increase following the latter treatment was less pronounced under ambient environmental conditions. These findings suggest the possibility that, in this *ex vivo* model system, the water retained by the tissue following humectant application is taken up but not necessarily retained in corneocyte cell bodies. This disagreement is not necessarily problematic: while corneometry is considered most sensitive to the topmost 15 to 45 μm of the interrogated sample, its bulk probing volume actually extends several tens of microns deeper into the skin albeit with decreasing sensitivity [211, 226]. This lack of spatial specificity may result in a significant portion of the viable epidermis and dermis being interrogated as well, which could explain the apparent discrepancy in the changes in corneocyte water content as measured by SRS imaging.

Of note, the diameter of cells treated with glycerin was also observed to gradually increase over the time course of the experiment under all conditions with the exception of glycerin treatment in the humid incubator environment. This observation may be interpreted as a transient swelling of the cells over time, however, without statistically

significant retention of hydration (Figure 5-7). This correlation between corneocyte size and hydration is generally consistent with previous findings assessed via cryo-scanning electron microscopy [217].

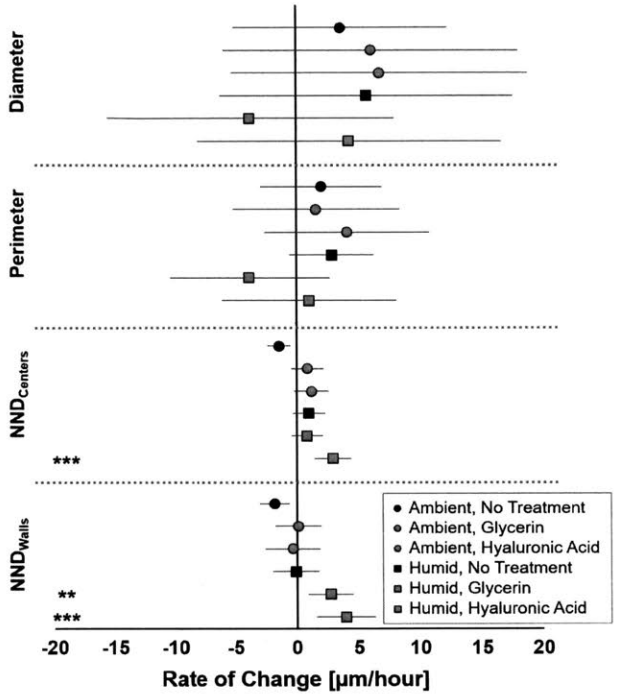

Figure 5-7: Morphological dynamics of *ex vivo* human corneocytes during rehydration under various environmental and treatment conditions. Data points correspond to the rate of change of each spatial metric in microns per hour with error bars showing the 95% confidence interval. Nearest neighbor distances are computed between corneocyte cell centers ($\text{NND}_{\text{Centers}}$) as well as between cell walls ($\text{NND}_{\text{Walls}}$). For the ambient condition without treatment (control), asterisks denote rates of change significantly different from zero; for all other conditions, they denote rates of change that are significantly different from the control (*: $p < 0.05$; **: $p < 0.01$; ***: $p < 0.001$, where p-values are adjusted using Holm-Bonferroni correction with $N = 36$ metrics).

Skin explants treated with hyaluronic acid and left to rehydrate under ambient conditions showed an overall decrease in terms of intracellular water content, although these changes differed in magnitude from their untreated counterparts in a statistically significant manner. Indeed, under ambient conditions, the intracellular water loss was slowed, while the humid and warm environment of the incubator was found to exacerbate the water loss rate. This overall trend is consistent with that observed in samples treated with glycerin. Interestingly, the intracellular lipid content in the

hyaluronic acid treated explants under ambient conditions was now found to decrease at a significantly accelerated rate relative to the untreated samples. It is also worth noting that some aspects of cellular morphology were also impacted by hyaluronic acid treatment under ambient conditions. In particular, the hyaluronic acid treatment under the humid and warm conditions of the tissue incubator resulted in increased distances between corneocyte cell centers and their walls, suggestive of tissue swelling as a result of increased hydration.

It is also worth examining the overall similarities and differences in the samples kept at room temperature relative to those maintained in the tissue incubator at 37°C, 5% atmospheric CO_2, and 95% relative humidity between measurements. The warm and humid environment of the incubator was found to significantly affect the water and lipid loss rates, with intracellular loss rates increasing 2- and 3-fold, respectively, relative to the untreated sample under ambient conditions. The extracellular water and lipid contents were also found to decrease significantly, which was otherwise only observed in the case of hyaluronic acid treatment under ambient conditions. Despite this radical shift in water content throughout the stratum corneum, the corneometer nevertheless measured a dramatic rise in skin hydration, similar in magnitude to a topical application of glycerin under ambient conditions. This discrepancy highlights the difference in probing volumes between corneometry and water content assessment via SRS microscopy.

When skin samples were treated with either glycerin or hyaluronic acid and maintained in the incubator between measurements, the observed trends generally resembled those of untreated incubated skin: the intracellular and extracellular water and lipid loss rates increased significantly, despite corneometry showing a marked increase in terms of skin hydration. Corneocyte morphology, however, was generally found to remain unaffected, other than in the particular case of hyaluronic acid treatment under humid and warm conditions as noted above.

A summary of all observable metrics that show variability over time is presented in Table 5.2. As demonstrated by corneometry, skin samples required the warm and humid environment of the incubator and/or a topical application of glycerin or

Table 5.2: Summary of observed changes over the time course of skin explant rehydration. (N/C: no change; +++, ++, +: strong, moderate, and modest increase, respectively; − − −, − −, −: strong, moderate, and modest decrease, respectively.)

METRIC	AMBIENT ENVIRONMENT			HUMID ENVIRONMENT		
	No treatment	Glycerin	Hyaluronic acid	No treatment	Glycerin	Hyaluronic acid
Corneometry						
Corneometer	−	+++	+	+++	+++	+++
Water content						
Intracellular	−−	+	−	−−−	−−−	−−−
Extracellular	N/C	N/C	N/C	−−−	−−−	−−−
IER	N/C	N/C	N/C	N/C	N/C	N/C
Lipid content						
Intracellular	N/C	N/C	−	−−−	−−−	−−−
Extracellular	N/C	N/C	−	−−−	−−−	−−−
IER	N/C	N/C	N/C	N/C	N/C	N/C
Lipid-to-water ratio						
Intracellular	+	−−	N/C	N/C	−	N/C
Extracellular	N/C	N/C	N/C	N/C	N/C	N/C
Morphology						
Cell diameter	N/C	N/C	N/C	N/C	N/C	N/C
Cell perimeter	N/C	N/C	N/C	N/C	N/C	N/C
$NND_{Centers}$	N/C	N/C	N/C	N/C	N/C	+
NND_{Walls}	N/C	N/C	N/C	N/C	+	++

hyaluronic acid in order to rehydrate. The SRS imaging results point to an interesting suggestion that the stratum corneum itself may not retain or increase its water content within corneocytes during glycerin and hyaluronic acid induced rehydration. In fact, in this *ex vivo* model system, the SRS imaging results indicate that the rate of intracellular water loss from the stratum corneum accelerated for all conditions under the warm and humid incubator conditions. It should be noted that calculations carried out on the CARS images (data not shown) show the opposite overall trend, an effect that is hypothesized to arise from two factors. First, as noted above, structural changes to the skin are likely to cause changes to the non-resonant signal contribution that contaminates the CARS signal. Second, an additional non-resonant contribution in the CARS images arises from the glycerin and hyaluronic acid treatments themselves, creating a false increase in apparent water content. The SRS imaging data, which instead scales linearly with molecular concentration and does not contain non-resonant signal contributions, clearly points to a net dehydration effect in all tested model samples.

Interestingly, this finding does not exactly agree with conventional understanding of stratum corneum behavior, warranting further discussion. First, it should be

kept in mind that while the data is generated from many dozens of cells over many tissue samples, all samples were derived from a small set of subjects who underwent surgery. Discarded *ex vivo* tissue samples from these procedures were transported under cold, wet conditions prior to processing and placement into the tissue explant culture system for one to three days. It is therefore important to note that this *ex vivo* skin explant model may not be entirely representative of normal, healthy skin. Despite this fact, skin explant models are used widely in biological, cosmetic, and drug studies [163, 221, 14], highlighting the importance of understanding how they respond to various challenges and conditions on the cellular level.

Second, the dehydration approach used in this study approximated, but did not match, normal skin drying in humans. Dry skin *in vivo* involves changes and alterations in skin cellular biology that can occur over the course of days and weeks. The drying method used here created a bulk dehydration of thinned skin samples in mere hours, and may have driven the skin to states not normally experienced *in vivo*. While this caveat may not apply to skin undergoing the initial stages of dehydration, it may indeed affect rehydration. As this dehydration/rehydration approach is used in research [227, 163], it is important to understand the implications of findings derived from such models.

It is furthermore worth recalling that CRS imaging modalities are non-destructive techniques that assesses chemical content directly based on the intrinsic molecular vibrations of the chemical groups of interest. Other techniques have previously been used to study stratum corneum hydration including high pressure freezing before freeze substitution [228] and cryo-scanning electron microscopy [217], although in using such investigational approaches, it cannot be excluded that the harsh tissue processing protocols affect the integrity of the corneocytes themselves. CRS microscopy methods therefore offer the advantage of requiring little-to-no sample preparation, and have already been used to pursue dermatological investigations in human subjects [229]. Having an established framework for processing CRS image data using linear mixed effect models, investigations can further be performed on human volunteers in order to ascertain stratum corneum hydration dynamics in the most ideal

biological context *in vivo*.

The discrepancy in hydration between corneometry and CRS imaging in the present model system is thought to arise from both the volumes of tissue interrogates and the nature of the measurement itself. Nonlinear optical imaging techniques such as SRS are able to probe focal volumes on the scale of the cubic micron with three-dimensional spatial resolution. In contrast, the current industry standard for hydration measurements, corneometry, is known to integrate signals over several tens of microns and can encompass all layers of the epidermis beyond the stratum corneum as well as a portion of the dermis within human skin. Whereas CRS imaging directly measures the concentration of given molecular species such as water, corneometry indirectly measures tissue water content via quantification of capacitance. This difference highlights the need for complementary chemically sensitive CRS microscopy techniques with corneometry. The CRS imaging method developed for this study does indeed suggest something unexpected occurring to the stratum corneum, a finding that is not anticipated by the corneometry measurements alone. The *ex vivo* models in this study experienced major, opposite changes in water content between bulk tissue and the stratum corneum under conditions that were expected to lead to tissue rehydration.

These results strongly suggest the need for future studies that make use of improved model systems, increased subject numbers, and perhaps a pivot to *in vivo* experiments. For the reasons discussed above, improved tissue sources and model systems should be explored. Optimized and traceable skin explant cultures can now be purchased from commercial vendors such as Genoskin Inc., providing improved tissue cultures that remain viable for substantially longer time courses than models such as those used in the present study. Genoskin and similar vendors can also provide tissues from a wider range of donors, which can increase subject numbers to ensure that results arise from respective populations. Ultimately, however, these experiments should transition away from model systems to *in vivo* studies. Skin culture models are only a way to prolong the eventual decay of *ex vivo* skin tissue, and dehydration/rehydration models can never fully match real dry skin.

To meet these clinical research needs, we are developing new, portable CARS and SRS microscopy systems with the goal of carrying out *in vivo* CRS imaging of skin in the near future. A portable clinic-ready imaging system will be key to visualize dry or compromised skin and capture the full biological dynamics of treatment response. Such an instrument can also incorporate additional detection methods and imaging modalities, including two-photon excited fluorescence (TPEF), which can be used to probe coenzymes such as flavin and nicotinamide adenine dinucleotides (FAD and NADH, respectively) to probe metabolic perturbations [164, 14]; transient and sum-frequency absorption (TA and SFA, respectively) to probe the strong absorptive properties of pigments and chromophores such as melanin species and hemoglobin [52, 51, 8]; as well as second-harmonic generation (SHG), which relies on the birefringent nature of collagen fibers to generate a strong signal that maps oriented extracellular matrix proteins without the use of exogenous labels [230]. These imaging techniques can be judiciously combined with one another to best complement standard measurement techniques to tease out the detailed biological response to dehydration and rehydration.

In the present study, investigations were limited to the stratum corneum, where each imaging field of view typically contained a few tens of corneocytes that, together with the extracellular space, translated to tens of observations. In exploring other layers of skin with additional nonlinear imaging techniques such as those described above, this methodological approach to assessing imaging metrics therefore allows one to easily record many hundreds or even thousands of observables, each defined by a handful of categorical descriptors such as patient number or treatment condition. Programming languages such as Matlab and Python lend themselves particularly well to processing such datasets, as the computations involve iterative processing of multichannel image data with binary masks generated via manual segmentation. The image analysis then returns a data table where each row corresponds to an individual observation, and each vector corresponds to either a descriptor (e.g. patient number, treatment condition, timepoint, etc.) or an observed metric (e.g. water content, lipid content, cell diameter, etc.). Such data formats are ideal for statistical software

packages such as R, where linear mixed effect models can serve to identify longitudinal trends and differences between treatment conditions.

Further work in assessing chemical content across the various strata of human skin using CRS microscopy (and other complementary nonlinear optical imaging methods) may also further inform the development of new topical formulations; combining these imaging toolkits with corneometry will further shed light on both the microscopic and macroscopic effects of topical treatment strategies.

5.3 Materials and Methods

5.3.1 Tissue Culture and Processing

Human skin samples were obtained from discarded tissues resulting from elective patient surgeries in compliance with the institutional review board of Massachusetts General Hospital (MGH IRB protocol #2015P001267). Upon receiving the skin samples, they were immediately trimmed to remove the subcutaneous fat, and subsequently cut into square pieces approximately 1 to 2 cm^2 in size. The skin samples were then placed on a nutritive gel bed consisting of complete cell medium supplemented with 2% agarose and placed in an incubator at 37°C with 5% atmospheric CO_2 and 95% relative humidity.

5.3.2 Corneometer Measurements

Skin hydration state was measured on *ex vivo* human skin explants using a corneometer (Corneometer CM 825, Courage+Khazaka Electronic GmbH, Cologne, Germany) according to the manufacturer's instructions. For each measurement, the probe was applied to the skin which then outputs a readout in arbitrary units ranging from 0 to 120. Prior work has served to classify the corneometer readouts obtained from 349 volunteers, where values below 30 indicate very dry skin; measurements ranging from 30 to 40 correspond to dry skin; and values above 40 are considered normal [209]. It is worth noting, however, that these classifications were determined based on data

acquired from intact patient skin; the cutoffs between very dry, dry, and normal skin for *ex vivo* human skin explants that have been maintained in an incubator at 37°C with high humidity are likely to differ.

5.3.3 CRS Microscopy

CRS imaging was performed using a dual-output femtosecond pulsed laser source (Insight DeepSee, Spectra-Physics, Santa Clara, CA). One output is widely tunable from 680 to 1300 nm and is used as the pump beam in all CRS experiments, while the other output, fixed at 1040 nm, is used as the Stokes beam. Imaging lipids requires tuning the pump beam to 803 nm in order to probe the symmetric CH_2 stretching vibrational mode at 2845 cm^{-1}, which generates an anti-Stokes signal at 654 nm. Proteins can be probed at a slightly higher energy using a pump wavelength of 796 nm to collect the 645 nm anti-Stokes light, where the CH_3 stretching vibration at 2950 cm^{-1} has been associated with protein signatures. Finally, the OH vibrational stretching mode at 3220 cm^{-1} can be probed by tuning the pump beam to 779 nm, generating anti-Stokes light at 623 nm. The laser beams were combined using a dichroic mirror and routed to the input port of a commercial inverted microscope (FV1000, Olympus, Tokyo, Japan), where imaging was performed using a 1.20 NA objective (UPLSAPO 60XW, Olympus, Tokyo, Japan). Laser powers were maintained below 40 mW at the output of the microscope objective for all skin imaging experiments. CARS detection was achieved using a photomultiplier tube (H7422PA-50, Hamamatsu Photonics, Hamamatsu City, Japan) with appropriate optical filters for detecting each respective anti-Stokes signal in an epi-configuration. For SRS, the Stokes beam intensity was modulated using an electro-optic modulator (EO-AM-R-20-C2, Thorlabs, Newton, NJ) driven at 20 MHz. The detector consisted of a commercial system comprised of a photodiode coupled to a lock-in amplifier (Lock-In Amplifier, APE GmbH, Berlin, Germany) placed downstream of the sample in a trans-configuration.

5.3.4 Image Analysis

Three-dimensional CRS image stacks of the stratum corneum under both hydrated and dehydrated conditions were acquired from the skin surface down to a depth of 15 μm at 1-μm intervals along the depth axis. The vibrational bands of lipids, proteins, and water were probed using both CARS and SRS imaging modalities, resulting in a total of 6 image stacks per imaging area, per timepoint, per treatment condition. Each image stack was then inspected visually and the most superficial slice containing clearly delineated corneocytes – i.e. the topmost slice underlying the keratin layer – was used for all subsequent image analysis. Each corneocyte image set was then processed using FIJI image processing software in order to manually segment corneocytes from the lipid SRS image and generate one region of interest (ROI) per corneocyte within a given field of view. The lipid channel was selected for manual segmentation due to the high contrast between the extracellular and intracellular chemical composition. Once all cells in the field of view were identified, the region of the image encompassing all the identified cells was also selected as an ROI itself. The cell ROIs were then subtracted from this region, resulting in a single ROI that can be used to analyze the extracellular space within the stratum corneum.

The ROIs are then all imported into Matlab (Mathworks, Natick, MA), where a custom image analysis routine applies the segmented masks to the imaging data from all 6 channels, allowing for average measurements of water, lipid, and protein content to be computed for each individual cell within a field of view, in addition to the extracellular space. The algorithm uses the ROI data to perform morphological analysis, where metrics such as cell diameter, perimeter, circularity, and nearest neighbor distances are computed. Applying the ROIs to the imaging data results in a variety of metrics that can be extracted beyond water, lipid, and protein content. Ratios can be computed to compare signals from intracellular and extracellular spaces, or to compare the content of one compound (e.g. lipid) to another (e.g. water) within a given ROI. In total, the image analysis routing returns 35 morphological and compositional metrics per imaging field of view, which are then subjected to statistical

analysis using linear regression models to identify trends and correlation between the imaging metrics and the corneometer measurements.

5.3.5 Skin Explant Dehydration

In order to investigate the dynamics of skin dehydration using CRS imaging, two sets of skin samples were used, where both samples were processed and maintained in an incubator as previously described in order to reach a steady state of hydration. The skin samples were then both removed from the incubator, whereupon skin hydration was measured using the corneometer and CRS imaging was performed on both sets. Next, one sample was maintained on the nutritive gel bed in order to preserve hydration; the other was left on a plastic dish under ambient atmospheric conditions (22°C, 24% relative humidity) to facilitate dehydration. Subsequent corneometer and CRS imaging measurements were then performed 2 more times at 1-hour intervals. This investigation was performed using specimens from 3 different patients. Of note, the third timepoint data for Patient #3 could not be collected, as the epidermis of the skin sample on the gel substrate was compromised after the second timepoint. For this reason, only the data collected from the first two timepoints for Patient #3 was included in the statistical analysis.

5.3.6 Skin Explant Rehydration

To study the effects of moisturizing compounds on dry skin, four sets of skin samples were necessary per patient. All samples were first processed and maintained in an incubator as described above in order to attain a stable hydrated state. Next, all samples were removed from the incubator and allowed to dry in plastic dishes under ambient atmospheric conditions for 2 hours to allow the skin to dry and reach a stable dehydrated state, as confirmed by corneometry. The samples were then subjected to corneometry and CRS imaging before undergoing moisturizer treatment in order to assess the hydration status of the baseline dehydrated state, to be used as the reference for all rehydration comparisons. To this aim, two moisturizing compounds

were used, namely 12% deuterated glycerin dissolved in water, and 0.25% hyaluronic acid dissolved in water, designed to match typical humectant concentrations found in commercial formulations [231, 232]. The deuterated form of glycerin was selected in order to avoid CRS signal generation from its CH_2 and OH moieties. This was not a concern in the case of hyaluronic acid for two reasons: (1) its concentration was nearly 50-fold lower, and (2) it does not contain any CH_2 groups. Thus, the only potential source of spectral cross-talk are the molecule's OH groups, but they are dwarfed in numbers by the surrounding water molecules. Of each treatment pair, one subset was returned to the incubator, while the other remained at ambient conditions. Additional CRS and corneometer measurements were obtained 2 more times at 1-hour intervals. As above, this investigation was also performed using specimens from 3 different patients. Of note, the samples treated with glycerin absorbed the formulation over the time course of the experiment, allowing for a straightforward assessment of the stratum corneum using corneometry and CRS imaging. The skin samples treated with hyaluronic acid, on the other hand, remained noticeably wet at their surface throughout the experimental time course, barring any assessment at the second timepoint without perturbing rehydration dynamics. For the final timepoint, the residual moisture on the skin surface was carefully wiped with delicate task wipers prior to data collection.

5.3.7 Statistical Analysis

Processed image data was analyzed using the notebooks written in the R language. Data was analyzed using R 3.4.1 within the RStudio environment with extra packages compiled from the R 3.4.3 distribution. Correlation tests were first used to assess whether certain image analysis outcomes were independent since spectral overlap between the probed vibrational bands of interest was considered a potential factor between different chemical weightings (e.g. lipid vs. protein). To examine correlation, Pearson's R was calculated between image analysis outcomes in a pairwise manner with a coefficient of correlation greater than 0.8 considered to be highly correlated. Highly correlated outcomes were considered potentially linked due to spectral overlap.

The outcomes calculated from image analysis such as cellular water content measured via SRS were each subjected to linear regression analysis for longitudinal data. Cell- and region-specific information was collected from 3 distinct imaging areas across multiple subjects. As these areas and subjects were statistically exchangeable, they were considered random factors in the analysis. Linear regression was performed through the use of linear mixed effect models using the *lme4* and *lmerTest* R packages. In the initial analysis, individual image analysis outcomes were tested serially via linear mixed effect model regression analysis where the timepoint was treated as a fixed factor. Subject was considered a random factor and tissue area considered a random factor nested within each subject. For each image analysis outcome, the effect size β, t-statistic, and p-value were calculated and tabulated. It should be noted that while a threshold of 0.05 is conventionally set for p-values in order to determine significance, linear regression was performed once for each imaging metric across all paired conditions. Thus, for the dehydration experiment, the Holm-Bonferroni correction should be used to compensate for family-wise error by adjusting the p-value threshold given the number of statistical tests run. In the case of both the dehydration and rehydration experiments, this therefore results in a corrective factor of 36.

To compare conditions and assess the effect of treatments, a linear mixed effect model regression equation was built using the categorical treatment condition values as independent indicator variables. The baseline comparator condition was set as ambient environment without topical treatment. The regression equation specifically included not only the timepoint of the outcome, but also a timepoint-condition interaction term to separately test whether the treatment condition was a modifier for the time-dependent outcome.

Chapter 6

Longitudinal Monitoring of Cancer Cell Subpopulations from *In Vitro* to *In Vivo* Using Fluorescence Photoconversion

6.1 Introduction

Fluorescent labeling strategies are widely used in microscopy applications in order to glean a proper understanding of the biomolecular mechanisms underlying normal and aberrant cellular behaviors [11, 30, 31]. These techniques are highly diverse: standard immunofluorescence (IF) can be used to tag proteins of interest with high specificity [32]; genetic engineering can allow for the genomic insertion of fluorescent reporter proteins to monitor expression of particular genes [33, 34, 35, 36, 37]; organelle-specific fluorescent dyes can also be used for quantitative and/or qualitative cytological measurements [38, 39, 40]. Such methods have been used to study key microscopic processes in models spanning monolayers and 3D spheroids *in vitro* [30, 38] all the way up to animal models and humans *in vivo* [233, 234, 235, 236, 237, 238]. However, despite their widespread adoption in microscopy, traditional fluorescence-

based techniques are static in their labeling. In other words, they cannot be used to monitor specific cell populations of interest that have been identified after the initial labeling step. For example, a population of fluorescently labeled stem cells cultured *in vitro* or injected in an animal xenograft model cannot be monitored longitudinally to study their differentiation, as the dye's fluorescence is an intrinsic molecular property and is therefore independent of the cell's phenotypic behavior [41, 44].

In fact, there exists a wide variety of applications where the monitoring of specific cell subpopulations over a particular time course would be of great biological relevance. Biomolecular reporters such as green fluorescent protein (GFP), for instance, can be useful in determining whether the cells in a cultured population express a particular gene [35, 36]. However, tracking the fate of specific expressing or non-expressing cells within the same culture over prolonged periods would pose a significant challenge [41]. This difficulty is of particular importance in the study of treatment resistance in the context of cancer. In an ideal scenario, cells of interest would first be identified based on the expression of some reporter protein. Those same cells would then be monitored over time as they are challenged with therapeutic strategies in order to ascertain the response to therapy and probe aspects of a cell population's heterogeneity [239]. One can also envision a similar challenge in the study of immune infiltration within cancerous lesions. For instance, by using the techniques discussed above, the rate of immune cell turnover in the context of immunosurveillance would be extremely challenging to quantify as there is no straightforward manner of distinguishing specific immune cells over a longitudinal series of imaging experiments. These examples highlight some of the current limitations in using conventional fluorescent labeling strategies, particularly in the context of cancer research on the cellular scale.

A great deal of effort has been dedicated to the development of photoconvertible fluorescent labels to fill this biotechnological niche [41, 42, 43, 44]. Much like any other fluorescent molecule, these reporters exhibit a characteristic excitation and emission profile. However, they are distinct from conventional labels in that their optical profile can be predictably and reproducibly converted to a new set of excita-

tion and emission characteristics. The particular set of optical signatures before and after conversion, as well as the reversibility of the process, are intrinsic properties of each photoconvertible reporter. Genetic reporter systems such as Kaede[240] and Dendra2[241] have been been found particularly useful[242], but the natural turnover of fluorescent proteins makes these labeling strategies transient. Many studies could benefit from a photoconvertable approach that has permanence over eight or even ten cell division cycles.

While the excitation and emission properties of fluorescent reporters can range from the ultraviolet all the way to the near-infrared (NIR) [30], the red end of the spectrum is typically of greatest value for intravital imaging. These longer wavelength signals have a lower tendency to be absorbed and scattered by tissues compared to their bluer counterparts. This allows for increased signal generation and collection, and thus maximizes penetration depth [11, 30, 45]. One such commercially available NIR fluorescent label known as DiR (1,1'-dioctadecyltetramethyl indotricarbocyanine iodide) is a membrane dye with excitation and emission peaks at 748 nm and 780 nm, respectively [41]. This particular dye has been shown to exhibit irreversible photoconversion upon irradiation with a mere 8 to 45 mW of 750 nm femtosecond pulses over a period as short as 5 to 20 seconds depending on the nature of the sample at hand (i.e. *in vitro* vs. *in vivo*) [41].

In the context of this study, we sought to demonstrate the use of DiR as a photoconvertible membrane dye for tracking specific cells in solid tissues. These include labeling ovarian cancer cells (OVCAR5) in both 2D monolayer and 3D spheroid cultures, performing photoconversion on a given subpopulation, and monitoring their development over time. The selective isolation of photoconverted cells derived from such *in vitro* cultures using fluorescence-activated cell sorting (FACS) is also demonstrated and highlights the applicability of this method to identify specific cells of interest within a given *in vitro* context. Finally, the photoconversion of DiR is also demonstrated in a melanoma (UACC62) xenograft model in a live zebrafish monitored longitudinally over several days. In building upon prior efforts elucidating the photoconvertible nature of DiR and similar cyanine dyes [41, 43, 44], these demonstra-

tions set the stage for novel avenues of research in the context of molecular pathology where longitudinal monitoring of cell lineages can offer insight pertaining to therapeutic response and acquired resistance.

6.2 Materials and Methods

6.2.1 Monolayer Cell Culture

The OVCAR5 cell line (Fox Chase Cancer Center) consists of human epithelial carcinoma cells and was derived from the ascitic fluid of a patient with progressive ovarian adenocarcinoma without prior cytotoxic treatment. Cells were plated onto 6-well glass-bottom plates (Cellvis P06-14-0-N, Mountain View, CA) and cultured using Roswell Park Memorial Institute (RPMI) culture medium (Corning 10-040-CV, Corning, NY) supplemented with 10% fetal bovine serum (FBS; Gibco 10437-028, Waltham, MA) and 1% penicillin-streptomycin (Corning 30-001-CI, Corning, NY). Each well was seeded with 6.5×10^4 cells and incubated at 37°C with 5% atmospheric CO_2 for 5 days prior to imaging.

In order to label the cells with DiR, the culture medium was first removed from each well and substituted with fresh medium containing 5μM of DiR. The cells were then incubated for 20 minutes at 37°C prior to two washing steps with Dulbecco's phosphate-buffered saline (DPBS without calcium and magnesium; Corning 21-031-CV, Corning, NY). Cells were maintained in DPBS for imaging, and switched back to complete culture medium for longitudinal monitoring.

6.2.2 3D Spheroid Culture

Ovarian cancer spheroids were cultured in a manner consistent with previously described methods [243]. Briefly, in order to generate 3D spheroids for *in vitro* culture, 120 μL of Matrigel basement membrane matrix (Corning 356234, Corning, NY) was first dispensed uniformly to fill the glass-bottom well of a 35 mm dish (MatTek Corporation P35G-0-14-C, Ashland, MA). The dish was then incubated at 37°C for 45

minutes. Next, a suspension of cells in complete medium was prepared with a final concentration of 18,600 cells/mL, such that a total volume of 200 μL of cell suspension was sufficient to seed the gel with roughly 3,700 cells. The volume was dispensed drop-wise onto the gel layer and incubated at 37°C for another 45 minutes. During the incubation time, a 2% v/v solution of Matrigel dissolved in complete culture medium was prepared, of which 1.8 mL was added to the dish following incubation for a final volume of 2 mL over the gel bed.

Every 2 days following the initial seeding, the culture medium was replaced with fresh medium containing 2% v/v Matrigel and 10 μM DiR in order to ensure complete preliminary staining throughout the entirety of the formed spheroids. By maintaining this routine over the course of 2 weeks, 3D ovarian cancer spheroids with diameters in the few hundred of microns are readily formed [243, 244].

6.2.3 Spheroid Disaggregation and Fluorescence-Activated Cell Sorting (FACS)

In order to isolate specific cells of interest from a sample of 3D tumor spheroids using FACS, the spheroids first required disaggregation. To this aim, the culture medium was first removed from the glass-bottom dish containing the spheroids. The dish was then filled with 1 mL of dispase solution (Corning 354235, Corning, NY) and incubated at 37°C for 2 hours to break down the Matrigel matrix. Following incubation, the dish was supplemented with 1 mL of 10 mM EDTA (ethylenediaminetetraacetic acid; Fisher Scientific BP120-500, Waltham, MA) in DPBS to stop the dispase reaction. Next, cells were collected and centrifuged at 250 g for 5 minutes. The supernatant was then removed, and the cell pellet was washed two additional times with fresh DPBS and centrifugation at 250 g for 5 minutes each time. Next, the cell pellet was resuspended in 3 mL of 0.05% trypsin protease solution (GE Healthcare HyClone Trypsin Protease SH30236.01, Chicago, IL) and incubated at 37°C for 10 minutes. The protease solution was then neutralized by adding 5 mL of complete culture medium following incubation. The cells were then centrifuged one last time

at 250 g for 5 minutes, and resuspended in 500 μL of FACS buffer consisting of DPBS supplemented with 5 mL of FBS (1% v/v), 2 mM EDTA, and 25 mM HEPES (4-(2-hydroxyethyl)-1-piperazineethanesulfonic acid; Corning 25-060-CI, Corning, NY). The resulting cell suspension was then sorted using a commercial FACS system (BD FACSAria, Franklin Lakes, NJ), where gating parameters were determined based on the intensities of two fluorescence channels set to capture fluorescence within the 640-680 nm and 750-810 nm ranges.

6.2.4 Zebrafish Xenograft Model

To generate a short term xenograft model of melanoma, UACC62 melanoma cells were first cultured *in vitro* using complete cell medium (RPMI supplemented with 10% FBS and 1% penicillin-streptomycin). For staining the melanoma cells with DiR, the culture medium was first removed prior to washing with DPBS. Next, the cells were then exposed to a 5 μM solution of DiR in complete culture medium and incubated at 37°C for 20 minutes. The cells were then washed twice with DPBS before reintroducing them to fresh complete culture medium and allowing them to incubate at 37°C for an additional 20 minutes prior to xenografting.

For the transplantation procedure, zebrafish were handled in full compliance with a protocol approved by the institutional animal care and use committee (IACUC) of Massachusetts General Hospital (MGH IACUC protocol #2011-N-000127). The injection procedure is similar to previously reported methods [245, 246]. First, DiR-labeled cells were collected and resuspended such that a final volume of 5 μL containing 1.5 to 2 million cells could be used for the xenograft. Fish were anesthetized by placing them in a dish containing tricaine solution (0.16 mg/mL). Next, each fish was held dorsal side up for the retro-orbital injection, which was performed using a Hamilton syringe. With the bevel side up, the syringe was positioned at an angle of 45° relative to the plane of the fish; if the fish's eye were a clock, the syringe was placed pointing at the 7:00 position of the eye and inserted 1–2 mm into the tissue. Following the injection, the fish was allowed to recover in fresh water for 7 days prior to photoconversion experiments.

6.2.5 Fluorescence Microscopy

Confocal fluorescence microscopy was performed using a commercial inverted microscope (Olympus FV1000 IX81, Tokyo, Japan). All image data was recorded with a bit depth of 12, i.e. pixel intensities had a dynamic range from 0 to 4095. The 635 nm continuous wave (CW) laser line was used as the excitation for both standard and photoconverted DiR for all imaging experiments. Lambda-scan image stacks were acquired from 650 nm to 790 nm in 5 nm steps, with a spectral bandwidth of 10 nm at each step.

In the case of the *in vivo* xenograft model, cellular fluorescence was captured sequentially: signals emitted between 650 nm and 690 nm were first recorded, followed by the fluorescence from 760 nm to 800 nm. Z-stacks were acquired over a depth of 300 μm with a step size of 10 μm, using the fish's eye as a fiducial marker to ensure the same field of view was revisited at each experimental time point.

6.2.6 Photoconversion

A femtosecond pulsed laser source tuned to a center wavelength of 750 nm (Spectra-Physics InSight DeepSee, Santa Clara, CA) was used to photoconvert the DiR label [41]. The laser light was routed into the optical input port of the confocal microscope described in Sec. 6.2.5. The total power at the output of the microscope objective was kept below 25 mW for all imaging experiments, whether *in vitro* or *in vivo*. The pixel dwell time was limited to 4 μs/pixel, resulting in an approximate scan time of 1 second per frame for a region 512 $\times$ 512 pixels in size. Each ROI was thus raster-scanned over the course of 15 to 30 seconds in order to achieve complete and uniform photoconversion of the DiR label across the entire field of view.

6.2.7 Image Analysis

All image analysis was performed using Matlab R2017a (MathWorks, Natick, MA). In order to generate the fluorescence emission profiles of standard and photoconverted DiR, the pixel intensities of each image slice within a given lambda-scan were summed

together. Thus, each spectral image stack was reduced in size from 512 × 512 × 29 pixels to a single 29-element vector, with each element corresponding to the total fluorescence intensity from the entire field of view within a given 10-nm spectral window. A similar process was used to obtain the emission profiles of specific regions of interest within a field of view, where the pixels strictly within the ROI were summed together.

For the xenograft model, given that the z-stacks were acquired sequentially (650-690 nm first, followed by 760-800 nm), image registration was required to properly align the two datasets. To facilitate this process, maximum intensity projections were computed for both z-stacks to generate 2D renditions of the 3D datasets. The projections were then smoothed using a 2D Gaussian kernel with a standard deviation of 0.75. The corresponding fluorescent signals from the 650-690 nm and 760-800 nm channels were then visually matched on a cell-by-cell basis using the control point selection tool in Matlab (*cpselect()*). For each image pair, 150 to 250 control point pairs were manually identified. Next, a geometric transform was computed to fit the control point pairs via a local weighted mean transformation with 50 nearest points using the *fitgeotrans()* Matlab function.

The processed fluorescence intensity images were then overlaid, with the 650-690 nm channel in green (G) and the 760-800 nm channel in red (R), thus generating the images in the top row of Fig. 6-5. The scatter plots in the middle row were generated by plotting each pixel's green channel intensity against that of its red channel, resulting in data representation visually reminiscent of flow cytometry scatter plots. Finally, the fluorescent signals were gated using two experimentally-derived criteria to generate the discrete images in the bottom row. First, a pixel was identified as containing DiR if the combined intensity exceeded exceeded a threshold, i.e. if $G + R > Thesh$. Next, if $G > R/3 + Subthresh$ then the DiR was classified as photoconverted; if $G < R/3 + Subthresh$, then it was considered standard, i.e. its native non-converted form. In this manner, pixels that remained black were determined not to contain any detectable levels of DiR. On the other hand, pixels that were either green or red were classified as containing photoconverted or standard DiR,

respectively.

6.3 Results and Discussion

6.3.1 Photoconversion in Monolayers *In Vitro*

Ovarian cancer cells (OVCAR5) were first grown *in vitro* and allowed to reach confluence before labeling with DiR. Upon illumination with 635 nm laser light, the bright fluorescence signals observed from the stained cells revealed the two characteristic DiR emission peaks located around 660 nm and 760 nm as can be seen in the plotted emission spectra in Fig. 6-1. By encoding every probed emission wavelength from the scan to a color scale element from Matlab's "hot" color map, the two standard DiR peaks result in a vivid yellow false color. On the other hand, photoconverted DiR exhibits 2 notable spectral features that distinguish it from its standard counterpart: (1) a marked increase in fluorescence emission at 660 nm, and (2) the elimination of the second peak at 760 nm. This results in a dark red false color, allowing for a simple and intuitive visual distinction between converted and unconverted cells.

Building upon these results, fresh OVCAR5 cells were newly plated and stained with DiR prior to imaging with 635 nm illumination. A single region of interest (ROI) 636 μm $\times$ 636 μm in size (i.e. a full field of view at 20$\times$ magnification) was photoconverted on Day 0, where Fig. 6-2(a) and Fig. 6-2(b) show the ROI before and after photoconversion, respectively. The same ROI was then revisited daily over the next 48 hours and imaged at both 10$\times$ and 20$\times$ magnification (Fig. 6-2(c-f)). As expected, the cells were observed to be growing normally and retained sufficient amounts of the DiR dye to generate readily detectable fluorescence signals despite multiple cell divisions. Interestingly, after 48 hours following the initial seeding, labeling, and photoconversion, the borders of the ROI became blurred as cells labeled with standard DiR are seen to infiltrate the area and, conversely, cells with photoconverted DiR are observed to expand beyond their site of origin.

Given the permanent spectral shift, this methodology can be widely used in *in vitro*

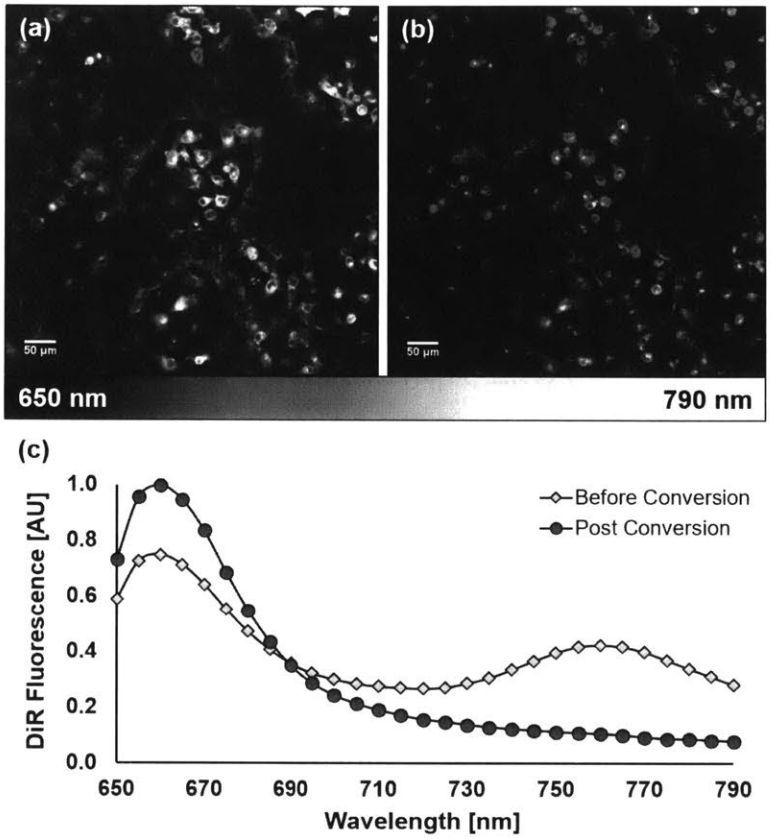

Figure 6-1: *In vitro* monolayer model of ovarian cancer showcasing the fluorescence of DiR before (a) and after (b) photoconversion, with associated fluorescence spectra summed across the entire field of view (c).

settings where temporal dynamics are of particular scientific interest. For example, cell lines genetically modified with the ability report the expression of a gene of interest using fluorescent proteins can all be uniformly stained with DiR. Then, cells that do express the reporter protein can be photoconverted *in situ* while imaging to permanently mark which individual cells within the heterogeneous population express the gene of interest on Day 0. In this manner, this subpopulation of interest can be monitored within the context of its heterogeneous environment over a time course spanning several days or even weeks as it is challenged with various therapeutic strategies. This methodology would therefore allow one to monitor the genetic state of specific individual cells over time, offering insight pertaining to the expression dynamics of the gene of interest. This methodology can also be applied to cellular co-cultures in order to monitor key interaction parameters of interest between specific

members of either cell population.

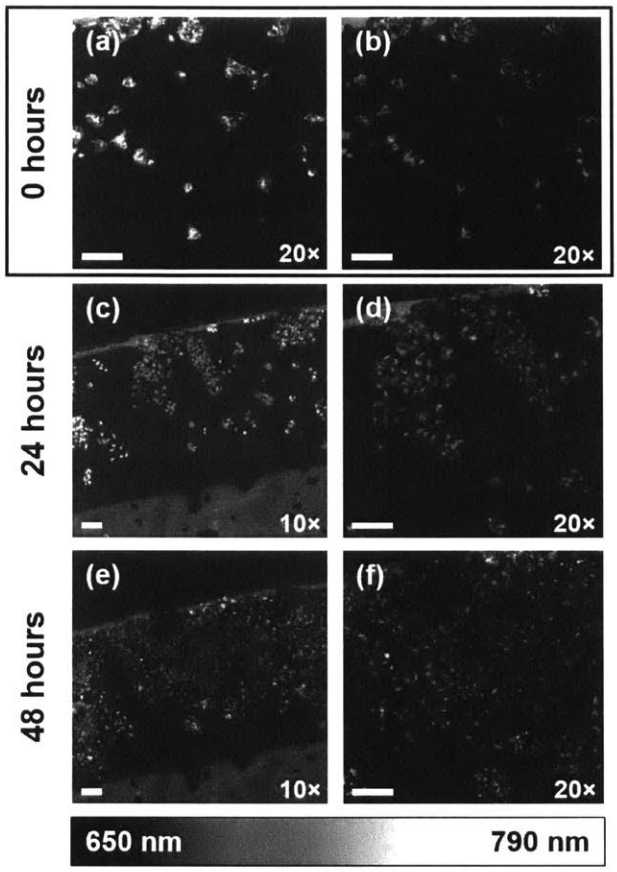

Figure 6-2: Longitudinal monitoring of an ovarian cancer cell subpopulation of interest, seen before (a) and after (b) photoconversion on Day 0. The same field of view was revisited 24 hours (c,d) and 48 hours (e,f) following the photoconversion process to monitor the cellular proliferation over time. All scale bars correspond to 100 μm. Images in (a,b,d,f) and (c,e) were acquired at 20× and 10× magnification, respectively.

6.3.2 Photoconversion in 3D Spheroids *In Vitro* and FACS

While cellular monolayers cultured *in vitro* are advantageous for study given their ease of use and simplicity, they are not representative of cancer *in vivo*. Indeed, interactions with extracellular matrix elements and neighboring cells in all three spatial dimensions can significantly influence tumor pathophysiology. Three-dimensional *in vitro* tumor culture models can replicate many of the molecular and structural features of human tumors, and therefore offer a convenient middle ground between *in*

vitro monolayer cultures and live animal experiments *in vivo* [243].

There are many situations where a specific subpopulation of cells within a tumor spheroid may be of interest. For instance, one may want to differentiate between the cells located towards the core of a spheroid rather than those on its periphery to study biochemical pathways related to hypoxia in the context of cancer pathogenesis [243, 244, 247]. Alternatively, one may expose cultured tumors to particular chemical gradients in order to model the diffusion of therapeutic compounds, and study the resulting tumor response at the cellular population level. In such cases, the ability to visualize, target, and permanently label a portion of the studied tumor would be of significant value, as it would allow one to correlate longitudinal observations with spatially-resolved subpopulations of interest within a tumor throughout its development.

In order to demonstrate this application, OVCAR5 cells were grown on a bed of Matrigel, a commercially available gelatinous culture substrate that mimics extracellular matrix and favors the formation of 3D spheroids [243, 244]. Once these cellular clusters reached a few hundred microns in diameter, a subpopulation of cells along the topmost peripheral section of a tumor spheroid was targeted for photoconversion as seen in Fig. 6-3. An ROI defined within the targeted area revealed the signature twin peaks of standard DiR at 660 nm and 760 nm prior to photoconversion. Following the conversion process, the second peak was found to disappear while the first peak's signal increased as expected (Fig. 6-3(c)). In examining a second ROI defined outside the targeted area, the emission signature of standard DiR was preserved all throughout the procedure. Some minor photobleaching was observed and helps to explain the modest drop in fluorescence signal.

Given a partially photoconverted tumor spheroid where the optical contrast permanently identifies specific cells of interest, it follows that a manner for isolating said cells for subsequent expansion and study would be of great practical value. For example, in the context of ovarian cancer metastasis, spheroids are known to spread intraperitoneally and continue growing at distant sites along the walls of the peritoneum [243]. Here, one may seek to optically label the cancer cells in contact with

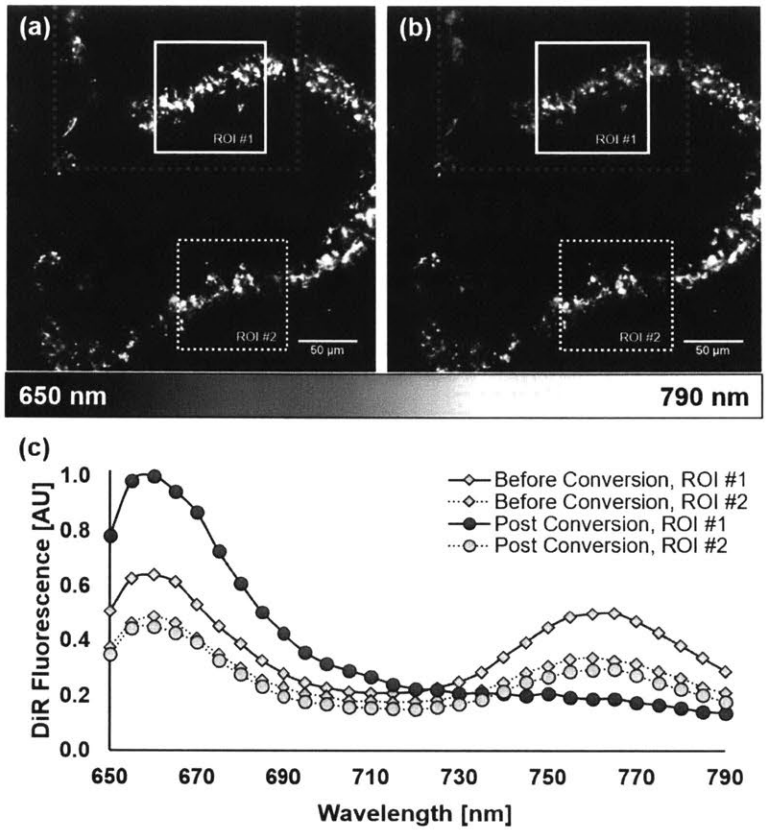

Figure 6-3: 3D tumor spheroid of ovarian cancer cells before (a) and after (b) photoconversion of the topmost peripheral region indicated by the gray box. Two regions of interest (ROI) have been selected within the image, where ROI #1 encompassed photoconverted cells while ROI #2 did not. The corresponding fluorescence spectra are shown in (c), where solid and dashed lines refer to ROIs #1 and #2, and diamonds and circles refer to before and after photoconversion, all respectively.

the endothelial cells along the peritoneal walls to later study their protein expression.

To demonstrate the applicability of this platform for such a scenario, 3D *in vitro* spheroids of OVCAR5 cells were grown across the entire surface of a glass-bottom dish filled with Matrigel-rich media and cultured over the course of 2 weeks. This favored the formation of hundreds of spheroids that are each comprised of many hundreds more cells [243, 244]. After registering the location of each spheroid via visual microscopy inspection, the photoconversion routine was automated. At each location, the external pulsed 750 nm laser light was used to illuminate a coarsely-defined z-stack through approximately one half of the spheroids. They were then disaggregated and prepared for cell sorting via FACS.

The fluorescence captured from a representative sampling of the disaggregated tumor cells revealed two distinct populations of labeled cells as shown in Fig. 6-4(a). The fluorescence intensity from the NIR emission band of DiR is shown on the horizontal axis, while the vertical axis indicates red fluorescence, which is markedly increased upon photoconversion. Following the sorting process via FACS, the isolated non-converted and photoconverted cells were plated and cultured as shown in Fig. 6-4(b,c). These results show that not only was the DiR label retained in the cell membrane despite the multiple processing and handling steps, but both its standard and photoconverted forms were present at readily detectable levels. Moreover, the spectral shift following the photoconversion process was indeed found to be permanent and irreversible, as verified in Fig. 6-4.

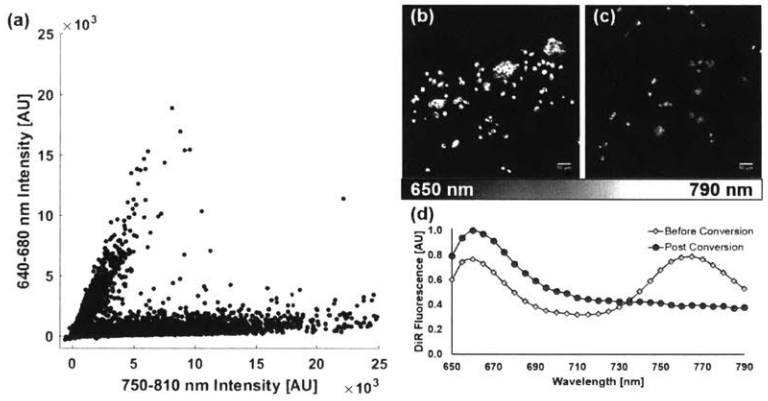

Figure 6-4: FACS plot of a cell sample from disaggregated, partially photoconverted ovarian cancer spheroids (a), and subsequent seeding of sorted non-converted (b) and photoconverted (c) cells. The fluorescence spectra from the sorted cells are shown in (d), demonstrating the irreversible nature of *in situ* DiR photoconversion.

This methodology is therefore particularly applicable in contexts where an especially small subpopulation of cells are of interest for subsequent experimentation. Using *in situ* photoconversion, these cells can be isolated via FACS and then expanded *in vitro* to generate large numbers of cells from the subpopulation of interest.

6.3.3 Photoconversion in Zebrafish Xenograft Model *In Vivo*

Finally, in the context of *in vivo* imaging, there are many scenarios where the labeling of one cellular subpopulation of interest may be of use. One such example is that of lineage tracing in the context of metastasis: given an initially heterogeneous population of cells within the primary tumor, there is a persistent and challenging need to identify which ones are the first to spread; which ones divide most rapidly; and which cell subpopulations grow and expand despite therapeutic administration.

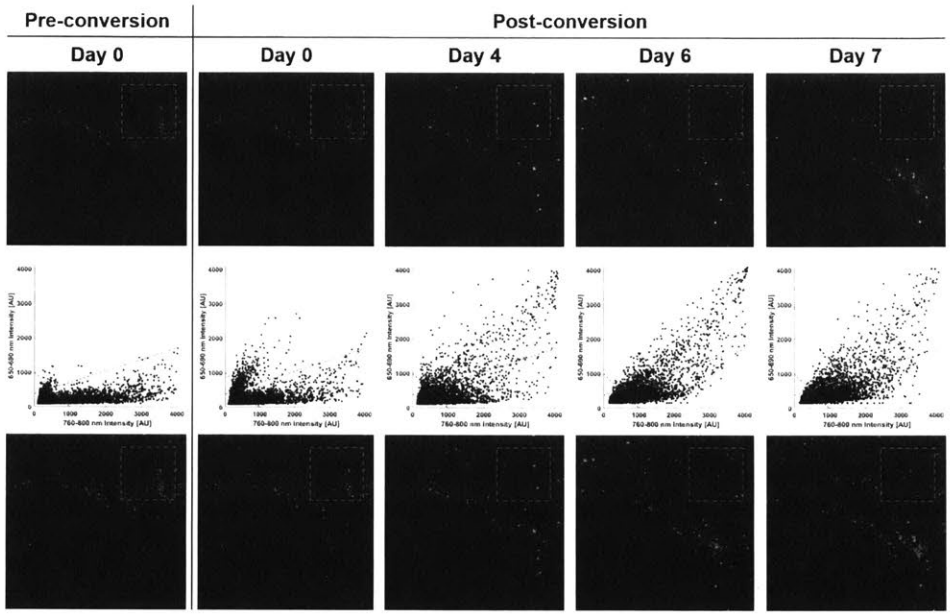

Figure 6-5: *In vivo* longitudinal monitoring of a photoconverted subpopulation of melanoma cells indicated by the gray box in a zebrafish xenograft model following *in situ* photoconversion. In all images, the eye is located at the bottom-left of the field of view and was consistently used as a fiducial marker throughout the experimental time course to ensure monitoring of the same area over time. The top row shows a colored overlay of the two collected fluorescence emission bands, namely 650-690 nm in green and 760-800 nm in red. The middle row shows a scatter plot of each pixel, where green and red channel intensities are plotted against one another in order to generate a representation visually reminiscent of flow cytometry plots. The red dashed lines in the scatter plots correspond to the gating criteria to identify pixels containing either photoconverted or standard DiR. These gates are then used to recolor the images from the top row, where the images in the bottom row show photoconverted and standard DiR fluorescence in green and red, respectively.

In order to better model such a scenario, melanoma cells were first cultured and labeled with DiR. They were then injected retro-orbitally in zebrafish to produce

melanoma xenograft models *in vivo*. After 7 days, the fish were anesthetized and imaged using confocal fluorescence microscopy with 635 nm illumination to visualize the implanted DiR-labeled melanoma cells behind the eye as seen in the leftmost column of Fig. 6-5 (top panel). A small field of view roughly 364 μm $\times$ 364 μm in size containing several tens of cells was then arbitrarily selected for photoconversion. The overlay in the second column of Fig. 6-5 shows the 760-800 nm intensity in red, while the 650-690 nm signal is shown in green.

The added convenience of such a platform is that images can be processed in a manner similar to flow cytometric analysis, where pixel intensities can be shown in a scatter plot that visually relates one channel's intensity to that of the other. This familiar data representation then allows for a straightforward gating of the fluorescence signals to identify cellular subpopulations of interest over time in a wide variety of platforms ranging from *in vitro* to *in vivo*. Indeed, as can be appreciated in the bottommost row of Fig. 6-5, the initial cluster of cells within the photoconverted ROI is clearly visualized on Day 0 and is then seen spreading over the course of the following week, reaching areas far beyond the original photoconversion site. This demonstration is of particular value in the context of *in vivo* animal models of metastasis, where one may photoconvert cells at the primary tumor site that are more or less likely to metastasize. As tumors then form at distant anatomical sites, their spectral signatures would allow one to infer specifically which cells from the heterogeneous primary tumor were the ones to metastasize. The major advantage of this approach, in particular for patient xenograft studies, is that this photoconversion method does not require cellular genomic manipulation as is the case with fluorescent reporters. Cells never have to be transformed, grown on hard plastic surfaces, or exposed to cell culture conditions to prepare for photolabeling. This has the advantage of preserving tumor cellular heterogeneity and may allow for photoconversion techniques to be used with minced tumor implantation models [248].

6.4 Conclusion

The advent of photoconvertible dyes in the context of biomedical imaging has provided the optics community with a toolkit that allows for the selective labeling of a specific cellular subpopulation of interest where the parameter of interest is identified visually *in situ*. This predictable and convenient conversion process, non-invasively triggered via an external pulsed near-infrared laser source, is further perpetuated to the daughter cells of the converted targets thus greatly facilitating longitudinal studies of heterogeneous cell populations.

The implications for future avenues of research are numerous. Combining this NIR photoconversion methodology with *in vivo* flow cytometry in an animal model [249, 250, 251], for example, would allow one to not only count the number of cells circulating within a particular vascular network, but to identify which cells have already been counted by triggering 750 nm pulsed light irradiation for photoconversion following each detection of a circulating non-converted cell. The DiR labeling the cell would thus be permanently photoconverted and would allow one to obtain highly accurate counts of circulating cells by avoiding repetitious counts.

In another scenario, one may seek to characterize the *in vivo* response to therapy of a growing tumor exposed to injected therapeutics. For instance, animal models fitted with window chambers for direct observation of the implanted tumor may be imaged periodically over a defined time course to study the response of individual cells to the therapy over time [252, 253]. By photoconverting responsive (or non-responsive) cells at particular time points in the days and weeks following treatment, a more complete portrait of therapeutic response in the context of cancer treatment can be ascertained.

It is worth noting that the photoconversion of DiR can be completed within seconds rather than minutes of raster-scanning across the targeted area. This can greatly accelerate experimental protocols compared to the use of other photoconvertible agents such as Dendra2 that require conversion times on the order of several minutes in addition to genetic engineering [254, 255]. The simplicity of the presented

approach, where labeling merely requires a brief incubation period in the presence of the dye without harsh permeabilizing agents, can be easily adopted by scientists with minimal experience using photobiological assays. The potential applications of photoconversion technology in the field of cancer research are thus widely diverse, given the minimally invasive nature and simplicity of the presented methodology.

Chapter 7

In Vivo Imaging of the Melanomagenesis-Associated Pigment Pheomelanin Using CARS and SFA

7.1 Introduction

The yearly global incidence of melanoma is over 232,000 individuals, with more than 55,000 of those diagnosed succumbing to the disease [100]. Individuals with fair skin and red hair exhibit the highest risk for developing melanoma [256], with evidence suggesting the red/blond pigment known as pheomelanin may elevate melanoma risk through both UV radiation-dependent and -independent mechanisms. Moreover, red-haired melanoma patients often develop amelanotic lesions, so-called due to the absence of macroscopically detectable dark eumelanin pigments within the visible tumor margin. Because they are harder to recognize upon examination, these tumors are frequently diagnosed at more advanced stages and are associated with higher mortality [257]. Similar amelanotic melanomas arise in mice bred on the $Mc1r^{e/e}$ genetic background, which recapitulates the red-haired, fair-skinned phenotype. The non-

visible pheomelanin in these lesions was found to functionally contribute to melanoma formation, as the introduction of an albino allele onto the same genetic background abrogated melanoma risk [258]. Although the ability to identify and monitor pheomelanin within skin is vital to improve our understanding of the underlying biology of these lesions, no tools exist for real-time, *in vivo* characterization of the pigment.

Studies using Raman spectroscopy to explore the pigment of red bird feathers previously suggested that a unique vibrational band centered between 2000–2100 cm^{-1} may be a marker for pheomelanin. However, it was not clear if this weak vibrational resonance could be used for *in situ* identification of the red pigment. Coherent anti-Stokes Raman scattering (CARS) microscopy, a label-free vibrational imaging technique based on Raman scattering, offers significantly enhanced signal levels compared to spontaneous Raman scattering, and may be suitable for non-invasively identifying pheomelanin inside the skin in real time. Here, we show that the distribution of pheomelanin in cells and tissues can be visually characterized non-destructively and non-invasively *in vivo* with CARS microscopy. We validated our CARS imaging strategy *in vitro* to *in vivo* using synthetic pheomelanin, isolated melanocytes, and the $Mc1r^{e/e}$ red-haired mice model. Nests of pheomelanotic melanocytes were observed in the red-haired animals, but not in the genetically matched $Mc1r^{e/e}$; $Tyr^{c/c}$ ("albino-red-haired") mice. Importantly, samples from human amelanotic melanomas imaged with CARS microscopy exhibited strong pheomelanotic signals. This is the first time, to our knowledge, that pheomelanin has been visualized and spatially localized in melanocytes, skin, or human amelanotic melanomas.

7.2 Results and Discussion

7.2.1 Synthetic Pheomelanin

To demonstrate that CARS microscopy can selectively and sensitively visualize pheomelanin, the pigment was synthesized following an established procedure that makes use of the mushroom tyrosinase enzyme [259]. When distributed as small particles

in a water/hexane emulsion, synthetic pheomelanin was found to yield a very strong CARS signal whose vibrational spectrum corresponds to that observed with Raman spectroscopy (Figure 7-1) [260, 261].

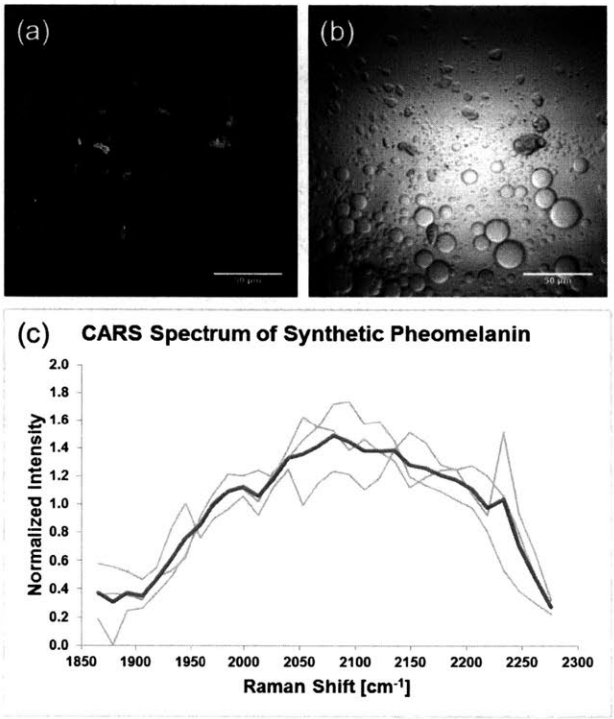

Figure 7-1: Synthetic pheomelanin in a 4:1 water:hexane emulsion. (a) CARS image acquired at $\omega_P\omega_S = 2000$ cm^{-1}. Pheomelanin is observed as small, insoluble aggregates with bright CARS intensity. The surrounding water/hexane bubbles show low-level non-resonant CARS background. (b) Trans-illumination image acquired with the 861 nm pump beam. (c) CARS spectrum of synthetic pheomelanin referenced to the wavelength-independent non-resonant signal from a glass coverslip, normalized by area under the curve. Three synthetic pheomelanin samples were measured, with each spectrum shown in gray; the curve in red corresponds to the mean of the three measurements.

7.2.2 Pheomelanin in FACS-Sorted Mouse Melanocytes

With the ability to visualize and spectroscopically confirm the presence of pheomelanin using CARS microscopy, the next step was the detection of naturally-occurring pheomelanin. Red-haired mice (Mc1r$^{e/e}$) were bred to incorporate B6.Cg-Gt(ROSA) 26Sor$^{tm6(CAG-ZsGreen1)Hze}$ (Jackson Laboratory catalog #007906) or B6.Cg-Gt(ROSA) 26Sor$^{tm9(CAG-tdTomato)Hze}$ (Jackson Laboratory catalog #007909) and melanocyte tar-

geted CRE (Tyr-CRE) [262], thereby enabling FACS-based isolation of neonatal ZsGreen or tdTomato fluorescent tagged melanocytes. A detailed protocol regarding melanocyte extraction can be found in Section 7.3.6. The tdTomato mice were sacrificed, their skin harvested, and dermal cells sorted based on fluorescence of both tdTomato and FITC-labeled antibodies tagging c-Kit, a surface marker [263]. ZsGreen-labelled mice underwent a similar procedure, with melanocytes selected via their ZsGreen and c-Kit signals. The sorted melanocytes were fixed, and imaged with both CARS and confocal fluorescence microscopy.

As shown in Figure 7-2, pheomelanin signals exhibited the predicted perinuclear localization of melanosomes. As a control, genetically matched tdTomato-tagged, tyrosinase-deficient ($Mc1r^{e/e}$, $Tyr^{c/c}$) "albino-red-haired" mouse-derived melanocytes were subjected to the same analysis and no visible pheomelanin signals were observed (Figure 7-3). Importantly, CARS spectra acquired from the red-haired mice, but not the albino red-haired mice, matched CARS spectra collected from synthetic pheomelanin, confirming the ability of coherent Raman scattering imaging to selectively visualize the red pigment within cells.

7.2.3 *Ex Vivo*, *In Vivo*, and Histological Visualization of Pheomelanin in Mouse Skin

With the evidence that pheomelanin may be selectively visualized in isolated genetically defined cells, we explored the detection and localization of pheomelanin within intact mouse skin. *Ex vivo* ear skin from C57BL/6 ($Mc1r^{e/e}$, $Tyr^{+/+}$) red-haired mice proved to be an advantageous sample, as brightfield images acquired alongside CARS could be used to verify the location of melanin within the tissue. Under the eyepiece, pheomelanotic cells in the thin ear skin appeared brown-red, with visible cell bodies and dendrites (Figure 7-4). Individual pheomelanin-containing organelles were distinctly visualized via CARS imaging and co-localized with the pigmented areas observable by brightfield microscopy.

To translate these findings, CARS imaging was carried *in vivo* on red-haired mouse

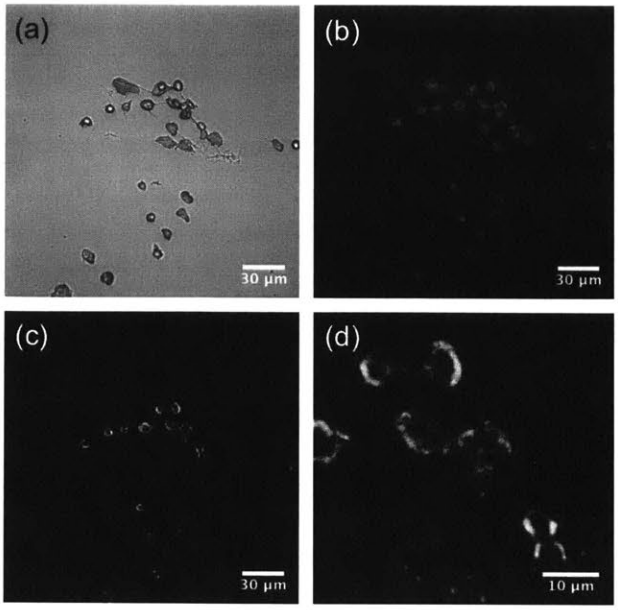

Figure 7-2: Melanocytes isolated from red-haired C57BL/6 ($Mc1r^{e/e}$, $Tyr^{+/+}$) mice exhibit strong CARS signal at $\omega_P - \omega_S = 2000$ cm^{-1}. (a) Trans-illumination image acquired with the pump beam, where the overall shape of the cells can be well visualized. (b) Confocal fluorescence image of tdTomato. (c) False color (Green fire blue colormap in ImageJ) CARS image mapping intracellular pheomelanin distribution. (d) 4×-zoomed view of (c) showing a perinuclear distribution of signal intensity, consistent with the known biology of protective melanin caps.

($Mc1r^{e/e}$, $Tyr^{+/+}$) ears. Identical patterns of pheomelanin-rich cells were found (Figure 7-5). Importantly, these *ex vivo* and *in vivo* experiments were repeated for both control albino-red ($Mc1r^{e/e}$, $Tyr^{c/c}$) and albino ($Mc1r^{+/+}$, $Tyr^{c/c}$) mice: no visible pheomelanin signals could be observed in the skin of these animals.

To confirm these measurements and positively identify the observed pheomelanin-rich cells as melanocytes, thin sections (5 μm in thickness) were prepared from $Mc1r^{e/e}$, $Tyr^{+/+}$ red-haired mouse ears for histology and immunohistochemistry (IHC). As the red fluorescence from eosin was found to interfere with the CARS signal, immunostained slides where accompanied by an adjacent unstained slide for coherent Raman imaging. Sry-related HMG-BOX gene 10 (Sox10) is a nuclear transcription factor that participates in neural crest development and in the specification and differentiation of cells of the melanocytic lineage. Sox10 is expressed in Schwann cells and melanocytes/melanomas [264], making it a specific marker for

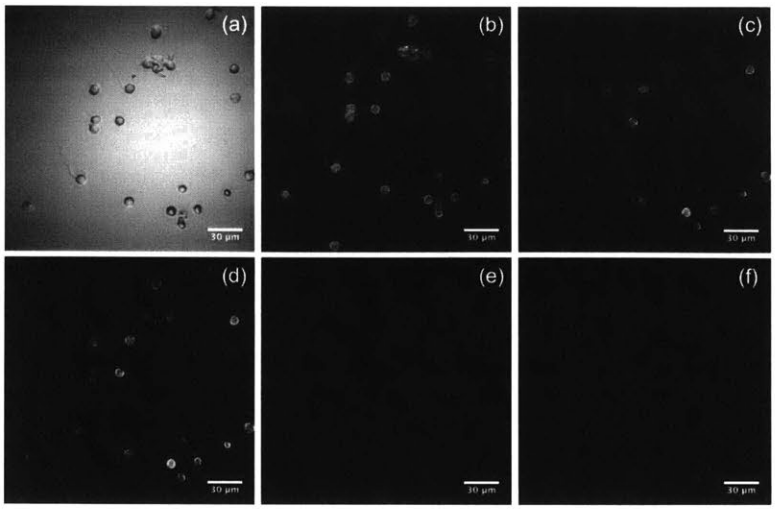

Figure 7-3: Melanocytes isolated from albino-red C57BL/6 ($Mc1r^{e/e}$ $Tyr^{c/c}$) mice exhibit negligible CARS signal at $\omega_P - \omega_S = 2000$ cm^{-1}. (a) Trans-illumination image acquired with the 861 nm pump beam. (b) Confocal fluorescence image of tdTomato. (c) False color CARS image acquired with pump ($\lambda_P = 861$ nm) and Stokes beams ($\lambda_S = 1040$ nm). (d) False color image acquired only using the pump beam, showing prominent two-photon fluorescence signals from tdTomato. (e) False color image acquired only using the Stokes beam, showing weak two-photon fluorescence signals from tdTomato. (f) False color image illustrating the true CARS signal obtained by subtracting tdTomato fluorescence in (d) and (e) from the raw CARS image in (c).

dermal melanocytes. Figure 7-6(a) shows IHC staining for Sox10 (EP268, Cell Marque), where the pheomelanin-containing melanocytes were found to be Sox10 positive. Pheomelanin stores inside the red-haired mouse skin can also be seen under brightfield illumination in the adjacent unstained slide, as shown in Figure 7-6(b). When imaging the same unstained slide with CARS targeting the pheomelanin vibrational band, bright pheomelanin signals were found corresponding to the pigmented areas seen under brightfield and in the Sox10 positive areas via IHC. A separate experiment was also conducted to image a different mouse ear sample without IHC staining, such that CARS imaging can be performed directly on the haematoxylin-stained slice. As shown in Figure 7-7, pheomelanotic stores are observed as bright granular structures, consistent with imaging data shown in Figure 7-6.

In order to further cross-validate the pheomelanin signals from the CARS images, we also simultaneously performed sum frequency absorption (SFA) imaging in a multimodal configuration, where SFA microscopy is an imaging toolkit that enables

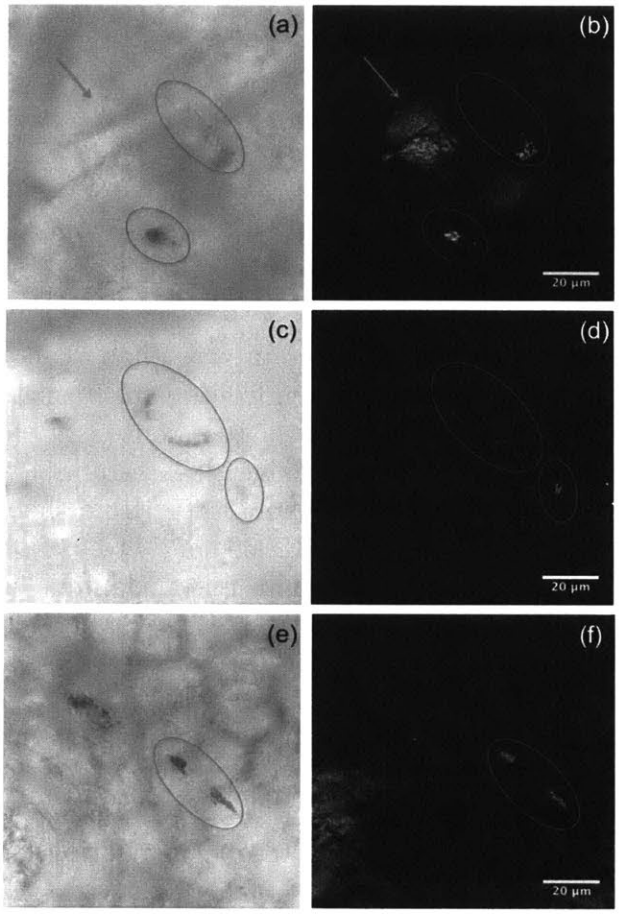

Figure 7-4: Imaging of pheomelanin stores in red-haired mouse ear skin. (a,c,e) Brightfield trans-illumination image acquired from the microscope eyepiece. (b,d,f) Maximal projection view of CARS image stack of the mouse ear, showing bright granules from the pheomelanin stores (red circles) within melanocytes and at the base of the hair follicle. A CARS image stack acquired with the pump beam set to 871 nm ($\omega_P - \omega_S = 1866$ cm^{-1}) was subtracted from the image stack acquired with the pump beam set to 861 nm ($\omega_P - \omega_S = 2000$ cm^{-1}) to minimize the non-resonant signal contribution from structures other than pheomelanin. Image stacks are 27 μm thick, with a step size of 1 μm. Note that an out-of-focus hair (blue arrow) caused a shadow in the trans-illumination image (a), whereas CARS is highly depth-resolved; therefore, the hair was not prominently seen in (b).

the visualization of light-absorbing molecules like pheomelanin [46, 49]. This optical process is characterized by a molecule's ability to simultaneously absorb two photons without the necessary involvement of an intermediate real energy level between the ground state and the final excited state. The signal was confirmed to arise from SFA and not stimulated Raman scattering (SRS) by tuning the pump wavelength

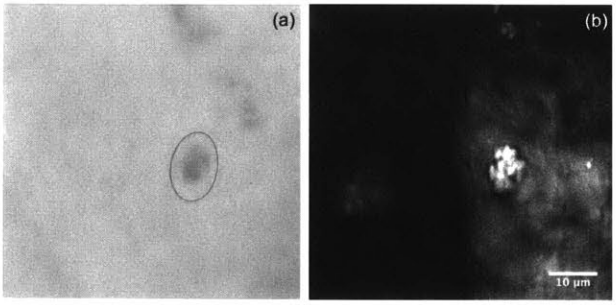

Figure 7-5: Imaging of pheomelanin stores in a red-haired mouse ear in vivo. (a) Brightfield trans-illumination image acquired from the microscope eyepiece. (b) Maximal projection view of CARS image stack of the mouse ear, showing bright signals from pheomelanin (red circle). A CARS image stack acquired with the pump beam set to 871 nm ($\omega_P - \omega_S = 1866$ cm^{-1}) was subtracted from the image stack acquired with pump beam set to 861 nm ($\omega_P - \omega_S = 2000$ cm^{-1}) to minimize the non-resonant signal contribution from structures other than pheomelanin. The image stack in (b) is 15 μm thick, with a step size of 1 μm.

across the expected pheomelanin Raman band. As no variation in signal intensity was observed, the signal was determined to arise solely from absorption contrast. As shown in Figure 7-6(e) and (f), a one-to-one correlation can be found between CARS and SFA images, indicating that pheomelanin within melanocytes can indeed be well visualized using CARS microscopy. It should be noted that the overlap of the CARS and SFA images with Figure 7-6(a) is not perfect, as each tissue slice is 5 μm thick. Moreover, the signal-to-noise ratio in the image shown in Figure 7-6(d) is reduced compared to that obtained in tissue due to the configuration of the imaging system: as the position of the CARS detector is in the epi-direction, the collected signal depends in part on back-scattering in order to redirect the forward-generated anti-Stokes light back into the microscope objective. Considering the 5 μm thickness of the tissue slice, the CARS image quality in this scenario does not benefit from the scattering properties of thick biological samples that would otherwise generate a much stronger signal [28]. It is also possible that the actual amount of pheomelanin in thin tissue slices is slightly diminished relative to intact tissue as a result of the frozen section preparation itself. Nevertheless, the consistency in spatial localization between the signals observed in Figure 7-6(d) and (e) indeed supports the ability of CARS microscopy to specifically visualize pheomelanin in a label-free manner.

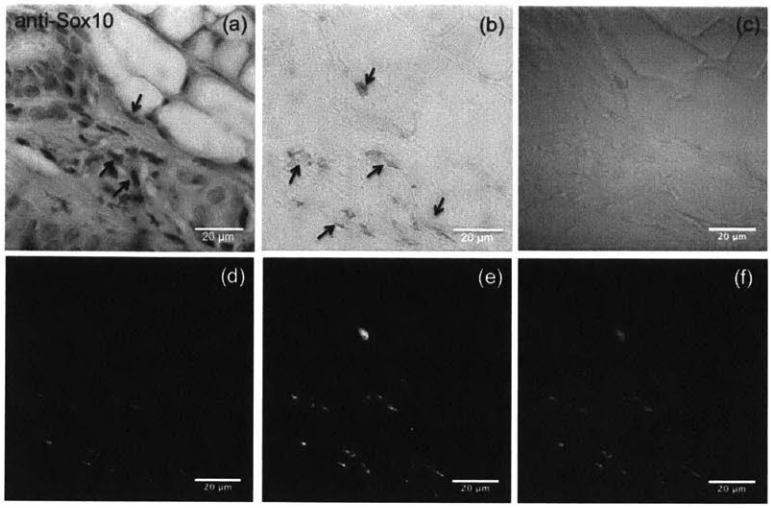

Figure 7-6: Imaging of pheomelanin stores in a red-haired (C57BL/6 ($Mc1r^{e/e}$, $Tyr^{+/+}$) mouse ear section (5 μm thickness). (a) Immunohistochemical stain of the mouse ear slide using anti-Sox-10 antibody (counterstain: haematoxylin), revealing melanocytes in red, some of which are indicated by black arrows for added clarity. (b) Image of an adjacent unstained 5 μm thick slide under brightfield illumination, revealing pheomelanin-rich deposits (shown by black arrows) consistent with the localization of the melanocytes in the adjacent slide shown in (a). (c) Trans-illumination image of the unstained slide shown in (b) acquired with the pump beam set to 861 nm. (d) CARS and (e) SFA images of the unstained slide shown in (b), revealing bright granular signals from pheomelanotic stores consistent with positive staining in (a) and pigmented areas in (b). (f) False-color overlaid image of (d) in green and (e) in red. A CARS image acquired with the pump beam set to 871 nm ($\omega_P - \omega_S = 1866$ cm^{-1}) was subtracted from the image acquired with the pump beam set to 861 nm ($\omega_P - \omega_S = 2000$ cm^{-1}) to minimize the non-resonant signal contribution from structures other than pheomelanin.

7.2.4 Pheomelanin Detection in Human Amelanotic Melanoma

With evidence showing that pheomelanin can be non-invasively visualized in synthetic, *in vitro*, *ex vivo*, and *in vivo* settings, we investigated whether pheomelanin could be visualized in human specimens, specifically in the context of amelanotic melanoma. This melanoma subtype is characterized by its lack of traditional brown-black pigmentation upon visual inspection, typically presents as a raised lesion on the skin that is reddish in color, and can easily be misdiagnosed due to its lack of dark pigmentation [265]. While the terminology seemingly implies the lack of any pigmentation, it is unclear whether some amelanotic melanoma lesions actually

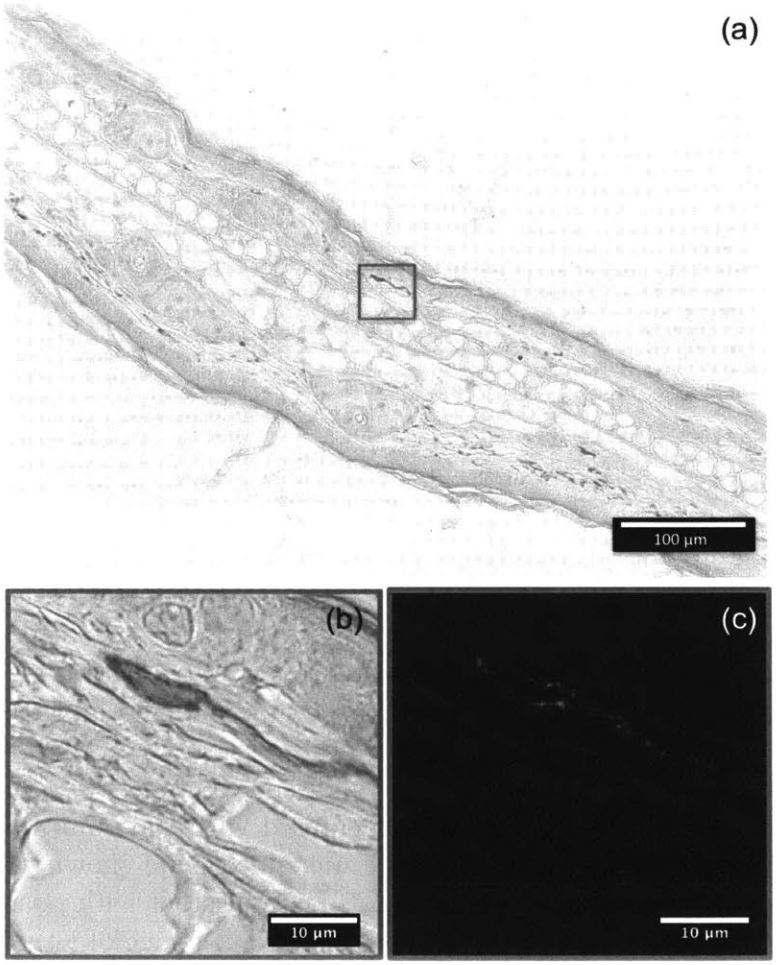

Figure 7-7: Imaging of pheomelanin stores in a red-haired mouse ear section (5 μm thickness). (a) Brightfield trans-illumination image of the haematoxylin-stained mouse ear slide. (b) Magnified view of the area marked by a red square in (a). Pheomelanotic stores are seen as slightly pigmented granules. (c) CARS image of the same field of view as (b), showing bright granular signals from pheomelanotic stores corresponding to the pigmented areas in (b). A CARS image acquired with the pump beam set to 871nm ($\omega_P - \omega_S = 1866$ cm^{-1}) was subtracted from the image acquired with the pump beam set to 861 nm ($\omega_P - \omega_S = 2000$ cm^{-1}) to minimize the non-resonant signal contribution from structures other than pheomelanin.

do harbor stores of pheomelanin that are simply indistinguishable from surrounding healthy skin. Moreover, recent studies [258] have indicated the oncogenic potential of pheomelanin in red-haired and fair-skinned backgrounds, raising the possibility that at least some seemingly unpigmented melanoma lesions may contain pheomelanin, but are undetectable to the naked eye. CARS imaging and spectroscopic measurements were performed on fixed and unstained sections (10 μm in thickness) from three

cutaneous amelanotic melanoma specimens. One such lesion can be seen in Figure 7-8(a) along with its corresponding H&E cross-section. Inspection of normal, healthy perilesional skin with CARS (Figure 7-8(c-e)) did not reveal detectable pheomelanin. Within the amelanotic melanoma lesion, however, strong pheomelanin CARS signals were observed indicating a high density of pheomelanin (representative images shown in Figure 7-8(f-h)). Pheomelanin was ultimately detected in all three patient samples imaged, with representative images from a second patient shown in Figure 7-8(i-k). This suggests that amelanotic melanoma lesions can indeed contain dense stores of pheomelanin, which may be detected non-invasively using CARS imaging.

It should be emphasized that the number of human samples surveyed in this work was limited to three, corresponding to the total number of amelanotic melanoma tissues available for study. In order to truly determine the incidence of pheomelanotic melanoma lesions among those diagnosed as "amelanotic", this proof-of-concept work will have to be expanded into a broader study: one where multiple CARS image stacks taken from a large patient cohort will be processed and statistically analyzed to gain insight that can impact clinical practice.

Indeed, it has been proposed that an intrinsic pheomelanin pathway may represent a biologically significant contributor to melanomagenesis [258]. Building a complete understanding of this contribution, however, has been hampered by an inability to spatially map and quantify pheomelanin within skin. While the detection and differentiation of melanins has been accomplished using pump-probe microscopy [48, 49, 266, 50], measurements of pigments' excited state can be complicated by compounds in the local environment (e.g. metals such as iron). Moreover, distinguishing melanin subtypes using pump-probe microscopy requires the acquisition of so-called "delay stacks", where images are sequentially acquired with varying time delay between the pump and probe beams in order to obtain transient absorption traces on a pixel-by-pixel basis. From there, melanin subtypes can be differentiated using post-processing techniques such as principal component [49] or phasor analyses [50]. However, each frame typically requires an acquisition time of several tens of seconds, leading to a total acquisition period ranging from 5 to 15 minutes for a sin-

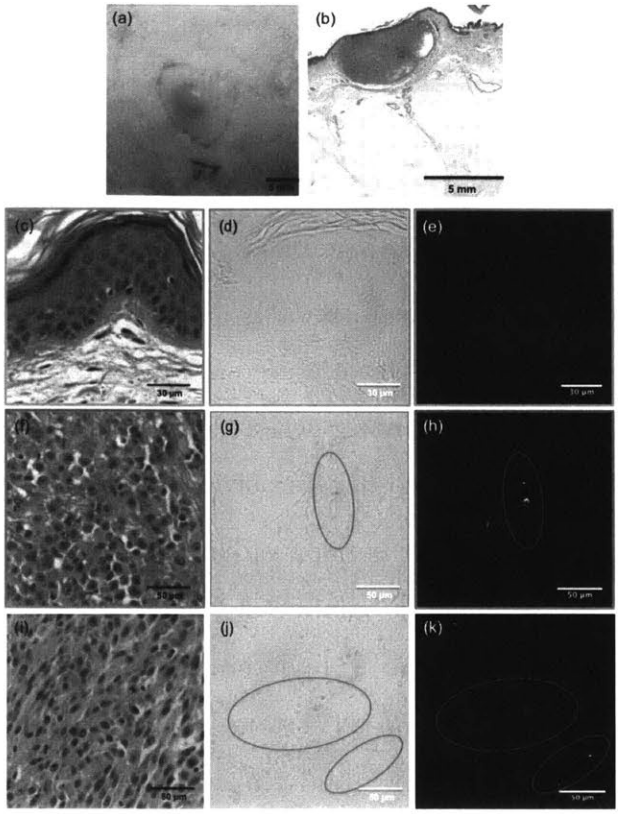

Figure 7-8: Imaging of human amelanotic melanoma. (a) Clinical photograph of one amelanotic melanoma lesion. (b) H&E stain of the patient slide (10× magnification). (c) Perilesional skin showing normal architecture of both epidermis and dermis. (d) Brightfield trans-illumination image acquired from the microscope eyepiece from the perilesional area. (e) CARS image of the same perilesional area compared to (d) (image acquired with pump beam wavelength at 841 nm ($\omega_P - \omega_S = 2275cm^{-1}$) was subtracted from the image acquired with pump beam wavelength at 855 nm ($\omega_P - \omega_S = 2081$ cm^{-1}) to minimize the non-resonant background from structures other than pheomelanin). (f) View of the amelanotic melanoma area showing high density of cells with no obvious sign of melanin. (g) Brightfield trans-illumination image acquired from the microscope eyepiece from an unstained slide of the melanoma area, showing slightly pigmented granular structures (red circle). (h) CARS image of the same tumor area compared to (g), with the same settings as for (e). Saturated bright pheomelanin signals were found (red circle) corresponding to the minimally pigmented region shown in (g). (i,j,k) Respectively H&E, trans-illumination, and CARS images of the tumor area of slides from a second amelanotic melanoma patient. Strong pheomelanin signals were again observed (red circles).

gle delay stack [50]. On the other hand, CARS imaging offers a specific, direct, and facile route for the detection of pheomelanin *in vivo* in real-time, since the detected signal arises from the generation of a new color of light mediated by the pheomelanin

pigment itself. In this regard, CARS microscopy offers many of the same benefits as multiphoton microscopy: the signal can be readily detected using an appropriate set of laser sources and optical filters, and has additionally been shown to operate up to video-rate imaging speeds [267].

Prior investigation of melanin pigments using spontaneous Raman spectroscopy found pheomelanin to harbor three broad vibrational peaks at 500, 1490, and 2000 cm^{-1}, while eumelanin was shown to have peaks at 500, 1380, and 1580 cm^{-1} [260, 261]. The first two peaks of pheomelanin as well as all those of eumelanin are located within the fingerprint region of the Raman spectrum; they are therefore unlikely to offer a straightforward route to highly specific detection of melanin pigment subtypes in the native context of human skin, as vibrational peaks from other chemical species would result in spectral interference. However, in the particular case of pheomelanin, the broad vibrational peak of interest in this study is located in the 2000-2100 cm^{-1} range [260, 261], well within the so-called "silent region" of the Raman spectrum of biological samples [28]. This spectral region, which ranges approximately from 1800 to 2700 cm^{-1}, is devoid of vibrational peaks that may arise from other endogenous biochemical moieties, making this particular band of pheomelanin an ideal target for future clinical CARS imaging with minimal interference from other compounds. It is worth nothing that the use of deuterated chemical groups as Raman reporters may interfere with pheomelanin imaging, as the carbon-deuterium vibrational band is located around 2200 cm^{-1}. In this highly special case, the use of hyperspectral coherent Raman imaging may be used to distinguish the peaks in the event of signal overlap between pheomelanin and deuterated probes. It should also be noted that the unlikely possibility of interference from eumelanin at the 2000-2100 cm^{-1} band was also investigated in the context of this study. Importantly, no coherent Raman signals could be detected from eumelanin within the pheomelanin Raman band range (data not shown), further strengthening the specificity of CARS for the direct visualization of pheomelanin without interference from its eumelanin counterpart.

In this work, the use of multiple genetically controlled systems, including the Mc1r mutant mice and their corresponding albino/red-haired controls ($Mc1r^{e/e}$, $Tyr^{c/c}$),

enabled confirmation of the CARS signal as specifically arising from pheomelanin since these animal models are incapable of producing eumelanin [258]. Interestingly, the strength of the observed anti-Stokes signal was far greater than anticipated based on the previously published spontaneous Raman scattering data [260, 261], indicating the possibility that the observed signal is resonantly enhanced [28].

Furthermore, for future work in translating this imaging modality for clinical studies, CARS microscopy has even been performed using a single laser source, where one portion of the laser light was used as the pump beam, while the remainder was routed through either a tapered fiber [268] or a photonic crystal fiber [269] in order to generate the Stokes beam. This flexibility in terms of optical design in conjunction with the chemical specificity offered by CARS imaging makes it a prime candidate as an imaging tool for future clinical investigations in human patients. In fact, as portable CARS systems are already commercially available [56], the translation of the presented technology for further investigation in research or clinical settings can be immediate and rapid. We believe this imaging approach will aid in improving our biological understanding of skin changes in the context of pheomelanin, including both UV-induced and UV-independent effects. This imaging approach may also help to refine our understanding of which cutaneous lesions are truly "amelanotic" as opposed to those that may be "pheomelanotic" and currently invisible to the naked eye. Additionally, the method may help to define inhomogeneously colored melanocytic or non-melanocytic lesions, whose "unpigmented" regions might contain detectable pheomelanin, and represent challenges in defining surgical margins. The ability to identify such lesions non-invasively and non-destructively will enable future studies investigating the impact of pheomelanin on melanoma formation, pathogenesis and metastasis in different human skin types. The prospect of utilizing this method to detect suspicious, pre-malignant lesions in high-risk (red-haired, fair-skinned) individuals, may offer new diagnostic tools able to translate knowledge from basic science to clinical application.

7.3 Materials and Methods

7.3.1 Mice

Mice with the Mc1r frameshift mutant allele ($Mc1r^{e/e}$) have a phenotype analogous to red-hair/fair-skin in humans (also caused by non-functional alleles of MC1R) [258]. As a control, we crossed these mice to the albino allele ($Mc1r^{e/e}$, $Tyr^{c/c}$), which ablates all melanin pigment production. All mouse strains were maintained on the C57BL/6 background.

7.3.2 CARS Microscopy

The CARS microscope was built over a customized confocal microscope (Olympus FV1000, Center Valley, PA, USA), which has an additional laser entry port to accept external light sources. CARS microscopy was performed using a dual output femtosecond pulsed laser system (Spectra-Physics Insight DeepSee, Santa Clara, CA, USA), where the first output is tunable from 680 to 1300 nm, while the second is fixed at 1040 nm. To achieve CARS imaging at the reported 2000 cm^{-1} band of pheomelanin, the 1040 nm output was chosen as the Stokes beam (ω_S), while the pump beam (ω_P) was set to 861 nm and 855 nm ($\omega_P - \omega_S = 2000cm^{-1}$ and $\omega_P - \omega_S = 2081cm^{-1}$, respectively), in order to generate anti-Stokes signals at 735 nm and 726 nm, respectively. A half-wave plate and a polarizer were placed at each of the two laser output ports of the DeepSee system to adjust beam power. To focus the beams onto the sample, a 1.20 NA 60× water immersion microscope objective (Olympus UPLSAPO 60XW, Center Valley, PA, USA) was used. The CARS signal was detected in the epi-direction using both a shortpass and a bandpass filter (Chroma ET750sp-2p8 and ET730/40m, Bellows Falls, VT, USA) placed in front of a thermoelectrically cooled photomultiplier tube (Hamamatsu H7422PA-50, Hamamatsu City, Japan). The sum power of the two beams at the objective was less than 10 mW for all experiments performed in this study. In order to correct for the non-resonant background signal generated in tissues, both resonant and non-resonant CARS images were obtained in

order to subtract the non-resonant contribution from the resonant CARS images. To this aim, the pump beam was tuned to either 841 nm or 871 nm (resulting in a Raman shift of 2275 cm^{-1} or 1866 cm^{-1}, respectively). In both of these non-resonant imaging settings, the background levels were found to be identical; the choice of tuning the pump beam to 841 nm or 871 nm was therefore simply based on the convenience of the experiment at hand. This correction was not necessary for cellular samples, as the signal detected in the epi-direction contains minimal contribution from back-scattered light and has inherently low non-resonant background [28].

7.3.3 SFA Microscopy

All SFA imaging experiments were performed simultaneously with CARS imaging on the same system as described above, using the same wavelengths and power levels. However, instead of detecting signal in the epi-direction, the SFA detector was placed downstream of the sample in the trans-direction. The 1040 nm beam was modulated at 20 MHz using an electro-optic modulator (ThorLabs EO-AM-R-20-C2, Newton, NJ, USA), and the modulation transfer from the 1040 nm beam to the pump beam was detected using a photodiode coupled to a lock-in amplifier (APE Lock-In Amplifier, Berlin, Germany). In order to restrict the light incident on the SFA detector to only that of the pump beam, a shortpass filter (ThorLabs FES0950, Newton, NJ, USA) was used to eliminate the 1040 nm light. Ordinarily, this detection setup would be sensitive to stimulated Raman scattering (SRS) signals as well. However, it was found that when imaging pheomelanin, the detected signal remained constant across a range spanning 1866 to 2275 cm^{-1}. This observation was additionally confirmed in synthetic pheomelanin samples, which showed the same temporal and wavelength tuning properties as the pheomelanin detected in tissue samples. This suggests that the signals obtained from pheomelanin are primarily a result of its absorptive properties, rather than its intrinsic vibrational modes.

7.3.4 Preparation of Synthetic Pheomelanin

Pheomelanin was synthesized following the protocol published by d'Ischia *et al.* [259]. The synthesized pheomelanin was then lyophilized to yield a dense, reddish-brown powder. To emulsify the pheomelanin, a small quantity (~0.1 mg) was placed in a 2 mL microcentrifuge tube, to which 1 mL H_2O and 0.25 mL hexane were added. The resulting mixture was sonicated for two cycles of three minutes each to generate an emulsion of pheomelanin microparticles. The sample was then sandwiched between a glass slide and a coverslip with an imaging spacer (Grace Bio-Labs Secure-Seal, Bend, OR). To prevent sample evaporation, the edges of the coverslip were sealed to the glass slide with nail polish.

7.3.5 CARS Spectral Data Acquisition and Processing

In order to generate CARS spectra of pheomelanin samples, the pump wavelength was tuned from 841 nm to 871 nm in single nanometer increments. For each wavelength value, 3 images were acquired: the first with only the pump beam, the second with only the Stokes beam, and the third with both. While the first two image sets showed only minimal intensity, they nevertheless corresponded to the weak multiphoton fluorescence of pheomelanin and were thus subtracted from the CARS images to isolate the coherent Raman signal. In order to normalize the CARS signal against a neutral reference, the sample's glass coverslip was also imaged under the same conditions. Glass produces a non-resonant background signal that is invariant across the spectral range of interest, justifying its use as a reference to compensate for wavelength-dependent intensity variations that may arise from the optical components throughout the imaging system.

In order to generate the spectra, the 31 corrected CARS images were first summed together, and the resulting image was binarized to generate a mask. The mask was then applied to all CARS and glass images in order to isolate the regions corresponding to pheomelanin. The masked CARS images were then divided by the masked glass images on a pixel-by-pixel basis, and the resulting ratiometric values were averaged to

obtain a single data point for a given wavelength. This process was iterated across all 31 sampled wavelengths, and the resulting spectra were normalized by the area under the curve and multiplied by a factor of 30 (corresponding to $n-1$ data points) such that a flat spectral response was centered at a normalized value of 1 across the entire spectral range. The experiment was performed in triplicate, where each individual spectrum is plotted in gray and the mean of the three measurements is plotted in red. As an added control, the analysis was repeated for the image background by inverting the binary mask generated earlier. Given that the image background signal arises from the non-resonant background generated by the water and hexane emulsion, the analysis performed on the background revealed a flat spectrum centered at 1, as expected.

7.3.6 Melanocyte Extraction

Two mouse strains were utilized to isolate neonatal cutaneous melanocytes: 1) $Mc1r^{e/e}$: K14-SCFTg+ [258]; Tyr-CreTg+ [262]: B6.Cg-Gt(ROSA) $26Sor^{tm9(CAG-tdTomato)Hze}$/J (Jackson Laboratory catalog #007909) and 2) $Mc1r^{e/e}$: K14-SCFTg+; Tyr-Cre: B6.Cg-Gt(ROSA) $26Sor^{tm6(CAG-ZsGreen1)Hze}$/J (Jackson Laboratory catalog #007906) were used as sources of neonatal pheomelanotic cutaneous melanocytes. The K14-SCF transgene mimics human epidermal expression of SCF and enhances the yield of cutaneous melanocytes [258]. Melanocyte targeted fluorescent tags were generated using the constitutive Tyr:Cre transgene [262]. Neonates (day 2) were euthanized. The truncal skin was peeled away and washed twice with PBS containing Pen:Strep and Fungizone. The skin was then placed in a 60 mm tissue culture dish with 3 mL of dispase (25 mg/mL) and placed in a 37°C, 5% CO_2 incubator for 2 hours. The epidermal layer was peeled away and incubated in another 60 mm tissue culture dish containing 3 mL of 0.25% trypsin for 15 minutes at 37°C. The skin tissue was washed in 10 mL of Hams F10 medium containing 10% FBS, ten times. The cells removed using this procedure were then washed and suspended in PBS that contained DNAse I (50 μg/mL) and 5 mM EDTA. The cells were sorted for the highest expression of either tdTomato or ZsGreen in a BD FACSAria II SORP cell sorter. ZsGreen cells

were excited with a 488 nm laser and detected with a 525/50 nm bandpass filter; tdTomato cells were excited with a 561 nm laser and detected with a 582/15 nm bandpass filter. To confirm the identity of the melanocyte population, the tdTomato cells in another experiment were counterstained with FITC c-Kit, a surface marker for both melanocytes and mast cells. When imaging FACS-isolated cells using CARS microscopy, the presence of fluorescent proteins in the sample (i.e. tdTomato and ZsGreen) sometimes resulted in a background signal generated via two-photon excitation fluorescence from either or both the pump and Stokes lasers. To correct for this, a raw CARS image was first acquired using both lasers; then, two-photon fluorescence images were acquired by using each laser beam individually. The resulting fluorescence images were then subtracted from the raw CARS image in order to isolate the true CARS signal from the sample.

7.3.7 Mouse Ear Imaging

For *ex vivo* mouse ear imaging, the ear tissue was acquired via ear punch (ϕ = 3 mm). A commercial hair removal lotion (Nair, Church & Dwight Co., Inc., Princeton, NJ) was used to remove fine hairs from the ear tissue. The sample was then sandwiched between a coverslip and a glass slide, and imaged as described above. For *in vivo* mouse ear imaging, the mice were anesthetized with isoflurane mixed with 0.2 L/min oxygen and 0.8 L/min air via face mask. Fine hairs were removed using the same hair removal lotion as in the *ex vivo* sample. The ear was then fixed onto a coverslip using double-sided tape, and imaged as described above. All studies and procedures involving animal subjects were approved by the Institutional Animal Care and Use Committee of Massachusetts General Hospital, and were conducted strictly in accordance with the approved animal handling protocols.

Chapter 8

Outlook and Future Perspectives

Nonlinear optical imaging technologies comprise a subset of microscopy tools that have been gaining considerable momentum in terms of their applicability in cancer research over the past couple of decades. Since the first uses of multiphoton fluorescence imaging [9] and coherent Raman scattering microscopy [53], these nonlinear modalities have undergone several generations of technological advancement. The past decade alone has seen considerable efforts on topics ranging from signal processing and algorithm development on the software side, to improved detector design and fiber optic implementation for endoscopic applications on the hardware side.

A variety of biotechnological advances are sure to maintain the forward momentum of these nonlinear optical techniques. One example in the field of coherent Raman scattering is the use of alkyne tags of varying length and isotopic mass, which can be used as CARS and SRS labels due to their sharp characteristic vibrational peaks. With the added benefit of their small relative size, they can be used in a manner that is minimally perturbative to study various biomolecular processes of interest, foregoing the need for bulkier fluorescent reporters [270]. These tagging techniques are of particular interest in the case of pharmacokinetic and pharmacodynamics (PK/PD) studies, where the visualization of small-molecule drugs or the solvents carrier molecules themselves may be of interest. In such contexts, the use of Raman-active tags for CRS imaging may offer a solution that allows for accurate and specific imaging of the compound of interest without significantly altering

its biochemical properties. Another still is in the development of next-generation photoconvertible fluorescent dyes, where efforts are converging on the development of two-photon photoconvertible reporters, which would allow for a high degree of conversion selectivity *in situ* [43].

It is also worth emphasizing the various engineering efforts at institutions that have focused on the acceleration of imaging speed through creative hardware innovations. One exemplary group at MIT has pioneered the application of multiphoton imaging in a wide-field setting using temporal focusing in order to allow for acquisition of three-dimensional datasets in very short periods of time [271]. Such technologies can prove to be a useful tool for *in vivo* monitoring of rapid-timescale biological events such as cancer cell migration in the context of metastasis. Parallel advancements in the field of CRS imaging include the advent of hyperspectral modalities, typically achieved either through spectral focusing or wavelength tuning. With further development in the field of hyperspectral SRS imaging in particular, interpretation of pathology slides may be greatly simplified and rendered possible in the operating room itself, foregoing the need to prepare, stain, and examine samples over the course of days [57]. Indeed, the combination of hyperspectral SRS imaging and machine learning in the image analysis space can offer pathologists an intuitive false-color rendering of the pathological sample, reminiscent of conventional H&E staining. In turn, this familiar visualization would save a considerable amount of time and hospital resources, ultimately benefiting patient health.

The application of these powerful advanced microscopy toolkits to cancer research has taken the nonlinear optical community several decades of combined and complementary effort, and the current results are indeed remarkable. With some of the clinical specificities and sensitivities of Raman technologies exceeding 95% (see 2), their application in the context of cancer research is growing still, with improvements being published every year. Naturally, the next step and perhaps the biggest challenge yet is the widespread adoption and successful translation of these technologies to the clinic.

In order to propel the adoption of these advanced technologies into the therapeutic

work flow, a considerable amount of conscientious effort must be dedicated to the interpretation of the various images that are generated. For example, it cannot be expected of a dermatologist to learn the specifics of fluorescence lifetime imaging in order to develop an intuition for the range of NADH lifetimes within the cells of a suspicious lesion that may be indicative of skin cancer. Similarly, a pathologist cannot be expected to examine the individual Raman spectra of a hyperspectral SRS image set to identify whether the margins of a resected sample are positive. It is in these contexts that clinical research will be of great use in order to develop a large body of reference data that has been validated by pathologists. These datasets can then be used to train machine learning algorithms such that image features and/or diagnostic results can be provided directly to the healthcare professional in order to best guide medical decision-making.

Of course, this is not to say that the outputs of these complex tools must be reduced to a straightforward binary response. However, the current state of imaging complexity in the research space is unlikely to offer informative value to a healthcare professional in a realistic hospital setting. An ideal middle ground, for example, would be to highlight regions of interest within the imaged sample that may be of particular clinical interest. One can also envision complementing these highlighted regions with some probability or other numerical or categorical indicator of disease likelihood. These metrics may then serve the medical team to inform them whether a certain clinical risk is worth taking, when considering the patients overall health status.

All things considered, nonlinear optical technologies are unlikely to bear an impact on clinical work flow unless a variety of biomedical engineering factors are taken into account. These imaging tools must offer clinicians sensitivity and specificity in order for them to obtain as much clinically relevant information as possible, all while maintaining affordability. Furthermore, they must operate at rapid acquisition speeds; tools like FLIM, for example, require several minutes of imaging time, which may be prohibitively long in some clinical contexts. Finally, once the data is acquired, the analysis and interpretation must be performed at a similarly rapid pace in a manner

that informs the medical staff and guides their decision-making, rather than providing a direct diagnosis or medical recommendation. Investing in both technological advancements of imaging hardware as well as next-generation image analysis using machine learning and artificial intelligence are likely to accelerate the adoption of advanced microscopy technologies in the clinical space, contributing the improved patient care, survivability, and well-being.

Appendix A

MATLAB Scripts and Functions

A.1 Simulation of Binary Mixture

```
1  %---Initializations
2  close all;
3  clear all;
4  clc;
5
6  saveFiles = 0;  %Flag determining whether or not files are
       saved
7  saveFig = 0;    %Flag determining whether or not figures are
       saved
8  tic;            %Start timer
9
10 %---Define simulation parameters
11 numPixelsY = 512;
12 numPixelsX = numPixelsY;
13
14 %---Photons per pixel: 1000
15 tau_error = 0.05;
```

```
16 tauTheoretical_A = 2.5E-9;                          %Coumarin 6
17 tauSigma_A = tau_error*tauTheoretical_A;
18 tauTheoretical_B = 1E-9*[0.77  1.21  3.71  4.78];   %NADH
19 tauSigma_B = tau_error*tauTheoretical_B;
20 alpha_error = 0.15;
21 alpha1_B = 0.15;
22 alpha1_sigma_B = alpha_error*alpha1_B;
23 alpha1_Image_B = alpha1_B + alpha1_sigma_B*randn(numPixelsY,
       numPixelsX);
24 alpha2_B = 0.25;
25 alpha2_sigma_B = alpha_error*alpha2_B;
26 alpha2_Image_B = alpha2_B + alpha2_sigma_B*randn(numPixelsY,
       numPixelsX);
27 alpha3_B = 0.35;
28 alpha3_sigma_B = alpha_error*alpha3_B;
29 alpha3_Image_B = alpha3_B + alpha3_sigma_B*randn(numPixelsY,
       numPixelsX);
30 alpha4_B = 0.25;
31 alpha4_sigma_B = alpha_error*alpha4_B;
32 alpha4_Image_B = alpha4_B + alpha4_sigma_B*randn(numPixelsY,
       numPixelsX);
33 totalNumPhotonsSignal = 1000;
34
35 %---Define number of spurious noise photons
36 totalnumPhotonsNoise_A = 0;      %Set noise to 0 for compound
       A
37 photonCountImageNoise_A = totalnumPhotonsNoise_A*ones(
       numPixelsY,numPixelsX);
38 totalnumPhotonsNoise_B = 0;      %Set noise to 0 for compound
       B
```

```
39 photonCountImageNoise_B = totalnumPhotonsNoise_B*ones(
       numPixelsY,numPixelsX);
40 totalnumPhotonsNoise_Mix = 0;    %Set noise to 0 for mixture
41 photonCountImageNoise_Mix = totalnumPhotonsNoise_Mix*ones(
       numPixelsY,numPixelsX);
42
43 %--Mixture generation following sin^2 and cos^2 distributions
44 x = linspace(0,pi,numPixelsX);                %Define support
       vector
45 conc_A = repmat(sin(x).^2,[numPixelsY,1]);  %Define
       distribution of A
46 conc_B = repmat(cos(x).^2,[numPixelsY,1]);  %Define
       distribution of B
47 cmap_A = hot(512);                           %Colormap for A (
       red hot)
48 cmap_B = fliplr(cmap_A);                     %Colormap for B (
       cyan hot)
49
50 %--Display theoretical concentration maps of A and B
51 f21 = figure;
52 imagesc(conc_A,[0  1]);
53 colormap(cmap_A);
54 colorbar;
55 axis image;
56 title('Theoretical Concentration Map of Compound A');
57 f31 = figure;
58 imagesc(conc_B,[0  1]);
59 colormap(cmap_B);
60 colorbar;
61 axis image;
```

```
62 title('Theoretical Concentration Map of Compound B');
63
64 %--Save figures, if specified
65 if saveFig
66     saveas(f21,['ConcentrationMapA_Theoretical_' num2str(
       numPixelsY) ...
67         'px' num2str(totalNumPhotonsSignal) 'ph.tif']);
68     saveas(f31,['ConcentrationMapB_Theoretical_' num2str(
       numPixelsY) ...
69         'px' num2str(totalNumPhotonsSignal) 'ph.tif']);
70 end
71
72 %--Set phasor transform and histogram parameters
73 harmonicNumber = 1;
74 steps = 0.0025;
75 freq0 = 80E6;
76 histogramThreshold = 0.001;
77 cmap = 'jet';
78 drawEllipse_A = 0;
79 drawIntercepts_A = 0;
80 drawEllipse_B = 0;
81 drawIntercepts_B = 0;
82 drawEllipse_Mix = 0;
83 drawIntercepts_Mix = 0;
84 numSpecies_A = 1;
85 numSpecies_B = 1;
86 numSpecies_Mix = 2;
87
88 %--Set image parameters
89 imageParameters_A = default_imageParameters(tauTheoretical_A)
```

```
    ;
90  imageParameters_A.tau_sigma = tauSigma_A;    %Compound A
    lifetime uncertainty
91  imageParameters_A.display = 1;               %Flag for
    displaying computation progress
92  plots_A.G = zeros(numPixelsY,numPixelsX);    %Initialize G-
    array for A
93  plots_A.S = plots_A.G;                       %Initialize S-
    array for A
94  imageParameters_B = default_imageParameters(tauTheoretical_B)
    ;
95  imageParameters_B.tau_sigma = tauSigma_B;    %Compound B
    lifetime uncertainty
96  imageParameters_B.display = 1;               %Flag for
    displaying computation progress
97  plots_B.G = zeros(numPixelsY,numPixelsX);    %Initialize G-
    array for B
98  plots_B.S = plots_B.G;                       %Initialize S-
    array for B
99  imageParameters_Mix = default_imageParameters([
    tauTheoretical_A ...
100      tauTheoretical_B]);
101 imageParameters_Mix.tau_sigma = [imageParameters_A.tau_sigma
    ...
102      imageParameters_B.tau_sigma];           %Compound A and B
         lifetime uncertainties
103 imageParameters_Mix.display = 1;             %Flag for
    displaying computation progress
104 plots_Mix.G = zeros(numPixelsY,numPixelsX); %Initialize G-
    array for mixture
```

```
105 plots_Mix.S = plots_Mix.G;                    %Initialize S-
    array for mixture
106
107 photonCountImageSignal_A = totalNumPhotonsSignal*...
108     ones(numPixelsY,numPixelsX);                %Create
        reference intensity image A
109 decayImage_A = simulateDecayImage(photonCountImageSignal_A
    ,...
110     photonCountImageNoise_A,imageParameters_A); %Create decay
        image A
111 photonCountImageSignal_B = round(totalNumPhotonsSignal*cat
    (3,...
112     alpha1_Image_B,alpha2_Image_B,...
113     alpha3_Image_B,alpha4_Image_B)); %Create reference
        intensity image B
114 decayImage_B = simulateDecayImage(photonCountImageSignal_B
    ,...
115     photonCountImageNoise_B,imageParameters_B); %Create decay
        image B
116 photonCountImageSignal_Mix = round(totalNumPhotonsSignal*cat
    (3,...
117     conc_A,conc_B.*alpha1_Image_B,conc_B.*alpha2_Image_B,...
118     conc_B.*alpha3_Image_B,conc_B.*alpha4_Image_B)); %Create
        overlaid mixture intensity image
119 photonCountImageSignal_sum_Mix = sum(
    photonCountImageSignal_Mix,3); %Create mixture intensity
    image
120 decayImage_Mix = simulateDecayImage(
    photonCountImageSignal_Mix,...
121     photonCountImageNoise_Mix,imageParameters_Mix); %Create
```

```
        mixture decay image
%%
%---Compute phasor transforms for all 3 decay images
for m = 1:numPixelsY
    for n = 1:numPixelsX
        decayPixel = phasorTransform(decayImage_A(m,n),
            harmonicNumber);
        plots_A.G(m,n) = decayPixel.G;
        plots_A.S(m,n) = decayPixel.S;
        clear decayPixel;
        decayPixel = phasorTransform(decayImage_B(m,n),
            harmonicNumber);
        plots_B.G(m,n) = decayPixel.G;
        plots_B.S(m,n) = decayPixel.S;
        clear decayPixel;
        decayPixel = phasorTransform(decayImage_Mix(m,n),
            harmonicNumber);
        plots_Mix.G(m,n) = decayPixel.G;
        plots_Mix.S(m,n) = decayPixel.S;
        clear decayPixel;
    end
end

%---Generate phasor plots for all sets of transformed decay
    images
tau_A = phasorPlot(plots_A.G, plots_A.S,...
    harmonicNumber, steps, freq0, histogramThreshold, cmap,...
    drawEllipse_A, drawIntercepts_A, numSpecies_A);
f11 = gcf;
title('Phasor Plot of Compound A');
```

```
147 tau_B = phasorPlot(plots_B.G, plots_B.S, ...
148     harmonicNumber, steps, freq0, histogramThreshold, cmap, ...
149     drawEllipse_B, drawIntercepts_B, numSpecies_B);
150 f12 = gcf;
151 title('Phasor Plot of Compound B');
152 [tau_MixB, tau_MixA] = phasorPlot(plots_Mix.G, plots_Mix.S, ...
153     harmonicNumber, steps, freq0, histogramThreshold, cmap, ...
154     drawEllipse_Mix, drawIntercepts_Mix, numSpecies_Mix);
155 f13 = gcf;
156 title('Phasor Plot of Mixture');
157
158 %--Save figures, if specified
159 if saveFig
160     saveas(f11, ['PhasorPlot_A_' num2str(numPixelsY) ...
161         'px' num2str(totalNumPhotonsSignal) 'ph.tif']);
162     saveas(f12, ['PhasorPlot_B_' num2str(numPixelsY) ...
163         'px' num2str(totalNumPhotonsSignal) 'ph.tif']);
164     saveas(f13, ['PhasorPlot_Mixture_' num2str(numPixelsY) ...
165         'px' num2str(totalNumPhotonsSignal) 'ph.tif']);
166 end
167
168 %--Reformat phasor coordinate arrays into column vectors
169 plots_A.G = reshape(plots_A.G, [numel(plots_A.G) 1]);
170 plots_A.S = reshape(plots_A.S, [numel(plots_A.S) 1]);
171 plots_A.Z = [plots_A.G, plots_A.S];
172 plots_B.G = reshape(plots_B.G, [numel(plots_B.G) 1]);
173 plots_B.S = reshape(plots_B.S, [numel(plots_B.S) 1]);
174 plots_B.Z = [plots_B.G, plots_B.S];
175 plots_Mix.G = reshape(plots_Mix.G, [numel(plots_Mix.G) 1]);
176 plots_Mix.S = reshape(plots_Mix.S, [numel(plots_Mix.S) 1]);
```

```
177 plots_Mix.Z = [plots_Mix.G, plots_Mix.S];
178
179 %--Compute Euclidean distances between Z arrays
180 ed_MixB = sqrt(sum((plots_Mix.Z - mean(plots_B.Z)).^2,2));
181 ed_MixA = sqrt(sum((plots_Mix.Z - mean(plots_A.Z)).^2,2));
182
183 %--Compute k-arrays associated with Euclidean distances
      calculated above
184 %Mixture
185 k_ed_MixA = reshape(ed_MixA./(ed_MixA+ed_MixB),[numPixelsY
      numPixelsX]);
186 k_ed_MixB = reshape(ed_MixB./(ed_MixA+ed_MixB),[numPixelsY
      numPixelsX]);
187
188 %--Compute Mahalanobis distances between Z arrays
189 md_MixB = sqrt(mahal(plots_Mix.Z, plots_B.Z));
190 md_AB_Ref = sqrt(mahal(mean(plots_A.Z), plots_B.Z));
191 md_MixA = sqrt(mahal(plots_Mix.Z, plots_A.Z));
192 md_BA_Ref = sqrt(mahal(mean(plots_B.Z), plots_A.Z));
193
194 %--Compute k-arrays associated with Mahalanobis distances
      calculated above
195 %Mixture
196 k_md_MixA0 = md_MixA/md_BA_Ref;
197 k_md_MixB0 = md_MixB/md_AB_Ref;
198 k_md_MixA = (k_md_MixA0 + (1-k_md_MixB0))/2;
199 k_md_MixB = (k_md_MixB0 + (1-k_md_MixA0))/2;
200
201 k_md_MixA(k_md_MixA > 1) = 1;
202 k_md_MixA(k_md_MixA < 0) = 0;
```

```
203 k_md_MixA = reshape(k_md_MixA,[numPixelsY numPixelsX]);
204
205 k_md_MixB(k_md_MixB > 1) = 1;
206 k_md_MixB(k_md_MixB < 0) = 0;
207 k_md_MixB = reshape(k_md_MixB,[numPixelsY numPixelsX]);
208
209 %--Display computed distribution estimates images
210 %Mahalanobis map of compound A in Mixture image
211 f22 = figure;imagesc(k_md_MixB,[0 1]);axis image;colormap(
      cmap_A);colorbar;
212 title('Mahalanobis Concentration Map of Compound A');
213 %Mahalanobis map of compound B in Mixture image
214 f32 = figure;imagesc(k_md_MixA,[0 1]);axis image;colormap(
      cmap_B);colorbar;
215 title('Mahalanobis Concentration Map of Compound B');
216 %Euclidean map of compound A in Mixture image
217 f23 = figure;imagesc(k_ed_MixB,[0 1]);axis image;colormap(
      cmap_A);colorbar;
218 title('Euclidean Concentration Map of Compound A');
219 %Euclidean map of compound B in Mixture image
220 f33 = figure;imagesc(k_ed_MixA,[0 1]);axis image;colormap(
      cmap_B);colorbar;
221 title('Euclidean Concentration Map of Compound B');
222
223 %--Save figures, if specified
224 if saveFig
225     saveas(f22,['ConcentrationMapA_Mahalanobis_' num2str(
          numPixelsY) ...
226         'px' num2str(totalNumPhotonsSignal) 'ph.tif']);
227     saveas(f32,['ConcentrationMapB_Mahalanobis_' num2str(
```

```
        numPixelsY) ...
228         'px' num2str(totalNumPhotonsSignal) 'ph.tif']);
229     saveas(f23,['ConcentrationMapA_Euclidean_' num2str(
        numPixelsY) ...
230         'px' num2str(totalNumPhotonsSignal) 'ph.tif']);
231     saveas(f33,['ConcentrationMapB_Euclidean_' num2str(
        numPixelsY) ...
232         'px' num2str(totalNumPhotonsSignal) 'ph.tif']);
233 end
234
235 %Column-wise means of compound A in Mixture image
236 f41 = figure;
237 plot(1:numPixelsX,sin(x).^2,'k','LineWidth',1.5); hold on;
238 plot(1:numPixelsX,mean(k_md_MixB),'r:','LineWidth',3);
239 plot(1:numPixelsX,mean(k_ed_MixB),'b:','LineWidth',3);
240 xlabel('Column Index');
241 ylabel('Relative Concentration');
242 xlim([1 numPixelsX]);
243 ylim([-0.1 1.1]);
244 title('Column-wise Means of Compound A Contribution');
245 legend('Simulation','Mahalanobis','Euclidean','Location','
    NorthEast');
246
247 %Column-wise means of compound B in Mixture image
248 f42 = figure;
249 plot(1:numPixelsX,cos(x).^2,'k','LineWidth',1.5); hold on;
250 plot(1:numPixelsX,mean(k_md_MixA),'r:','LineWidth',3);
251 plot(1:numPixelsX,mean(k_ed_MixA),'b:','LineWidth',3);
252 xlabel('Column Index');
253 ylabel('Relative Concentration');
```

```
254 xlim([1 numPixelsX]);
255 ylim([-0.1 1.1]);
256 title('Column-wise Means of Compound B Contribution');
257 legend('Simulation','Mahalanobis','Euclidean','Location','
      SouthEast');
258
259 %--Save figures, if specified
260 if saveFig
261     saveas(f41,['ColumnWiseMeans_A_' num2str(numPixelsY) ...
262         'px' num2str(totalNumPhotonsSignal) 'ph.tif']);
263     saveas(f42,['ColumnWiseMeans_B_' num2str(numPixelsY) ...
264         'px' num2str(totalNumPhotonsSignal) 'ph.tif']);
265 end
266
267 %--Save workspace, if specified
268 if saveFiles
269     d = datetime;
270     save(['Simulation_' ...
271         num2str(d.Year,'%04.4u') num2str(d.Month,'%02.2u')
              ...
272         num2str(d.Day,'%02.2u') '_' num2str(d.Hour,'%02.2u')
              ...
273         num2str(d.Minute,'%02.2u') '.mat'],'-v7.3');
274 end
275
276 %--Display total elapsed simulation time
277 elapsedTime = toc;
278 fprintf(['\n   Total simulation time: ' ...
279     num2str(floor(elapsedTime/3600),'%02.2u') ':' ...
280     num2str(rem(floor(elapsedTime/60),60),'%02.2u') ':' ...
```

```
281     num2str(rem(round(elapsedTime),60),'%02.2u') '\n' ...
282     '\n    saveFiles = ' num2str(saveFiles) ...
283     '\n    saveFig   = ' num2str(saveFig) ...
284     '\n\n']);
```

A.2 Simulation of Ternary Mixture

```
1  %--Initializations
2  close all;
3  clear all;
4  clc;
5
6  saveFiles = 0;  %Flag determining whether or not files are
       saved
7  saveFig = 0;    %Flag determining whether or not figures are
       saved
8  tic;            %Start timer
9
10 %--Define simulation parameters
11 numPixelsY = 512;
12 numPixelsX = numPixelsY;
13
14 %--Photons per pixel: 1000
15 tau_error = 0.05;
16 tauTheoretical_A = 4.1E-9;
17 tauSigma_A = tau_error*tauTheoretical_A;
18 tauTheoretical_B = 1.6E-9;
19 tauSigma_B = tau_error*tauTheoretical_B;
20 tauTheoretical_C = 0.6E-9;
21 tauSigma_C = tau_error*tauTheoretical_C;
```

```
22 totalNumPhotonsSignal = 1000;
23
24 %--Define number of spurious noise photons
25 totalnumPhotonsNoise_A = 0;      %Set noise to 0 for compound
     A
26 photonCountImageNoise_A = totalnumPhotonsNoise_A*ones(
     numPixelsY,numPixelsX);
27 totalnumPhotonsNoise_B = 0;      %Set noise to 0 for compound
     B
28 photonCountImageNoise_B = totalnumPhotonsNoise_B*ones(
     numPixelsY,numPixelsX);
29 totalnumPhotonsNoise_C = 0;      %Set noise to 0 for compound
     B
30 photonCountImageNoise_C = totalnumPhotonsNoise_C*ones(
     numPixelsY,numPixelsX);
31 totalnumPhotonsNoise_Mix = 0;    %Set noise to 0 for mixture
32 photonCountImageNoise_Mix = totalnumPhotonsNoise_Mix*ones(
     numPixelsY,numPixelsX);
33
34 %--Mixture generation following 3 phase-shifted cosine
     functions
35 x = linspace(0,2*pi,numPixelsX);     %Define support vector
36 y1 = (1+cos(x))/2;
37 y2 = (1+cos(x+2*pi/3))/2;
38 y3 = (1+cos(x-2*pi/3))/2;
39 yy1 = y1./(y1+y2+y3);
40 yy2 = y2./(y1+y2+y3);
41 yy3 = y3./(y1+y2+y3);
42 conc_A = repmat(y1,[numPixelsY,1]); %Define distribution of A
43 conc_B = repmat(y2,[numPixelsY,1]); %Define distribution of B
```

```
44 conc_C = repmat(y3,[numPixelsY,1]); %Define distribution of B
45 cmap_A = hot(512);                   %Colormap for A (red hot)
46 cmap_B = circshift(cmap_A,1,2);      %Colormap for B (cyan hot
       )
47 cmap_C = circshift(cmap_A,2,2);      %Colormap for B (magenta
       hot)
48 %%
49 %--Display theoretical concentration maps of A, B, and C
50 f21 = figure;
51 imagesc(repmat(yy1,[numPixelsY,1]),[0  1]);
52 colormap(cmap_A);
53 colorbar;
54 axis image;
55 title('Theoretical Concentration Map of Compound A');
56 f31 = figure;
57 imagesc(repmat(yy2,[numPixelsY,1]),[0  1]);
58 colormap(cmap_B);
59 colorbar;
60 axis image;
61 title('Theoretical Concentration Map of Compound B');
62 f41 = figure;
63 imagesc(repmat(yy3,[numPixelsY,1]),[0  1]);
64 colormap(cmap_C);
65 colorbar;
66 axis image;
67 title('Theoretical Concentration Map of Compound C');
68 %%
69 %--Save figures, if specified
70 if saveFig
71     saveas(f21,'ConcentrationMapA_Theoretical_Tern512px.tif')
```

```
        ;
72      saveas(f31,'ConcentrationMapB_Theoretical_Tern512px.tif')
        ;
73      saveas(f41,'ConcentrationMapC_Theoretical_Tern512px.tif')
        ;
74  end
75
76  %--Set phasor transform and histogram parameters
77  harmonicNumber = 1;
78  steps = 0.0025;
79  freq0 = 80E6;
80  histogramThreshold = 0.001;
81  cmap = 'jet';
82  drawEllipse_A = 0;
83  drawIntercepts_A = 0;
84  drawEllipse_B = 0;
85  drawIntercepts_B = 0;
86  drawEllipse_C = 0;
87  drawIntercepts_C = 0;
88  drawEllipse_Mix = 0;
89  drawIntercepts_Mix = 0;
90  numSpecies_A = 1;
91  numSpecies_B = 1;
92  numSpecies_C = 1;
93  numSpecies_Mix = 2;
94
95  %--Set image parameters
96  imageParameters_A = default_imageParameters(tauTheoretical_A)
    ;
97  imageParameters_A.tau_sigma = tauSigma_A;    %Compound A
```

```
    lifetime uncertainty
98  imageParameters_A.display = 1;                %Flag for
    displaying computation progress
99  plots_A.G = zeros(numPixelsY,numPixelsX);     %Initialize G-
    array for A
100 plots_A.S = plots_A.G;                        %Initialize S-
    array for A
101 imageParameters_B = default_imageParameters(tauTheoretical_B)
    ;
102 imageParameters_B.tau_sigma = tauSigma_B;    %Compound B
    lifetime uncertainty
103 imageParameters_B.display = 1;                %Flag for
    displaying computation progress
104 plots_B.G = zeros(numPixelsY,numPixelsX);     %Initialize G-
    array for B
105 plots_B.S = plots_B.G;                        %Initialize S-
    array for B
106 imageParameters_C = default_imageParameters(tauTheoretical_C)
    ;
107 imageParameters_C.tau_sigma = tauSigma_C;    %Compound C
    lifetime uncertainty
108 imageParameters_C.display = 1;                %Flag for
    displaying computation progress
109 plots_C.G = zeros(numPixelsY,numPixelsX);     %Initialize G-
    array for C
110 plots_C.S = plots_C.G;                        %Initialize S-
    array for C
111 imageParameters_Mix = default_imageParameters([
    tauTheoretical_A ...
112     tauTheoretical_B,tauTheoretical_C]);
```

```
113 imageParameters_Mix.tau_sigma = [imageParameters_A.tau_sigma
    ...
114     imageParameters_B.tau_sigma,imageParameters_C.tau_sigma];
            %Compound A, B, C uncertainties
115 imageParameters_Mix.display = 1;              %Flag for
    displaying computation progress
116 plots_Mix.G = zeros(numPixelsY,numPixelsX); %Initialize G-
    array for mixture
117 plots_Mix.S = plots_Mix.G;                   %Initialize S-
    array for mixture
118
119 photonCountImageSignal_A = totalNumPhotonsSignal*...
120     ones(numPixelsY,numPixelsX);                %Create
        reference intensity image A
121 decayImage_A = simulateDecayImage(photonCountImageSignal_A
    ,...
122     photonCountImageNoise_A,imageParameters_A); %Create decay
         image A
123 photonCountImageSignal_B = totalNumPhotonsSignal*...
124     ones(numPixelsY,numPixelsX);                %Create
        reference intensity image B
125 decayImage_B = simulateDecayImage(photonCountImageSignal_B
    ,...
126     photonCountImageNoise_B,imageParameters_B); %Create decay
         image B
127 photonCountImageSignal_C = totalNumPhotonsSignal*...
128     ones(numPixelsY,numPixelsX);                %Create
        reference intensity image C
129 decayImage_C = simulateDecayImage(photonCountImageSignal_C
    ,...
```

```
130      photonCountImageNoise_C, imageParameters_C); %Create decay
             image C
131 photonCountImageSignal_Mix = round(totalNumPhotonsSignal*cat
    (3,...
132      conc_A, conc_B, conc_C));                    %Create
         overlaid mixture intensity image
133 photonCountImageSignal_sum_Mix = sum(
    photonCountImageSignal_Mix,3); %Create mixture intensity
    image
134 decayImage_Mix = simulateDecayImage(
    photonCountImageSignal_Mix,...
135      photonCountImageNoise_Mix, imageParameters_Mix); %Create
         mixture decay image
136
137 %--Compute phasor transforms for all 3 decay images
138 for m = 1:numPixelsY
139      for n = 1:numPixelsX
140          decayPixel = phasorTransform(decayImage_A(m,n),
                 harmonicNumber);
141          plots_A.G(m,n) = decayPixel.G;
142          plots_A.S(m,n) = decayPixel.S;
143          clear decayPixel;
144          decayPixel = phasorTransform(decayImage_B(m,n),
                 harmonicNumber);
145          plots_B.G(m,n) = decayPixel.G;
146          plots_B.S(m,n) = decayPixel.S;
147          clear decayPixel;
148          decayPixel = phasorTransform(decayImage_C(m,n),
                 harmonicNumber);
149          plots_C.G(m,n) = decayPixel.G;
```

```
150             plots_C.S(m,n) = decayPixel.S;
151             clear decayPixel;
152             decayPixel = phasorTransform(decayImage_Mix(m,n),
                    harmonicNumber);
153             plots_Mix.G(m,n) = decayPixel.G;
154             plots_Mix.S(m,n) = decayPixel.S;
155             clear decayPixel;
156         end
157 end
158
159 %--Generate phasor plots for all sets of transformed decay
        images
160 tau_A = phasorPlot(plots_A.G, plots_A.S,...
161         harmonicNumber, steps, freq0, histogramThreshold, cmap,...
162         drawEllipse_A, drawIntercepts_A, numSpecies_A);
163 f11 = gcf;
164 title('Phasor Plot of Compound A');
165 tau_B = phasorPlot(plots_B.G, plots_B.S,...
166         harmonicNumber, steps, freq0, histogramThreshold, cmap,...
167         drawEllipse_B, drawIntercepts_B, numSpecies_B);
168 f12 = gcf;
169 title('Phasor Plot of Compound B');
170 tau_C = phasorPlot(plots_C.G, plots_C.S,...
171         harmonicNumber, steps, freq0, histogramThreshold, cmap,...
172         drawEllipse_C, drawIntercepts_C, numSpecies_C);
173 f13 = gcf;
174 title('Phasor Plot of Compound C');
175 [tau_Mix1, tau_Mix2] = phasorPlot(plots_Mix.G, plots_Mix.S,...
176         harmonicNumber, steps, freq0, histogramThreshold, cmap,...
177         drawEllipse_Mix, drawIntercepts_Mix, numSpecies_Mix);
```

```
178 f14 = gcf;
179 title('Phasor Plot of Mixture');
180
181 %--Save figures, if specified
182 if saveFig
183     saveas(f11,'PhasorPlot_A_Tern512px.tif');
184     saveas(f12,'PhasorPlot_B_Tern512px.tif');
185     saveas(f13,'PhasorPlot_C_Tern512px.tif');
186     saveas(f14,'PhasorPlot_Mixture_Tern512px.tif');
187 end
188
189 %--Reformat phasor coordinate arrays into column vectors
190 plots_A.G = reshape(plots_A.G,[numel(plots_A.G) 1]);
191 plots_A.S = reshape(plots_A.S,[numel(plots_A.S) 1]);
192 plots_A.Z = [plots_A.G,plots_A.S];
193 plots_B.G = reshape(plots_B.G,[numel(plots_B.G) 1]);
194 plots_B.S = reshape(plots_B.S,[numel(plots_B.S) 1]);
195 plots_B.Z = [plots_B.G,plots_B.S];
196 plots_C.G = reshape(plots_C.G,[numel(plots_C.G) 1]);
197 plots_C.S = reshape(plots_C.S,[numel(plots_C.S) 1]);
198 plots_C.Z = [plots_C.G,plots_C.S];
199 plots_Mix.G = reshape(plots_Mix.G,[numel(plots_Mix.G) 1]);
200 plots_Mix.S = reshape(plots_Mix.S,[numel(plots_Mix.S) 1]);
201 plots_Mix.Z = [plots_Mix.G,plots_Mix.S];
202
203 %--Compute Euclidean triangular areas
204 A_ref.G = mean(plots_A.G(:));
205 B_ref.G = mean(plots_B.G(:));
206 C_ref.G = mean(plots_C.G(:));
207 A_ref.S = mean(plots_A.S(:));
```

```
208 B_ref.S = mean(plots_B.S(:));
209 C_ref.S = mean(plots_C.S(:));
210 refArea = polyarea([A_ref.G B_ref.G C_ref.G],[A_ref.S B_ref.S
        C_ref.S]);
211
212 k_ed_A = zeros(size(plots_A.G));
213 k_ed_B = k_ed_A;
214 k_ed_C = k_ed_A;
215
216 for p = 1:numel(k_ed_A)
217     k_ed_A(p) = polyarea([plots_Mix.G(p) B_ref.G C_ref.G],...
218         [plots_Mix.S(p) B_ref.S C_ref.S])/refArea;
219     k_ed_B(p) = polyarea([A_ref.G plots_Mix.G(p) C_ref.G],...
220         [A_ref.S plots_Mix.S(p) C_ref.S])/refArea;
221     k_ed_C(p) = polyarea([A_ref.G B_ref.G plots_Mix.G(p)],...
222         [A_ref.S B_ref.S plots_Mix.S(p)])/refArea;
223 end
224
225 k_ed_A = reshape(k_ed_A,[numPixelsY numPixelsX]);
226 k_ed_B = reshape(k_ed_B,[numPixelsY numPixelsX]);
227 k_ed_C = reshape(k_ed_C,[numPixelsY numPixelsX]);
228
229 %---Display computed distribution estimates images
230 %Euclidean map of compound A in Mixture image
231 f23 = figure;imagesc(k_ed_A,[0 1]);axis image;colormap(cmap_A
      );colorbar;
232 title('Euclidean Concentration Map of Compound A');
233 %Euclidean map of compound B in Mixture image
234 f33 = figure;imagesc(k_ed_B,[0 1]);axis image;colormap(cmap_B
      );colorbar;
```

```
235 title('Euclidean Concentration Map of Compound B');
236 %Euclidean map of compound B in Mixture image
237 f43 = figure;imagesc(k_ed_C,[0 1]);axis image;colormap(cmap_C
    );colorbar;
238 title('Euclidean Concentration Map of Compound C');
239
240 %---Save figures, if specified
241 if saveFig
242     saveas(f23,'ConcentrationMapA_Euclidean_Tern512px.tif');
243     saveas(f33,'ConcentrationMapB_Euclidean_Tern512px.tif');
244     saveas(f43,'ConcentrationMapC_Euclidean_Tern512px.tif');
245 end
246
247 %%
248 %---Compute Mahalanobis distances between Z arrays
249 plots_A.Zmean = mean(plots_A.Z);
250 plots_B.Zmean = mean(plots_B.Z);
251 plots_C.Zmean = mean(plots_C.Z);
252
253 md_MixA = sqrt(mahal(plots_Mix.Z,plots_A.Z));
254 md_MixB = sqrt(mahal(plots_Mix.Z,plots_B.Z));
255 md_MixC = sqrt(mahal(plots_Mix.Z,plots_C.Z));
256
257 k_md_A = zeros(size(plots_A.G));
258 k_md_B = k_md_A;
259 k_md_C = k_md_A;
260
261 for p = 1:numel(k_md_A)
262     m_MixA = (plots_Mix.S(p)-plots_A.Zmean(2))/(plots_Mix.G(p
        )-plots_A.Zmean(1));
```

```
263     b_MixA = plots_A.Zmean(2) - m_MixA*plots_A.Zmean(1);
264     m_BC = (plots_B.Zmean(2)-plots_C.Zmean(2))/(plots_B.Zmean
            (1)-plots_C.Zmean(1));
265     b_BC = plots_B.Zmean(2) - m_BC*plots_B.Zmean(1);
266     Y_MixA_BC = @(g) m_MixA*g + b_MixA - (m_BC*g + b_BC);
267     R_BC.G = fzero(Y_MixA_BC,0.5);
268     R_BC.S = Y_MixA_BC(R_BC.G);
269     R_BC.Z = [R_BC.G R_BC.S];
270     md_R_BC = sqrt(mahal(R_BC.Z,plots_A.Z));
271     k_md_A(p) = 1 - md_MixA(p)/md_R_BC;
272
273     m_MixB = (plots_Mix.S(p)-plots_B.Zmean(2))/(plots_Mix.G(p
            )-plots_B.Zmean(1));
274     b_MixB = plots_B.Zmean(2) - m_MixB*plots_B.Zmean(1);
275     m_AC = (plots_A.Zmean(2)-plots_C.Zmean(2))/(plots_A.Zmean
            (1)-plots_C.Zmean(1));
276     b_AC = plots_A.Zmean(2) - m_AC*plots_A.Zmean(1);
277     Y_MixB_AC = @(g) m_MixB*g + b_MixB - (m_AC*g + b_AC);
278     R_AC.G = fzero(Y_MixB_AC,0.5);
279     R_AC.S = Y_MixB_AC(R_AC.G);
280     R_AC.Z = [R_AC.G R_AC.S];
281     md_R_AC = sqrt(mahal(R_AC.Z,plots_B.Z));
282     k_md_B(p) = 1 - md_MixB(p)/md_R_AC;
283
284     m_MixC = (plots_Mix.S(p)-plots_C.Zmean(2))/(plots_Mix.G(p
            )-plots_C.Zmean(1));
285     b_MixC = plots_C.Zmean(2) - m_MixC*plots_C.Zmean(1);
286     m_AB = (plots_A.Zmean(2)-plots_B.Zmean(2))/(plots_A.Zmean
            (1)-plots_B.Zmean(1));
287     b_AB = plots_A.Zmean(2) - m_AB*plots_A.Zmean(1);
```

```
288         Y_MixC_AB = @(g) m_MixC*g + b_MixC - (m_AB*g + b_AB);
289         R_AB.G = fzero(Y_MixC_AB,0.5);
290         R_AB.S = Y_MixC_AB(R_AB.G);
291         R_AB.Z = [R_AB.G R_AB.S];
292         md_R_AB = sqrt(mahal(R_AB.Z, plots_C.Z));
293         k_md_C(p) = 1 - md_MixC(p)/md_R_AB;
294     end
295     %%
296     k_md_A = reshape(k_md_A,[numPixelsY numPixelsX]);
297     k_md_B = reshape(k_md_B,[numPixelsY numPixelsX]);
298     k_md_C = reshape(k_md_C,[numPixelsY numPixelsX]);
299
300     %---Display computed distribution estimates images
301     %Mahalanobis map of compound A in Mixture image
302     f22 = figure;imagesc(k_md_A,[0 1]);axis image;colormap(cmap_A
            );colorbar;
303     title('Mahalanobis Concentration Map of Compound A');
304     %Mahalanobis map of compound B in Mixture image
305     f32 = figure;imagesc(k_md_B,[0 1]);axis image;colormap(cmap_B
            );colorbar;
306     title('Mahalanobis Concentration Map of Compound B');
307     %Mahalanobis map of compound B in Mixture image
308     f42 = figure;imagesc(k_md_C,[0 1]);axis image;colormap(cmap_C
            );colorbar;
309     title('Mahalanobis Concentration Map of Compound C');
310
311     %---Save figures, if specified
312     if saveFig
313         saveas(f22,'ConcentrationMapA_Mahalanobis_Tern512px.tif')
                ;
```

```
314     saveas(f32,'ConcentrationMapB_Mahalanobis_Tern512px.tif')
            ;
315     saveas(f42,'ConcentrationMapC_Mahalanobis_Tern512px.tif')
            ;
316 end
317
318 %%
319 %Column-wise means of compound A in Mixture image
320 f51 = figure;
321 plot(1:numPixelsX,yy1,'k','LineWidth',1.5); hold on;
322 plot(1:numPixelsX,mean(k_md_A),'r:','LineWidth',3);
323 plot(1:numPixelsX,mean(k_ed_A),'b:','LineWidth',3);
324 xlabel('Column Index');
325 ylabel('Relative Concentration');
326 xlim([1 numPixelsX]);
327 ylim([-0.1 1.1]);
328 title('Column-wise Means of Compound A Contribution');
329 legend('Simulation','Mahalanobis','Euclidean','Location','
        NorthEast');
330
331 %Column-wise means of compound B in Mixture image
332 f52 = figure;
333 plot(1:numPixelsX,yy2,'k','LineWidth',1.5); hold on;
334 plot(1:numPixelsX,mean(k_md_B),'r:','LineWidth',3);
335 plot(1:numPixelsX,mean(k_ed_B),'b:','LineWidth',3);
336 xlabel('Column Index');
337 ylabel('Relative Concentration');
338 xlim([1 numPixelsX]);
339 ylim([-0.1 1.1]);
340 title('Column-wise Means of Compound B Contribution');
```

```
341 legend('Simulation','Mahalanobis','Euclidean','Location','
      NorthEast');
342
343 %Column-wise means of compound B in Mixture image
344 f53 = figure;
345 plot(1:numPixelsX,yy3,'k','LineWidth',1.5); hold on;
346 plot(1:numPixelsX,mean(k_md_C),'r:','LineWidth',3);
347 plot(1:numPixelsX,mean(k_ed_C),'b:','LineWidth',3);
348 xlabel('Column Index');
349 ylabel('Relative Concentration');
350 xlim([1 numPixelsX]);
351 ylim([-0.1 1.1]);
352 title('Column-wise Means of Compound C Contribution');
353 legend('Simulation','Mahalanobis','Euclidean','Location','
      NorthEast');
354
355 %--Save figures, if specified
356 if saveFig
357     saveas(f51,'ColumnWiseMeans_A_Tern512px.tif');
358     saveas(f52,'ColumnWiseMeans_B_Tern512px.tif');
359     saveas(f53,'ColumnWiseMeans_C_Tern512px.tif');
360 end
361 %%
362 %--Save workspace, if specified
363 if saveFiles
364     d = datetime;
365     save(['Simulation_' ...
366         num2str(d.Year,'%04.4u') num2str(d.Month,'%02.2u')
              ...
367         num2str(d.Day,'%02.2u') '_' num2str(d.Hour,'%02.2u')
```

```
            ...
368         num2str(d.Minute,'%02.2u') '.mat'],'-v7.3');
369 end
370
371 %---Display total elapsed simulation time
372 elapsedTime = toc;
373 fprintf(['\n    Total simulation time: ' ...
374     num2str(floor(elapsedTime/3600),'%02.2u') ':' ...
375     num2str(rem(floor(elapsedTime/60),60),'%02.2u') ':' ...
376     num2str(rem(round(elapsedTime),60),'%02.2u') '\n' ...
377     '\n    saveFiles = ' num2str(saveFiles) ...
378     '\n    saveFig   = ' num2str(saveFig) ...
379     '\n\n']);
```

A.3 MATLAB Functions for Phasor Analysis

A.3.1 Loading Default Simulated Image Parameters

```
1 function imageParameters = default_imageParameters(tau)
2 %default_traceParameters Generate default decay trace
      simulation parameters
3 %   DEFAULT_TRACEPARAMETERS() generates a set of default
      fluorescence decay
4 %   trace parameters given the specified number of
      fluorescence species
5 %   (numExponentials).
6
7     %---If no lifetimes are specified, use default value of 2
          ns
8     if isempty(tau)
9         imageParameters.tau = 2E-9;
```

```
10      %--Otherwise, use lifetimes specified by user
11      elseif isnumeric(tau)
12          imageParameters.tau = tau;
13      %--Check for error in input
14      else
15          error('    ERROR: Input must be empty or numeric
                scalar or array.');
16      end
17
18      %--Reshape lifetime array to row vector
19      imageParameters.tau = reshape(imageParameters.tau,...
20          [1 numel(imageParameters.tau)]);
21      %--Default uncertainty on lifetime value: 0 ns
22      imageParameters.tau_sigma = zeros(size(imageParameters.
            tau));
23      %--Default number of temporal bins: 256
24      imageParameters.numTimeBins = 256;
25      %--Default laser repetition frequency: 80 MHz
26      imageParameters.freq0 = 80E6;
27      %--Boolean value specifying whether a photon detection
            event exceeding
28      %the laser repetition period should be wrapped to the
            next cycle or
29      %redrawn from the Poissonian distribution
30      imageParameters.wrapLongEvents = 1;
31      %--Boolean value specifying whether progress text should
            be displayed
32      imageParameters.display = 0;
33
34      %--Load reference instrument response function (IRF) file
```

```
35      load('IRF_t0_AUC1.mat','IRF','IRF_N');
36      %--IRF and IRF_N are the raw photon counts of the
            instrument response
37      %function as well the number of photons in the IRF trace
38      imageParameters.IRF = IRF;
39      imageParameters.IRF_N = IRF_N;
40      %--Create temporal basis row vector
41      imageParameters.t = (1/(imageParameters.freq0*
            imageParameters.numTimeBins))*...
42           (0:imageParameters.numTimeBins-1);
43      %--Initialize probability distributions with and without
            IRF
44      imageParameters.prob = zeros(length(imageParameters.tau)
            ,...
45           imageParameters.numTimeBins);
46      imageParameters.prob_IRF = imageParameters.prob;
47  end
```

A.3.2 Simulating a Decay Image

```
1   function decayImage = simulateDecayImage(...
2       photonCountImageSignal,photonCountImageNoise,
            imageParameters)
3   %simulateDecayImage Generate a simulated fluorescence decay (
        FLIM) image
4   %   SIMULATEDECAYIMAGE() generates a fluorescence decay trace
        given the number
5   %   of time bins (numTimeBins), the laser repetition
        frequency in Hz (freq0;
6   %   typically 76 MHz or 80 MHz for most ultrafast laser
        sources), the
```

```
7  %   theoretical lifetime (tauTheoretical) in seconds, the
       number of photons
8  %   to be included in the trace (numPhotons), the harmonic
       number of the
9  %   phasor transform (harmonicNumber), and a flag to
       determine whether or
10 %   not events that occur with an arrival time exceeding the
       laser
11 %   repetition period are wrapped into the subsequent
       detection period
12 %   (wrapLongEvents).
13 %
14 %   The function outputs phasor coordinates (G,S) of the
       input decay trace,
15 %   as well as an estimate of the fluorescence lifetime
       assuming a single
16 %   exponential model (i.e. tauExperimental =
17 %   S/(harmonicNumber*2*pi*freq0*G))
18 %
19 %   Assumptions:
20 %   > cmap should be a Matlab colormap (e.g. parula, jet, hot
       , etc.)
21 %   > numSpecies must be either 1 or 2
22 %
23 %   Default values:
24 %   > numTimeBins = 256
25 %   > freq0 = 80E6
26 %   > numPhotons = 5000*ones(1,length(tauTheoretical));
27 %   > harmonicNumber = 1
28 %   > wrapLongEvents = 1
```

```
29
30      %--Check for consistency in image dimensions
31      if size(photonCountImageSignal,1) ~= size(
            photonCountImageNoise,1) || ...
32              size(photonCountImageSignal,2) ~= size(
                    photonCountImageNoise,2)
33          error('   ERROR: Signal and noise images size
                mismatch.');
34      else
35          numPixelsY = size(photonCountImageSignal,1);
36          numPixelsX = size(photonCountImageSignal,2);
37      end
38
39      %--If image parameters aren't specified, use defaults
40      if isempty(imageParameters)
41          imageParameters = default_imageParameters([]);
42      elseif isnumeric(imageParameters)
43          tau = imageParameters;
44          clear imageParameters;
45          imageParameters = default_imageParameters(tau);
46          clear tau;
47      elseif ~isstruct(imageParameters)
48          error('   ERROR: ''imageParameters'' should be struct
                or numeric lifetime value.');
49      end
50
51      %--Check that lifetime is defined
52      if ~isfield(imageParameters,'tau')
53          error(['   ERROR: Attempted to simulate decay (FLIM)
                image'...
```

```
54              'with undefined fluorescence lifetime.']);
55      end
56
57      %--Count number of fluorescent species
58      numExponentials = length(imageParameters.tau);
59
60      %--Set default values if unspecified
61      if ~isfield(imageParameters,'tau_sigma')
62          imageParameters.tau_sigma = zeros(1,numExponentials);
63      end
64      if ~isfield(imageParameters,'numTimeBins')
65          imageParameters.numTimeBins = 256;
66      end
67      if ~isfield(imageParameters,'freq0')
68          imageParameters.freq0 = 80E6;
69      end
70      if ~isfield(imageParameters,'wrapLongEvents')
71          imageParameters.wrapLongEvents = 1;
72      end
73
74      %--Define laser repetition period.
75      T = 1/imageParameters.freq0;
76
77      %--Check for consistency in number of fluorescent species
78      if size(photonCountImageSignal,3) ~= numExponentials ||
            ...
79              length(imageParameters.tau_sigma) ~=
                  numExponentials
80          error(['   ERROR: Inputs for lifetime and photon
                counts per fluorophore '...
```

```
81              'are mismatched.']);
82      end
83
84      %--Initialize decayImage structure
85      decayImage(numPixelsY,numPixelsX).N = [];
86      for m = 1:numPixelsY
87          for n = 1:numPixelsX
88              %--Generate a row vector containing all arrival
                    times for each photon.
89              decayImage(m,n).N = sum(photonCountImageSignal(m,
                    n,:)) + ...
90                  photonCountImageNoise(m,n);
91              for p = 1:length(imageParameters.tau)
92                  tau = imageParameters.tau(p) +
                        imageParameters.tau_sigma(p)*randn;
93                  imageParameters.prob(p,:) = (1/tau)*exp(...
94                      -imageParameters.t/tau);
95                  prob_IRF = conv(imageParameters.prob(p,:),...
96                      imageParameters.IRF);
97                  imageParameters.prob_IRF(p,:) = ...
98                      prob_IRF(1:imageParameters.numTimeBins);
99              end
100
101             R = zeros(1,decayImage(m,n).N);
102             R_IRF = R;
103
104             R(1:photonCountImageSignal(m,n,1)) = datasample
                    (...
105                 imageParameters.t,photonCountImageSignal(m,n
                        ,1),...
```

```
106                 'Weights',imageParameters.prob(1,:));
107             R_IRF(1:photonCountImageSignal(m,n,1)) =
                    datasample(...
108                 imageParameters.t,photonCountImageSignal(m,n
                        ,1),...
109                 'Weights',imageParameters.prob_IRF(1,:));
110
111             if imageParameters.wrapLongEvents == 1
112                 R(R>T) = rem(R(R>T),T);
113                 R_IRF(R_IRF>T) = rem(R_IRF(R_IRF>T),T);
114             else
115                 error('   ERROR: Non-wrapped events aren''t a
                        functionality yet.');
116 %                   while size(R(R>T),2) > 0
117 %                       k = find(R>T);
118 %                       for p = 1:size(R(R>T),2)
119 %                           R(k(p)) = exprnd(imageParameters.
    tau(1) + ...
120 %                               imageParameters.tau_sigma(1)*
    randn);
121 %                       end
122 %                   end
123             end
124             if numExponentials > 1
125                 for p = 2:numExponentials
126                     R(sum(photonCountImageSignal(m,n,1:p-1))
                            + ...
127                         (1:photonCountImageSignal(m,n,p))) =
                                datasample(...
128                         imageParameters.t,
```

```
                    photonCountImageSignal(m,n,p) ,...
129                 'Weights',imageParameters.prob(p,:));
130                 R_IRF(sum(photonCountImageSignal(m,n,1:p
                    -1)) + ...
131                 (1:photonCountImageSignal(m,n,p))) =
                    datasample(...
132                 imageParameters.t,
                    photonCountImageSignal(m,n,p) ,...
133                 'Weights',imageParameters.prob_IRF(p
                    ,:));
134                 if imageParameters.wrapLongEvents == 1
135                 R(R>T) = rem(R(R>T),T);
136                 R_IRF(R_IRF>T) = rem(R_IRF(R_IRF>T),T
                    );
137                 else
138                 error('   ERROR: Non-wrapped events
                    aren''t a functionality yet.');
139 %                   while size(R(R>T),2) > 0
140 %                       k = find(R>T);
141 %                       for n = 1:size(R(R>T),2)
142 %                           R(k(n)) = exprnd(
    imageParameters.tau(m) + ...,
143 %                                   imageParameters.
    tau_sigma(m)*randn);
144 %                       end
145 %                   end
146                 end
147             end
148         end
149         if sum(photonCountImageNoise(:))
```

```
150         traceNoise = T*rand(1,photonCountImageNoise(m
                ,n));
151         R(sum(photonCountImageSignal(m,n,:)) + ...
152             (1:photonCountImageNoise(m,n))) = ...
153             traceNoise;
154         R_IRF(sum(photonCountImageSignal(m,n,:)) +
                ...
155             (1:photonCountImageNoise(m,n))) = ...
156             traceNoise;
157     end
158
159     %--If specified by user, wrap long events onto
            next period. Otherwise,
160     %  as long as there are photons with arrival
            times exceeding the laser
161     %  repetition period, replace them with a newly
            simulated arrival time
162     %  to force a sub-period arrival time for all
            simulated events.
163
164     %--Generate the decay trace and the support
            vector via histogramming.
165     [decayImage(m,n).trace,decayImage(m,n).t] =
            histcounts(R,...
166         [imageParameters.t T]);
167     decayImage(m,n).trace_IRF = histcounts(R_IRF,[
            imageParameters.t T]);
168     decayImage(m,n).t = decayImage(m,n).t(1:end-1);
169     if ~isequal(decayImage(m,n).t,imageParameters.t)
170         error('   ERROR: Time domain definition
```

```
                    mismatch.');
171             end
172             decayImage(m,n).freq0 = imageParameters.freq0;
173             decayImage(m,n).numTimeBins = imageParameters.
                    numTimeBins;
174             decayImage(m,n).IRF = imageParameters.IRF;
175             decayImage(m,n).IRF_N = imageParameters.IRF_N;
176         end
177         if imageParameters.display
178             if m < numPixelsY
179                 fprintf(['\n   Finished simulating row #'
                        num2str(m) ' of ' num2str(numPixelsY) '...
                        ']);
180             else
181                 fprintf(['\n   Finished simulating row #'
                        num2str(m) ' of ' num2str(numPixelsY) '.'
                        ]);
182                 fprintf('\n   Successfully generated
                        simulated FLIM data!\n');
183             end
184         end
185     end
186 end
```

A.3.3 Performing the Phasor Transform

```
1 function decayPixelOut = phasorTransform(decayPixelIn,
      harmonicNumber)
2 %phasorTransform Transform temporal decay into phasor
3 %   PHASORTRANSFORM() transforms a temporal fluorescence
      decay trace into a
```

```
4 %   pair of phasor coordinates, G and S, and computes an
      experimental
5 %   fluorescence lifetime (tauExperimental) using the
      relation tau =
6 %   S/(n*omega*G), where n is the harmonic number (
      harmonicNumber) and
7 %   omega is the angular laser repetition frequency defined
      as 2*pi*freq0.
8 %
9 %   Assumptions:
10 %  > Decay spans entire interpulse period and begins at t =
      0.
11 %
12 %  Default values:
13 %  > freq0 = 80E6
14 %  > harmonicNumber = 1
15
16    %--Check if freq0 is specified; if not, force default
         value
17    if isempty(decayPixelIn)
18        decayPixelIn = simulateDecayTrace([]);
19    elseif isnumeric(decayPixelIn)
20        decayPixelOut.trace = decayPixelIn;
21        decayPixelOut.trace_IRF = zeros(size(decayPixelOut.
             trace));
22        clear decaySampleIn;
23        decayPixelIn.trace = decayPixelOut.trace;
24        decayPixelIn.trace_IRF = decayPixelOut.trace_IRF;
25    elseif ~isstruct(decayPixelIn)
26        error('   ERROR: ''decaySampleIn'' should be struct
```

```
        or numeric array.');
27      end
28      if isempty(harmonicNumber)
29          harmonicNumber = 1;
30      end
31      if ~isfield(decayPixelIn,'trace')
32          error(['   ERROR: Attempted to perform phasor
                transform '...
33              'on undefined decay trace.']);
34      elseif isfield(decayPixelIn,'N')
35          if ~isequal(sum(decayPixelIn.trace),decayPixelIn.N)
                || ...
36                  ~isequal(sum(decayPixelIn.trace_IRF),
                        decayPixelIn.N)
37              error(['   ERROR: Decay trace was not found to
                    contain '...
38                  'specified number of photons.']);
39          end
40      end
41
42      if ~isfield(decayPixelIn,'freq0')
43          decayPixelIn.freq0 = 80E6;
44      end
45      if ~isfield(decayPixelIn,'t')
46          decayPixelIn.t = 0:1/(decayPixelIn.freq0*256):255/(
                decayPixelIn.freq0*256);
47      end
48
49      if decayPixelIn.freq0 ~= 1/(decayPixelIn.t(end)+
            decayPixelIn.t(2))
```

```
50          error('   ERROR: Laser repetition frequency does not
                match time bin edges.');
51      elseif length(decayPixelIn.trace) ~= length(decayPixelIn.
            t)
52          error('   ERROR: Decay trace and time vector size
                mismatch');
53      end
54
55      %--Define angular laser repitition frequency
56      omega=2*pi*decayPixelIn.freq0;
57      decayPixelOut = decayPixelIn;
58
59      %--Compute G and S via trapezoidal numerical integration
60      decayPixelOut.G_ref = trapz(decayPixelIn.IRF .* ...
61          cos(omega * harmonicNumber * decayPixelIn.t)) / ...
62          trapz(decayPixelIn.IRF);
63      decayPixelOut.S_ref = trapz(decayPixelIn.IRF .* ...
64          sin(omega * harmonicNumber * decayPixelIn.t)) / ...
65          trapz(decayPixelIn.IRF);
66      decayPixelOut.G2_ref = trapz(decayPixelIn.IRF .* ...
67          cos(omega * 2*harmonicNumber * decayPixelIn.t)) / ...
68          trapz(decayPixelIn.IRF);
69      decayPixelOut.S2_ref = trapz(decayPixelIn.IRF .* ...
70          sin(omega * 2*harmonicNumber * decayPixelIn.t)) / ...
71          trapz(decayPixelIn.IRF);
72      m0_ref = decayPixelOut.G_ref - 4*decayPixelOut.G2_ref;
73      m1_ref = decayPixelOut.S_ref - 2*decayPixelOut.S2_ref;
74      m2_ref = -decayPixelOut.G_ref + decayPixelOut.G2_ref;
75      m3_ref = -decayPixelOut.S_ref + 0.5*decayPixelOut.S2_ref;
76      delta_ref = m2_ref*m0_ref - m1_ref^2;
```

```
77      theta1_ref = (m3_ref*m0_ref - m2_ref*m1_ref)/delta_ref;
78      theta2_ref = (m3_ref*m1_ref - m2_ref^2)/delta_ref;
79      a1_ref = (theta1_ref - sqrt(theta1_ref^2 - 4*theta2_ref))
           /2;
80      a2_ref = (theta1_ref + sqrt(theta1_ref^2 - 4*theta2_ref))
           /2;
81      f2_ref = (decayPixelOut.G_ref - (1+(harmonicNumber*a1_ref
           )^2)^(-1))/...
82          ((1+(harmonicNumber*a2_ref)^2)^(-1) - (1+(
               harmonicNumber*a1_ref)^2)^(-1));
83      if f2_ref < 0
84          f2_ref = 0;
85      elseif f2_ref > 1
86          f2_ref = 1;
87      end
88      f1_ref = 1-f2_ref;
89      decayPixelOut.biexp.tau_ref = [a1_ref a2_ref]/omega;
90      decayPixelOut.biexp.f_ref = [f1_ref f2_ref];
91      decayPixelOut.G = trapz(decayPixelIn.trace .* ...
92          cos(omega * harmonicNumber * decayPixelIn.t)) / ...
93          trapz(decayPixelIn.trace);
94      decayPixelOut.S = trapz(decayPixelIn.trace .* ...
95          sin(omega * harmonicNumber * decayPixelIn.t)) / ...
96          trapz(decayPixelIn.trace);
97      decayPixelOut.G2 = trapz(decayPixelIn.trace .* ...
98          cos(omega * 2*harmonicNumber * decayPixelIn.t)) / ...
99          trapz(decayPixelIn.trace);
100     decayPixelOut.S2 = trapz(decayPixelIn.trace .* ...
101         sin(omega * 2*harmonicNumber * decayPixelIn.t)) / ...
102         trapz(decayPixelIn.trace);
```

```
103     m0 = harmonicNumber^2*decayPixelOut.G - (2*harmonicNumber
            )^2*decayPixelOut.G2;
104     m1 = harmonicNumber*decayPixelOut.S - (2*harmonicNumber)*
            decayPixelOut.S2;
105     m2 = -decayPixelOut.G + decayPixelOut.G2;
106     m3 = -decayPixelOut.S/harmonicNumber + decayPixelOut.S2
            /(2*harmonicNumber);
107     delta = m2*m0 - m1^2;
108     theta1 = (m3*m0 - m2*m1)/delta;
109     theta2 = (m3*m1 - m2^2)/delta;
110     a1 = (theta1 - sqrt(theta1^2 - 4*theta2))/2;
111     a2 = (theta1 + sqrt(theta1^2 - 4*theta2))/2;
112     f2 = (decayPixelOut.G - (1+(harmonicNumber*a1)^2)^(-1))
            /...
113          ((1+(harmonicNumber*a2)^2)^(-1) - (1+(harmonicNumber*
                a1)^2)^(-1));
114     if f2 < 0
115          f2 = 0;
116     elseif f2 > 1
117          f2 = 1;
118     end
119     f1 = 1-f2;
120     decayPixelOut.biexp.tau = [a1 a2]/omega;
121     decayPixelOut.biexp.f = [f1 f2];
122     decayPixelOut.G_IRF = trapz(decayPixelIn.trace_IRF .* ...
123          cos(omega * harmonicNumber * decayPixelIn.t)) / ...
124          trapz(decayPixelIn.trace_IRF);
125     decayPixelOut.S_IRF = trapz(decayPixelIn.trace_IRF .* ...
126          sin(omega * harmonicNumber * decayPixelIn.t)) / ...
127          trapz(decayPixelIn.trace_IRF);
```

```
128     decayPixelOut.G2_IRF = trapz(decayPixelIn.trace_IRF .*
            ...
129          cos(omega * 2*harmonicNumber * decayPixelIn.t)) / ...
130          trapz(decayPixelIn.trace_IRF);
131     decayPixelOut.S2_IRF = trapz(decayPixelIn.trace_IRF .*
            ...
132          sin(omega * 2*harmonicNumber * decayPixelIn.t)) / ...
133          trapz(decayPixelIn.trace_IRF);
134     m0_IRF = decayPixelOut.G_IRF - 4*decayPixelOut.G2_IRF;
135     m1_IRF = decayPixelOut.S_IRF - 2*decayPixelOut.S2_IRF;
136     m2_IRF = -decayPixelOut.G_IRF + decayPixelOut.G2_IRF;
137     m3_IRF = -decayPixelOut.S_IRF + 0.5*decayPixelOut.S2_IRF;
138     delta_IRF = m2_IRF*m0_IRF - m1_IRF^2;
139     theta1_IRF = (m3_IRF*m0_IRF - m2_IRF*m1_IRF)/delta_IRF;
140     theta2_IRF = (m3_IRF*m1_IRF - m2_IRF^2)/delta_IRF;
141     a1_IRF = (theta1_IRF - sqrt(theta1_IRF^2 - 4*theta2_IRF))
            /2;
142     a2_IRF = (theta1_IRF + sqrt(theta1_IRF^2 - 4*theta2_IRF))
            /2;
143     f2_IRF = (decayPixelOut.G_IRF - (1+(harmonicNumber*a1_IRF
            )^2)^(-1))/...
144          ((1+(harmonicNumber*a2_IRF)^2)^(-1) - (1+(
                harmonicNumber*a1_IRF)^2)^(-1));
145     if f2_IRF < 0
146          f2_IRF = 0;
147     elseif f2_IRF > 1
148          f2_IRF = 1;
149     end
150     f1_IRF = 1-f2_IRF;
151     decayPixelOut.biexp.tau_IRF = [a1_IRF a2_IRF]/omega;
```

```
152     decayPixelOut.biexp.f_IRF = [f1_IRF  f2_IRF];
153
154     %--Compute experimental fluorescence lifetime
155     decayPixelOut.N = sum(decayPixelOut.trace);
156     if isfield(decayPixelIn,'N')
157         if decayPixelOut.N ~= decayPixelIn.N
158             error('    ERROR: Photon counting mismatch.');
159         end
160     end
161     decayPixelOut.freq0 = decayPixelIn.freq0;
162     decayPixelOut.t = decayPixelIn.t;
163     decayPixelOut.harmonicNumber = harmonicNumber;
164     decayPixelOut.phi_ref = atan(decayPixelOut.S_ref /
          decayPixelOut.G_ref);
165     decayPixelOut.m_ref = sqrt(decayPixelOut.G_ref^2 +
          decayPixelOut.S_ref^2);
166     decayPixelOut.phi2_ref = atan(decayPixelOut.S2_ref /
          decayPixelOut.G2_ref);
167     decayPixelOut.m2_ref = sqrt(decayPixelOut.G2_ref^2 +
          decayPixelOut.S2_ref^2);
168     decayPixelOut.phi = atan(decayPixelOut.S / decayPixelOut.
          G);
169     decayPixelOut.m = sqrt(decayPixelOut.G^2 + decayPixelOut.
          S^2);
170     decayPixelOut.phi2 = atan(decayPixelOut.S2 /
          decayPixelOut.G2);
171     decayPixelOut.m2 = sqrt(decayPixelOut.G2^2 +
          decayPixelOut.S2^2);
172     decayPixelOut.phi_IRF = atan(decayPixelOut.S_IRF /
          decayPixelOut.G_IRF);
```

```
173     decayPixelOut.m_IRF = sqrt(decayPixelOut.G_IRF^2 +
            decayPixelOut.S_IRF^2);
174     decayPixelOut.phi2_IRF = atan(decayPixelOut.S2_IRF /
            decayPixelOut.G2_IRF);
175     decayPixelOut.m2_IRF = sqrt(decayPixelOut.G2_IRF^2 +
            decayPixelOut.S2_IRF^2);
176     decayPixelOut.phi_corr = decayPixelOut.phi_IRF -
            decayPixelOut.phi_ref;
177     decayPixelOut.m_corr = decayPixelOut.m_IRF/decayPixelOut.
            m_ref;
178
179     decayPixelOut.tauP_ref = (1/(omega*harmonicNumber)) * ...
180         tan(decayPixelOut.phi_ref);
181     decayPixelOut.tauM_ref = (1/(omega*harmonicNumber)) * ...
182         abs(sqrt(1/decayPixelOut.m_ref^2 - 1));
183     decayPixelOut.tauP = (1/(omega*harmonicNumber)) * ...
184         tan(decayPixelOut.phi);
185     decayPixelOut.tauM = (1/(omega*harmonicNumber)) * ...
186         abs(sqrt(1/decayPixelOut.m^2 - 1));
187     decayPixelOut.tauP_IRF = (1/(omega*harmonicNumber)) * ...
188         tan(decayPixelOut.phi_IRF);
189     decayPixelOut.tauM_IRF = (1/(omega*harmonicNumber)) * ...
190         abs(sqrt(1/decayPixelOut.m_IRF^2 - 1));
191     decayPixelOut.tauP_corr = (1/(omega*harmonicNumber)) *
        ...
192         tan(decayPixelOut.phi_corr);
193     decayPixelOut.tauM_corr = (1/(omega*harmonicNumber)) *
        ...
194         abs(sqrt(1/decayPixelOut.m_corr^2 - 1));
195
```

```
196     decayPixelOut.phi_sigma_ref = ...
197         sqrt(1-decayPixelOut.m2_ref*cos(2*decayPixelOut.
                phi_ref-decayPixelOut.phi2_ref))/...
198         (decayPixelOut.m_ref * sqrt(2*decayPixelIn.IRF_N));
199     decayPixelOut.m_sigma_ref = ...
200         sqrt(1 - 2*decayPixelOut.m_ref^2 + ...
201         decayPixelOut.m2_ref*cos(2*decayPixelOut.phi_ref-
                decayPixelOut.phi2_ref))/...
202         sqrt(2*decayPixelIn.IRF_N);
203     decayPixelOut.phi_sigma = ...
204         sqrt(1-decayPixelOut.m2*cos(2*decayPixelOut.phi-
                decayPixelOut.phi2))/...
205         (decayPixelOut.m * sqrt(2*decayPixelOut.N));
206     decayPixelOut.m_sigma = ...
207         sqrt(1 - 2*decayPixelOut.m^2 + ...
208         decayPixelOut.m2*cos(2*decayPixelOut.phi-
                decayPixelOut.phi2))/...
209         sqrt(2*decayPixelOut.N);
210     decayPixelOut.phi_sigma_IRF = ...
211         sqrt(1-decayPixelOut.m2_IRF*cos(2*decayPixelOut.
                phi_IRF-decayPixelOut.phi2_IRF))/...
212         (decayPixelOut.m_IRF * sqrt(2*decayPixelOut.N));
213     decayPixelOut.m_sigma_IRF = ...
214         sqrt(1 - 2*decayPixelOut.m_IRF^2 + ...
215         decayPixelOut.m2_IRF*cos(2*decayPixelOut.phi_IRF-
                decayPixelOut.phi2_IRF))/...
216         sqrt(2*decayPixelOut.N);
217     decayPixelOut.phi_sigma_corr = sqrt(decayPixelOut.
          phi_sigma_ref^2 + ...
218         decayPixelOut.phi_sigma_IRF^2);
```

```
219     decayPixelOut.m_sigma_corr = sqrt(decayPixelOut.
            m_sigma_ref^2 + ...
220          decayPixelOut.m_sigma_IRF^2);
221
222     decayPixelOut.tauP_sigma_ref = decayPixelOut.
            phi_sigma_ref/(omega*harmonicNumber*...
223          (cos(decayPixelOut.phi_ref))^2);
224     decayPixelOut.tauM_sigma_ref = decayPixelOut.m_sigma_ref
            /(omega*harmonicNumber*...
225          decayPixelOut.m_ref^2 * sqrt(1 - decayPixelOut.m_ref
                ^2));
226     decayPixelOut.tauP_sigma = decayPixelOut.phi_sigma/(omega
            *harmonicNumber*...
227          (cos(decayPixelOut.phi))^2);
228     decayPixelOut.tauM_sigma = decayPixelOut.m_sigma/(omega*
            harmonicNumber*...
229          decayPixelOut.m^2 * sqrt(1 - decayPixelOut.m^2));
230     decayPixelOut.tauP_sigma_IRF = decayPixelOut.
            phi_sigma_IRF/(omega*harmonicNumber*...
231          (cos(decayPixelOut.phi_IRF))^2);
232     decayPixelOut.tauM_sigma_IRF = decayPixelOut.m_sigma_IRF
            /(omega*harmonicNumber*...
233          decayPixelOut.m_IRF^2 * sqrt(1 - decayPixelOut.m_IRF
                ^2));
234     decayPixelOut.tauP_sigma_corr = decayPixelOut.
            phi_sigma_corr/(omega*harmonicNumber*...
235          (cos(decayPixelOut.phi_corr))^2);
236     decayPixelOut.tauM_sigma_corr = decayPixelOut.
            m_sigma_corr/(omega*harmonicNumber*...
237          decayPixelOut.m_corr^2 * sqrt(1 - decayPixelOut.
```

```
        m_corr^2));
238
239     decayPixelOut.tauP_interval_ref = decayPixelOut.tauP_ref
          + ...
240         1.96*[-decayPixelOut.tauP_sigma_ref decayPixelOut.
              tauP_sigma_ref];
241     decayPixelOut.tauM_interval_ref = decayPixelOut.tauM_ref
          + ...
242         1.96*[-decayPixelOut.tauM_sigma_ref decayPixelOut.
              tauM_sigma_ref];
243     decayPixelOut.tauP_interval = decayPixelOut.tauP + ...
244         1.96*[-decayPixelOut.tauP_sigma decayPixelOut.
              tauP_sigma];
245     decayPixelOut.tauM_interval = decayPixelOut.tauM + ...
246         1.96*[-decayPixelOut.tauM_sigma decayPixelOut.
              tauM_sigma];
247     decayPixelOut.tauP_interval_IRF = decayPixelOut.tauP_IRF
          + ...
248         1.96*[-decayPixelOut.tauP_sigma_IRF decayPixelOut.
              tauP_sigma_IRF];
249     decayPixelOut.tauM_interval_IRF = decayPixelOut.tauM_IRF
          + ...
250         1.96*[-decayPixelOut.tauM_sigma_IRF decayPixelOut.
              tauM_sigma_IRF];
251     decayPixelOut.tauP_interval_corr = decayPixelOut.
          tauP_corr + ...
252         1.96*[-decayPixelOut.tauP_sigma_corr decayPixelOut.
              tauP_sigma_corr];
253     decayPixelOut.tauM_interval_corr = decayPixelOut.
          tauM_corr + ...
```

```
254            1.96*[-decayPixelOut.tauM_sigma_corr decayPixelOut.
                   tauM_sigma_corr];
255        decayPixelOut.F_P_ref = (decayPixelOut.tauP_sigma_ref/
               decayPixelOut.tauP_ref)*...
256             sqrt(decayPixelIn.IRF_N);
257        decayPixelOut.F_M_ref = (decayPixelOut.tauM_sigma_ref/
               decayPixelOut.tauM_ref)*...
258             sqrt(decayPixelIn.IRF_N);
259        decayPixelOut.F_P = (decayPixelOut.tauP_sigma/
               decayPixelOut.tauP)*...
260             sqrt(decayPixelOut.N);
261        decayPixelOut.F_M = (decayPixelOut.tauM_sigma/
               decayPixelOut.tauM)*...
262             sqrt(decayPixelOut.N);
263        decayPixelOut.F_P_IRF = (decayPixelOut.tauP_sigma_IRF/
               decayPixelOut.tauP_IRF)*...
264             sqrt(decayPixelOut.N);
265        decayPixelOut.F_M_IRF = (decayPixelOut.tauM_sigma_IRF/
               decayPixelOut.tauM_IRF)*...
266             sqrt(decayPixelOut.N);
267        decayPixelOut.F_P_corr = (decayPixelOut.tauP_sigma_corr/
               decayPixelOut.tauP_corr)*...
268             sqrt(decayPixelOut.N);
269        decayPixelOut.F_M_corr = (decayPixelOut.tauM_sigma_corr/
               decayPixelOut.tauM_corr)*...
270             sqrt(decayPixelOut.N);
271    end
```

A.3.4 Generating the Phasor Plot

```
1  function varargout = phasorPlot(G,S,harmonicNumber,steps,
```

```
    freq0 ,...
2       histogramThreshold ,cmap, drawEllipse , drawIntercepts ,
            numSpecies)
3 %phasorPlot  Plot a phasor or a phasor array onto (G,S)
    coordinate map.
4 %   PHASORPLOT() plots either a single phasor or an array of
    phasors onto a
5 %   phasor plot given inpute phasor coordinates G and S. The
    harmonic
6 %   number (harmonicNumber) used to compute the phasor
    coordinates must be
7 %   specified (otherwise, the default value 1 will be assumed
    ). The 2D
8 %   histogram step size (steps), the laser repetition
    frequency (freq0),
9 %   the minimum fraction of phasors a given 2D bin must
    contain to be
10 %   displayed on the phasor plot relative to the maximum bin
    count
11 %   (histogramThreshold), the colormap to be used for
    displaying the phasor
12 %   plot (cmap), a flag to specify whether or not an ellipse
    should be
13 %   fitted and drawn around the phasor cluster (drawEllipse),
     and the
14 %   number of fluorescent species (numSpecies) must also be
    specified.
15 %   Otherwise, they will all be set to their default values.
16 %
17 %   The function either outputs a single lifetime if
```

```
numSpecies = 1, or
% both the short and long lifetimes if numSpecies = 2.
%
% Assumptions:
% > cmap should be a Matlab colormap (e.g. parula, jet, hot
, etc.)
% > numSpecies must be either 1 or 2
%
% Default values:
% > harmonicNumber = 1
% > steps = 0.0025
% > freq0 = 80E6
% > histogramThreshold = 0.001
% > cmap = 'jet'
% > drawEllipse = 0
% > numSpecies = 1

%--Initialize flags
flagLongInfinite = 0;
flagShortZero = 0;

%--Set default values if unspecified
if isempty(harmonicNumber)
    harmonicNumber = 1;
end
if isempty(steps)
    steps = 0.0025;
end
if isempty(freq0)
    freq0 = 80E6;
```

```
46      end
47      if isempty(histogramThreshold)
48          histogramThreshold = 0.001;
49      end
50      if isempty(cmap)
51          cmap = 'jet';
52      end
53      if isempty(drawEllipse)
54          drawEllipse = 0;
55      end
56      if isempty(drawIntercepts)
57          drawIntercepts = 1;
58      end
59      if isempty(numSpecies)
60          numSpecies = 1;
61      end
62
63      %---Rearrange G and S into column vectors
64      if size(G,2) > 1 || size(S,2) > 1
65          G = reshape(G,[numel(G) 1]);
66          S = reshape(S,[numel(S) 1]);
67      end
68      %---Remove NaN values and define Z array
69      G(isnan(G)) = [];
70      S(isnan(S)) = [];
71      Z = [G,S];
72
73      %---Define histogram bin centers and number of bins
74      G_bins = 0:steps:1;
75      S_bins = 0:steps:1;
```

```
76      G_NumBins = length(G_bins);
77      S_NumBins = length(S_bins);
78      %--Sort all (G,S) coordinate values into bins
79      G_i = round(interp1(G_bins,1:G_NumBins,G,'linear','extrap
            '));
80      S_i = round(interp1(S_bins,1:S_NumBins,S,'linear','extrap
            '));
81      %--Remove bin values outside the range [1,NumBins]
82      G_i = max(min(G_i,G_NumBins),1);
83      S_i = max(min(S_i,S_NumBins),1);
84      %--Compute bin counts
85      H = accumarray([S_i(:) G_i(:)],1,[S_NumBins G_NumBins]);
86
87      %--Plot 2D histogram using bin counts and (G,S) bin
            centers
88      figure;
89      imagesc(G_bins,S_bins,H);
90      %--Apply specified Matlab colormap (default: jet)
91      cmap_fh = str2func(cmap);
92      j = cmap_fh(round(1/histogramThreshold));
93      %--Force sub-threshold bin counts to appear as white
94      if strcmp(cmap,'hot')
95          j(1,:) = 0.85*ones(1,3);
96      else
97          j(1,:) = ones(1,3);
98      end
99
100     %--Apply colormap
101     colormap(j);
102     %--Add and label colorbar
```

```
103     cb = colorbar;
104     ylabel(cb,'Phasor Counts')
105     set(gca,'Ydir','Normal')
106     hold on
107
108     %--Calculate the eigenvectors and eigenvalues
109     covMatrix = cov(Z,'omitrows');
110     [V,D] = eig(covMatrix);
111
112     %--Get the index of the largest eigenvector
113     eigenvalueMajor = max(sum(D));
114     eigenvalueMinor = min(sum(D));
115     if D(1) == eigenvalueMajor
116         eigenvectorMajor = V(:,1);
117     else
118         eigenvectorMajor = V(:,2);
119     end
120
121     %--Calculate the angle between the x-axis and the largest
            eigenvector
122     angleMajor = atan2(eigenvectorMajor(2),eigenvectorMajor
        (1));
123
124     %--This angle can be anywhere between -pi and pi; this
        shift ensures
125     %  that it is between 0 and 2*pi.
126     if(angleMajor < 0)
127         angleMajor = angleMajor + 2*pi;
128     end
129
```

```
130     %--Compute phasor cluster mean coordinates
131     Z_mean = mean(Z,'omitnan');
132
133     %--Get the 95% confidence interval error ellipse
134     theta = linspace(0,2*pi);
135     G_mean = Z_mean(1);
136     S_mean = Z_mean(2);
137     a = sqrt(eigenvalueMajor * chi2inv(0.95,2));
138     b = sqrt(eigenvalueMinor * chi2inv(0.95,2));
139
140     %--The ellipse in x and y coordinates
141     ellipseGS = [a*cos(theta);b*sin(theta)]';
142
143     %--Define rotation matrix
144     R = [cos(angleMajor) sin(angleMajor); -sin(angleMajor)
            cos(angleMajor)];
145
146     %--Rotate the ellipse to angle angleMajor
147     ellipseGS_R = ellipseGS * R;
148
149     %--Draw the error ellipse
150     if drawEllipse
151         plot(ellipseGS_R(:,1)+G_mean,ellipseGS_R(:,2)+S_mean,
                'g','LineWidth',1);
152     end
153
154     %---UNIVERSAL CIRCLE, FITTING, ETC---%
155     %--Plot universal circle
156     g = 0:0.001:1;
157     semicircle = sqrt(0.25 - (g-0.5).^2);
```

```
158     plot(g,semicircle,'r','LineWidth',1);
159     axis equal tight;
160     axis([0 1 0 0.6]);
161     xlabel('G');
162     ylabel('S');
163
164     %--Calculate lifetimes
165     majorAxis = @(g) (eigenvectorMajor(2)/eigenvectorMajor(1)
            )*(g-G_mean)+S_mean;
166 %       semicircle = @(g) sqrt(0.25 - (g-0.5).^2);
167     intersectionMajorAxisSemicircle = @(g) sqrt(0.25 - (g
            -0.5).^2) - ...
168         (eigenvectorMajor(2)/eigenvectorMajor(1))*(g-G_mean)-
                S_mean;
169     [~,maxIntersectionIndex] = max(
            intersectionMajorAxisSemicircle(g));
170
171     try
172         G_inter1 = fzero(intersectionMajorAxisSemicircle,[0 g
                (maxIntersectionIndex)]);
173     catch
174         warning('Warning: Long lifetime computed to be
                infinite.');
175         G_inter1 = 0;
176         flagLongInfinite = 1;
177     end
178     try
179         G_inter2 = fzero(intersectionMajorAxisSemicircle,[g(
                maxIntersectionIndex) 1]);
180     catch
```

```
181         warning('Warning: Short lifetime computed to be less
                than 0 ps.');
182         G_inter2 = 1;
183         flagShortZero = 1;
184     end
185
186     S_inter1 = majorAxis(G_inter1);
187     S_inter2 = majorAxis(G_inter2);
188
189     omega = 2*pi*freq0;
190
191     if numSpecies == 1
192         varargout{1} = S_mean/(harmonicNumber*omega*G_mean);
193         if drawIntercepts
194             if (G_inter1-G_mean)^2+(S_inter1-S_mean)^2 < (
                    G_inter2-G_mean)^2+(S_inter2-S_mean)^2
195                 plot(G_inter1,S_inter1,...
196                     'Marker','d','Color',[0 0.666 0],'
                            LineWidth',1,'MarkerFaceColor',[0
                            0.666 0]);
197             else
198                 plot(G_inter2,S_inter2,...
199                     'Marker','d','Color',[0 0.666 0],'
                            LineWidth',1,'MarkerFaceColor',[0
                            0.666 0]);
200             end
201
202         end
203     else
204         if ~flagShortZero
```

```
205             varargout{1} = S_inter2/(harmonicNumber*omega*
                    G_inter2);    % Short lifetime in seconds
206         else
207             varargout{1} = 0;
208         end
209         if ~flagLongInfinite
210             varargout{2} = S_inter1/(harmonicNumber*omega*
                    G_inter1);    % Long lifetime in seconds
211         else
212             varargout{2} = Inf;
213         end
214         if drawIntercepts
215             plot([G_inter1 G_inter2],[S_inter1 S_inter2],...
216                 'Marker','d','Color',[0 0.666 0],'LineWidth'
                        ,1,'MarkerFaceColor',[0 0.666 0]);
217         end
218     end
219 end
```

Bibliography

[1] Shaoxin Li, Yanjiao Zhang, Junfa Xu, Linfang Li, Qiuyao Zeng, Lin Lin, Zhouyi Guo, Zhiming Liu, Honglian Xiong, and Songhao Liu. Noninvasive prostate cancer screening based on serum surface-enhanced raman spectroscopy and support vector machine. *Applied Physics Letters*, 105(9):091104, 2014.

[2] Brindha Elumalai, Aruna Prakasarao, Bharanidharan Ganesan, Koteeswaran Dornadula, and Singaravelu Ganesan. Raman spectroscopic characterization of urine of normal and oral cancer subjects. *Journal of Raman Spectroscopy*, 46(1):84–93, 2015.

[3] Shangyuan Feng, Shaohua Huang, Duo Lin, Guannan Chen, Yuanji Xu, Yongzeng Li, Zufang Huang, Jianji Pan, Rong Chen, and Haishan Zeng. Surface-enhanced raman spectroscopy of saliva proteins for the noninvasive differentiation of benign and malignant breast tumors. *International Journal of Nanomedicine*, 10(1):537–547, 2015.

[4] Zhiwei Huang, Annette McWilliams, Harvey Lui, David I. McLean, Stephen Lam, and Haishan Zeng. Near-infrared raman spectroscopy for optical diagnosis of lung cancer. *International Journal of Cancer*, 107(6):1047–1052, 2003.

[5] Monika Gniadecka, Peter Alshede Philipsen, Sonja Wessel, Robert Gniadecki, Hans Christian Wulf, Sigurdur Sigurdsson, Ole Faurskov Nielsen, Daniel Højgaard Christensen, Jana Hercogova, Kristian Rossen, Henrik Klem Thomsen, and Lars Kai Hansen. Melanoma diagnosis by raman spectroscopy and neural networks: Structure alterations in proteins and lipids in intact cancer tissue. *Journal of Investigative Dermatology*, 122(2):443–449, 2004.

[6] Senada Koljenović, Lin-P'ing Choo-Smith, Tom C. Bakker Schut, Johan M. Kros, Herbert J. van den Berge, and Gerwin J. Puppels. Discriminating vital tumor from necrotic tissue in human glioblastoma tissue samples by raman spectroscopy. *Laboratory Investigation*, 82(10):1265–1277, 2002.

[7] Christian W. Freudiger, Rolf Pfannl, Daniel A. Orringer, Brian G. Saar, Minbiao Ji, Qing Zeng, Linda Ottoboni, Wei Ying, Christian Waeber, John R. Sims, Philip L. De Jager, Oren Sagher, Martin A. Philbert, Xiaoyin Xu, Santosh Kesari, X. Sunney Xie, and Geoffrey S. Young. Multicolored stain-free histopathology with coherent raman imaging. *Laboratory Investigation*, 92:1492–1502, 2012.

[8] Hequn Wang, Sam Osseiran, Vivien Igras, Alexander J. Nichols, Elisabeth M. Roider, Joachim Pruessner, Hensin Tsao, David E. Fisher, and Conor L. Evans. In vivo coherent raman imaging of the melanomagenesis-associated pigment pheomelanin. *Scientific Reports*, 6:37986, 2016.

[9] Winfried Denk, James H. Strickler, and Watt W. Webb. Two-photon laser scanning fluorescence microscopy. *Science*, 248(4951):73–76, 1990.

[10] Enrico Gratton, Sophie Breusegem, Jason D. B. Sutin, Qiaoaio Ruan, and Nicholas P. Barry. Fluorescence lifetime imaging for the two-photon microscope: time-domain and frequency-domain methods. *Journal of Biomedical Optics*, 8(3):381–391, 2003.

[11] Jeff W. Lichtman and José-Angel Conchello. Fluorescence microscopy. *Nature Methods*, 2(12):910–919, 2005.

[12] W. Becker, A. Bergmann, M. A. Hink, K. König, K. Benndorf, and C. Biskup. Fluorescence lifetime imaging by time-correlated single-photon counting. *Microscopy Research and Technique*, 63(1):58–66, 2004.

[13] Alex J. Walsh, Joe T. Sharick, Melissa C. Skala, and Hope T. Beier. Temporal binning of time-correlated single photon counting data improves exponential decay fits and imaging speed. *Biomedical Optics Express*, 7(4):1385–1399, 2016.

[14] Sam Osseiran, Elisabeth M. Roider, Hequn Wang, Yusuke Suita, Michael Murphy, David E. Fisher, and Conor L. Evans. Non-euclidean phasor analysis for quantification of oxidative stress in ex vivo human skin exposed to sun filters using fluorescence lifetime imaging microscopy. *Journal of Biomedical Optics*, 22(12):125004, 2017.

[15] Michael Evers, Nunciada Salma, Sam Osseiran, Malte Casper, Reginald Birngruber, Conor L. Evans, and Dieter Manstein. Enhanced quantification of metabolic activity for individual adipocytes by label-free flim. *Scientific Reports*, 8(1):8757, 2018.

[16] Sinyoung Jeong, Maiko Hermsmeier, Sam Osseiran, Akira Yamamoto, Usha Nagavarapu, Kin F. Chan, and Conor L. Evans. Visualization of drug distribution of a topical minocycline gel in human facial skin. *Biomedical Optics Express*, 9(7):3434–3448, 2018.

[17] Michelle A. Digman, Valeria R. Caiolfa, Moreno Zamai, and Enrico Gratton. The phasor approach to fluorescence lifetime imaging analysis. *Biophysical Journal*, 94(2):L14–L16, 2008.

[18] Martin Štefl, Nicholas G. James, Justin A. Ross, and David M. Jameson. Applications of phasors to in vitro time-resolved fluorescence measurements. *Analytical Biochemistry*, 410(1):62–69, 2011.

[19] Barry R. Masters and Peter T. C. So. *Handbook of Biomedical Nonlinear Optical Microscopy.* Oxford University Press, 2008.

[20] Derek A. Long. *The Raman Effect: A Unified Treatment of the Theory of Raman Scattering by Molecules.* John Wiley & Sons Ltd, 2002.

[21] Paul L. Stiles, Jon A. Dieringer, Nilam C. Shah, and Richard P. Van Duyne. Surface-enhanced raman spectroscopy. *Annual Review of Analytical Chemistry*, 1:601–626, 2008.

[22] Catherine Louis and Olivier Pluchery. *Gold nanoparticles for physics, chemistry and biology.* World Scientific, 2017.

[23] Gary Wiederrecht. *Handbook of nanoscale optics and electronics.* Academic Press, 2010.

[24] Bhavya Sharma, Renee R. Frontiera, Anne-Isabelle Henry, Emilie Ringe, and Richard P. Van Duyne. Sers: Materials, applications, and the future. *Materials Today*, 15(1–2):16–25, 2012.

[25] Robert W. Boyd. *Nonlinear Optics.* Academic Press, 3rd edition, 2008.

[26] Yuen-Ron Shen. *The Principles of Nonlinear Optics.* John Wiley & Sons Inc, 2003.

[27] Delong Zhang, Ping Wang, Mikhail N. Slipchenko, and Ji-Xin Cheng. Fast vibrational imaging of single cells and tissues by stimulated raman scattering microscopy. *Accounts of Chemical Research*, 47(8):2282–2290, 2014.

[28] Conor L. Evans and X. Sunney Xie. Coherent anti-stokes raman scattering microscopy: Chemical imaging for biology and medicine. *Annual Review of Analytical Chemistry*, 1:883–909, 2008.

[29] Charles H. Camp Jr and Marcus T. Cicerone. Chemically sensitive bioimaging with coherent raman scattering. *Nature Photonics*, 9(5):295–305, 2015.

[30] Ben N. G. Giepmans, Stephen R. Adams, Mark H. Ellisman, and Roger Y. Tsien. The fluorescent toolbox for assessing protein location and function. *Science*, 312(5771):217–224, 2006.

[31] Rainer Pepperkok and Jan Ellenberg. High-throughput fluorescence microscopy for systems biology. *Nature Reviews Molecular Cell Biology*, 7(9):690–696, 2006.

[32] Vadim Zinchuk, Olga Zinchuk, and Teruhiko Okada. Quantitative colocalization analysis of multicolor confocal immunofluorescence microscopy images: Pushing pixels to explore biological phenomena. *Acta Histochemica Et Cytochemica*, 40(4):101–111, 2007.

[33] Martin Chalfie, Yuan Tu, Ghia Euskirchen, William W. Ward, and Douglas C. Prasher. Green fluorescent protein as a marker for gene expression. *Science*, 263(5148):802–805, 1994.

[34] George H. Patterson, Susan M. Knobel, Wallace D. Sharif, Steven R. Kain, and David W. Piston. Use of the green fluorescent protein and its mutants in quantitative fluorescence microscopy. *Biophysical Journal*, 73(5):2782–2790, 1997.

[35] Roger Y. Tsien. The green fluorescent protein. *Annual Review of Biochemistry*, 67(11):509–544, 1998.

[36] Jennifer Lippincott-Schwartz and George H. Patterson. Development and use of fluorescent protein markers in living cells. *Science*, 300(5616):87–91, 2003.

[37] Nathan C. Shaner, Robert E. Campbell, Paul A. Steinbach, Ben N. G. Giepmans, Amy E. Palmer, and Roger Y. Tsien. Improved monomeric red, orange and yellow fluorescent proteins derived from discosoma sp. red fluorescent protein. *Nature Biotechnology*, 22(12):1567–1572, 2004.

[38] Jefferson Chan, Sheel C. Dodani, and Christopher J. Chang. Reaction-based small-molecule fluorescent probes for chemoselective bioimaging. *Nature Chemistry*, 4(12):973–984, 2012.

[39] Takuya Terai and Tetsuo Nagano. Small-molecule fluorophores and fluorescent probes for bioimaging. *Pflügers Archiv European Journal of Physiology*, 465(3):347–359, 2013.

[40] Wang Xu, Zebing Zeng, Jian-Hui Jiang, Young-Tae Chang, and Lin Yuan. Discerning the chemistry in individual organelles with small-molecule fluorescent probes. *Angewandte Chemie International Edition*, 55(44):13658–13699, 2016.

[41] Alicia L. Carlson, Joji Fujisaki, Juwell Wu, Judith M. Runnels, Raphaël Turcotte, Cristina Lo Celso, David T. Scadden, Terry B. Strom, and Charles P. Lin. Tracking single cells in live animals using a photoconvertible near-infrared cell membrane label. *PLOS ONE*, 8(8):e69257, 2013.

[42] Daria M. Shcherbakova, Prabuddha Sengupta, Jennifer Lippincott-Schwartz, and Vladislav V. Verkhusha. Photocontrollable fluorescent proteins for superresolution imaging. *Annual Review of Biophysics*, 43:303–329, 2014.

[43] Sheldon J. J. Kwok, Myunghwan Choi, Brijesh Bhayana, Xueli Zhang, Chongzhao Ran, and Seok-Hyun Yun. Two-photon excited photoconversion of cyanine-based dyes. *Scientific Reports*, 6:23866, 2016.

[44] Raphaël Turcotte, Juwell W. Wu, and Charles P. Lin. Intravital multiphoton photoconversion with a cell membrane dye. *Journal of Biophotonics*, 10(2):206–210, 2017.

[45] R. Rox Anderson and John A. Parrish. The optics of human skin. *Journal of Investigative Dermatology*, 77(1):13–19, 1981.

[46] Dan Fu, Tong Ye, Thomas E. Matthews, Gunay Yurtsever, and Warren S. Warren. Two-color, two-photon, and excited-state absorption microscopy. *Journal of Biomedical Optics*, 12(5):054004, 2007.

[47] Dan Fu, Tong Ye, Thomas E. Matthews, Benny J. Chen, Gunay Yurtserver, and Warren S. Warren. High-resolution in vivo imaging of blood vessels without labeling. *Optics Letters*, 32(18):2641–2643, 2007.

[48] Dan Fu, Tong Ye, Thomas E. Matthews, James M. Grichnik, Lian Hong, John D. Simon, and Warren S. Warren. Probing skin pigmentation changes with transient absorption imaging of eumelanin and pheomelanin. *Journal of Biomedical Optics*, 13(5):054036, 2008.

[49] Thomas E. Matthews, Ivan R. Piletic, M. Angelica Selim, Mary Jane Simpson, and Warren S. Warren. Pump-probe imaging differentiates melanoma from melanocytic nevi. *Science Translational Medicine*, 3(71):71ra15, 2011.

[50] Jesse W. Wilson, Simone Degan, Christina S. Gainey, Tanya Mitropoulos, Mary Jane Simpson, Jennifer Y. Zhang, and Warren S. Warren. Comparing in vivo pump-probe and multiphoton fluorescence microscopy of melanoma and pigmented lesions. *Journal of Biomedical Optics*, 20(5):051012, 2014.

[51] Ilyas Saytashev, Rachel Glenn, Gabrielle A. Murashova, Sam Osseiran, Dana Spence, Conor L. Evans, and Marcos Dantus. Multiphoton excited hemoglobin fluorescence and third harmonic generation for non-invasive microscopy of stored blood. *Biomedical Optics Express*, 7(9):3449–3460, 2016.

[52] Conor L. Evans. Nonlinear optical microscopy for melanoma: Challenges, tools and opportunities. *Photochemistry and Photobiology*, 2018.

[53] Andreas Zumbusch, Gary R. Holtom, and X. Sunney Xie. Three-dimensional vibrational imaging by coherent anti-stokes raman scattering. *Physical Review Letters*, 82(20):4142–4145, 1999.

[54] Lauren A. Austin, Sam Osseiran, and Conor L. Evans. Raman technologies in cancer diagnostics. *Analyst*, 141(2):476–503, 2016.

[55] Christian W. Freudiger, Wei Min, Brian G. Saar, Sijia Lu, Gary R. Holtom, Chengwei He, Jason C. Tsai, Jing X. Kang, and X. Sunney Xie. Label-free biomedical imaging with high sensitivity by stimulated raman scattering microscopy. *Science*, 322(5909):1857–1861, 2008.

[56] M. Weinigel, H. G. Breunig, M. Kellner-Höfer, R. Bückle, M. E. Darvin, M. Klemp, J. Lademann, and K. König. In vivo histology: optical biopsies with chemical contrast using clinical multiphoton/coherent anti-stokes raman scattering tomography. *Laser Physics Letters*, 11(5):055601, 2014.

[57] Christian W. Freudiger, Wenlong Yang, Gary R. Holtom, Nasser Peyghambarian, X. Sunney Xie, and Khanh Q. Kieu. Stimulated raman scattering microscopy with a robust fibre laser source. *Nature Photonics*, 8(2):153–159, 2014.

[58] Kenny Kong, Catherine Kendall, Nicholas Stone, and Ioan Notingher. Raman spectroscopy for medical diagnostics from in-vitro biofluid assays to in-vivo cancer detection. *Advanced Drug Delivery Reviews*, 89:121–134, 2015.

[59] Qiang Tu and Chang Chang. Diagnostic applications of raman spectroscopy. *Nanomedicine: Nanotechnology, Biology and Medicine*, 8(5):545–558, 2012.

[60] Pavel Matousek and Michael D. Morris. *Emerging Raman Applications and Techniques in Biomedical and Pharmaceutical Fields.* Springer, 2010.

[61] Desiree S. Grubisha, Robert J. Lipert, Hye-Young Park, Jeremy Driskell, and Marc D. Porter. Femtomolar detection of prostate-specific antigen: An immunoassay based on surface-enhanced raman scattering and immunogold labels. *Analytical Chemistry*, 75(21):5936–5943, 2003.

[62] Greta Del Mistro, Silvia Cervo, Elena Mansutti, Riccardo Spizzo, Alfonso Colombatti, Pietro Belmonte, Renzo Zucconelli, Agostino Steffan, Valter Sergo, and Alois Bonifacio. Surface-enhanced raman spectroscopy of urine for prostate cancer detection: a preliminary study. *Analytical and Bioanalytical Chemistry*, 407(12):3271–3275, 2015.

[63] Aditi Sahu, Sharada Sawant, Hitesh Mamgain, and C. Murali Krishna. Raman spectroscopy of serum: an exploratory study for detection of oral cancers. *Analyst*, 138(14):4161–4174, 2013.

[64] Duo Lin, Jianji Pan, Hao Huang, Guannan Chen, Sufang Qiu, Hong Shi, Weiwei Chen, Yun Yu, Shangyuan Feng, and Rong Chen. Label-free blood plasma test based on surface-enhanced raman scattering for tumor stages detection in nasopharyngeal cancer. *Scientific Reports*, 4:4751, 2014.

[65] Aditi Sahu, Nikhila Nandakumar, Sharada Sawant, and C. Murali Krishna. Recurrence prediction in oral cancers: a serum raman spectroscopy study. *Analyst*, 140(7):2294–2301, 2015.

[66] Shangyuan Feng, Duo Lin, Juqiang Lin, Zufang Huang, Guannan Chen, Yongzeng Li, Shaohua Huang, Jianhua Zhao, Rong Chen, and Haishan Zeng. Saliva analysis combining membrane protein purification with surface-enhanced raman spectroscopy for nasopharyngeal cancer detection. *Applied Physics Letters*, 104(7):073702, 2014.

[67] J. L. Pichardo-Molina, C. Frausto-Reyes, O Barbosa-García, R Huerta-Franco, J. L. González-Trujillo, C. A. Ramírez-Alvarado, G. Gutiérrez-Juárez, and C. Medina-Gutiérrez. Raman spectroscopy and multivariate analysis of serum samples from breast cancer patients. *Lasers in Medical Science*, 22(4):229–236, 2007.

[68] T. Bhattacharjee, A. Khan, G. Maru, A. Ingle, and C. Murali Krishna. A preliminary raman spectroscopic study of urine: diagnosis of breast cancer in animal models. *Analyst*, 140(2):456–466, 2015.

[69] Michael Jermyn, Kelvin Mok, Jeanne Mercier, Joannie Desroches, Julien Pichette, Karl Saint-Arnaud, Liane Bernstein, Marie-Christine Guiot, Kevin Petrecca, and Frederic Leblond. Intraoperative brain cancer detection with raman spectroscopy in humans. *Science Translational Medicine*, 7(274):274ra19, 2015.

[70] Abigail S. Haka, Zoya Volynskaya, Joseph A. Gardecki, Jon Nazemi, Joanne Lyons, David Hicks, Maryann Fitzmaurice, Ramachandra R. Dasari, Joseph P. Crowe, and Michael S. Feld. In vivo margin assessment during partial mastectomy breast surgery using raman spectroscopy. *Cancer Research*, 66(6):3317–3322, 2006.

[71] Allison Stelling, Reiner Salzer, Matthias Kirsch, Stephan B. Sobottka, Kathrin Geiger, Edmund Koch, Gabriele Schackert, and Gerald Steiner. Intra-operative optical diagnostics with vibrational spectroscopy. *Analytical and Bioanalytical Chemistry*, 400(9):2745–2753, 2011.

[72] Michael B. Fenn, Petros Xanthopoulos, Georgios Pyrgiotakis, Stephen R. Grobmyer, Panos M. Pardalos, and Larry L. Hench. Raman spectroscopy for clinical oncology. *Advances in Optical Technologies*, 2011:213783, 2011.

[73] Rebecca L. Siegel, Kimberly D. Miller, and Ahmedin Jemal. Cancer statistics, 2015. *CA: A Cancer Journal for Clinicians*, 65(1):5–29, 2015.

[74] Christopher J. Frank, Douglas C. B. Redd, Ted S. Gansler, and Richard L. McCreery. Characterization of human breast biopsy specimens with near-ir raman spectroscopy. *Analytical Chemistry*, 66(3):319–326, 1994.

[75] Christopher J. Frank, Richard L. McCreery, and Douglas C.B. Redd. Raman spectroscopy of normal and diseased human breast tissues. *Analytical Chemistry*, 67(5):777–783, 1995.

[76] Ramasamy Manoharan, Karen Shafer, Lev Perelman, Jun Wu, Kun Chen, Geurt Deinum, Maryann Fitzmaurice, Jonathan Myles, Joseph Crowe, Ramachandra R. Dasari, and Michael S. Feld. Raman spectroscopy and fluorescence photon migration for breast cancer diagnosis and imaging. *Photochemistry and Photobiology*, 67(1):15–22, 1998.

[77] Karen E. Shafer-Peltier, Abigail S. Haka, Maryann Fitzmaurice, Joseph Crowe, Jonathan Myles, Ramachandra R. Dasari, and Michael S. Feld. Raman microspectroscopic model of human breast tissue: implications for breast cancer diagnosis in vivo. *Journal of Raman Spectroscopy*, 33(7):552–563, 2002.

[78] Abigail S. Haka, Karen E. Shafer-Peltier, Maryann Fitzmaurice, Joseph Crowe, Ramachandra R. Dasari, and Michael S. Feld. Diagnosing breast cancer by using raman spectroscopy. *Proceedings of the National Academy of Sciences*, 102(35):12371–12376, 2005.

[79] Jakub Surmacki, Beata Brozek-Pluska, Radzislaw Kordek, and Halina Abramczyk. The lipid-reactive oxygen species phenotype of breast cancer. raman spectroscopy and mapping, pca and plsda for invasive ductal carcinoma and invasive lobular carcinoma. molecular tumorigenic mechanisms beyond warburg effect. *Analyst*, 140(7):2121–2133, 2015.

[80] Melissa M. Mariani, Lindsey J. Maccoux, Christian Matthäus, Max Diem, Jan G. Hengstler, and Volker Deckert. Micro-raman detection of nuclear membrane lipid fluctuations in senescent epithelial breast cancer cells. *Analytical Chemistry*, 82(10):4259–4263, 2010.

[81] Beata Brozek-Pluska, Jacek Musial, Radzislaw Kordek, Elena Bailo, Thomas Dieing, and Halina Abramczyk. Raman spectroscopy and imaging: applications in human breast cancer diagnosis. *Analyst*, 137(16):3773–3780, 2012.

[82] Shazza Rehman, Zanyar Movasaghi, Art T. Tucker, Simon P. Joel, Jawwad A. Darr, Alexander V. Ruban, and Ihtesham U. Rehman. Raman spectroscopic analysis of breast cancer tissues: identifying differences between normal, invasive ductal carcinoma and ductal carcinoma in situ of the breast tissue. *Journal of Raman Spectroscopy*, 38(10):1345–1351, 2007.

[83] Kenny Kong, Fazliyana Zaabar, Emad Rakha, Ian Ellis, Alexey Koloydenko, and Ioan Notingher. Towards intra-operative diagnosis of tumours during breast conserving surgery by selective-sampling raman micro-spectroscopy. *Physics in Medicine & Biology*, 59(20):6141–6152, 2014.

[84] Jose E. Gonzalez, Richard G. Caldwell, and Jonas Valaitis. Calcium oxalate crystals in the breast. pathology and significance. *The American Journal of Surgical Pathology*, 15(6):586–591, 1991.

[85] Abigail S. Haka, Karen E. Shafer-Peltier, Maryann Fitzmaurice, Joseph Crowe, Ramachandra R. Dasari, and Michael S. Feld. Identifying microcalcifications in benign and malignant breast lesions by probing differences in their chemical composition using raman spectroscopy. *Cancer Research*, 62(18):5375–5380, 2002.

[86] Nicholas Stone and Pavel Matousek. Advanced transmission raman spectroscopy: A promising tool for breast disease diagnosis. *Cancer Research*, 68(11):4424–4430, 2008.

[87] Ishan Barman, Narahara Chari Dingari, Anushree Saha, Sasha McGee, Luis H. Galindo, Wendy Liu, Donna Plecha, Nina Klein, Ramachandra Rao Dasari,

and Maryann Fitzmaurice. Application of raman spectroscopy to identify microcalcifications and underlying breast lesions at stereotactic core needle biopsy. *Cancer Research*, 73(11):3206–3215, 2013.

[88] Yaliang Yang, Fuhai Li, Liang Gao, Zhiyong Wang, Michael J. Thrall, Steven S. Shen, Kelvin K. Wong, and Stephen T. C. Wong. Differential diagnosis of breast cancer using quantitative, label-free and molecular vibrational imaging. *Biomedical Optics Express*, 2(8):2160–2174, 2011.

[89] Shoji Kaminaka, Hiroya Yamazaki, Toshiaki Ito, Eiichi Kohda, and Hiro-o Hamaguchi. Near-infrared raman spectroscopy of human lung tissues: possibility of molecular-level cancer diagnosis. *Journal of Raman Spectroscopy*, 32(2):139–141, 2001.

[90] Liang Gao, Zhiyong Wang, Fuhai Li, Ahmad A. Hammoudi, Michael J. Thrall, Philip T. Cagle, and Stephen T. C. Wong. Differential diagnosis of lung carcinoma with coherent anti-stokes raman scattering imaging. *Archives of Pathology & Laboratory Medicine*, 136(12):1502–1510, 2012.

[91] Liang S. Gao, Fuhai Li, Yaliang Yang, Jiong Xing, Ahmad A. Hammoudi, Hong Zhao, Yubo Fan, Kelvin K. Wong, Zhiyong Wang, Stephen T. Wong, Michael J. Thrall, Philip T. Cagle, and Yehia Massoud. On-the-spot lung cancer differential diagnosis by label-free, molecular vibrational imaging and knowledge-based classification. *Journal of Biomedical Optics*, 16(9):096004, 2011.

[92] Nicholas D. Magee, Julien S. Villaumie, Eric T. Marple, Madeleine Ennis, J. Stuart Elborn, and John J. McGarvey. Ex vivo diagnosis of lung cancer using a raman miniprobe. *The Journal of Physical Chemistry B*, 113(23):8137–8141, 2009.

[93] M. Gniadecka, H. C. Wulf, N. N. Mortensen, O. F. Nielsen, and D. H. Christensen. Diagnosis of basal cell carcinoma by raman spectroscopy. *Journal of Raman Spectroscopy*, 28(2–3):125–129, 1997.

[94] Annieke Nijssen, Tom C. B. Schut, Freerk Heule, Peter J. Caspers, Donal P. Hayes, Martino H. A. Neumann, and Gerwin J. Puppels. Discriminating basal cell carcinoma from its surrounding tissue by raman spectroscopy. *Journal of Investigative Dermatology*, 119(1):64–69, 2002.

[95] Annieke Nijssen, Kees Maquelin, Luis F. Santos, Peter J. Caspers, Tom C. B. Schut, Jan C. den Hollander, Martino H. A. Neumann, and Gerwin J. Puppels. Discriminating basal cell carcinoma from perilesional skin using high wavenumber raman spectroscopy. *Journal of Biomedical Optics*, 12(3):034004, 2007.

[96] Nadine Vogler, Tobias Meyer, Denis Akimov, Ines Latka, Christoph Krafft, Niels Bendsoe, Katarina Svanberg, Benjamin Dietzek, and Jürgen Popp. Multimodal

imaging to study the morphochemistry of basal cell carcinoma. *Journal of Biophotonics*, 3(10–11):728–736, 2010.

[97] Sandro Heuke, Nadine Vogler, Tobias Meyer, Denis Akimov, Franziska Kluschke, Hans-Joachim Röwert-Huber, Jürgen Lademann, Benjamin Dietzek, and Jürgen Popp. Detection and discrimination of non-melanoma skin cancer by multimodal imaging. *Healthcare*, 1(1):64–83, 2013.

[98] Benito Bodanese, Fabrício Luiz Silveira, Renato Amaro Zângaro, Marcos Tadeu T. Pacheco, Carlos Augusto Pasqualucci, and Landulfo Silveira Jr. Discrimination of basal cell carcinoma and melanoma from normal skin biopsies in vitro through raman spectroscopy and principal component analysis. *Photomedicine and Laser Surgery*, 30(7):381–387, 2012.

[99] Benito Bodanese, Landulfo Silveira Jr, Regiane Albertini, Renato Amaro Zângaro, and Marcos Tadeu Tavares Pacheco. Differentiating normal and basal cell carcinoma human skin tissues in vitro using dispersive raman spectroscopy: A comparison between principal components analysis and simplified biochemical models. *Photomedicine and Laser Surgery*, 28(S1):S119–S127, 2010.

[100] Jacques Ferlay, Isabelle Soerjomataram, Rajesh Dikshit, Sultan Eser, Colin Mathers, Marise Rebelo, Donald Maxwell Parkin, David Forman, and Freddie Bray. Cancer incidence and mortality worldwide: Sources, methods and major patterns in globocan 2012. *International Journal of Cancer*, 136(5):E359–E386, 2015.

[101] Senada Koljenović, Tom C. Bakker Schut, Rolf Wolthuis, B. de Jong, L. Santos, Peter J. Caspers, Johan M. Kros, and Gerwin J. Puppels. Tissue characterization using high wave number raman spectroscopy. *Journal of Biomedical Optics*, 10(3):031116, 2005.

[102] S. Koljenović, T. C. Bakker Schut, R. Wolthuis, A. J. P. E. Vincent, G. Hendriks-Hagevi, L. Santos, J. M. Kros, and G. J. Puppels. Raman spectroscopic characterization of porcine brain tissue using a single fiber-optic probe. *Analytical chemistry*, 79(2):557–564, 2007.

[103] Christoph Krafft, Stephan B. Sobottka, Gabriele Schackert, and Reiner Salzer. Raman and infrared spectroscopic mapping of human primary intracranial tumors: a comparative study. *Journal of Raman Spectroscopy*, 37(1–3):367–375, 2006.

[104] Christoph Krafft, Birhanu Belay, Norbert Bergner, Bernd F. M. Romeike, Rupert Reichart, Rolf Kalff, and Jürgen Popp. Advances in optical biopsy — correlation of malignancy and cell density of primary brain tumors using raman microspectroscopic imaging. *Analyst*, 137(23):5533–5537, 2012.

[105] Norbert Bergner, Anna Medyukhina, Kathrin D. Geiger, Matthias Kirsch, Gabriele Schackert, Christoph Krafft, and Jürgen Popp. Hyperspectral unmixing of raman micro-images for assessment of morphological and chemical parameters in non-dried brain tumor specimens. *Analytical and Bioanalytical Chemistry*, 405(27):8719–8728, 2013.

[106] Conor L. Evans, Xiaoyin Xu, Santosh Kesari, X. Sunney Xie, Stephen T. C. Wong, and Geoffrey S. Young. Chemically-selective imaging of brain structures with cars microscopy. *Optics Express*, 15(19):12076–12087, 2007.

[107] Ortrud Uckermann, Roberta Galli, Sandra Tamosaityte, Elke Leipnitz, Kathrin D. Geiger, Gabriele Schackert, Edmund Koch, Gerald Steiner, and Matthias Kirsch. Label-free delineation of brain tumors by coherent anti-stokes raman scattering microscopy in an orthotopic mouse model and human glioblastoma. *PLOS ONE*, 9(9):e107115, 2014.

[108] Tobias Meyer, Norbert Bergner, Christoph Krafft, Denis Akimov, Benjamin Dietzek, Jürgen Popp, Christiane Bielecki, Bernd F. M. Romeike, Rupert Reichart, and Rolf Kalff. Nonlinear microscopy, infrared, and raman microspectroscopy for brain tumor analysis. *Journal of Biomedical Optics*, 16(2):021113, 2011.

[109] Minbiao Ji, Daniel A. Orringer, Christian W. Freudiger, Shakti Ramkissoon, Xiaohui Liu, Darryl Lau, Alexandra J. Golby, Isaiah Norton, Marika Hayashi, Nathalie Y. R. Agar, Geoffrey S. Young, Cathie Spino, Sandro Santagata, Sandra Camelo-Piragua, Keith L. Ligon, Oren Sagher, and X. Sunney Xie. Rapid, label-free detection of brain tumors with stimulated raman scattering microscopy. *Science Translational Medicine*, 5(201):201ra119, 2013.

[110] Bruce A. Ruggeri, Faye Camp, and Sheila Miknyoczki. Animal models of disease: Pre-clinical animal models of cancer and their applications and utility in drug discovery. *Biochemical Pharmacology*, 87(1):150–161, 2014.

[111] Abdelilah Beljebbar, Sylvain Dukic, Nadia Amharref, and Michel Manfait. Ex vivo and in vivo diagnosis of c6 glioblastoma development by raman spectroscopy coupled to a microprobe. *Analytical and Bioanalytical Chemistry*, 398(1):477–487, 2010.

[112] Matthias Kirsch, Gabriele Schackert, Reiner Salzer, and Christoph Krafft. Raman spectroscopic imaging for in vivo detection of cerebral brain metastases. *Analytical and Bioanalytical Chemistry*, 398(4):1707–1713, 2010.

[113] Moritz F. Kircher, Adam de la Zerda, Jesse V. Jokerst, Cristina L. Zavaleta, Paul J. Kempen, Erik Mittra, Ken Pitter, Ruimin Huang, Carl Campos, Frezghi Habte, Robert Sinclair, Cameron W. Brennan, Ingo K. Mellinghoff, Eric C. Holland, and Sanjiv S. Gambhir. A brain tumor molecular imaging strategy using a new triple-modality mri-photoacoustic-raman nanoparticle. *Nature Medicine*, 18(5):829–834, 2012.

[114] Hazem Karabeber, Ruimin Huang, Pasquale Iacono, Jason M. Samii, Ken Pitter, Eric C. Holland, and Moritz F. Kircher. Guiding brain tumor resection using surface-enhanced raman scattering nanoparticles and a hand-held raman scanner. *ACS Nano*, 8(10):9755–9766, 2014.

[115] Kevin Petrecca, Marie-Christine Guiot, Valerie Panet-Raymond, and Luis Souhami. Failure pattern following complete resection plus radiotherapy and temozolomide is at the resection margin in patients with glioblastoma. *Journal of Neuro-Oncology*, 111(1):19–23, 2013.

[116] T. Bhattacharjee, Piyush Kumar, G. Maru, A. Ingle, and C. Murali Krishna. Swiss bare mice: a suitable model for transcutaneous in vivo raman spectroscopic studies of breast cancer. *Lasers in Medical Science*, 29(1):325–333, 2014.

[117] Jun Qian, Li Jiang, Fuhong Cai, Dan Wang, and Sailing He. Fluorescence-surface enhanced raman scattering co-functionalized gold nanorods as near-infrared probes for purely optical in vivo imaging. *Biomaterials*, 32(6):1601–1610, 2011.

[118] U. S. Dinish, Ghayathri Balasundaram, Young-Tae Chang, and Malini Olivo. Actively targeted in vivo multiplex detection of intrinsic cancer biomarkers using biocompatible sers nanotags. *Scientific Reports*, 4:4075, 2014.

[119] Sinyoung Jeong, Yong-il Kim, Homan Kang, Gunsung Kim, Myeong Geun Cha, Hyejin Chang, Kyung Oh Jung, Young-Hwa Kim, Bong-Hyun Jun, Do Won Hwang, Yun-Sang Lee, Hyewon Youn, Yoon-Sik Lee, Keon Wook Kang, Dong Soo Lee, and Dae Hong Jeong. Fluorescence-raman dual modal endoscopic system for multiplexed molecular diagnostics. *Scientific Reports*, 5:9455, 2015.

[120] Harvey Lui, Jianhua Zhao, David McLean, and Haishan Zeng. Real-time raman spectroscopy for in vivo skin cancer diagnosis. *Cancer Research*, 72(10):2491–2500, 2012.

[121] Hequn Wang, Jianhua Zhao, Anthony M. D. Lee, Harvey Lui, and Haishan Zeng. Improving skin raman spectral quality by fluorescence photobleaching. *Photodiagnosis and Photodynamic Therapy*, 9(4):299–302, 2012.

[122] Jianhua Zhao, Harvey Lui, Sunil Kalia, and Haishan Zeng. Real-time raman spectroscopy for automatic in vivo skin cancer detection: an independent validation. *Analytical and Bioanalytical Chemistry*, 407(27):8373–8379, 2015.

[123] Johannes Schleusener, Patrycja Gluszczynska, Carina Reble, Ingo Gersonde, Jürgen Helfmann, Joachim W. Fluhr, Jürgen Lademann, Joachim Röwert-Huber, Alexa Patzelt, and Martina C. Meinke. In vivo study for the discrimination of cancerous and normal skin using fibre probe-based raman spectroscopy. *Experimental Dermatology*, 24(10):767–772, 2015.

[124] P. A. Philipsen, L. Knudsen, M. Gniadecka, M. H. Ravnbak, and H. C. Wulf. Diagnosis of malignant melanoma and basal cell carcinoma by in vivo nir-ft raman spectroscopy is independent of skin pigmentation. *Photochemical & Photobiological Sciences*, 12(5):770–776, 2013.

[125] Liang Lim, Brandon S. Nichols, Michael R. Migden, Narasimhan Rajaram, Jason Reichenberg, Mia K. Markey, Merrick I. Ross, and James W. Tunnell. Clinical study of noninvasive in vivo melanoma and nonmelanoma skin cancers using multimodal spectral diagnosis. *Journal of Biomedical Optics*, 19(11):117003, 2014.

[126] Valery P. Zakharov, Ivan A. Bratchenko, Dmitry N. Artemyev, Oleg O. Myakinin, Dmitry V. Kornilin, Sergey V. Kozlov, and Alexander A. Moryatov. Comparative analysis of combined spectral and optical tomography methods for detection of skin and lung cancers. *Journal of Biomedical Optics*, 20(2):025003, 2015.

[127] S. P. Singh, Atul Deshmukh, Pankaj Chaturvedi, and C. Murali Krishna. Raman spectroscopy in head and neck cancers: Toward oncological applications. *Journal of Cancer Research and Therapeutics*, 8(6):126–132, 2012.

[128] S. P. Singh, Atul Deshmukh, Pankaj Chaturvedi, and C. Murali Krishna. In vivo raman spectroscopic identification of premalignant lesions in oral buccal mucosa. *Journal of Biomedical Optics*, 17(10):105002, 2012.

[129] S. P. Singh, Aditi Sahu, Atul Deshmukh, Pankaj Chaturvedi, and C. Murali Krishna. In vivo raman spectroscopy of oral buccal mucosa: a study on malignancy associated changes (mac)/cancer field effects (cfe). *Analyst*, 138(14):4175–4182, 2013.

[130] Zhiwei Huang, Mads Sylvest Bergholt, Wei Zheng, Kan Lin, Khek-Yu Ho, Ming Teh, and Khay-Guan Yeoh. In vivo early diagnosis of gastric dysplasia using narrow-band image-guided raman endoscopy. *Journal of Biomedical Optics*, 15(3):037017, 2010.

[131] Zhiwei Huang, Seng Khoon Teh, Wei Zheng, Kan Lin, Khek Yu Ho, Ming Teh, and Khay Guan Yeoh. In vivo detection of epithelial neoplasia in the stomach using image-guided raman endoscopy. *Biosensors and Bioelectronics*, 26(2):383–389, 2010.

[132] Mads Sylvest Bergholt, Wei Zheng, Kan Lin, Khek Yu Ho, Ming Teh, Khay Guan Yeoh, Jimmy Bok Yan So, and Zhiwei Huang. Raman endoscopy for in vivo differentiation between benign and malignant ulcers in the stomach. *Analyst*, 135(12):3162–3168, 2010.

[133] Mads Sylvest Bergholt, Wei Zheng, Kan Lin, Khek Yu Ho, Ming Teh, Khay Guan Yeoh, Jimmy Bok Yan So, and Zhiwei Huang. In vivo diagnosis of

gastric cancer using raman endoscopy and ant colony optimization techniques. *International Journal of Cancer*, 128(11):2673–2680, 2011.

[134] Catherine Kendall, John Day, Joanne Hutchings, Brian Smith, Neil Shepherd, Hugh Barr, and Nicholas Stone. Evaluation of raman probe for oesophageal cancer diagnostics. *Analyst*, 135(12):3038–3041, 2010.

[135] L. Max Almond, Jo Hutchings, Gavin Lloyd, Hugh Barr, Neil Shepherd, John Day, Oliver Stevens, Scott Sanders, Martin Wadley, Nick Stone, and Catherine Kendall. Endoscopic raman spectroscopy enables objective diagnosis of dysplasia in barrett's esophagus. *Gastrointestinal Endoscopy*, 79(1):37–45, 2014.

[136] Mads S. Bergholt, Wei Zheng, Kan Lin, Zhiwei Huang, Khek Yu Ho, Khay Guan Yeoh, Ming Teh, and Jimmy Bok Yan So. Characterizing variability in in vivo raman spectra of different anatomical locations in the upper gastrointestinal tract toward cancer detection. *Journal of Biomedical Optics*, 16(3):037003, 2011.

[137] Mads Sylvest Bergholt, Wei Zheng, Kan Lin, Khek Yu Ho, Ming Teh, Khay Guan Yeoh, Jimmy Bok Yan So, and Zhiwei Huang. Combining near-infrared-excited autofluorescence and raman spectroscopy improves in vivo diagnosis of gastric cancer. *Biosensors and Bioelectronics*, 26(10):4104–4110, 2011.

[138] M. S. Bergholt, W. Zheng, K. Lin, K. Y. Ho, M. Teh, K. G. Yeoh, J. B. Y. So, and Z. Huang. In vivo diagnosis of esophageal cancer using image-guided raman endoscopy and biomolecular modeling. *Technology in Cancer Research & Treatment*, 10(2):103–112, 2011.

[139] Shiyamala Duraipandian, Mads Sylvest Bergholt, Wei Zheng, Khek Yu Ho, Ming Teh, Khay Guan Yeoh, Jimmy Bok Yan So, Asim Shabbir, and Zhiwei Huang. Real-time raman spectroscopy for in vivo, online gastric cancer diagnosis during clinical endoscopic examination. *Journal of Biomedical Optics*, 17(8):081418, 2012.

[140] Mads Sylvest Bergholt, Wei Zheng, Khek Yu Ho, Ming Teh, Khay Guan Yeoh, Jimmy Bok Yan So, Asim Shabbir, and Zhiwei Huang. Fiber-optic raman spectroscopy probes gastric carcinogenesis in vivo at endoscopy. *Journal of Biophotonics*, 6(1):49–59, 2013.

[141] Mads Sylvest Bergholt, Wei Zheng, Khek Yu Ho, Ming Teh, Khay Guan Yeoh, Jimmy Bok Yan So, Asim Shabbir, and Zhiwei Huang. Fiberoptic confocal raman spectroscopy for real-time in vivo diagnosis of dysplasia in barrett's esophagus. *Gastroenterology*, 146(1):27–32, 2014.

[142] Jianfeng Wang, Kan Lin, Wei Zheng, Khek Yu Ho, Ming Teh, Khay Guan Yeoh, and Zhiwei Huang. Comparative study of the endoscope-based bevelled and volume fiber-optic raman probes for optical diagnosis of gastric dysplasia in

vivo at endoscopy. *Analytical and Bioanalytical Chemistry*, 407(27):8303–8310, 2015.

[143] Jianfeng Wang, Kan Lin, Wei Zheng, Khek Yu Ho, Ming Teh, Khay Guan Yeoh, and Zhiwei Huang. Simultaneous fingerprint and high-wavenumber fiber-optic raman spectroscopy improves in vivo diagnosis of esophageal squamous cell carcinoma at endoscopy. *Scientific Reports*, 5:12957, 2015.

[144] Mads Sylvest Bergholt, Wei Zheng, Kan Lin, Jianfeng Wang, Hongzhi Xu, Jian-lin Ren, Khek Yu Ho, Ming Teh, Khay Guan Yeoh, and Zhiwei Huang. Characterizing variability of in vivo raman spectroscopic properties of different anatomical sites of normal colorectal tissue towards cancer diagnosis at colonoscopy. *Analytical Chemistry*, 87(2):960–966, 2015.

[145] Elizabeth Vargis, Elizabeth M. Kanter, Shovan K. Majumder, Matthew D. Keller, Richard B. Beaven, Gautam G. Rao, and Anita Mahadevan-Jansen. Effect of normal variations on disease classification of raman spectra from cervical tissue. *Analyst*, 136(14):2981–2987, 2011.

[146] Shiyamala Duraipandian, Wei Zheng, Joseph Ng, Jeffrey J. H. Low, A. Ilancheran, and Zhiwei Huang. In vivo diagnosis of cervical precancer using raman spectroscopy and genetic algorithm techniques. *Analyst*, 136(20):4328–4336, 2011.

[147] Shiyamala Duraipandian, Wei Zheng, Joseph Ng, Jeffrey J. H. Low, A. Ilancheran, and Zhiwei Huang. Simultaneous fingerprint and high-wavenumber confocal raman spectroscopy enhances early detection of cervical precancer in vivo. *Analytical Chemistry*, 84(14):5913–5919, 2012.

[148] Shiyamala Duraipandian, Wei Zheng, Joseph Ng, Jeffrey J. Low, Arunachalam Ilancheran, and Zhiwei Huang. Near-infrared-excited confocal raman spectroscopy advances in vivo diagnosis of cervical precancer. *Journal of Biomedical Optics*, 18(6):067007, 2013.

[149] Rubina S. Shaikh, Tapas Kumar Dora, Supriya Chopra, Amita Maheshwari, Deodhar K. Kedar, Rekhi Bharat, and C. Murali Krishna. In vivo raman spectroscopy of human uterine cervix: exploring the utility of vagina as an internal control. *Journal of Biomedical Optics*, 19(8):087001, 2014.

[150] Joannie Desroches, Michael Jermyn, Kelvin Mok, Cédric Lemieux-Leduc, Jeanne Mercier, Karl St-Arnaud, Kirk Urmey, Marie-Christine Guiot, Eric Marple, Kevin Petrecca, and Frédéric Leblond. Characterization of a raman spectroscopy probe system for intraoperative brain tissue classification. *Biomedical Optics Express*, 6(7):2380–2397, 2015.

[151] June K Robinson. Sun exposure, sun protection, and vitamin d. *Jama*, 294(12):1541–1543, 2005.

[152] Elisabeth Thieden, Peter A. Philipsen, Jane Sandby-Møller, and Hans Christian Wulf. Sunscreen use related to uv exposure, age, sex, and occupation based on personal dosimeter readings and sun-exposure behavior diaries. *Archives of Dermatology*, 141(8):967–973, 2005.

[153] Adèle C. Green, Gail M. Williams, Valerie Logan, and Geoffrey M. Strutton. Reduced melanoma after regular sunscreen use: Randomized trial follow-up. *Journal of Clinical Oncology*, 29(3):257–263, 2011.

[154] Michael Huncharek and Bruce Kupelnick. Use of topical sunscreens and the risk of malignant melanoma: A meta-analysis of 9067 patients from 11 case-control studies. *American Journal of Public Health*, 92(7):1173–1177, 2002.

[155] Kerry M. Hanson, Enrico Gratton, and Christopher J. Bardeen. Sunscreen enhancement of uv-induced reactive oxygen species in the skin. *Free Radical Biology and Medicine*, 41(8):1205–1212, 2006.

[156] Jutta Kockler, Michael Oelgemöller, Sherryl Robertson, and Beverley D. Glass. Photostability of sunscreens. *Journal of Photochemistry and Photobiology C: Photochemistry Reviews*, 13(1):91–110, 2012.

[157] Chikako Nishigori, Yukari Hattori, and Shinya Toyokuni. Role of reactive oxygen species in skin carcinogenesis. *Antioxidants and Redox Signaling*, 6(3):561–570, 2004.

[158] Kerry M. Hanson and Christopher J. Bardeen. Application of nonlinear optical microscopy for imaging skin. *Photochemistry and Photobiology*, 85(1):33–44, 2009.

[159] Mark Rinnerthaler, Johannes Bischof, Maria Karolin Streubel, Andrea Trost, and Klaus Richter. Oxidative stress in aging human skin. *Biomolecules*, 5(2):545–589, 2015.

[160] Steven Q. Wang and Henry W. Lim. *Principles and Practice of Photoprotection.* Springer, 2016.

[161] Kyle P. Quinn, Evangelia Bellas, Nikolaos Fourligas, Kyongbum Lee, David L. Kaplan, and Irene Georgakoudi. Characterization of metabolic changes associated with the functional development of 3d engineered tissues by non-invasive, dynamic measurement of individual cell redox ratios. *Biomaterials*, 33(21):5341–5348, 2012.

[162] Kyle P. Quinn, Gautham V. Sridharan, Rebecca S. Hayden, David L. Kaplan, Kyongbum Lee, and Irene Georgakoudi. Quantitative metabolic imaging using endogenous fluorescence to detect stem cell differentiation. *Scientific Reports*, 3:3432, 2013.

[163] Biana Godin and Elka Touitou. Transdermal skin delivery: Predictions for humans from in vivo, ex vivo and animal models. *Advanced Drug Delivery Reviews*, 59(11):1152–1161, 2007.

[164] Irene Georgakoudi and Kyle P. Quinn. Optical imaging using endogenous contrast to assess metabolic state. *Annual Review of Biomedical Engineering*, 14:351–367, 2012.

[165] Melissa C. Skala, Kristin M. Riching, Annette Gendron-Fitzpatrick, Jens Eickhoff, Kevin W. Eliceiri, John G. White, and Nirmala Ramanujam. In vivo multiphoton microscopy of nadh and fad redox states, fluorescence lifetimes, and cellular morphology in precancerous epithelia. *Proceedings of the National Academy of Sciences*, 104(49):19494–19499, 2007.

[166] Ahmed A. Heikal. Intracellular coenzymes as natural biomarkers for metabolic activities and mitochondrial anomalies. *Biomarkers in Medicine*, 4(2):241–263, 2010.

[167] Rupsa Datta, Alba Alfonso-García, Rachel Cinco, and Enrico Gratton. Fluorescence lifetime imaging of endogenous biomarker of oxidative stress. *Scientific Reports*, 5:9848, 2015.

[168] Carlo Amadeo Alonzo, Sevasti Karaliota, Dimitra Pouli, Zhiyi Liu, Katia P. Karalis, and Irene Georgakoudi. Two-photon excited fluorescence of intrinsic fluorophores enables label-free assessment of adipose tissue function. *Scientific Reports*, 6:31012, 2016.

[169] Steven Q. Wang and Henry W. Lim. Current status of the sunscreen regulation in the united states: 2011 food and drug administration's final rule on labeling and effectiveness testing. *Journal of the American Academy of Dermatology*, 65(4):863–869, 2011.

[170] R. P. Stokes and B. L. Diffey. The feasibility of using fluorescence spectroscopy as a rapid, non-invasive method for evaluating sunscreen performance. *Journal of Photochemistry and Photobiology B: Biology*, 50(2–3):137–143, 1999.

[171] Ann Cantrell, David J. McGarvey, and T. George Truscott. Photochemical and photophysical properties of sunscreens. In *Comprehensive Series in Photosciences*, volume 3, chapter 26, pages 495–519. Elsevier, 2001.

[172] Karsten Koenig. Hybrid multiphoton multimodal tomography of in vivo human skin. *IntraVital*, 1(1):11–26, 2012.

[173] Joanna Xylas, Antonio Varone, Kyle P. Quinn, Dimitra Pouli, Margaret E. McLaughlin-Drubin, Hong-Thao Thieu, Maria L. Garcia-Moliner, Michael House, Martin Hunter, Karl Munger, and Irene Georgakoudi. Noninvasive assessment of mitochondrial organization in three-dimensional tissues reveals changes associated with cancer development. *International Journal of Cancer*, 136(2):322–332, 2015.

[174] Adam D. Dunkelberger, Ryan D. Kieda, Brett M. Marsh, and F. Fleming Crim. Picosecond dynamics of avobenzone in solutio. *The Journal of Physical Chemistry A*, 119(24):6155–6161, 2015.

[175] Thomas B. Fitzpatrick. The validity and practicality of sun-reactive skin types i through vi. *Archives of Dermatology*, 124(6):869–871, 1988.

[176] Madhu A. Pathak, Kowichi Jimbow, George Szabo, and Thomas B. Fitzpatrick. Sunlight and melanin pigmentation. In *Photochemical and Photobiological Reviews*, volume 1, chapter 5, pages 211–239. Springer, 1976.

[177] Pirmin H. Lakner, Michael G. Monaghan, Yvonne Möller, Monilola A. Olayioye, and Katja Schenke-Layland. Applying phasor approach analysis of multiphoton flim measurements to probe the metabolic activity of three-dimensional in vitro cell culture models. *Scientific Reports*, 7:42730, 2017.

[178] Chiara Stringari, Jamison L. Nourse, Lisa A. Flanagan, and Enrico Gratton. Phasor fluorescence lifetime microscopy of free and protein-bound nadh reveals neural stem cell differentiation potential. *PLOS ONE*, 7(11):e48014, 2012.

[179] Thomas H. Chia, Anne Williamson, Dennis D. Spencer, and Michael J. Levene. Multiphoton fluorescence lifetime imaging of intrinsic fluorescence in human and rat brain tissue reveals spatially distinct nadh binding. *Optics Express*, 16(6):4237–4249, 2008.

[180] Mohammad A. Yaseen, Jason Sutin, Weicheng Wu, Buyin Fu, Hana Uhlirova, Anna Devor, David A. Boas, and Sava Sakadžić. Fluorescence lifetime microscopy of nadh distinguishes alterations in cerebral metabolism in vivo. *Biomedical Optics Express*, 8(5):2368–2385, 2017.

[181] P. C. Mahalanobis. On the generalized distance in statistics. *Proceedings of the National Institute of Sciences of India*, 2(1):49–55, 1936.

[182] R. M. Lavker, D. A. Veres, C. J. Irwin, and K. H. Kaidbey. Quantitative assessment of cumulative damage from repetitive exposures to suberythemogenic doses of uva in human skin. *Photochemistry and Photobiology*, 62(2):348–352, 1995.

[183] Sepideh Maleki, Sandeep Gopalakrishnan, Zahra Ghanian, Reyhaneh Sepehr, Heather Schmitt, Janis T. Eells, and Mahsa Ranji. Optical imaging of mitochondrial redox state in rodent model of retinitis pigmentosa. *Journal of Biomedical Optics*, 18(1):016004, 2013.

[184] Kerry M Hanson and Robert M Clegg. Observation and quantification of ultraviolet-induced reactive oxygen species in ex vivo human skin. *Photochemistry and Photobiology*, 76(1):57–63, 2002.

[185] John M. Allen, Cindy J. Gossett, and Sandra K. Allen. Photochemical formation of singlet molecular oxygen ($^1o_2$) in illuminated aqueous solutions of p-aminobenzoic acid (paba). *Journal of Photochemistry and Photobiology B: Biology*, 32(1–2):33–37, 1996.

[186] John M. Allen, Cynthia J. Gossett, and Sandra K. Allen. Photochemical formation of singlet molecular oxygen in illuminated aqueous solutions of several commercially available sunscreen active ingredients. *Chemical Research in Toxicology*, 9(3):605–609, 1996.

[187] E. Gilbert, F. Pirot, V. Bertholle, L. Roussel, F. Falson, and K. Padois. Commonly used uv filter toxicity on biological functions: review of last decade studies. *International Journal of Cosmetic Science*, 35(3):208–219, 2013.

[188] Karsten König, Anthony P. Raphael, Li Lin, Jeffrey E. Grice, H. Peter Soyer, H. Georg Breunig, Michael S. Roberts, and Tarl W. Prow. Applications of multiphoton tomographs and femtosecond laser nanoprocessing microscopes in drug delivery research. *Advanced Drug Delivery Reviews*, 63(4–5):388–404.

[189] Peter J. Verveer and Philippe I. H. Bastiaens. Evaluation of global analysis algorithms for single frequency fluorescence lifetime imaging microscopy data. *Journal of Microscopy*, 209(1):1–7, 2003.

[190] A. H. A. Clayton, Q. S. Hanley, and P. J. Verveer. Graphical representation and multicomponent analysis of single-frequency fluorescence lifetime imaging microscopy data. *Journal of Microscopy*, 213(1):1–5, 2004.

[191] Paolo P. Provenzano, Kevin W. Eliceiri, and Patricia J. Keely. Multiphoton microscopy and fluorescence lifetime imaging microscopy (flim) to monitor metastasis and the tumor microenvironment. *Clinical & Experimental Metastasis*, 26(4):357–370, 2009.

[192] Hsing-Wen Wang, Vladimir Ghukasyan, Chien-Tsun Chen, Yau-Huei Wei, Han-Wen Guo, Jia-Sin Yu, and Fu-Jen Kao. Differentiation of apoptosis from necrosis by dynamic changes of reduced nicotinamide adenine dinucleotide fluorescence lifetime in live cells. *Journal of Biomedical Optics*, 13(5):054011, 2008.

[193] Riccardo Cicchi, Alfonso Crisci, Alessandro Cosci, Gabriella Nesi, Dimitrios Kapsokalyvas, Saverio Giancane, Marco Carini, and Francesco S. Pavone. Time- and spectral-resolved two-photon imaging of healthy bladder mucosa and carcinoma in situ. *Optics Express*, 18(4):3840–3849, 2010.

[194] Farzad Fereidouni, Arjen N. Bader, and Hans C. Gerritsen. Spectral phasor analysis allows rapid and reliable unmixing of fluorescence microscopy spectral images. *Optics Express*, 20(12):12729–12741, 2012.

[195] A. A. Romanovsky. Skin temperature: its role in thermoregulation. *Acta Physiologica*, 210(3):498–507, 2014.

[196] Yasmine Belkaid and Julia A. Segre. Dialogue between skin microbiota and immunity. *Science*, 346(6212):954–959, 2014.

[197] Amanda Zimmerman, Ling Bai, and David D. Ginty. The gentle touch receptors of mammalian skin. *Science*, 346(6212):950–954, 2014.

[198] Daniel D. Bikle. Vitamin d metabolism and function in the skin. *Molecular and Cellular Endocrinology*, 347(1–2):80–89, 2011.

[199] Ehrhardt Proksch, Johanna M. Brandner, and Jens-Michael Jensen. The skin: an indispensable barrier. *Experimental Dermatology*, 17(12):1063–1072, 2008.

[200] A. V. Rawlings and C. R. Harding. Moisturization and skin barrier function. *Dermatologic Therapy*, 17(s1):43–48, 2004.

[201] Sylvie Verdier-Sévrain and Frédéric Bonté. Skin hydration: a review on its molecular mechanisms. *Journal of Cosmetic Dermatology*, 6(2):75–82, 2007.

[202] Akemi Ishida-Yamamoto, Satomi Igawa, and Mari Kishibe. Order and disorder in corneocyte adhesion. *The Journal of Dermatology*, 38(7):645–654, 2011.

[203] C. R. Harding, A. Watkinson, A. V. Rawlings, and I. R. Scott. Dry skin, moisturization and corneodesmolysis. *International Journal of Cosmetic Science*, 22(1):21–52, 2000.

[204] Anthony V. Rawlings and Paul J. Matts. Stratum corneum moisturization at the molecular level: An update in relation to the dry skin cycle. *Journal of Investigative Dermatology*, 124(6):1099–1110, 2005.

[205] Marie Lodén. Role of topical emollients and moisturizers in the treatment of dry skin barrier disorders. *American Journal of Clinical Dermatology*, 4(11):771–788, 2003.

[206] A. V. Rawlings. Trends in stratum corneum research and the management of dry skin conditions. *International Journal of Cosmetic Science*, 25(1–2):63–95, 2003.

[207] Marie Lodén. Effect of moisturizers on epidermal barrier function. *Clinics in Dermatology*, 30(3):286–296, 2012.

[208] Claudia L. Froebe, F. Anthony Simion, H. Ohlmeyer, Linda D. Rhein, Jairajh Mattai, Robert H. Cagan, and Stig E. Friberg. Prevention of stratum corneum lipid phase transitions in vitro by glycerol — an alternative mechanism for skin moisturization. *Journal of the Society of Cosmetic Chemists*, 41(1):51–65, 1990.

[209] U. Heinrich, U. Koop, M.-C. Leneveu-Duchemin, K. Osterrieder, S. Bielfeldt, C. Chkarnat, J. Degwert, D. Häntschel, S. Jaspers, H.-P. Nissen, M. Rohr, G. Schneider, and H. Tronnier. Multicentre comparison of skin hydration in

terms of physical-, physiological-and product-dependent parameters by the capacitive method (corneometer cm 825). *International Journal of Cosmetic Science*, 25(1–2):45–53, 2003.

[210] Peter Clarys, Ron Clijsen, and André O. Barel. Influence of probe application pressure on in vitro and in vivo capacitance (corneometer cm 825®) and conductance (skicon 200 ex®) measurements. *Skin Research and Technology*, 17(4):445–450, 2011.

[211] Peter Clarys, Ron Clijsen, Jan Taeymans, and André O. Barel. Hydration measurements of the stratum corneum: comparison between the capacitance method (digital version of the corneometer cm 825®) and the impedance method (skicon-200ex®). *Skin Research and Technology*, 18(3):316–323, 2012.

[212] Esko Alanen, Jouni Nuutinen, Kirsi Nicklén, Tapani Lahtinen, and Jukka Mönkkönen. Measurement of hydration in the stratum corneum with the moisturemeter and comparison with the corneometer. *Skin Research and Technology*, 10(1):32–37, 2004.

[213] J. W. Fluhr, R. Darlenski, N. Lachmann, C. Baudouin, P. Msika, C. De Belilovsky, and J.-P. Hachem. Infant epidermal skin physiology: adaptation after birth. *British Journal of Dermatology*, 166(3):483–490, 2012.

[214] Weon Ju Lee, Jun Young Kim, Chang Hyun Song, Hong Dae Jung, Su Hyun Lee, Seok-Jong Lee, and Do Won Kim. Disruption of barrier function in dermatophytosis and pityriasis versicolor. *The Journal of Dermatology*, 38(11):1049–1053, 2011.

[215] Assaf Eliezer Sagiv, Shabtay Dikstein, and Arieh Ingber. The efficiency of humectants as skin moisturizers in the presence of oil. *Skin Research and Technology*, 7(1):32–35, 2001.

[216] Jeffrey L. Sugarman, Joachim W. Fluhr, Ashley J. Fowler, Thomas Bruckner, Thomas L. Diepgen, and Mary L. Williams. The objective severity assessment of atopic dermatitis score: An objective measure using permeability barrier function and stratum corneum hydration with computer-assisted estimates for extent of disease. *Archives of Dermatology*, 139(11):1417–1422, 2003.

[217] Joke A. Bouwstra, Anko de Graaff, Gert S. Gooris, Jaap Nijsse, Johann W. Wiechers, and Adriaan C. van Aelst. Water distribution and related morphology in human stratum corneum at different hydration levels. *Journal of Investigative Dermatology*, 120(5):750–758, 2003.

[218] Volker Andresen, Stephanie Alexander, Wolfgang-Moritz Heupel, Markus Hirschberg, Robert M. Hoffman, and Peter Friedl. Infrared multiphoton microscopy: subcellular-resolved deep tissue imaging. *Current Opinion in Biotechnology*, 20(1):54–62, 2009.

[219] Herbert Schneckenburger, Petra Weber, Michael Wagner, Thomas Bruns, Verena Richter, Sarah Schickinger, and Rainer Wittig. Multidimensional fluorescence microscopy in live cell imaging — a mini review. *Photonics & Lasers in Medicine*, 1(1):35–40, 2012.

[220] Chris Xu, Warren Zipfel, Jason B. Shear, Rebecca M. Williams, and Watt W. Webb. Multiphoton fluorescence excitation: new spectral windows for biological nonlinear microscopy. *Proceedings of the National Academy of Sciences*, 93(20):10763–10768, 1996.

[221] Nisma Mujahid, Yanke Liang, Ryo Murakami, Hwan Geun Choi, Allison S. Dobry, Jinhua Wang, Yusuke Suita, Qing Yu Weng, Jennifer Allouche, Lajos V. Kemeny, Andrea L. Hermann, Elisabeth M. Roider, Nathanael S. Gray, and David E. Fisher. A uv-independent topical small-molecule approach for melanin production in human skin. *Cell Reports*, 19(11):2177–2184, 2017.

[222] Dan Fu, Gary Holtom, Christian Freudiger, Xu Zhang, and Xiaoliang Sunney Xie. Hyperspectral imaging with stimulated raman scattering by chirped femtosecond lasers. *The Journal of Physical Chemistry B*, 117(16):4634–4640, 2013.

[223] Eric O. Potma, Wim P. de Boeij, Peter J. M. van Haastert, and Douwe A. Wiersma. Real-time visualization of intracellular hydrodynamics in single living cells. *Proceedings of the National Academy of Sciences*, 98(4):1577–1582, 2001.

[224] Thomas Hellerer, Annika M. K. Enejder, and Andreas Zumbusch. Spectral focusing: High spectral resolution spectroscopy with broad-bandwidth laser pulses. *Applied Physics Letters*, 85(1):25–27, 2004.

[225] Wolfgang Langbein, Israel Rocha-Mendoza, and Paola Borri. Coherent anti-stokes raman micro-spectroscopy using spectral focusing: theory and experiment. *Journal of Raman Spectroscopy*, 40(7):800–808, 2009.

[226] Joachim W. Fluhr, Max Gloor, Sabrina Lazzerini, Peter Kleesz, Romano Grieshaber, and Enzo Berardesca. Comparative study of five instruments measuring stratum corneum hydration (corneometer cm 820 and cm 825, skicon 200, nova dpm 9003, dermalab). part i. in vitro. *Skin Research and Technology*, 5(3):161–170, 1999.

[227] Joachim W. Fluhr, Kenneth R. Feingold, and Peter M. Elias. Transepidermal water loss reflects permeability barrier status: validation in human and rodent in vivo and ex vivo models. *Experimental Dermatology*, 15(7):483–492, 2006.

[228] Stephan Pfeiffer, Gabriele Vielhaber, Jens-Peter Vietzke, Klaus-Peter Wittern, Ulrich Hintze, and Roger Wepf. High-pressure freezing provides new information on human epidermis: Simultaneous protein antigen and lamellar lipid structure preservation. study on human epidermis by cryoimmobilization. *Journal of Investigative Dermatology*, 114(5):1030–1038, 2000.

[229] X. Chen, P. Gasecka, F. Formanek, J.-B. Galey, and H. Rigneault. In vivo single human sweat gland activity monitoring using coherent anti-stokes raman scattering and two-photon excited autofluorescence microscopy. *British Journal of Dermatology*, 174(4):803–812, 2016.

[230] Paul J. Campagnola and Leslie M. Loew. Second-harmonic imaging microscopy for visualizing biomolecular arrays in cells, tissues and organisms. *Nature Biotechnology*, 21(11):1356–1360, 2003.

[231] J. W. Fluhr, R. Darlenski, and C. Surber. Glycerol and the skin: holistic approach to its origin and functions. *British Journal of Dermatology*, 159(1):23–34, 2008.

[232] Vincenzo Liguori, Claire Guillemin, Gian F. Pesce, René O. Mirimanoff, and Jacques Bernier. Double-blind, randomized clinical study comparing hyaluronic acid cream to placebo in patients treated with radiotherapy. *Radiotherapy and Oncology*, 42(2):155–161, 1997.

[233] Ralph Weissleder, Ching-Hsuan Tung, Umar Mahmood, and Alexei Bogdanov Jr. In vivo imaging of tumors with protease-activated near-infrared fluorescent probes. *Nature Biotechnology*, 17(4):375–378, 1999.

[234] Christoph Bremer, Ching-Hsuan Tung, and Ralph Weissleder. In vivo molecular target assessment of matrix metalloproteinase inhibition. *Nature Medicine*, 7(6):743–748, 2001.

[235] Vasilis Ntziachristos, Christoph Bremer, and Ralph Weissleder. Fluorescence imaging with near-infrared light: new technological advances that enable in vivo molecular imaging. *European Radiology*, 13(1):195–208, 2003.

[236] Adrian L. Polglase, Wendy J. McLaren, Stewart A. Skinner, Ralf Kiesslich, Markus F. Neurath, and Peter M. Delaney. A fluorescence confocal endomicroscope for in vivo microscopy of the upper- and the lower-gi tract. *Gastrointestinal Endoscopy*, 62(5):686–695, 2005.

[237] Philipp J. Keller and Ernst H. K. Stelzer. Quantitative in vivo imaging of entire embryos with digital scanned laser light sheet fluorescence microscopy. *Current Opinion in Neurobiology*, 18(6):624–632, 2008.

[238] Raja Atreya, Helmut Neumann, Clemens Neufert, Maximilian J. Waldner, Ulrike Billmeier, Yurdagül Zopf, Marcus Willma, Christine App, Tino Münster, Hermann Kessler, Stefanie Maas, Bernd Gebhardt, Ralph Heimke-Brinck, Eva Reuter, Frank Dörje, Tilman T. Rau, Wolfgang Uter, Thomas D. Wang, Ralf Kiesslich, Michael Vieth, Ewald Hannappel, and Markus F. Neurath. In vivo imaging using fluorescent antibodies to tumor necrosis factor predicts therapeutic response in crohn's disease. *Nature Medicine*, 20(3):313–318, 2014.

[239] Ipsita Dey-Guha, Anita Wolfer, Albert C. Yeh, John G. Albeck, Revati Darp, Eduardo Leon, Julia Wulfkuhle, Emanuel F. Petricoin III, Ben S. Wittner, and Sridhar Ramaswamy. Asymmetric cancer cell division regulated by akt. *Proceedings of the National Academy of Sciences*, 108(31):12845–12850, 2011.

[240] Ryoko Ando, Hiroshi Hama, Miki Yamamoto-Hino, Hideaki Mizuno, and Atsushi Miyawaki. An optical marker based on the uv-induced green-to-red photoconversion of a fluorescent protein. *Proceedings of the National Academy of Sciences*, 99(20):12651–12656, 2002.

[241] Dmitriy M. Chudakov, Sergey Lukyanov, and Konstantin A. Lukyanov. Tracking intracellular protein movements using photoswitchable fluorescent proteins ps-cfp2 and dendra2. *Nature Protocols*, 2(8):2024–2032, 2007.

[242] Ethel R. Pereira, Dmitriy Kedrin, Giorgio Seano, Olivia Gautier, Eelco F. J. Meijer, Dennis Jones, Shan-Min Chin, Shuji Kitahara, Echoe M. Bouta, Jonathan Chang, Elizabeth Beech, Han-Sin Jeong, Michael C. Carroll, Alphonse G. Taghian, and Timothy P. Padera. Lymph node metastases can invade local blood vessels, exit the node, and colonize distant organs in mice. *Science*, 359(6382):1403–1407, 2018.

[243] Conor L. Evans, Imran Rizvi, Tayyaba Hasan, and Johannes F. de Boer. In vitro ovarian tumor growth and treatment response dynamics visualized with time-lapse oct imaging. *Optics Express*, 17(11):8892–8906, 2009.

[244] Oliver J. Klein, Brijesh Bhayana, Yong Jin Park, and Conor L. Evans. In vitro optimization of etnbs-pdt against hypoxic tumor environments with a tiered, high-content, 3d model optical screening platform. *Molecular Pharmaceutics*, 9(11):3171–3182, 2012.

[245] Emily K. Pugach, Pulin Li, Richard White, and Leonard Zon. Retro-orbital injection in adult zebrafish. *Journal of Visualized Experiments*, (34):e1645, 2009.

[246] Inês M. Tenente, Qin Tang, John C. Moore, and David M. Langenau. Normal and malignant muscle cell transplantation into immune compromised adult zebrafish. *Journal of Visualized Experiments*, (94):e52597, 2014.

[247] Emmanuel Roussakis, Zongxi Li, Alexander J. Nichols, and Conor L. Evans. Oxygen-sensing methods in biomedicine from the macroscale to the microscale. *Angewandte Chemie International Edition*, 54(29):8340–8362, 2015.

[248] James K. Williams, David Entenberg, Yarong Wang, Alvaro Avivar-Valderas, Michael Padgen, Ashley Clark, Julio A. Aguirre-Ghiso, James Castracane, and John S. Condeelis. Validation of a device for the active manipulation of the tumor microenvironment during intravital imaging. *IntraVital*, 5(2):e1182271, 2016.

[249] J. Novak, I. Georgakoudi, X. Wei, A. Prossin, and C. P. Lin. In vivo flow cytometer for real-time detection and quantification of circulating cells. *Optics Letters*, 29(1):77–79, 2004.

[250] Irene Georgakoudi, Nicolas Solban, John Novak, William L. Rice, Xunbin Wei, Tayyaba Hasan, and Charles P. Lin. In vivo flow cytometry : A new method for enumerating circulating cancer cells. *Cancer Research*, 64(15):5044–5047, 2004.

[251] Valery V. Tuchin, Attila Tárnok, and Vladimir P. Zharov. In vivo flow cytometry: A horizon of opportunities. *Cytometry Part A*, 79A(10):737–745, 2011.

[252] Greg M. Thurber, Katy S. Yang, Thomas Reiner, Rainer H. Kohler, Peter Sorger, Tim Mitchison, and Ralph Weissleder. Single-cell and subcellular pharmacokinetic imaging allows insight into drug action in vivo. *Nature Communications*, 4:1504, 2013.

[253] Michael J. Mitchell, Rakesh K. Jain, and Robert Langer. Engineering and physical sciences in oncology: challenges and opportunities. *Nature Reviews Cancer*, 17(11):659–675, 2017.

[254] Nikolay S. Makarov, Claudiu Cirloganu, Joseph W. Perry, Konstantin A. Lukyanov, and Kyril M. Solntsev. Steady-state and time-resolved spectroscopic studies of green-to-red photoconversion of fluorescent protein dendra2. *Journal of Photochemistry and Photobiology A: Chemistry*, 280:5–13, 2014.

[255] Kimberly L. McArthur and Joseph R. Fetcho. Key features of structural and functional organization of zebrafish facial motor neurons are resilient to disruption of neuronal migration. *Current Biology*, 27(12):1746–1756, 2017.

[256] Claus Garbe and Ulrike Leiter. Melanoma epidemiology and trends. *Clinics in Dermatology*, 27(1):3–9, 2009.

[257] Seth M. Noar, Jessica G. Myrick, Brenda Morales-Pico, and Nancy E. Thomas. Development and validation of the comprehensive indoor tanning expectations scale. *JAMA Dermatology*, 150(5):512–521, 2014.

[258] Devarati Mitra, Xi Luo, Ann Morgan, Jin Wang, Mai P. Hoang, Jennifer Lo, Candace R. Guerrero, Jochen K. Lennerz, Martin C. Mihm, Jennifer A. Wargo, Kathleen C. Robinson, Suprabha P. Devi, Jillian C. Vanover, John A. D'Orazio, Martin McMahon, Marcus W. Bosenberg, Kevin M. Haigis, Daniel A. Haber, Yinsheng Wang, and David E. Fisher. An ultraviolet-radiation-independent pathway to melanoma carcinogenesis in the red hair/fair skin background. *Nature*, 491:449–453, 2012.

[259] Marco d'Ischia, Kazumasa Wakamatsu, Alessandra Napolitano, Stefania Briganti, José-Carlos Garcia-Borron, Daniela Kovacs, Paul Meredith, Alessandro Pezzella, Mauro Picardo, Tadeusz Sarna, John D. Simon, and Shosuke Ito.

Melanins and melanogenesis: methods, standards, protocols. *Pigment Cell & Melanoma Research*, 26(5):616–633, 2013.

[260] Ismael Galván, Alberto Jorge, Kazuma Ito, Keisuke Tabuchi, Francisco Solano, and Kazumasa Wakamatsu. Raman spectroscopy as a non-invasive technique for the quantification of melanins in feathers and hairs. *Pigment Cell & Melanoma Research*, 26(6):917–923, 2013.

[261] Ismael Galván, Alberto Jorge, Francisco Solano, and Kazumasa Wakamatsu. Vibrational characterization of pheomelanin and trichochrome f by raman spectroscopy. *Spectrochimica Acta Part A: Molecular and Biomolecular Spectroscopy*, 110:55–59, 2013.

[262] Véronique Delmas, Silvia Martinozzi, Yveline Bourgeois, Martin Holzenberger, and Lionel Larue. Cre-mediated recombination in the skin melanocyte lineage. *Genesis*, 36(2):73–80, 2003.

[263] Severine Tabone-Eglinger, Monique Wehrle-Haller, Nicole Aebischer, Marie-Claude Jacquier, and Bernhard Wehrle-Haller. Membrane-bound kit ligand regulates melanocyte adhesion and survival, providing physical interaction with an intraepithelial niche. *The FASEB Journal*, 26(9):3738–3753, 2012.

[264] Raymond L. Barnhill, Michael W. Piepkorn, and Klaus J. Busam. *Pathology of melanocytic nevi and melanoma*. Springer Science & Business Media, 2014.

[265] Susan E. Koch and Julie R. Lange. Amelanotic melanoma: the great masquerader. *Journal of the American Academy of Dermatology*, 42(5):731–734, 2000.

[266] Mary Jane Simpson, Jesse W. Wilson, M. Anthony Phipps, Francisco E. Robles, M. Angelica Selim, and Warren S. Warren. Nonlinear microscopy of eumelanin and pheomelanin with subcellular resolution. *Journal of Investigative Dermatology*, 133(7):1822–1826, 2013.

[267] Conor L. Evans, Eric O. Potma, Mehron Puoris'haag, Daniel Côté, Charles P. Lin, and X. Sunney Xie. Chemical imaging of tissue in vivo with video-rate coherent anti-stokes raman scattering microscopy. *Proceedings of the National Academy of Sciences*, 102(46):16807–16812, 2005.

[268] Tak W. Kee and Marcus T. Cicerone. Simple approach to one-laser, broadband coherent anti-stokes raman scattering microscopy. *Optics Letters*, 29(23):2701–2703, 2004.

[269] Tak W. Kee, Hongxia Zhao, and Marcus T. Cicerone. One-laser interferometric broadband coherent anti-stokes raman scattering. *Optics Express*, 14(8):3631–3640, 2006.

[270] Lu Wei, Zhixing Chen, Lixue Shi, Rong Long, Andrew V. Anzalone, Luyuan Zhang, Fanghao Hu, Rafael Yuste, Virginia W. Cornish, and Wei Min. Super-multiplex vibrational imaging. *Nature*, 544(7651):465–470, 2017.

[271] Christopher J. Rowlands, Demian Park, Oliver T. Bruns, Kiryl D. Piatkevich, Dai Fukumura, Rakesh K. Jain, Moungi G. Bawendi, Edward S. Boyden, and Peter T. C. So. Wide-field three-photon excitation in biological samples. *Light: Science & Applications*, 6(5):e16255, 2017.